Realistic Integration of Sorption Processes in Transport Codes for Long-Term Safety Assessments

Conducted by:

GRS - 297

Gesellschaft für Anlagen-
und Reaktorsicherheit
(GRS) mbH

Realistic Integration of Sorption Processes in Transport Codes for Long-Term Safety Assessments

Ulrich Noseck (GRS)
Vinzenz Brendler (HZDR)
Judith Flügge (GRS)
Madlen Stockmann (HZDR)
Susan Britz (GRS)
Michael Lampe (G-CSC)
Johannes Schikora (HZDR)
Anke Schneider (GRS)

September 2012

Acknowledgement:

This report was prepared under the contract Nos. 02 E 10518 and 02 E 10528 by the Federal Ministry of Economics and Technology (BMWi).

The work was conducted by the Gesellschaft für Anlagen- und Reaktorsicherheit (GRS) mbH and the Helmholtz-Zentrum Dresden-Rossendorf e.V. (HZDR).

The authors are responsible for the content of the report.

GRS - 297
ISBN 978-3-939355-76-2

Keywords:
Climate Change, Groundwater, Long-Term Safety Analysis, Modeling, Radionuclide Transport, Smart K_d, Sorption

Zusammenfassung

Als Teil eines Langzeitsicherheitsnachweises für Endlager für radioaktive Abfälle sind unter anderem Szenarien zu betrachten, bei denen es zu einer Mobilisierung von Radionukliden aus den Abfällen und damit zu deren Transport durch das Endlagersystem kommen kann. Eine potenzielle Barriere im System eines Endlagers stellt neben dem Wirtsgestein auch das darüber liegende Deckgebirge dar. Der Transport durch die Geosphäre wird für viele Radionuklide durch Sorption an Oberflächen vorhandener Mineralphasen, die durch die geochemischen Bedingungen bestimmt wird und zeitlich und räumlich erheblich variieren kann, verlangsamt. In bisher verwendeten Transportprogrammen wird die Rückhaltung der Radionuklide über zeitlich und räumlich konstante Verteilungskoeffizienten (K_d-Werte) beschrieben.

Eine Verbesserung der Modellierung sollte den Einfluss der wichtigsten geochemischen Parameter auf die Sorption beinhalten. Eine Möglichkeit hierfür stellt das sogenannte Smart K_d-Konzept dar. Ein solcher Modellansatz basiert auf mechanistischen Oberflächenkomplexierungsmodellen (SCM), die hier mit einem „Bottom-Up-Ansatz“ kombiniert werden. Dabei wird die Sorption eines Elements an einem Sediment einer hydrogeologischen Einheit als Summe der Sorption des Elements an jeder einzelnen Mineralfraktion beschrieben. Jedes Sediment besteht dabei aus einer definierten Zusammensetzung verschiedener Minerale. In dieser Arbeit wurde eine Implementierung des Smart K_d-Konzepts in das Transportprogramm r^3t, das zur Simulation des Schadstofftransportes durch große Modellgebiete über sehr lange Zeiträume in der Langzeitsicherheitsanalyse eingesetzt wird, umgesetzt. In der ersten Entwicklungsstufe wurde ein typisches sedimentäres System, das Steinsalz- und Tonformationen in Norddeutschland überlagert, betrachtet. Das ausgewählte System kann grob in drei verschiedene hydrogeologische Einheiten unterteilt werden: einen oberen Grundwasserleiter, einen Aquitard und einen unteren Grundwasserleiter. Oberer und unterer Grundwasserleiter sind durch hydraulische Fenster im dazwischenliegenden Aquitard verbunden. Jede hydrogeologische Einheit ist durch eine spezifische mineralogische Zusammensetzung charakterisiert. Um die Sorbate (Element-Mineral-Paare) auf eine handhabbare Zahl zu beschränken, wurde die Anzahl der betrachteten Minerale und Elemente begrenzt. Die Auswahl der Mineralphasen basiert zum einen auf Daten aus Berichten zur Petrographie von Proben, die aus verschiedenen Bohrkernen vom Standort Gorleben genommen wurden. Zum anderen ging ihre Relevanz hinsichtlich der Sorption bzw. ihres

Einflusses auf die geochemischen Bedingungen in die Auswahl ein. Als wichtigste Minerale wurden Quarz, K-Feldspat, Muskovit, Gibbsit, Goethit, Calcit, Kaolinit und Illit ausgewählt. Für die Elemente wurden drei Gruppen berücksichtigt: Elemente, die als Radionuklide auftreten, Konkurrenzkationen hinsichtlich der Sorption und komplexbildende Liganden. Die Auswahl der Elemente der ersten Gruppe basiert auf ihrer Relevanz für die Langzeitsicherheit, der Frage, ob sie überhaupt sorbieren und der Verfügbarkeit ausreichender und vertrauenswürdiger thermodynamischer Daten. Für die zweite und dritte Gruppe ist der Einfluss auf die Sorption der Radionuklide und die Frage, ob sie in relevanten Konzentrationen im natürlichen System vorhanden sind, bzw. aus dem Endlager freigesetzt werden können, entscheidend. Letztlich wurden Ni, Se, Cs, Cm, Am, Pu, U, Th, Np, Ra, Ca, Fe, Al, CO_3^{2-}, und SiO_3^{2-} ausgewählt.

Für die Untersuchungen und Rechnungen in diesem Projekt wurde eine eigene thermodynamische Datenbasis (ESTRAL.dat) erstellt, die (i) Daten für Spezies in Lösung und für feste Mineralphasen sowie (ii) Sorptionsdaten für repräsentative Sorbate enthält. Dazu wurden die publizierten Daten für die ausgewählten Elemente und Mineralphasen identifiziert und im Detail überprüft. Da für einige relevante Mineralphasen – speziell für Feldspäte und Glimmer – keine Sorptionsparameter für Oberflächenkomplexmodelle vorhanden waren, wurden zusätzlich Batch-Experimente mit Cs^+, Sr^{2+} und Eu^{3+} an Orthoklas und Muskovit durchgeführt. Anhand von Titrationskurven für beide Minerale und den Ergebnissen aus den Batch-Sorptionsexperimenten wurden thermodynamische Daten bestimmt und in die ESTRAL-Datenbasis aufgenommen.

Die Sorption von Radionukliden an den Mineralphasen wird durch geochemische Einflussgrößen, wie pH-Wert, Temperatur, Ionenstärke (im Wesentlichen gegeben durch die Salzkonzentration) oder Konzentration von Komplexbildnern und Konkurrenzkationen bestimmt. Um die Komplexität und die Rechenzeit möglichst klein zu halten, wurde die Anzahl der Parameter begrenzt und nur diejenigen berücksichtigt, die einen starken Einfluss auf die Sorptionsprozesse haben. Als geochemische Parameter wurden pH-Wert, Ionenstärke sowie die Konzentration von Ca, DIC (gelöster anorganischer Kohlenstoff; Dissolved Inorganic Carbon) und des jeweiligen Radionuklids (Elements) ausgewählt. Zusätzlich wurden weitere Komplexbildner und Konkurrenzkationen (Si, Al und Fe) indirekt berücksichtigt. Hierbei wurde angenommen, dass die Konzentrationen der Ionen SiO_3^{2-}, Al^{3+} und Fe^{3+} primär durch das Gleichgewicht mit der löslichkeitsbestimmenden Mineralphase Quarz, Gibbsit,

bzw. Hämatit bestimmt wird. Daher konnten deren Konzentrationen direkt als Teil der Berechnungsprozedur für die K_d -Werte generiert werden.

Für jede Kombination Element/Sediment werden K_d-Werte als Funktion der ausgewählten geochemischen Einflussgrößen berechnet und in mehrdimensionalen Matrizen abgelegt. Diese Berechnung erfolgt mit dem geochemischen Speziationscode PHREEQC. Parametervariationen wurden mit dem Programm UCODE durchgeführt. Sensitivitäts- und Unsicherheitsanalysen der K_d-Werte wurden realisiert, in dem der Code SimLab als äußere Routine an die beiden Rechencodes PHREEQC und UCODE gekoppelt wurde.

Mittelwerte der berechneten Verteilungskoeffizienten wurden mit Ergebnissen aus experimentellen Untersuchungen an Gorleben Sedimenten verglichen. Die Ergebnisse zeigen eine gute Übereinstimmung für die meisten der zehn ausgewählten Radionuklide. Weiterhin zeigen die Sensitivitätsanalysen, dass für alle zehn Radionuklide der pH-Wert, die DIC- und die Ca-Konzentration die wichtigsten Einflussgrößen in dem hier betrachteten Bereich darstellen.

Um den hier verwendeten „Bottom-Up-Ansatz“ zu überprüfen, wurden zwei Testfälle ausgewählt. Zum einen wurden zusätzliche Sorptionsexperimente mit Eu^{3+} an einem speziellen Mineralgemisch aus Quarz, Orthoklas und Muskovit („Synthetisches Sediment“) unter Variation von pH-Wert, Elementkonzentration und Volumen / Masse Verhältnis durchgeführt. Neben der erfolgreichen Überprüfung, ob die Beiträge der einzelnen Mineralphasen die Sorption am Sediment adäquat beschreiben, geben die gut übereinstimmenden Ergebnisse auch Vertrauen in die neu abgeleiteten Sorptionsdatensätze für Eu an Orthoklas und Muskovit. Zum anderen wurde anhand von Daten aus Batch-Sorptionsexperimenten aus der Literatur überprüft, ob der Modellansatz, die Sorptionsmodelle und die zugehörigen Parameter das Sorptionsverhalten von Uran an natürlichen und synthetischen Feinsanden gut beschreiben. Generell zeigen die Testrechnungen eine gute Übereinstimmung zwischen Modell und Experiment und untermauern damit das hier entwickelte und angewendete Konzept.

Ein Kernstück des Projekts ist das konzeptuelle Modell für die Implementierung der relevanten geochemischen Prozesse in den Transportcode. Wie oben beschrieben wurden als geochemische Einflussgrößen der pH-Wert, die Ionenstärke sowie die Konzentration von DIC, Ca und der zehn Radionuklide ausgewählt. Eine wichtige

Annahme ist, dass die Wechselwirkung der Radionuklide untereinander und ihr Einfluss auf die geochemischen Bedingungen vernachlässigt werden kann, da sie nur in Spurenkonzentrationen auftreten. Die Zulässigkeit dieser Annahme wurde in Testrechnungen bestätigt. Deshalb wurde der Schwerpunkt auf die Behandlung der vier anderen Einflussgrößen gelegt. Eine zentrale Frage ist die Behandlung des pH-Werts, der nicht nur durch den Transport der Protonen, sondern auch durch Reaktion mit gelösten Ionen (hauptsächlich DIC und Ca) und den Mineralphasen der Sedimente bestimmt wird. Entsprechend der Ergebnisse der Standortuntersuchungen sind die wichtigsten Reaktionen in den Grundwasserleitern von Gorleben Calcit-Auflösung, mikrobieller Abbau von sedimentärem organischem Kohlenstoff, der zu erhöhten CO_2-Partialdrücken führt und die Auflösung von Feldspäten. Ionenaustauschprozesse, die hauptsächlich im Aquitard und an den Grenzflächen zum oberen Grundwasserleiter auftreten, wurden nicht betrachtet, um die Komplexität des Systems möglichst gering zu halten. Kern des Konzepts ist der Einfluss der Calcitauflösung und ausfällung auf den pH-Wert, wie sie in vielen natürlichen Systemen beobachtet wird.

Um die Implementierung des Konzepts in das Rechenprogramm r^3t und seine Leistungsfähigkeit zu überprüfen, wurden drei Anwendungsfälle ausgewählt. Zwei 1D-Testfälle wurden verwendet, um das entwickelte Konzept auf Plausibilität zu überprüfen. Die Testfälle wurden so ausgelegt, dass zeitliche chemische Veränderungen die Auflösung bzw. Ausfällung von Calcit bewirken und diese wiederum den pH-Wert sowie die Konzentration von DIC und Ca verändern. Als Konsequenz davon werden der K_d-Wert und damit der Transport der Radionuklide beeinflusst. Die Ergebnisse der 1D-Rechnungen sind plausibel und zeigen die erfolgreiche Implementierung des Smart K_d-Konzepts in das Rechenprogramm r^3t. Außerdem wurde ein 2D-Testfall untersucht. Dieser 2D-Fall wurde aus den erwarteten Einflüssen zukünftiger Klimaänderungen auf die hydraulischen Bedingungen in norddeutschen Grundwassersystemen abgeleitet. Damit stellt er einen Rechenfall dar, der durchaus in einem Safety Case für ein potentielles Endlager in Norddeutschland zu betrachten wäre. Die Simulationen zeigen, dass die geochemischen Einflussparameter den erwarteten Trends folgen und wie sie gegenseitig voneinander abhängen. Die K_d-Werte verändern sich entsprechend der Änderungen in den geochemischen Einflussparametern. Der pH-Wert hat dabei den stärksten Effekt auf die Smart K_d-Werte für die meisten Elemente mit Ausnahme von Th und Pu, bei denen der Einfluss der DIC-Konzentration noch entscheidender ist. Die Abhängigkeiten treten zu unterschiedlichen Zeiten an verschiedenen Orten auf und werden durch Strömungs- und

Transportcharakteristika geprägt, die wiederum aus Änderungen in den Randbedingungen für verschiedene Klimazustände und –übergänge resultieren. Die Ergebnisse sind erfolgversprechend und zeigen, dass die Methode in der Lage ist, chemische Veränderungen über lange Zeiträume in großen Modellgebieten und ihren Einfluss auf die Radionuklidsorption mit akzeptablen Rechenkosten zu beschreiben. Damit erfüllt das Konzept die Anforderungen der Langzeitsicherheitsanalyse. Weitere Testrechnungen sind notwendig, um den entsprechend modifizierten Transportcode weiter zu qualifizieren. In einfachen wie auch komplexeren Modellrechnungen ist die Anwendbarkeit des Modells für weitere Variationen der geochemischen Einflussgrößen, der Modellgeometrie, der Heterogenität und der Komplexität der Strömung zu zeigen.

In einer nächsten Entwicklungsstufe sollten auch Redoxreaktionen und Ionenaustausch berücksichtigt werden. Speziell die Redoxbedingungen haben große Auswirkungen auf die Sorption redoxsensitiver Radionuklide, für die im Rahmen der hier vorgestellten Studie angenommen wurde, dass sie in oxidierter Form vorliegen. Zudem sollte der Einfluss weiterer Konkurrenzkationen und Komplexbildner auf die Radionuklidsorption im Detail untersucht und mit dem hier entwickelten Ansatz simuliert werden. Schließlich sollte auch die Anwendung des Konzepts auf hochsalinare Bedingungen, wie sie in den tieferen Grundwasserleitern in Norddeutschland anzutreffen sind, durch Anwendung des Pitzer-Formalismus getestet werden.

Abstract

One important aspect in long-term safety assessment is related to radionuclide transport in geologic formations. In order to assess its consequences over assessment periods of one million years numerical models describing flow and transport are applied. Sorption on mineral surfaces is the most relevant process retarding radionuclide transport. On the one hand an increased transport time might cause a decrease in radionuclide concentration by radioactive decay. On the other hand it might increase concentrations of dose-relevant daughter nuclides in decay chains.

In order to treat the radionuclide sorption processes in natural systems close to reality the so-called smart K_d-concept is implemented into the transport program r^3t, which is applied to large model areas and very long time scales in long-term safety assessment. In the first stage this approach is developed for a typical sedimentary system covering rock salt and clay formations in Northern Germany. The smart K_d-values are based on mechanistic surface complexation models (SCM), varying in time and space and depending on the actual geochemical conditions, which might change in the future e. g. due to the impact of climate changes. The concept developed and introduced here is based on a feasible treatment of the most relevant geochemical parameters in the transport code as well as on a matrix of smart K_d-values calculated in dependence on these parameters.

The implementation of the concept comprises the selection of relevant elements and minerals to be considered, an experimental program to fill data gaps of the thermodynamic sorption database, an uncertainty and sensitivity analysis to identify the most important environmental parameters influencing sorption of long-term relevant radionuclides, the creation of a matrix with K_d-values dependent on the selected environmental parameters, and the development and realisation of the conceptual model for treatment of temporal and spatial changes of the geochemical conditions.

The implementation of this concept into the transport code r^3t, particularly the feasibility and capability of the method is tested by two kinds of application cases. 1D test cases are used to check the plausibility of the development in a relatively simple system, where chemical changes cause dissolution or precipitation of calcite, which in turn affect the pH-value, the DIC and Ca concentrations. In consequence the K_d-value and therewith the transport of the radionuclides is impacted. The results of the 1D calcula-

tions are plausible showing the applicability of this approach to implement the smart K_d-concept. One 2D test case is considered and results show that the method is able to describe long-term chemical changes in large model areas including their impact on radionuclide sorption. A further positive aspect is that these calculations are performed with acceptable calculation costs.

Table of contents

1 Introduction

In Germany, high-level radioactive waste is to be disposed of in deep geological formations. Long-term safety assessments have to be carried out as part of the post-closure safety case for radioactive waste repositories. According to the German safety requirements for heat-generating radioactive waste an assessment period of one million years has to be regarded /BMU 10/. Although the assessment is focussed on the proof of a safe contaiment of the waste in the so-called contaiment providing rock zone, scenarios, which lead to the mobilization of radionuclides from the waste and to their transport through the repository system, cannot be excluded and need to be adressed in long-term safety assessment. During transport through the repository system sorption on mineral surfaces of rocks and technical materials is an important retardation process for radionuclides. Besides dispersion and dilution, the increased travel time due to retardation leads to a reduction of their concentration and thus of the radiation exposure because of additional radioactive decay of many radionuclides during transport. On the other hand, retarding the transport of a mother nuclide could lead to an elevated generation of daughter nuclides and, in case the daughter nuclide is dose relevant, to an elevated radiation exposure. Describing the sorption as realistically as possible is therefore one important aspect in long-term safety assessment.

Spatially and temporally constant sorption coefficients, K_d-values, for each hydrogeological unit are currently used in transport codes for long-term safety assessment. However, temporally and spatially variable geochemical conditions could lead to significant changes in the sorption of different radionuclides. Therefore, a description of sorption as a transient parameter depending on environmental parameters is required. An advanced methodology to handle variable sorption in form of the newly established “smart K_d-values” in codes for long-term safety assessments is being developed and tested here. Exemplarily, the radionuclide transport in a sedimentary system overlying salt and clay formations in Northern Germany is regarded.

In the considered assessment period of one million years geochemical changes are likely be caused by long-term climate changes. Such climate changes may lead to events like a transgression of the sea and the inundation of the respective site, or to the formation of permafrost in the sedimentary overburden. In case of a seawater

transgression water with a higher salinity than groundwater leads to geochemical changes in the sedimentary system. In case of permafrost low mineralised meltwater can intrude unfrozen aquifers and by this change the groundwater conditions, particularly if an inland ice sheet occurs in close vicinity of the respective site.

In a first step this concept is developed for the transport in a sedimentary overburden. However, such geochemical changes will also occur in other geological formations and other parts of the repository system, which will be considered in future development stages. Examples, where a concept of transient modelling of K_d-values has been applied, are /SAM 09/ and /SCH 08/. In order to test the validity of the K_d approach and use of solubility limits nuclide sorption and precipitation for a bentonite barrier in the near field of a repository in granite was reagarded in /SAM 09/. Reactive transport models have been used to study the evolution of the geochemistry of the bentonite barrier, simultaneously to the transport of radionuclides considering the elements Ni, Cs, and U. The most useful result obtained with the reactive transport models is the dependence of the distribution coefficients (K_d) of the transported species on environmental parameters, such as pH, Eh and ionic strength. The implementation of a K_d that depends on environmental parameters (such as pH, ionic strength or the dissolved concentration of the transported species) into the performance assessment (PA) code was capable of reproducing the results obtained with the reactive transport models. In /SCH 08/ time-dependent K_d-values have been applied to take into account the degradation of cement in a disposal chamber for low and intermediate level waste (LLW and ILW). In the degradation phase cement stone is transferred into calcite, which is described by a linear function for the decrease of cement stone and increase of calcite. The overall distribution coefficient changes in dependence of the amount of both phases, since the sorption of the radionuclides strongly differs for both materials.

In this report the newly developed concept and its application to one- and two-dimensional application cases is presented. In a first step the most relevant elements and mineral phases are identified and selected as described in section 2. Section 3 shows the data situation for thermodynamic sorption modelling of the system and identifies lacking data. A series of batch experiments have been performed to fill the most crucial data gaps (section 4). Section 5 describes the determination of the governing environmetal data with highest influence on sorption and section 6 the calculation of K_d-matrices as function of the environmental parameters. The whole

concept for implementation of the “smart K_d” into the transport programme is described in section 7 and its application in section 8.

2 Compilation of relevant elements, minerals and sediments

2.1 Identification and selection of mineral phases

The sedimentary rock above the salt dome Gorleben consists mainly of tertiary and quaternary sands and clays /KLI 02/. The major constituent of quaternary Elsterian, Saalian and Weichselian sediments is quartz. Sandy sediments contain about 85 wt% quartz and 10 wt% feldspar /ART 98/. The argillaceous to silty sediments are dominated by higher contents of clay minerals and calcite, which is ubiquitous in glacial moraines /GRI XX/. Minor constituents are feldspars and mica (muscovite) and accessory minerals are gypsum and dolomite. Tab. 2.1 shows an overview of all relevant site-specific minerals in the Gorleben sediments.

In order to limit the number of minerals, only those were selected that are commonly found as major (> 25 wt%) or minor phases (5 – 25 wt%) in sediments, and are important for the geochemical conditions on the transport pathway and the sorption processes. In the following it is distinguished between “transport relevant” and “sorption relevant” minerals:

1. Transport relevant minerals affect the geochemical conditions in the different hydrogeological units and have to be included in transport calculations (e. g. quartz, feldspars, calcite).

2. Sorption relevant minerals are important for sorption processes of radionuclides released from the repository.

Our reasons and arguments for the selection of minerals are documented in Tab. 2.1 in detail based on /MAS 85/. Minerals with similar structure and composition were grouped. All relevant minerals for the project are marked in italics. All abbreviations for minerals are marked with asterisk and correspond to the international code after /KRE 83/.

Generally, salt minerals (e. g. halite, sylvite, polyhalite, kainite, carnallite) are not relevant for this project due to their high solubility. Nevertheless, the groundwater directly above the salt dome is strongly impacted by salt dissolution at the contact to the salt dome and sorption processes are reduced by the high ionic strength of this water.

Therefore, salt minerals were not taken into account as transport or sorption relevant minerals within the sedimentary units. Contents of dissolved salt minerals in groundwater were considered by a respective sodium and chloride concentration.

Tab. 2.1 Compilation of site-specific minerals in sedimentary rock above the Gorleben salt dome

Mineral	Abb.*	Formula	Description
(1) PRIMARY SILICATE MINERALS			
Quartz	Qtz	SiO_2	Quartz as the major constituent in the Gorleben aquifer system is generally relevant and will be taken into account in all calculations. Supplementary SCM data were used from amorphous Silica.
Feldspars			
Albite	Ab	$NaAlSi_3O_8$	Feldspars are ubiquitous in the sediments and relevant for both transport and sorption calculations. For sorption studies all SCM data will be grouped because of the sparsely populated data matrix. Additional batch experiments (section 4) are performed for K-feldspar (orthoclase) which has a higher weathering stability than plagioclase (albite, anorthite). For some scoping transport calculations orthoclase and anorthite are selected as representative mineral phases.
Anorthite	An	$CaAl_2Si_2O_8$	
Orthoclase	Or	$KAlSi_3O_8$	
Microcline	Mc	$KAlSi_3O_8$	

Italics: Selected mineral phases for transport and sorption studies.

* All abbreviations correspond to the international code after /KRE 83/

Tab. 2.1 (cont.) Compilation of site-specific minerals in sedimentary rock above the Gorleben salt dome

Mineral	Abb.*	Formula	Description
Mica			
Muscovite	Ms	$KAl_3Si_3O_{10}(OH)_2$	Muscovite is the dominant mica mineral but a minor constituent in the Gorleben sediments. For sorption calculations data for muscovite and biotite are grouped because of the sparse SCM data sets.
Biotite	Bt	$K(Mg,Fe)_3[(OH)_2[(Al,Fe)Si_3O_{10}]$	
(2) CARBONATES			
Calcite	Cc	$CaCO_3$	Calcite mainly occurs in the upper aquifer and in the aquitard. In the argillaceous sediments calcite is a major constituent. Aragonite is irrelevant due to its higher solubility and its scarce occurrence. Dolomite is an accessory mineral (< 0.5 wt%) only found in few samples. Other carbonate minerals are also rare and irrelevant. Generally, for sorption studies all carbonates are not relevant because of their high solubility and dynamic surface. Calcite is selected as important mineral for transport calculations.
Aragonite	Arg	$CaCO_3$	
Dolomite	Dol	$CaMg(CO_3)_2$	

Italics: Selected mineral phases for transport and sorption studies.

* All abbreviations correspond to the international code after /KRE 83/

Tab. 2.1 (cont.) Compilation of site-specific minerals in sedimentary rock above the Gorleben salt dome

Mineral	Abb.*	Formula	Description
(3) SULFATES			
Anhydrite	Anh	$CaSO_4$	The sulfates are not primarily dealt with in this study because they are mostly found in the cap rock but not in the overlying sediments due to their high solubility. However, anhydrite and gypsum in the cap rock represent a Ca source for the groundwater in the overlying aquifers. In order to estimate the impact of this source, gypsum (anhydrite is predominantly converted to gypsum) is selected in some scoping transport calculations. Barite is an accessory mineral, but cannot be considered due to a lack of SCM data sets. Other sulfate minerals like kieserite ($MgSO_4 \cdot H_2O$) or jarosite ($FeSO_4$) are irrelevant.
Gypsum	Gp	$CaSO_4 \cdot H_2O$	
Barite	Brt	$BaSO_4$	

Italics: Selected mineral phases for transport and sorption studies.

* All abbreviations correspond to the international code after /KRE 83/

Tab. 2.1 (cont.) Compilation of site-specific minerals in sedimentary rock above the Gorleben salt dome

Mineral	Abb.*	Formula	Description
(4) CLAY MINERALS			
2-layer clay minerals			
Kaolinite	Kln	$Al_2Si_2O_5(OH)_4$	Kaolinite is chosen as a representative for 2-layer clay minerals (1:1 structure). It is ubiquitous in fine-grained sediments and very important as sorbent, e. g. for actinides like UO_2^{2+} and Am^{3+}.
Mixed-layer clay minerals			
Illite	Ill	$(K,Fe)Al_{2,6}Si_{3,15}O_{10}(OH)_2$	The 3-layer clay minerals (2:1 structure) illite and montmorillonite are important constituents of argillaceous Gorleben sediments. Both secondary weathering minerals are relevant as sorbent for actinides (Np, U, P) due to their silanol (SiOH) and aluminol (AlOH) groups at their surfaces. Because of the sparse SCM data sets they are grouped. With regard to transport calculations the impact of clays is exemplarily investigated using illite. In case of insufficient SCM data sets for illite and montmorillonite, SCM data from bentonite are used.
Montmorillonite	Mnt	$(Na,Mg,Fe)Al_1Si_4O_{10}[(OH)_2$	

Italics: Selected mineral phases for transport and sorption studies.

* All abbreviations correspond to the international code after /KRE 83/

Tab. 2.1 (cont.) Compilation of site-specific minerals in sedimentary rock above the Gorleben salt dome

Mineral	Abb.*	Formula	Description
Chlorite	Chl	$(Mg,Fe,Ca)Al_2Si_3O_{10}(OH)_8$	Chlorite, as 4-layer-clay mineral (3:1 structure), is a minor constituent in the sediments and considered as a representative mineral phase for the transport calculations. Regarding the sorption calculations, chlorite is assigned to the mixed-layer clay group.
(5) OXIDES AND HYDROXIDES			
Fe(III)-oxide/-hydroxides			
Goethite	Gt	FeOOH	During the weathering of iron-bearing minerals in humid climate, mostly goethite is crystallized. Additionally, at higher soil temperatures, hematite is formed. Both trivalent iron minerals are important for sorption and transport processes in the oxidation zone of Gorleben sediments. For sorption studies, the SCM data sets were grouped to Fe(III)-oxide/-hydroxide. Ferrihydrite is not considered due to the metastable ionic form (fast dehydration). Also magnetite which is weathering resistant and important as a sorbent is not considered due to its rare occurrence and our
Hematite	Hem	Fe_2O_3	
Ferrihydrite	-	$5Fe_2O_3.9H_2O$	

Italics: Selected mineral phases for transport and sorption studies.

* All abbreviations correspond to the international code after /KRE 83/

Tab. 2.1 (cont.) Compilation of site-specific minerals in sedimentary rock above the Gorleben salt dome

Mineral	**Abb.***	**Formula**	**Description**
Magnetite	Mag	$Fe^{II}(Fe^{III})_2O_4$	restriction to trivalent iron. Ilmenite is not relevant for this study due to its rare occurrence.
Ilmenite	Ilm	$FeTiO_3$	
Aluminumhydroxides			
Gibbsite	Gbs	$Al(OH)_3$	Besides the formation of clay minerals, mostly Al-hydroxides were precipitated by weathering of aluminum-bearing minerals. For sorption calculations all relevant hydrated Al-minerals as well as other Aluminumspecies ($AlOH_{amorph}$) are grouped to "Aluminumhydroxides" because of the sparse SCM data sets. The SCM data from γ-Alumina is not used due to its different crystal structure. For some scoping transport calculations the impact of gibbsite, which is the most common one of this group, is exemplarily investigated.
Boehmite	Bhm	AlO(OH)	
Diaspore	Dsp	AlO(OH)	

Italics: Selected mineral phases for transport and sorption studies.

* All abbreviations correspond to the international code after /KRE 83/

2.2 Definition of the sediment units

Since 1979, the Gorleben salt dome in Lower Saxony, Northern Germany, is being investigated by the Federal Institute for Geosciences and Natural Resources (BGR) and several other research organizations for its suitability to host a nuclear waste repository /KLI 07, KOE 07/. A comprehensive dataset is available on the geology and hydrogeology of the Gorleben salt dome and its overburden. Therefore it was chosen as a reference site for this work. The Gorleben-Rambow salt structure has a length of ca. 30 km and a varying width between 1.5 km and 4 km. It strikes SW-NE and is crossed by the river Elbe and its tributaries Löcknitz and Seege at the surface /KLI 07/.

2.3 Geology and hydrogeology of the reference site Gorleben

The Tertiary and Quaternary sedimentary overburden of the salt dome and its neighboring rim synclines form a system of aquifers and aquitards of up to 430 m thickness /KLI 02/. The basis of the regional flow system is represented by the Tertiary Rupel Clay. The Tertiary Lower Brown Coal Sands and Eochatt silts and the Quaternary Elsterian channel sands form the lower aquifer /LUD 02/. The aquitard is a set of the Tertiary Hamburg Clay and the Quaternary Lauenburg Clay Complex, which is superposed by Weichselian and Saalian sediments representing the upper aquifer /KLI 02/. Main structural elements of the system are the salt dome itself with the adjacent northwestern and southeastern rim synclines, a contact of the salt dome to the lower aquifer in a glacial meltwater channel, the so-called Gorleben channel, formed by glacial erosion during the Elsterian cold stage, and hydraulic windows in the intercalated aquitard, likewise formed by glacial erosion /KLI 07/.

The hydraulic system can be roughly divided into a lower aquifer, an intercalated aquitard and an upper aquifer (Fig. 2.1). Due to the contact of the Zechstein salt to the Quaternary aquifer in the Gorleben Channel, salt can be dissolved by the groundwater. The groundwater shows a stratification into an upper fresh water body and a lower salt water body /LUD 02/. The groundwater of the lower aquifer is generally saline, while the upper aquifer predominately shows fresh water conditions. Locally occurring hydraulic windows in the aquitard enable the exchange of groundwater between the two aquifers. The distinct relief of the basis of the fresh water body is caused by the relief of the aquitard as well as by the regional groundwater flow. The highest fresh water thicknesses occur in those areas of the rim synclines where the salt water descends due to

its higher density as well as where the aquitard is missing. The lowest thicknesses are found in the entire area of river beds and lowlands north of the river Elbe and above the Gorleben salt dome. The salt water/fresh water interface rises from the Gorleben Channel to the north and reaches the water table close to the river Elbe /KLI 07, LUD 02/.

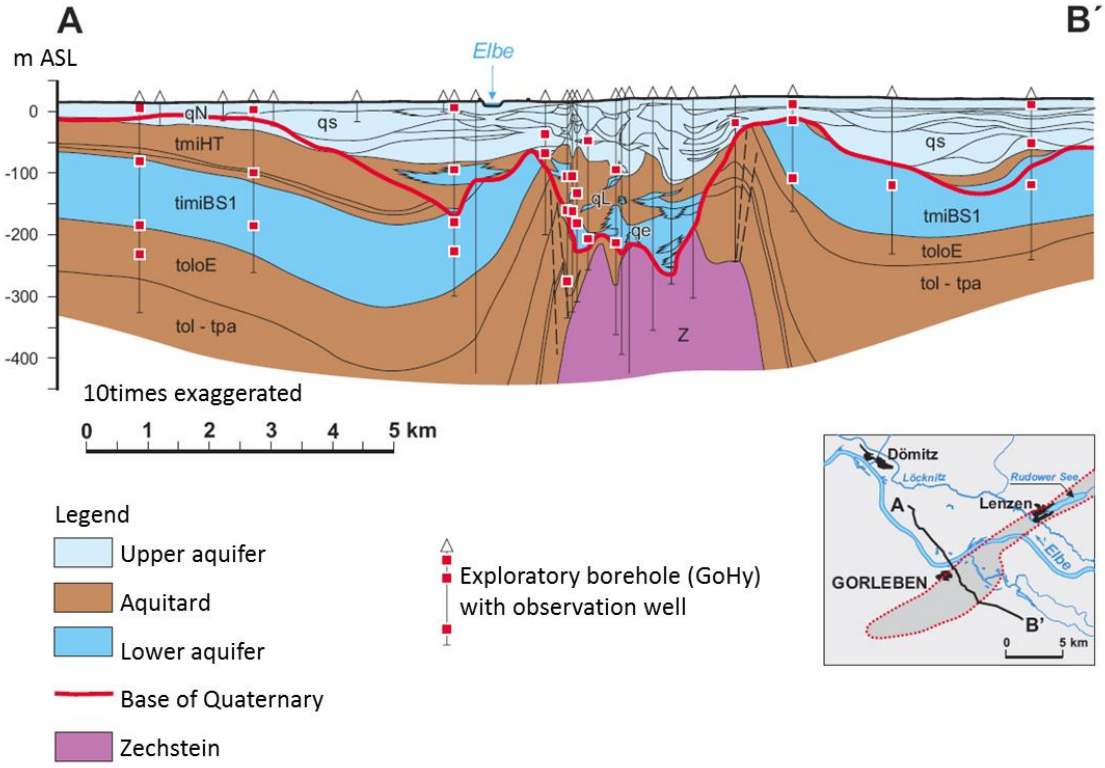

Fig. 2.1 Aquifer subdivision in the overburden of the Gorleben salt dome after /KLI 07/

In this project, the focus was on the sedimentary overburden above the Gorleben salt dome, which can be classified as follows /KLI 02, ZIR 03/:

- upper aquifer (UAF)
- aquitard (AT)
- lower aquifer (LAF).

The upper aquifer is a highly heterogeneous sequence of mainly Quaternary sediments originating from the Weichselian and Saalian cold stages. Lithologically, they can be denoted as arenaceous to pebbly meltwater deposits with a slight calciferous content /ZIR 03/.

The lower aquifer consists mainly of Tertiary Lower Brown Coal Sands and Quaternary sands of the Elsterian meltwater channels. Due to the hydrogeochemical processes, which are place emphasis on in our work, only its upper part is of special interest to us. To this end, the focus was on the sedimentary compositions found in the upper part of the lower aquifer. These sediments can be described as fine- to medium-grained arenaceous sands with a low content of silt and mica. They are generally free of calcium carbonate and show lignite beds in the upper parts. Due to their high content of quartz, they are assigned to the „Quartz Sand Group“ /ZIR 03/. The Elsterian meltwater sands show a sporadic content of brown coal and low contents of mica /ZIR 03/.

The two aquifers are hydraulically separated by an aquitard represented by the Lauenburg Clay Complex and the Hamburg Clay. These are argillaceous and silty sediments with a certain content of mica and calcium carbonate /ZIR 03/. Hydraulic windows enable the groundwater exchange between the two aquifers /KLI 02/.

In order to define representative mineral compositions for the three sedimentary units of the Gorleben overburden the weight-percentage of minerals in the sediments needed to be estimated. Comprehensive sediment analysis were carried out by Prof. Dr. Wolf-Dieter Grimm (Institut für Allgemeine und Angewandte Geologie, Universität München) and documented by the former Gesellschaft für Strahlenforschung (GSF) on behalf of the Physikalisch-Technische Bundesanstalt (PTB), formerly responsible for the implementing of waste repositories. These reports /GRI XX/ were consulted as well as different publications by the Bundesanstalt für Geowissenschaften und Rohstoffe (BGR) /KAN 92, ZIR 03/. Most of these reports comprise “only” qualitative analysis of the mineral phases (XRD) with a classification of major constituents (> 25 wt%), minor constituents (5 – 25 wt%) and accessories (< 5 wt%). The mineral compositions of the three sedimentary units of the Gorleben overburden as defined for our project are given in Tab. 2.2. Detailed explanatory statements for each mineral are given subsequently.

Tab. 2.2 Mean mineral composition of the three sedimentary units UAF, AT and LAF of the Gorleben overburden (in wt%)

Mineral	UAF	AT	LAF
	Saalian and Weichselian meltwater sands	Lauenburg Clay Complex	Miocene Lower Brown Coal Sands and Elsterian Sands
Quartz	85	25	85
Feldspar*	10	5	10
Muscovite	0.5	3	0.5
Gibbsite	0.5	n.r.	0.5
Goethite	0.5	2	0.5
Calcite	2	10	t
Kaolinite	1.5	15	3.5
Illite	n.r.	40	n.r.

* applicable for Albite, Anorthite, Orthoclase and Microcline
n.r. mineral phases not quantitativly relevant in the sedimentary unit
t mineral phases only relevant for transport processes

The specification of the lithological distribution was defined based on /ART 98/. Sediment samples of the upper aquifer were described in this paper as follows: „*As a solid phase, Pleistocene aeolian quartz sand was sampled from the near aquifer surface. According to X-ray fluorescence and X-ray diffraction analysis, the uniform fine sand (d_{10} = 0.12 mm and d_{50} = 0.18 mm, unconformity U = 1.7) consisted of about 85 % quartz, 10 to 15 % feldspar and < 5 % of other minerals, e. g., mica and others. Organic material was found to be < 0.5 %. The grain size analysis showed that silt part was about 0.25% and clay < 0.1 %".*

The sediments of the two different aquifers are extremely similar and hardly to distinguish. /GRI XX/ states that the distribution of the minerals is too irregular to assign a sediment to a geologic horizon and that merely the carbonate content is varying and specific for the upper aquifer. Thus, the fractions named by /ART 98/ were used for the definition of the mineral compositions of the upper and the lower aquifer. For all other specifications and for the description of the aquitard, approximations were carried out on the basis of analyses of the element concentrations and grain sizes given by /GRI XX/ and /KAN 92, ZIR 03/. No data were given for the Hamburg Clay. Hence, for the aquitard results for the Lauenburg Clay Complex were employed only.

According to /ART 98/ it is assumed that the aquifers consist of arenaceous sediments containing 85 wt% quartz and 10 wt% feldspar. The aquitard is dominated by argillaceous to silty components with a higher percentage of clay and calcite and less quartz. According to /GRI XX/ illite and quartz are the major constituents in all grain size fractions, while the feldspars are only ancillary constituents. Therefore, fractions of 25 wt% quartz and 5 wt% feldspar were assumed for the aquitard.

As another primary silicate muscovite (mica) is an accessory mineral in the sediments /GRI XX, ZIR 03/. In this work, mainly the UAF and the upper part of the LAF is of interest. /ZIR 03/ states that the upper part of the LAF has a low content of mica. The percentage of mica in the sediments of both aquifers was therefore set to 0.5 wt%. In contrast to that, the aquitard sporadically shows a higher content of mica than the aquifers /ZIR 03/ and was therefore denoted with a muscovite content of 3 wt%.

The alteration of primary silicates leads to the release of fragments containing silicic acid and aluminum. These fragments may form clay minerals such as kaolinite and illite as well as ferrous oxides and hydroxides. One of the stable weathering products is gibbsite, which /KAN 92/ states to be an accessory constituent of the aquifers. The content of gibbsite in the aquifers is set to 0.5 wt% and defined the aquitard as gibbsite-free due to the lower content of aluminum-bearing silicate minerals (e. g. feldspars, mica).

Another stable weathering product of the silicates is goethite, a representative of the Fe(III)-oxides/hydroxides. Highly soluble Fe^{2+} is released from ferrous silicates and then oxidized to Fe^{3+}, forming goethite with its typical brown color. The contents of goethite in the three sedimentary units were approximated from the contents of elemental iron after /GRI XX, KAN 92/ to 0.5 wt% for the aquifers and 2 wt% for the aquitard.

The content of clay minerals is naturally higher in the aquitard than in the aquifer /ZIR 03/. The approximation of the percentages by weight was based on the particle size analyses /GRI XX/. Kaolinite as a representative of the 1:1 phyllosilicate minerals is found as an accessory constituent of the aquifers (UAF: 1.5 wt%; LAF 3.5 wt%) and as an ancillary constituent in the aquitard (15 wt%). In the aquitard, illite as a representative of the 2:1 phyllosilicate minerals is found to be a major constituent (40 wt%), while no significant illite content was detected in the aquifers.

The Lauenburg Clay Complex is characterized by a high content of calcite (10 wt%) /GRI XX/. In contrast to that, the calcite content of both aquifers amounts to less than 2 wt% /GRI XX/, while /ZIR 03/ states that the upper part of the Lower Brown Coal Sands is virtually calcium carbonate-free. Therefore, and to achieve considerably differing results in the modeling of the geochemical processes, the lower aquifer was defined as calcite-free while the calcite content of the upper aquifer was set to a characteristic value of 2 wt% for the Saalian sediments according to /GRI XX/.

2.4 Identification and selection of elements

In order to define representative sorbates (pair of element and mineral phase) to be considered in the investigations and calculations within this project, the most relevant elements and mineral phases need to be identified. The selection of mineral phases is described elsewhere (section 2.1 and 2.2). In the following it is explained, how the relevant elements were selected.

In general the elements can be divided into two groups, (i) elements occurring as radionuclides and (ii) other matrix elements (directly or indirectly) affecting the geochemical conditions and particularly the sorption behaviour of the radionuclides.

For the radionuclides important criteria are their relevance with respect to the long-term safety and whether a significant sorption of these radionuclides on the selected mineral phases is expected. For the matrix elements two main groups can be distinguished,

- cations acting as competitive ions for the sorption sites and
- ligands, usually anions, forming complexes with the radionuclides and therewith usually decreasing their sorption.

2.4.1 Radionuclides relevant for long-term safety

In principle for performance assessment studies a selection of radionuclides to be considered in the calculations needs to be established. A compilation of results from such selection procedures used in German performance assessment studies can be found e. g. in /FOE 09/. A typical list of radionuclides taken into account for the near field and far field calculations is given in Tab. 2.3.

With respect to the radiation exposure of radionuclides in the biosphere a restricted number of fission and activation products turned out to be most relevant in recent studies /BUH 91/, /KEE 05/, /WOL 08/. In Tab. 2.3 these are marked in brown colour, where the lighter colour indicates a slightly lower relevance. In order to further restrict the number of sorbates (and therewith the number of contaminant – mineral pairs) particularly those elements were selected, where a significant impact of a variation in sorption on the dose is expected. Of course it is also regarded, whether a sorption is expected at all. Therefore, at this stage it is not consider weakly sorbing anionic nuclides such as Cl-36, C-14 and Mo-93 (occurring as MoO_4^-).

Tab. 2.3 Radionuclides typically considered in near field and far field calculations

Fission-/activation products			**Radionuclides from decay chains**			
H-3	Se-79	Pd-107	Cm-248	Cm-247	Cm-246	Cm-245
C-14	Rb-87	Sn-126	Pu-244	Am-243	Pu-242	Pu-241
Cl-36	Sr-90	I-129	Cm-244	Pu-239	U-238	Am-241
Ca-41	Mo-93	Cs-135	Pu-240	U-235	U-234	Np-237
Co-60	Zr-93	Cs-137	U-236	Pa-231	Th-230	U-233
Ni-59	Nb-94	Sm-151	Th-232		Ra-226	Th-229
Ni-63	Tc-99					

For the radionuclides from the decay chains, it is not only important, which nuclide contributes to the radiation exposure, but also the behaviour of mother nuclides can strongly impact the dose from daughter nuclides. Therefore, the actinide elements listed in the right part of Tab. 2.3 are all to be considered.

A final criterion for element selection is the availability of comprehensive and reliable thermodynamic data. For Zr and Tc there is still a severe lack of thermodynamic sorption data. For Sn, high uncertainties in the redox data have been recently identified and are currently under investigation, thus the issue of a planned NEA TDB data base document has been postponed, severely hampering the provision of a consistent thermodynamic data base. For Nb and Pa the thermodynamic data base in general is still not sufficient and straightforward chemical analogues are not available. As a result the following elements with radionuclides are selected: Ni, Se, Cs, Cm, Am, Pu, U, Th, Np and Ra.

It should be mentioned that for reasons of clarity redox reactions are not considered in this project. For redox sensitive elements usually the higher oxidation state is assumed, i. e. the following valencies are regarded: Np(V), Pu(IV), U(VI), and Se(VI).

In order to determine the maximum element concentrations, which are needed to establish the K_d-matrix, far field calculations for a scenario with relatively high radionuclide release rates from the near field were regarded (brine intrusion scenario). The calculations have been performed with a two-dimensional model described in detail in /KEE 05/.

The release of contaminated brine occurs in a spatially restricted area at the center of the contact of the salt dome to the lower aquifer and is treated as a point source. The highest radionuclide concentrations occur in the vicinity of the point source. Therefore, the concentrations of the relevant radionuclides considered here were taken slightly downstream from the point source. The maximum concentrations as calculated by /KEE 05/ are listed in Tab. 2.4 and Tab. 2.5.

Tab. 2.4 Maximum concentration for activation and fission products in mol m^{-3}

Activation and fission products					
C-14	$2 \cdot 10^{-5}$	Se-79	$4 \cdot 10^{-4}$	Sn-126	$2 \cdot 10^{-5}$
Cl-36	$2 \cdot 10^{-4}$	Zr-93	$7 \cdot 10^{-7}$	I-129	$2 \cdot 10^{-3}$
Ni-59	$2 \cdot 10^{-4}$	Mo-93	$1 \cdot 10^{-8}$	Cs-135	$8 \cdot 10^{-4}$
		Tc-99	$4 \cdot 10^{-4}$		

Tab. 2.5 Maximum concentration for the actinides in mol m^{-3}

Thorium decay chain		**Neptunium decay chain**		**Uranium decay chain**		**Americium decay chain**	
Pu-240	$2 \cdot 10^{-8}$	Cm-245	$2 \cdot 10^{-7}$	Pu-242	$2 \cdot 10^{-7}$	Am-243	$9 \cdot 10^{-7}$
U-236	$4 \cdot 10^{-6}$	Pu-241	$3 \cdot 10^{-10}$	U-238	$5 \cdot 10^{-4}$	Pu-239	$6 \cdot 10^{-6}$
Th-232	$8 \cdot 10^{-8}$	Am-241	$9 \cdot 10^{-9}$	U-234	$3 \cdot 10^{-7}$	U-235	$3 \cdot 10^{-5}$
		Np-237	$2 \cdot 10^{-5}$	Th-230	$4 \cdot 10^{-7}$	Pa-231	$3 \cdot 10^{-9}$
		U-233	$3 \cdot 10^{-7}$	Ra-226	$5 \cdot 10^{-8}$		
		Th-229	$8 \cdot 10^{-10}$				

Based on the concentrations shown in Tab. 2.4 and Tab. 2.5 maximum element concentrations are proposed for the calculations of the K_d-matrices (Tab. 2.6). For the acti-

nides the maximum concentrations are more than one order higher than the ones derived from Tab. 2.5 due to the fact that concentrations might be increased by built-up from the mother nuclides during transport (with the exception of U-238).

Tab. 2.6 Proposed maximum element concentrations [mol m^{-3}]

Element	Max. c [mol m^{-3}]	Element	Max. c [mol m^{-3}]	Element	Max. c [mol m^{-3}]
Se	10^{-3}	Cs	10^{-3}	Pu	10^{-4}
Zr	10^{-6}	C	10^{-4}	Np	10^{-3}
Mo	10^{-8}	Cl	10^{-3}	U	10^{-3}
Tc	10^{-3}	Ni	10^{-3}	Th	10^{-5}
Sn	10^{-4}	Cm	10^{-5}	Ra	10^{-3}
I	10^{-2}	Am	10^{-5}	Pa	10^{-7}

2.4.2 Other relevant elements

Beside the radionuclides other elements play a role, which might impact the sorption of the radionuclides. In general, two groups of ions can be distinguished: cations as concurrent sorbates and anions as ligands thereby usually increasing the respective radionuclide in solution. However, radionuclide ligand complexes might also sorb on surfaces increasing the immobile fraction of the radionuclide under specific conditions. Moreover, the major anions and cations defining the ionic strength have also to be considered.

2.4.2.1 Important cations

Major competing ions are cations, since under the near neutral geochemical conditions expected the surface charge of the mineral phase of overburden sediments is negative. Usually, the sorption strength of cations increases with their charge, although other properties like ionic radius and hydration of the ion play a role, too. Therefore, divalent and trivalent ions are more important than monovalent ones. Secondly, the concentration of the cation in solution impacts the magnitude of the competition effect.

In the natural sediment system considered, the major cations are Ca, Mg, Na, and K. Fe and Al occur in lower concentrations but might also be important, since they likely are present in the trivalent state. Additionally, Fe is expected to be released from the

repository since it is mobilized by the corrosion of the container material. For the calculations Ca, Fe and Al are selected. The monovalent cations Na and K are known to be very weakly sorbing cations, i. e. their role as competing ions can be neglected here but they affect the ionic strength.

2.4.2.2 Important ligands

The complexing ligands CO_3^{2-}, SO_4^{2-}, PO_4^{3-} and SiO_3^{2-} are important in natural systems. In highly mineralized waters Cl^- becomes also important. At Gorleben site organic ligands such as fulvic and humic acids are also relevant, since they can occur in quite high concentrations up to 200 mg C L^{-1} /BUC 00/.

However, to keep the system simple it is decided to not consider the organic ligands at this stage. From the inorganic ligands CO_3^{2-} is expected to play the strongest role, especially because in several areas of the overburden relatively high CO_2 partial pressures due to microbial degradation of SOC[1] are found. Besides CO_3^{2-}, in this first step SO_4^{2-} and SiO_3^{2-} will be included, since they also occur in relatively high concentrations at the site. These anions may – together with Cl^- – also affect the ionic strength.

2.4.3 Concentration ranges of relevant elements

As a basis to identify feasible concentration ranges for the selected elements groundwater data from Gorleben overburden and and results flow and transport calculations for radionuclides are evaluated.

2.4.3.1 Concentrations of relevant elements in the Gorleben groundwater

Typical groundwater compositions in the sedimentary overburden of the Gorleben salt dome are to be documented as a basis for geochemical modeling. Therefore, a comprehensive dataset was analysed /KLI 04/ considering the three hydrogeological units lower aquifer, aquitard and upper aquifer.

[1] SOC –Sedimentary Organic Carbon

Within the upper aquifer, the dominant groundwater is of the Ca-HCO_3-type. The groundwater of the lower aquifer is characterized by salt water conditions; hence it can be assigned to the Na-Cl-type. The aquitard features different groundwater types, mainly the Na-HCO_3- and the Na(Ca,Mg)-Cl-type. The three most important groundwater types in the area are therefore the Ca-HCO_3-, the Na-HCO_3- and the Na-Cl-type.

For geochemical transport modeling, the most important constituents of the groundwater are the following ions: Ca, Mg, Fe, Al, CO_3^{2-}, SO_4^{2-}, SiO_3^{2-}. Their concentrations and the concentrations of other major ions in groundwater samples were evaluated and are given in appendix A.3, Tab. A.2 to Tab. A.4. Negative concentrations (Fe, Al, SO_4^{2-}, HCO_3^-, SiO_2) and clearly outlying values (Fe, Al pH) of the dataset have been neglected. On that basis the concentrations for the three hydrogeological units are derived and given in Tab. 2.7.

Tab. 2.7 Initial groundwater composition in the three sedimentary units according to /KLI 04/

	Upper aquifer	**Aquitard**	**Lower aquifer**
pH	7.5	8.0	7.2
Concentration [mg L^{-1}]			
Ca	48.3	9.72	893
Al	0.05	0.47	0.31
HCO_3^-	165	218	290
Na	10.1	337	27900
Cl	12.47	18.23	46500
SiO_2	21.21	26.13	18.23

2.4.3.2 Concentrations of relevant elements in seawater

For the transport models, the geochemical composition of seawater, precipitation water and glacial meltwater is necessary to be known. The compounds of salt deposits were calculated from the composition of average seawater (appendix A.1, Tab. A.1 /LAN 02/). These values can be converted to the data given in Tab. 2.8, which are used for the calculations.

Tab. 2.8 Composition of seawater after /LAN 02/

	Molar mass [g mol^{-1}]	wt%	[g kg^{-1}]	[g m^{-3}]	[mol m^{-3}]	[mol m^{-3}][1]	Density [kg m^{-3}]
NaCl	58.453	2.73	27.3	27987.96	478.81	478.81	
$MgCl_2$	95.211	0.32	3.2	3280.64	34.46	68.91	
KCl	74.5513	0.07	0.7	717.64	9.63	9.63	
$MgSO_4$	120.365	0.23	2.3	2357.96	19.59	19.59	
$CaSO_4$	136.14	0.13	1.3	1332.76	9.79	9.79	1025.2
$Ca(HCO_3)_2$	162.102	0.02	0.2	205.04	1.26	1.26	
Cl-total						557.35	
K-total						9.63	

[1] Concentration of Cl and K, respectively, as components of the compounds named in the first column.

2.4.3.3 Concentrations of relevant elements in precipitation water

The concentration of relevant elements in precipitation water was taken from /MAT 94/ and is given for the relevant elements in Tab. 2.9.

Tab. 2.9 Chemical composition of precipitation water /MAT 94/

pH	5.6
Concentration [mol m^{-3}]	
Ca	$2.5 \cdot 10^{-2}$
Al	$1.5 \cdot 10^{-6}$
DIC	$2.0 \cdot 10^{-3}$
Na	$5.0 \cdot 10^{-2}$
Cl	$3.1 \cdot 10^{-3}$

2.4.3.4 Concentrations of relevant elements in glacial meltwater

As a glacial meltwater inflow into a model area in northern Germany is expected to result from melting inland ice sheets, the meltwater is expected to have a similar chemical composition as the ice. Typical values for major and trace elements are given in appendix A.2. The values for the pH-value and the relevant elements considered for

the calculations are shown in Tab. 2.10. The DIC concentration was taken from /MAT 94/ assuming that the effects of increased solubility in precipitation and decreased atmospheric CO_2 concentration during glacial compensate each other.

Tab. 2.10 Chemical composition of glacial meltwater according to /LEG 88/

pH	5.7
Concentration [mol m^{-3}]	
Ca	$5 \cdot 10^{-4}$
Al	$1.5 \cdot 10^{-6}$
DIC	$2.0 \cdot 10^{-3}$
Na	$2.7 \cdot 10^{-3}$
Cl	$2.5 \cdot 10^{-3}$

2.4.4 Conclusions for element selection

In order to keep the number of sorbates manageable the list of considered elements is constrained. For elements occurring as radionuclides the selection was based on their relevance for long-term safety, on the question whether they are sorbing at all and on the availability of comprehensive and reliable thermodynamic data. Additionally, relevant cations competing with the radionuclides and complexing ligands (or defining the background electrolyte), stemming from the natural system or released from the repository have been included. Summarizing the findings of all previous section within this chapter, a final element list can be composed as given in Tab. 2.11 below. Elements which are considered as environmental parameters E_i and therefore to be varied in their concentration are marked accordingly. Due to the sparse SCM data sets for Cm^{3+} and Pu^{4+} thermodynamic data from the chemical analogues Am^{3+} and Th^{4+} and their resulting smart K_d-values are used in r³t instead. Finally, also those elements are considered which do influence the speciation and thus form part of the ESTRAL.dat data base, too.

Tab. 2.11 List of selected elements

	Varied E_i	Considered in r^3t	Included in ESTRAL.dat	Remark
Ni	X	X	X	
Se	X	X	X	
Cs	X	X	X	
Cm		X		
Am	X	X	X	
Pu		X		
Th	X	X	X	
U	X	X	X	
Np	X	X	X	
Ra	X	X	X	
H	X		X	
Ca	X		X	
Al			X	
C	X		X	For carbonates
Fe			X	
K			X	
Mg			X	
Na			X	
Cl			X	
Si			X	For silicates
S			X	For sulfates

3 Evaluation of the data situation for the selected sorbates

For the investigations and calculations within this project, a separate thermodynamic data base had to be created. Therefore, the thermodynamic data for the representative elements and mineral phases were identified and extensively reviewed. The selection of these elements and minerals is described in section 2. In the following it is explained, how the relevant thermodynamic data for the ESTRAL.dat data base were selected.

In general the data can be divided into three groups: (i) thermodynamic data for the aqueous element species, (ii) thermodynamic data for solid mineral phases, and (iii) thermodynamic sorption data for the representative sorbates (pair of element and mineral). Evaluation criteria and the selection process as well as remarks to individual data records are given in the following section for all of these groups. The elements and phases to be considered are explained in section 2. For some of the elements thermodynamic data from chemical analogues have to be used to fill critical data gaps. This pertains to all three groups and is namely the case for

- trivalent lanthanides for Cm^{3+} & Am^{3+};
- Ce^{4+}, U^{4+}, and Np^{4+} for Pu^{4+} and Th^{4+};
- Ba^{2+} and Sr^{2+} for Ra^{2+}, and
- Rb^{+} for Cs^{+}.

3.1 Thermodynamic data for aqueous species

All necessary formation constants for aqueous complexes were collected from international referenced data bases. If this was not possible the original literature was evaluated. To ensure a high level of consistency, solubility products for mineral phases were taken form the same references whenever possible.

Primarily, the Nagra/PSI Chemical Thermodynamic Data Base Version 01/01 (Nagra/PSI TDB 01/01) formatted for PHREEQC /HUM 02/ was the basis for the ESTRAL.dat data base. In addition, data for the elements Ni, Th and Se, not appropriately covered by /HUM 02/, were taken from the NEA TDB reviews /GAM 05/, /RAN 08/ and /OLI 05/, respectively. In addition, all updates for actinide data published in

/GUI 03/ have also been incorporated. Another important addition was the $Ca_2UO_2(CO_3)_3$ aqueous complex with data taken from /BER 01/.

The relevance of various aqueous species, primarily Al and Si complexes, was reviewed within the ESTRAL.dat data base development. It has been found that most data for such species are from studies at pH < 4.0. Extrapolations to higher pH-values are not possible. Therefore, such complexes (e. g. $AmSiO(OH)_3^{2+}$, $FeSiO(OH)_3^{2+}$) were deleted from our data base.

3.2 Thermodynamic data of mineral phases

As for the aqueous species, /HUM 02/ was the primary source of thermodynamic data for solid phases. As for the aqueous species, the respective NEA TDB volumes /GUI 03/, /GAM 05/, /RAN 08/ and /OLI 05/ have been used to update data. Solid mineral phases, which are not relevant for this project, were deleted (e. g. graphite). However, for some solid mineral phases /HUM 02/ did not provide thermodynamic data. Therefore, solubility products for albite, anorthite, chlorite, illite, muscovite and montmorillonite have been supplemented from ThermoChimie Version 7b (ANDRA data base) /BRU 01/. For albite, low- and high temperature structural modifications are specified in the ANDRA data base. Here, the albite-low has been used, which is stable below 700 °C with an ordered Si-Al arrangement. Data for goethite, hematite and K-feldspar have been taken directly from the original literature. Thermodynamic data for K-feldspar have been calculated from logK(T)-functions found in /ARN 82/, /ARN 99a/, /ARN 99b/ using T = 298.15 K. Data for goethite have been taken from /COR 03/, primary data source is /SCH 63/ (solubility measurements). Data for hematite were taken from /WAG 69/. Generally, all values supplementary and changed with respect to /HUM 02/ are clearly marked in the ESTRAL.dat data base.

A summary of mineral phases defined to be relevant (Tab. 2.1) and their referenced solubility products (logK) is listed in Tab. 3.1.

Tab. 3.1 Thermodynamic data for relevant minerals

Mineral	Reaction	logK	Reference	
Albite [1]	$NaAlSi_3O_8 = Na^+ + Al^{3+} - 4H^+ + 3H_4SiO_4 - 4H_2O$	2,74	n.s.	A
Anorthite	$CaAl_2Si_2O_8 = Ca^{2+} + 2Al^{3+} - 8H^+ + 2H_4(SiO_4)$	25,31	n.s.	A
Calcite	$CaCO_3 = Ca^{2+} - H^+ + HCO_3^-$	1,85	/PLU 82/	N
Chlorite [2]	$(Mg_{2.964}Fe_{1.712}Fe_{0.215}Al_{1.116}Ca_{0.011})(Si_{2.633}Al_{1.367})O_{10}(OH)_8 = 0.011Ca^{2+} + 2.964Mg^{2+}$ $+ 0.215Fe^{3+} + 1.712Fe^{2+} + 2.483Al^{3+} - 17{,}468H^+ + 2.633H_4(SiO_4) + 7.468H_2O$	61,23	n.s.	A
Gibbsite	$Al(OH)_3 = Al^{3+} + 3H_2O - 3H^+$	7,76	/COX 89/	N
Goethite	$FeOOH = 2H_2O - 3H^+ + Fe^{3+}$	1,40	/SCH 63/	L
Gypsum	$CaSO_4{:}2H_2O = Ca^{2+} + SO_4^{2-} + 2H_2O$	-4,58	/NOR 90/	N
Hematite	$Fe_2O_3 = 3H_2O - 6H^+ + 2Fe^{3+}$	-3,76	/WAG 69/	L
Illite [3]	$K_{0.85}Fe_{0.25}Al_{2.6}Si_{3.15}O_{10}(OH)_2 = 0.850K^+ + 0.250Fe^{3+} + 2.6Al^{3+} - 9.4H^+$ $+ 3.15H_4(SiO_4) - 0.6H_2O$	10,07	n.s.	A
K-Feldspar	$KAlSi_3O_8 + 4H^+ + 4H_2O = Al^{3+} + 3H_4SiO_4 + K^+$	-2,88	/ARN 99a,b/	L
Kaolinite	$Al_2Si_2O_5(OH)_4 = 2Al^{3+} + 2Si(OH)_4 + H_2O - 6H^+$	7,44	/NOR 90/	N
Montmorillonite [4]	$Na_{0.33}Mg_{0.33}Fe_{0.67}Al_{1.0}Si_4O_{10}(OH)_2 = 0{,}33Na^{2+} + 0{,}33Mg^{2+} + 0.67Fe^{3+} + 1{,}0Al^{3+} - 6H^+$ $+ 4H_4(SiO_4) - 3.96H_2O$	2,89	n.s.	A
Muscovite	$KAl_3Si_3O_{10}(OH)_2 = K^+ + 3Al^{3+} - 10H^+ + 3H_4(SiO_4)$	14,00	n.s.	A
Quartz	$SiO_2 = Si(OH)_4 - 2H_2O$	-3,746	/GUN 00/	N

[1] Albite-low
[2] Chlorite-Cca-2
[3] Illite-Fe^{III}
[4] Fe-Montmorillonite-Na

n.s. complete reference not specified in ANDRA data base
A: ANDRA /BRU 01/
L: original literature
N: NAGRA/PSI /HUM 02/

For the model area a constant temperature field of 14 °C is assumed as a mean value between the natural 8 °C at the surface and 20 °C in 400 m depth. However, a conversion of the thermodynamic values from the reference temperature of 25 °C to 14 °C is not necessary. The expected reaction enthalpies $\Delta_r H$ for relevant mineral phases (e. g. anorthite, calcite and gibbsite) have been retrieved and used to predict the temperature effect on logK by means of the van't Hoff approximation, but the observed changes in the solubility always lie within the error limits. For goethite and hematite, however, $\Delta_r H$-values were not accessible in the original literature.

3.3 Thermodynamic sorption data

The sorption of radionuclides onto mineral surfaces is described by K_d-values based on Surface Complexation Models (SCM). To establish a respective data base, the following strategy was obeyed:

- In a first step, a literature survey mainly based on the RES³T data base helped to define the chemical system, i. e. the mineral properties and the set of surface species. (Rossendorf Expert System for Surface and Sorption Thermodynamics) /BRE 03/, which is available under www.hzdr.de/RES3T. RES³T is a digitized thermodynamic sorption data base and is implemented as a relational data base. This data base is mineral-specific and can therefore also be used for additive models of more complex solid phases such as rocks, sediments or soils.

- The value for the specific surface area is strongly dependent on the sample history and grain size fraction. It can not be generalized, so the respective experimentally determined values were used for the computations.

- All reaction constants were converted to infinite dilution (when necessary) by assigning activity coefficients based on the Davies-Equation /DAV 62/ to all dissolved species.

- Because the reported reaction constants are related to different site densities, it was necessary to convert the values to a reference state to enable comparison and averaging. Here, the procedure according to Kulik /KUL 02/ was followed, based on a reference surface site density of 2.31 sites nm^{-2}. This value of course was then also used for all subsequent predictive modeling.

- To keep the system as simple as possible, in no case was a distinction between strong and weak binding sites applied. The values of pK_1 and pK_2 for the two successive protolysis steps always refer to the following deprotonation reactions, with =X-OH denoting a generic neutral surface binding site:

  pK_1: $\quad =X\text{-}OH_2^+ = =X\text{-}OH + H^+$

  pK_2: $\quad =X\text{-}OH = =X\text{-}O^- + H^+$

- When the data situation was too sparse, various approximations were utilized to derive a sensible chemical model, namely the estimations based on crystallography and thermodynamics as published, e. g., by Sverjensky and co-workers /SVE 96/ or the extrapolation from chemically similar systems (with regard to both mineral and sorbent) by applying the Linear Free Energy Relationships (LFER) as, e. g., described by Dzombak and Morel /DZO 90/. If such approaches failed, a simple transfer of data from chemically similar systems (with identical charge) was accepted. There, as a last resort, parameters based on electrostatic double layer (EDL) terms different from the chosen SCM (here: DDLM, see below) were also taken into account. Preliminary uncertainty analysis /RIC 07/ showed for most cases that the sorption modeling error imposed by omitting a surface reaction totally is much larger than assigning a respective surface complex formation constant with large uncertainties.

- After normalization, the data records applying to the same reaction (mineral surface protolysis and surface complex formation) were compared and judged to identify and exclude outliers and doubtful data points. The remaining sets were then averaged to obtain respective model parameters and also an estimation of their uncertainty.

The Diffuse Double Layer /DZO 90/, /STU 70/, /HUA 73/ model (DDLM) was chosen as a rather straightforward SCM variant, again to keep the number of parameters at a minimum, but also because many published data sets are based on that SCM type. It is also one of the three models that are currently supported by the PHREEQC speciation code /PAR 99/.

The approach is based on a diffuse layer at the interface solid/aqueous electrolyte. An important advantage of this rather simple approach is that there are no electrostatic parameters required at all. It is assumed that: (i) All surface complexes are inner-sphere

complexes (ii) no surface complexes with the ions of the background electrolyte can be formed, (iii) two charge layers represent the mineral surface (diffuse layer and helmholtz layer, which is charge-free) and (iv) the correlation between surface charge and surface potential can be explicitly described by the Gouy-Chapman equation. Dependence on the ionic strength is taken into account as long as it is below 0.1 mol L^{-1}.

RES³T provides SCM data for the most relevant minerals (or mineral groups) within this project (Tab. 3.2). The data sets related to DDLM (given in brackets) are clearly preferred. Only in case of insufficient data sets, chemical analogues (both in terms of the sorbent and the sorptives), estimations/correlations or data related to other SCM models are used to enlarge the available data pool.

Tab. 3.2 Number of SCM data sets retrieved from RES³T /BRE 03/

Mineral/ Mineral group #	Quartz	Feldspars	Mica	Fe(III)-oxide/-hydroxides	Aluminum-hydroxides	Kaolinite	Mixed-layer clay minerals	Σ minerals
Radionuclides								
Cs^+, (Rb^+)	12	1 *	*	7	2		5	27
Ra^{2+}, (Sr^{2+}, Ba^{2+})	7 [2]	*	*	20		7	5	39 [2]
Ni^{2+}	9			6 [3]	2	5	22	44 [3]
Am^{3+}, Cm^{3+}, (REE)	19 [3]	*	*	40 [16]		9 [6]	65 [8]	133 [33]
Pu^{4+}, Th^{4+}, (Ce^{4+}, Np^{4+}, U^{4+})	8 [3]	*	*	40 [9]		4	13	65 [12]
NpO_2^+	3 [1]	#	6 [6]	18 [8]	11 [8]	2 [2]	6 [4]	46 [29]
UO_2^{2+}	64 [8]	2 [2]	5 [5]	196[66]	7	15 [9]	25 [12]	314 [102]
SeO_4^{2-}				15 [2]	1 [1]			16 [3]
Matrix components								
Ca^{2+}	7			10 [3]		4	6	27 [3]
Al^{3+}				3			4	7
Fe^{3+}	2			3				5
CO_3^{2-}				52 [4]				52 [4]
SiO_3^{2-}				10	2			12
SO_4^{2-}	1			23 [10]	4 [3]	2		30 [13]
Σ elements	132 [17]	3 [2]	11 [11]	443 [121]	29 [12]	48 [17]	151 [24]	817 [204]

Applicable for minerals described in Tab. 2.1 (including amorphous Silica and $Al(OH)_3$)
* Additional SCM-Data from batch experiments GRS
( ) Analogues
[ ] DDLM data sets only

With the exception of feldspars and mica, the data matrix is filled densly enough to allow for a robust modeling. Sorption data for missing mineral phases are obtained from batch experiments described in section 4 (Cs^+, Sr^{2+}, Eu^{3+} onto orthoclase/muscovite).

The selection of the main SCM parameters is described below in detail. All formation constants for surface complexes as well as the mineral surface protolysis values and their equations and references were included in the ESTRAL.dat data base (see attached PDF version).

3.3.1 Specific Surface Area (SSA)-values

Firstly, it is described, how data have been derived for those minerals, for which also sorption experiments (section 4) are performed within this project. SSA values have been measured for these materials from the same samples as used in the experiments. This concerns orthoclase, kaolinite, muscovite, and quartz, with the latter being investigated both in untreated and treated form. The treatment consisted in heating to 550 °C for 48 – 60 hours (to destroy organic material), repeated acid refluxing in 4M HNO_3 (to dissolve and remove traces of aluminum and iron oxides), repeated washing in deionized water, adjustment to pH 9 – 10 (to leach readily soluble silica), repeated acidic washing, and washing and decanting in deionized water for eight times /DAV 01/. The following methods have been applied: Multi-point N_2 method after Brunauer, Emmet and Teller (BET, NOVA 2000e, Quantachrome) in cooperation with iPAT, TU Braunschweig; Multi point N_2-BET (mod. Coulter SA 3100, Beckman Coulter, Fullerton, USA) by HZDR; and grain size determinations using a Laser Diffraction System (LRS, Helos & Sucell, Sympatec) in cooperation with iPAT, TU Braunschweig with subsequent data processing according to /BEN 44/. In addition, the manufacturer's specification for quartz has been used, too.

Secondly, data for other representative mineral phases in the model area Gorleben, which have not been used for sorption experiments, have to be derived. SSA-values for these materials have been selected from references in RES³T (without amorphous silica or alumina). Currently, there are different methods applied to derive SSA-values in RES³T (in descending order according to their usage): the BET sorption isotherms obtained with different gases (N_2, Ar, Kr, He, or mixtures thereof), geometrical calculation based on crystallographic data, water vapor adsorption, scanning electron microscopy, ethylene glycol monoethyl adsorption, 'Saers' method, methylene blue adsorption, or

rhodamin B adsorption. However, for this project only references with defined experimental techniques were used. References with unspecified or unknown techniques, e. g. assumption, not specified, literature, geometrical calculation, are not considered.

All SSA-values from sorption experiments as well as from references in RES³T are summarized in Tab. 3.3 with the last column giving the selected mean values.

Tab. 3.3 Specific surface areas (values in $m^2\ g^{-1}$) for minerals used in sorption experiments* and other representative mineral phases in the model area Gorleben

Reported uncertainties correspond to two sigmas (recommended values for averaging are highlighted in grey).

Method Mineral	BET (iPAT)	BET (HZDR)[1]	Mean RES³T	Fitted SSA (GRS)[2]	Grain size d_{10} [3] [µm]	Selected mean SSA
Quartz (untreated)*	0.3 [4]	0.7 ± 0.01	1.7 ± 0.7	-	2.5	0.5 ± 0.3
Quartz (treated)	-	0.8 ± 0.01	-	-	-	-
Orthoclase*	0.8	0.9 ± 0.01	0.2 - 22	15	2.4	15
Muscovite*	0.7	0.7 ± 0.01	1.4 - 5.2	6	49	6
Fe-minerals	-	-	48 ± 5	-	0.9 ± 0.8	48 ± 5
Gibbsite	-	-	26 ± 9	-	0.8 ± 0.1	26 ± 9
Kaolinite*	11	11 ± 0.04	16 ± 3	-	1	11 ± 0.03
MIxed-layer clay-mineral	-	-	55 ± 11	-	1.8 ± 1.5	55 ± 11

[1] Mean of twofold measurements of two samples
[2] Fitted SSA from mean BET (iPat and HZDR)
[3] d_{10} [µm] = effective grain size at 10 wt% sieving
[4] Manufacturer's specification

It has been shown that for quartz (untreated) and kaolinite, the averaged SSA values from both BET measurements (iPat and HZDR) compares well with references in RES³T and are taken for further modeling of K_d-values. The SSA for orthoclase and muscovite show a typical bimodal distribution. Here, the fitted SSA (section 4.4), which are in the upper range of the cited literature (Tab. 4.5), are used for further modeling. The SSA for gibbsite, Fe(III)-minerals and mixed-layer-clay minerals (montmorillonite, illite) are taken from references in RES³T (appendix).

In the course of the modeling of smart K_d-values, the initial calculated K_ds, which were obtained with primary selected mean SSA-values (Tab. 3.3), were much higher than expected for the Gorleben site. Obviously, it is important to consider the site-specific effective grain size for the modeling. The mean effective grain size for the three sedimentary units based on /GRI XX/ and is given in Tab. 3.4.

Tab. 3.4 Mean effective grain size for Gorleben sediments /GRI XX/

Sedimentary unit	d_{10} [µm]* $\pm$ 2σ
UAF	170 $\pm$ 50
AT	14 $\pm$ 30
LAF	139 $\pm$ 30

* d_{10} = effective grain size at 10 wt% sieving

Consequently, the primary SSA-values of known grain size (Tab. 3.3) were correlated with the site-specific grain size for Gorleben sediments. These correlated SSA-values for the relevant minerals are presented in Tab. 3.5.

Tab. 3.5 Recommended correlated values for specific surface area (SSA in $m^2\ g^{-1}$) for Gorleben minerals

Sedimentary unit Mineral/-group	UAF	AT	LAF
Quartz	0.007	0.09	0.009
Feldspars	0.21	2.55	0.257
Mica	1.72	20.86	2.10
Fe(III)-oxides/-hydroxides	0.26	3.19	0.32
Aluminumhydroxides	0.11	n.r.	0.14
Kaolinite	0.07	0.81	0.08
Mixed-layer clay minerals	n.r.	6.88	n.r.

n.r.: Mineral phases not relevant in the sedimentary unit

3.3.2 Surface protolysis constants (pK-values)

Concerning the surface protolysis the 2pK model has been selected as there are much more data published for this approach compared to the 1pK model. For those minerals possessing several chemically distinguishable reactive surface groups (e. g. silanol and

aluminol surface sites on clay minerals) generic sites have been used here. This affects both surface site densities (SSD) and pK-values. As generally the values of pK and SSD are not independent from each other a methodology to compare and average thermodynamic constants originating from different sources is required. Following the normalization concept recently introduced by /KUL 02/ and setting the reference site density Γ to 2.31 sites nm^{-2} /TUR 96/ and /DAV 90/ the protolysis constants as well as the surface complexation constants are normalized according the following equations:

$$log\ K^{n} = log\ K^{ex} + d \cdot log\ (\Gamma_{ex} / \Gamma_{n}), \qquad (3.1)$$

with the indices ex meaning the experimental value and n the normalized value. The factor d accounts for the denticity of the surface complex, i. e. to how many binding sites the surface species is bound simultaneously. For the most often encountered bidentate complexes d equals 2. In the special cases of protolysis constants, this equation changes into

$$pK_1^{n} = pK_1^{ex} + log\ (\Gamma_{ex} / \Gamma_{n}) \qquad (3.2)$$

for the first protolysis step: $=XOH_2^+ = =XOH + H^+$

and into

$$pK_2^{n} = pK_2^{ex} - log\ (\Gamma_{ex} / \Gamma_{n}) \qquad (3.3)$$

for the second one: $=XOH = =XO^- + H^+$.

All normalized pK-values for both protolysis steps are listed below in Tab. 3.6. The above equations allow for adjustments of pK (and log K) parameters to any other preferred SSD. As stated earlier, values related to the DDLM are preferred, only in case of missing data values from other EDL submodels are used.

Tab. 3.6 Recommended pK-values from RES³T and batch experiments* for both protolysis steps

Mineral/-group	pK_1 [1]	pK_2 [1]	No. of Ref. in RES³T [2]
Quartz	-1.13 ± -	6.92 ± 0.61	1/7
Feldspars	6.90 ± 0.87	7.72 ± 0.26	2*
Mica	6.42 ± 0.40	8.08 ± 0.44	2*
Fe(III)-oxides /-hydroxides	7.23 ± 0.29	9.73 ± 0.39	24
Aluminiumhydroxides	7.06 ± 0.60	9.84 ± 0.65	4
Kaolinite	8.44 ± 0.21	9.20 ± 1.06	2
Mixed-layer clay minerals	5.35 ± 0.75	7.94 ± 0.72	3

[1] Values normalized to reference binding site 2.31 sites nm^{-2} and corrected to I = 0 M using Davies equation. All reported uncertainties represent 95 % confidence limit (± 2σ).

[2] Original references are given in the attached ESTRAL.dat data base (PDF-version) and their full bibliographic details are cited in RES³T

3.3.3 Formation constants of the surface complexes (logK)

The necessary surface complexation constants (log K-values) for the representative sorbates (pair of element and minerals) are collected from RES³T as well as from the fit of experimental sorption data (section 4). Following the above equation (Eq. 1), all surface complexation constants (log K-values) are normalized to a reference binding site density of 2.31 sites nm^{-2} and are corrected to infinite dilution using Davies equation. However, it is very challenging to reach general consensus about stability constants for surface complexes, as i) they are specific for each combination of mineral and sorptive, thus often drastically limiting the amount of published data sets (with many combinations not covered by any data at all) and ii) the non-uniqueness of the chemical species set, i. e. the stoichiometry of the surface complexes.

The selection of the surface complexation constants is still under discussion due to their relevance. For those minerals of relevance for long term safety analyses where only very few respective data are published a pooling with mineralogical similar materials is done. Moreover, for various minerals where no formation constants for surface complexes have been published at all data from sorption experiments are used.

4 Batch experiments for contaminant/mineral systems

It is recognized that for some of the relevant mineral phases, particularly feldspars and mica almost no sorption parameters for surface complexation models are available (Tab. 3.2). On that basis mono-, bi-, tri- and tetravalent cations are applied to perform sorption experiments. Conducted batch experiments implement cesium (Cs^{+}), strontium (Sr^{2+}), europium (Eu^{3+}), and thorium (Th^{4+}) in combination with orthoclase and muscovite which are representative minerals for the Gorleben site.

The objectives of the conducted batch experiments include the assessment, evaluation as well as processing of the collected sorption data by means of the geochemical speciation code PHREEQC in combination with UCODE. In addition, the verification of the chosen bottom-up approach is also aimed to be verified (section 6.3.1).

PHREEQC is a geochemical modeling code for simulating chemical reactions and transport processes in water, including speciation and batch-reaction, 1D reactive transport, and inverse modeling. For speciation and batch-reaction calculations, PHREEQC numerically solves sets of nonlinear mole-balance and mass-action equations. The most recent version of PHREEQC may be obtained from the USGS via the URL http://wwwbrr.cr.usgs.gov/projects/GWC_coupled/phreeqc/.

UCODE is a universal parameter estimation modeling code that can be used with existing process models (software packages) to perform sensitivity analysis, data needs assessment, calibration, prediction, and uncertainty analysis. The only requirements involve text input and output files that need to be supplied by the applied process models. Furthermore, the required models have to be executed from a single batch file and simulated values need to be continuous functions of the parameter values /POE 05/. The first version of UCODE was released in 1998 /POE 98/. An updated version (UCODE_2005) was constructed using the JUPITER (Joint Universal Parameter Identification and Evaluation of Reliability) application programming interface conventions and modules /BAN 06/. The latter version is applied in this study. The most recent version of UCODE may be obtained from http://igwmc.mines.edu/freeware/ucode/. From here on, UCODE always serves as an abridged synonym for UCODE_2005.

The measured data sets are enclosed in this report and can be obtained from the appendix Tab. A.8 to Tab. A.12. The tables show data that have already been processed

by means of error estimation and calculation for every data value as well as corrections for outliers. Further and more detailed information regarding error calculations and data processing may be obtained from /BRI 11/. According error-assessment calculations are conducted regarding Cs^{+} and Sr^{2+}, respectively.

Prior to all batch experiments pretests are carried out to determine the minerals' composition, the best range of solid-liquid ratios, pH-conditions as well as element concentrations. Further information regarding undertaken pretests is described in detail in /BRI 11/.

Since the minerals are purchused from different merchants, preconditioning of the minerals vary significantly. To some extend, preconditioning treatments may impact the minerals' surfaces and hence result in altered surface complexation reactions and rates. According information and a detailed discussions on the minerals' conditioning processes can be obtained from /BRI 11/.

4.1 Overview

Via pretests best suitable geochemical conditions are defined for the planned batch experiments. Sorption data assessed via the final batch experiments are processed through PHREEQC in combination with the inverse parameter-estimation code UCODE aiming to obtain equilibrium constants (logK). Therefore surface complexation parameters (SCP) such as the surface site area (SSA), the surface site density (SSD) as well as protolysis constants (pK1 and pK2) of the applied minerals are required. In order to derive these mineral-specific constants titration experiments employing muscovite and orthoclase are conducted prior to the final batch experiments.

Tab. 4.1 offers an overview of the undertaken experiments, the developed PHREEQC models as well as the obtained SCP. The following sections deal with each experiment and its generated model in detail.

Tab. 4.1 General experimental overview including subsequent data processing, model-development and formation-constant assessment

Experiments	Model PHREEQC	Model input	Surface complexation parameter
Titration experiment Musco., Ortho.	Titration model (TM)	Equil. solution, titrants, protolysis const., surface verification (SSD, SSA, M/V), exchange (muco. only), mix-function	SSA, SSD, pK1, pK2
Batch experiment Ortho. - Cs^{+}, Sr^{2+}, Eu^{3+}	Surface complexation model (SCM)	Equil. Solution, equil. phases, protolysis & formation const., pH	logK
Batch experiment Musco. - Cs^{+}, Sr^{2+}, Eu^{3+}	SCM	s.a. + cation exchange, application of strong and weak bonding sites	logK a (strong site) logK b (weak site)

In addition to the listed experiments in Tab. 4.1 batch experiments applying Th^{4+} are also conducted. They are separately discussed in the appendix (section A.8.1).

4.2 Experimental set-up

The follwoing section offers a brief overview of the conducted batch and titration experiments. Generally, more detailed information on the experimental course of the study, applied methodologies and geochemical conditions can be obtained from /BRI 11/.

4.2.1 Titration experiments

Following the experimental set-up of /ARN 01/, the equilibrium solutions of muscovite and orthoclase are applied to conduct titration experiments in order to derive SCP such as pK-values, SSD, and SSA via computational evaluation of the data sets (section 4.4.1).

The samples are treated separately under argon atmosphere. 0.01 M HCl and 0.001 M NaOH solutions are applied for the titration of 80 ml 0.1 M sodium perchlorate ($NaClO_4$) and 1 g suspended solid phase (sediment fraction 63 – 200 µm). Titration starts after the background solution (0.1 M $NaClO_4$) is equilibrated with the mineral which takes approximately 4 months for muscovite and orthoclase, respectively. The titration-

program consists of an acid and accordingly base application of 60 – 2000 µL every 2 minutes.

4.2.2 Batch experiments

Fig. 4.1 illustrates the procedure of the experiments including pretests and the experimental course of the final batch experiments. Pretests are conducted in order to develop the experimental matrix for the batch experiments applying the elements Cs^{+}, Sr^{2+}, and Eu^{3+}.

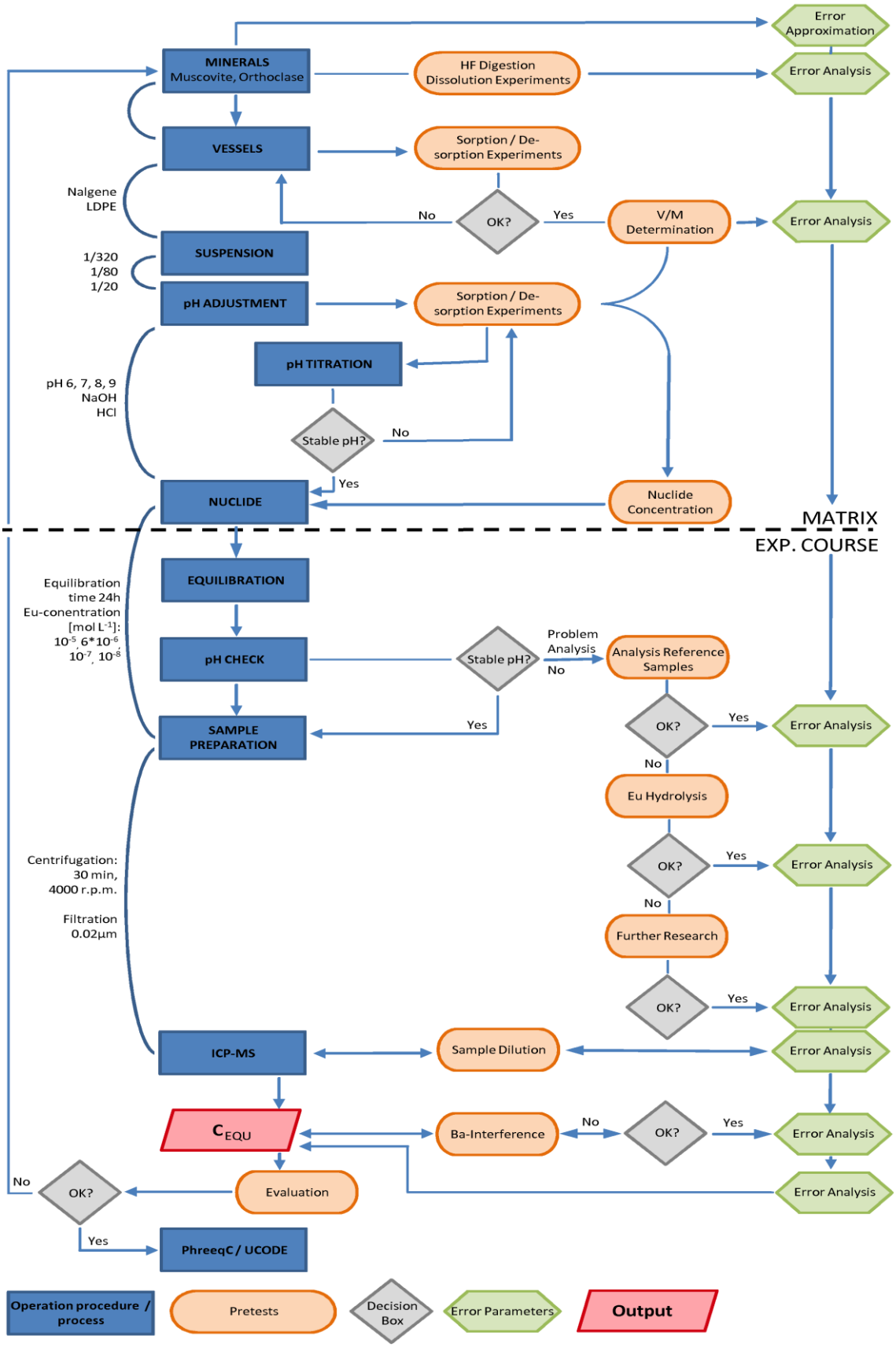

Fig. 4.1 Flow chart: experimental approach. Illustration of the procedural course of the pretests and of the final batch experiments

Tab. 4.2 shows the matrix of the experiments. Two solid-liquid ratios (M/V) are applied, each M/V covering element concentrations of 10^{-5}, 10^{-6}, 10^{-7}, and 10^{-8} mol L^{-1}. For every single concentration mineral suspensions composed of muscovite and orthoclase in 0.01 M $NaClO_4$ (inert background solution) are prepared with pH-values ranging between 4 and 9. Moreover, each combination is conducted three times for threefold measurements and subsequent statistical analysis. This experimental set-up results in 576 samples. The experiments are divided in two batches according to the minerals – hence, each mineral is represented by 288 samples, excluding undertaken Th^{4+} experiments.

Tab. 4.2 Matrix of the final batch experiments employing muscovite and orthoclase wit Cs^+, Sr^{2+}, and Eu^{3+}.

Element concentration, pH, and solid-liquid ratio (M/V) regarding each mineral and element are varied.

Parameters	**Muscovite & Orthoclase**
M/V [g ml^{-1}]	1/20, 1/80
Cs^+, Sr^{2+}, Eu^{3+} [mol L^{-1}]	10^{-5}, 10^{-6}, 10^{-7}, 10^{-8}
pH-range	3 – 9

At first, the minerals are sieved to 63 – 200 µm. Solid/liquid ratios of 1/20 g ml^{-1} and 1/80 g ml^{-1} are applied. Hence, 2 g and 0.5 g of the minerals are mixed with 40 ml background solution (0.01 M $NaClO_4$) in LDPE-vessels, respectively. By adding appropriate amounts of 0.01 M, 0.1 M, and 1 M HCl and NaOH to the suspensions the mentioned pH-values are employed over a time range of approximately three months for each mineral. Throughout the whole experiment the samples are shaken head first. After the suspensions show no significant pH variations over 24 hours, according element concentrations are added. The elements are obtained from ICP-MS CertiPUR normsolution (ICP Standard, 1000 mg L^{-1}, Merck KGaA, 64271 Darmstadt, Germany). Equilibration between the elements and the suspension is set to take place within 24 hours (/BRA 05a/, /ADE 94/). The samples are centrifuged at 4000 r.p.m. for 30 minutes and filtered through 0.02 µm Anotop syringe filters obtained from Whatman. Data acquisition is achieved via subsequent ICP-MS measurements.

4.3 Results

Following, the measured element concentration in solution after conducting the batch experiment is referred to as the equilibrium concentration.

First of all, the collected data is corrected for outliers. Outliers are identified by considering standard statistical procedures such as determining the standard deviation of the equilibrium concentration in the sample solutions regarding the threefold measurements. Each measurement whose absolute difference of the determined equilibrium concentration and the threefold measurements' mean is larger than the standard deviation is excluded from the data set.

Moreover, in order to determine percentage sorbed all measured equilibrium concentrations have to be corrected for errors relating to slight offsets regarding the solid-liquid ratio and for errors resulting from mineral dissolution. Hence theoretical initial element concentrations C_0 are defined. For e. g. Eu^+, C_0 comes up to 1520 $\mu g L^{-1}$ referring to 10^{-5} mol L^{-1} which serves as a start value for subsequent error analysis. Each equilibrium concentration is corrected, hence preventing calculated sorbate concentrations to be biased.

The entire data base is provided by means of Tab. A.8 to Tab. A.12 in the appendix. The attached tables also provide limits of quantification (LOQ) and limits of determination (LOD) as a means to estimate the measuring accuracy of the ICP-MS. Determined concentrations lying below the LOD are removed from the data base and are hence not represented in figures or tables.

All of the following illustrated results correspond to data that has already been processed through the elimination of biasing, measured values.

4.3.1 Titration experiments

Determined titration curves are illustrated in Fig. 4.2 a) and b). Data correspond well with expectations.

The pH-values of the equilibrated suspensions come up to 7.2 and 7.6 for muscovite and orthoclase, respectively. Furthermore, as expected the collected data reveals that

orthoclase is characterized by a slightly greater buffering capacity compared to muscovite. A more detailed discussion of the results presented in Fig. 4.2 can be obtained from section 4.4.1.

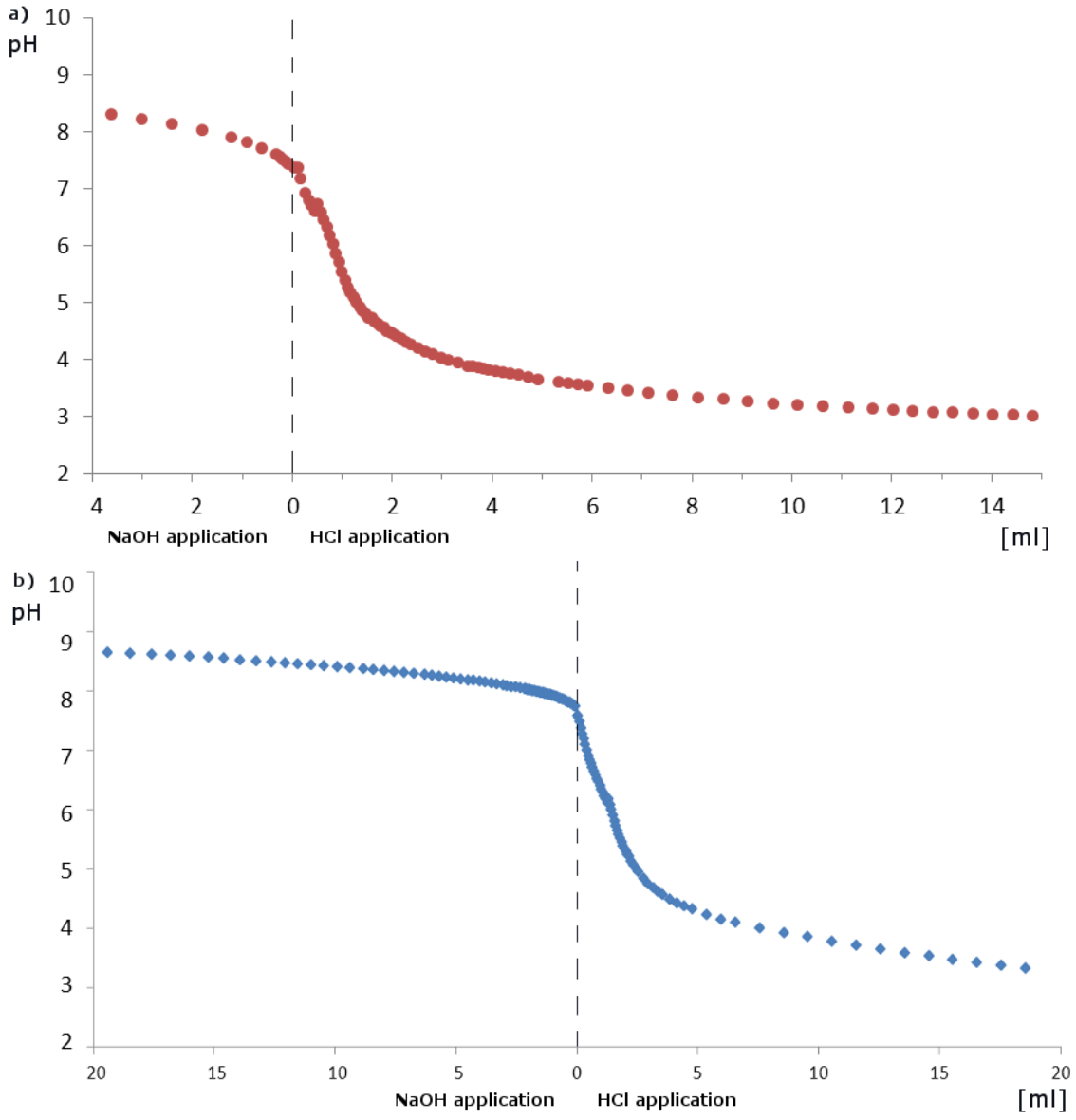

Fig. 4.2 Titration curves for muscovite a) and orthoclase b) conducted after /ARN 01/

4.3.2 Batch experiments involving Cs^+

Muscovite

Fig. 4.3 illustrates the collected data of muscovite-Cs^+ batch experiments. Fig. 4.3 b) shows clear concentration- and M/V-dependencies relating to higher sorbat concentrations with an increasing amount of applied mineral. Furthermore, higher monitored sorbat percentages associate with decreasing element concentrations, as expected.

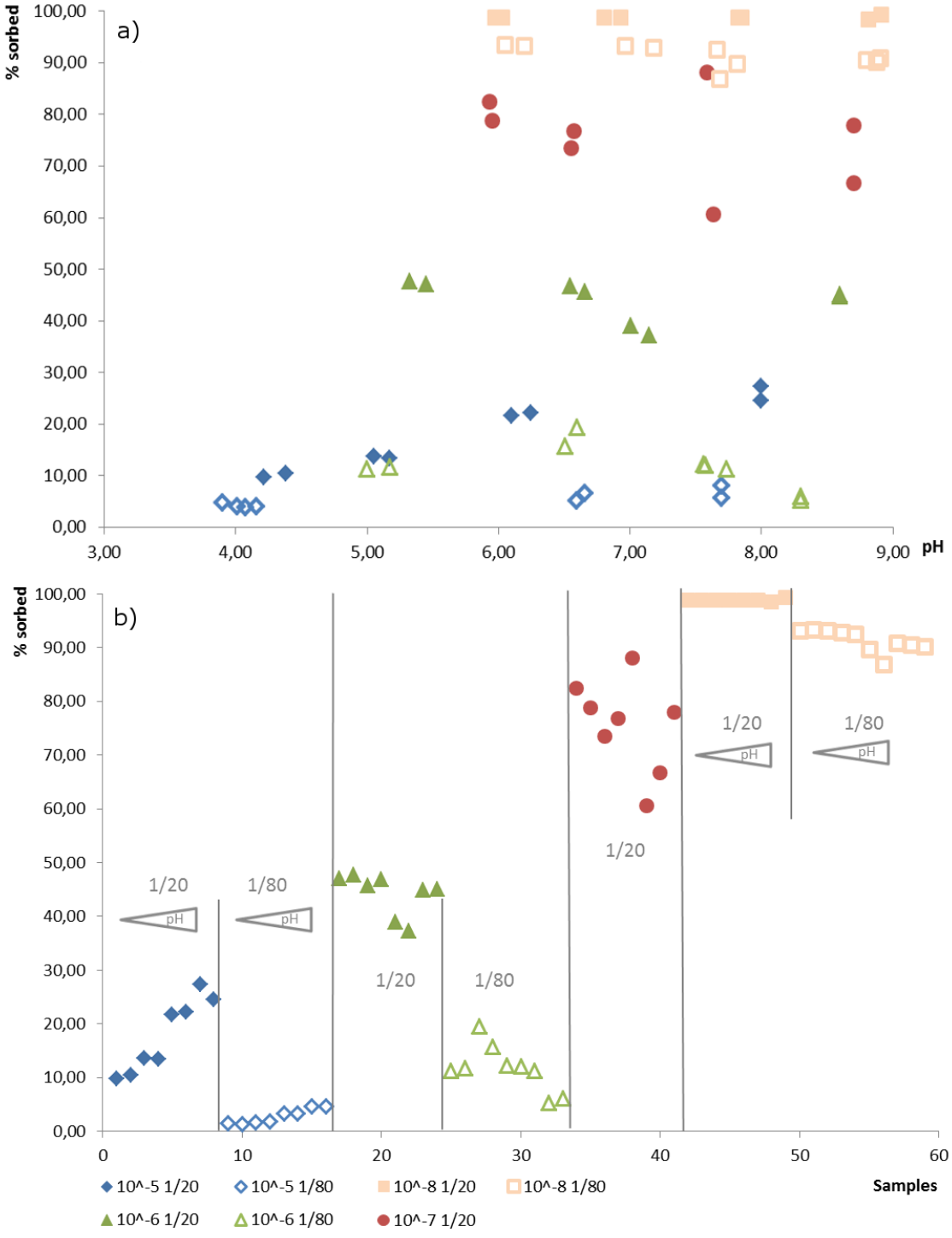

Fig. 4.3 Results of the muscovite-Cs^+ batch experiment

Figure a) offers pH-dependencies, figure b) illustrates the sorbat concentration in % of each sample. Different M/V, pH-conditions, and concentrations are displayed.

However, pH-dependencies are only significantly developed in environments holding high Cs^+ concentrations referring to 10^{-5} mol L^{-1}. Lower concentrations show no distinct dependence on the suspensions' pH which is indicated by evenly distributed sorption

data throughout the applied pH-conditions (Fig. 4.3 a)). Referring to initial Cs^+ concentrations of 10^{-7} mol L^{-1} and 10^{-8} mol L^{-1} the measured data might already represent the maximum of the effective sorbat concentration (sorption-plateau).

Orthoclase

Regarding the orthoclase-Cs^+ batch experiment, results do not meet any expectations made beforehand. In fact, results illustrated in Fig. 4.4 indicate procedural errors throughout the experiment.

No reasonable, reliable explanation can be found to describe decreasing relative amounts of sorbat concentration correlating with decreasing element application. Hence, data displayed in Fig. 4.4 are excluded from further data processing procedures.

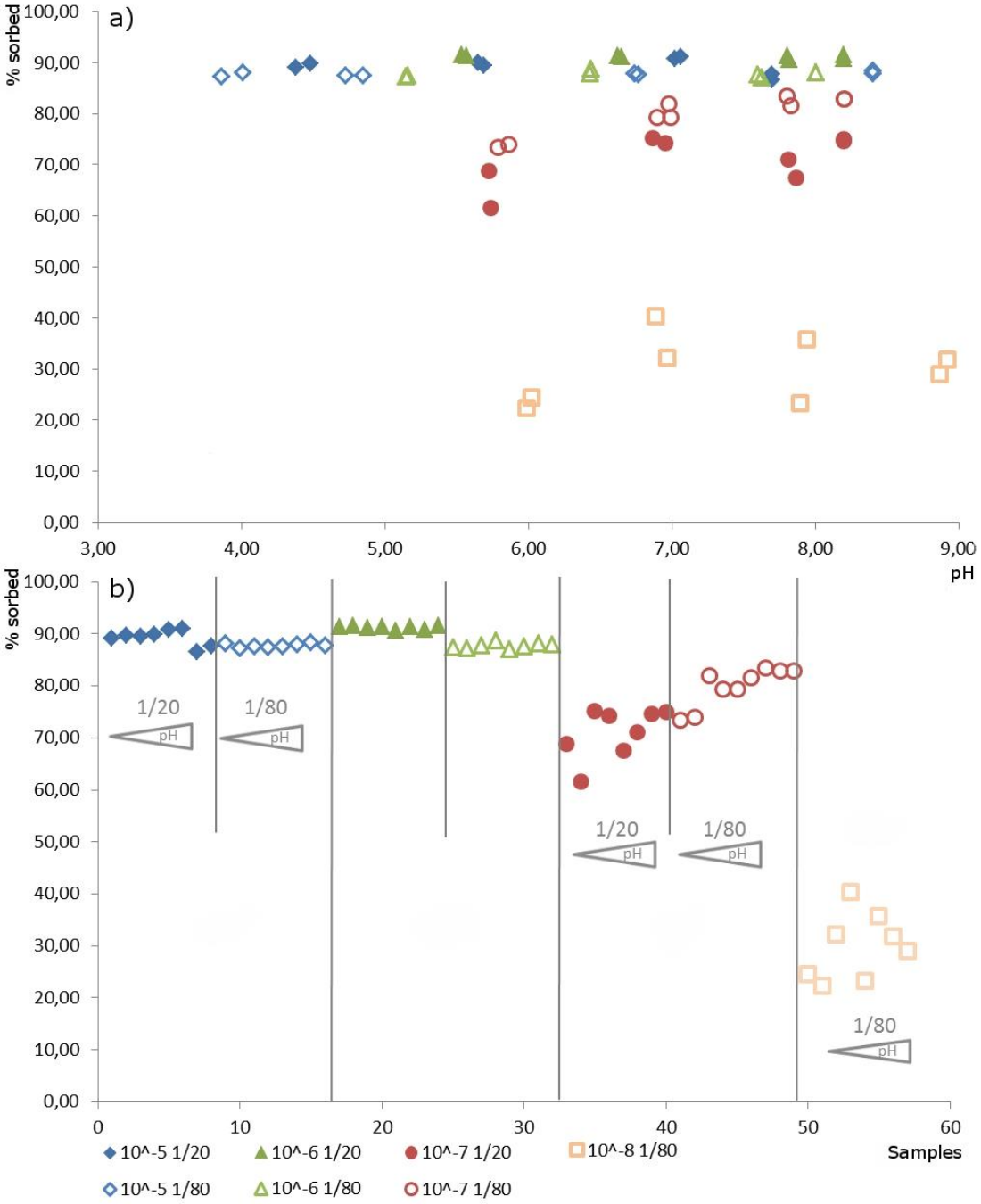

Fig. 4.4 Results of the orthoclase-Cs^+ batch experiment

Figure a) offers pH-dependencies, figure b) illustrates the sorbat concentration in % of each sample. Different M/V, pH-conditions, and concentrations are displayed.

4.3.3 Batch experiments involving Sr^{2+}

Due to technical constraints Sr^{2+} batch experiments only comprise three different element concentrations. The limit of quantification of the analytic device (ICP-MS) equals

10^{-4} mg L^{-1}. Hence, applied Sr^{2+}concentrations range between 10^{-5} mol L^{-1} and 10^{-7} mol L^{-1}.

Muscovite

As shown in Fig. 4.5 obtained results follow expectations, relating to distinct pH-dependences as well as weakly pronounced M/V-dependences. This is shown by the correlation of rising sorbat concentrations and increasing pH-conditions, as well as slightly lower sorbed Sr^{2+} concentrations regarding smaller solid-liquid ratios.

However, throughout the applied chemical conditions relative sorbat concentrations of 100% cannot be observed. Furthermore, Fig. 4.5 b) indicates that no explicit differences in sorption behavior based on varying element concentrations are monitored which results in similar relative sorbat amounts regardless of the initially applied Sr^{2+} concentration. Only data describing a Sr^{2+} concentration of 10^{-7} mol L^{-1}, M/V 1/20 displays higher relative sorbat concentrations compared to the rest of the experimental results.

However, overall the collected data-set shows great reproducibility and hence offers robust and reasonable results.

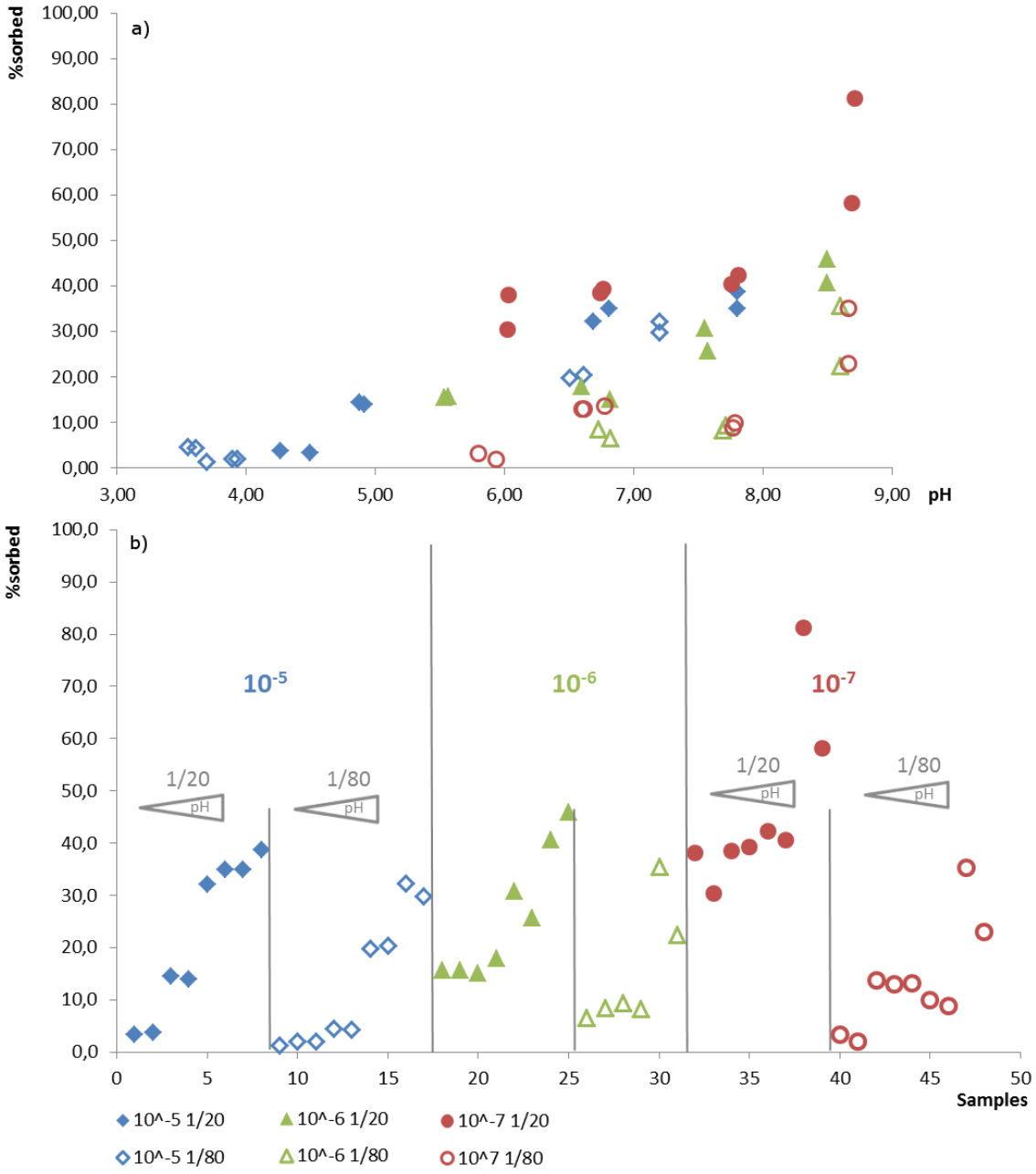

Fig. 4.5 Results of the muscovite-Sr^{2+} batch experiment

Figure a) offers pH-dependencies, figure b) illustrates the sorbat concentration in % of each sample. Different M/V, pH-conditions, and concentrations are displayed.

Orthoclase

Fig. 4.6 illustrates results obtained from Sr^{2+}-orthoclase batch experiments. Regarding Sr^{2+} concentrations of 10^{-5} mol L^{-1} and 10^{-6} mol L^{-1} the collected data represents expected dependencies and characteristics. A strong pH-influence can be observed which is represented by rising sorbat concentrations correlating with increasing pH

conditions. Moreover, the figure clearly shows the applied concentration's impact referring to higher relative sorbat amounts relating to decreasing element applications. The influence of the solid-liquid ratio is not explicitly indicated and shows only minor impact on the measurements.

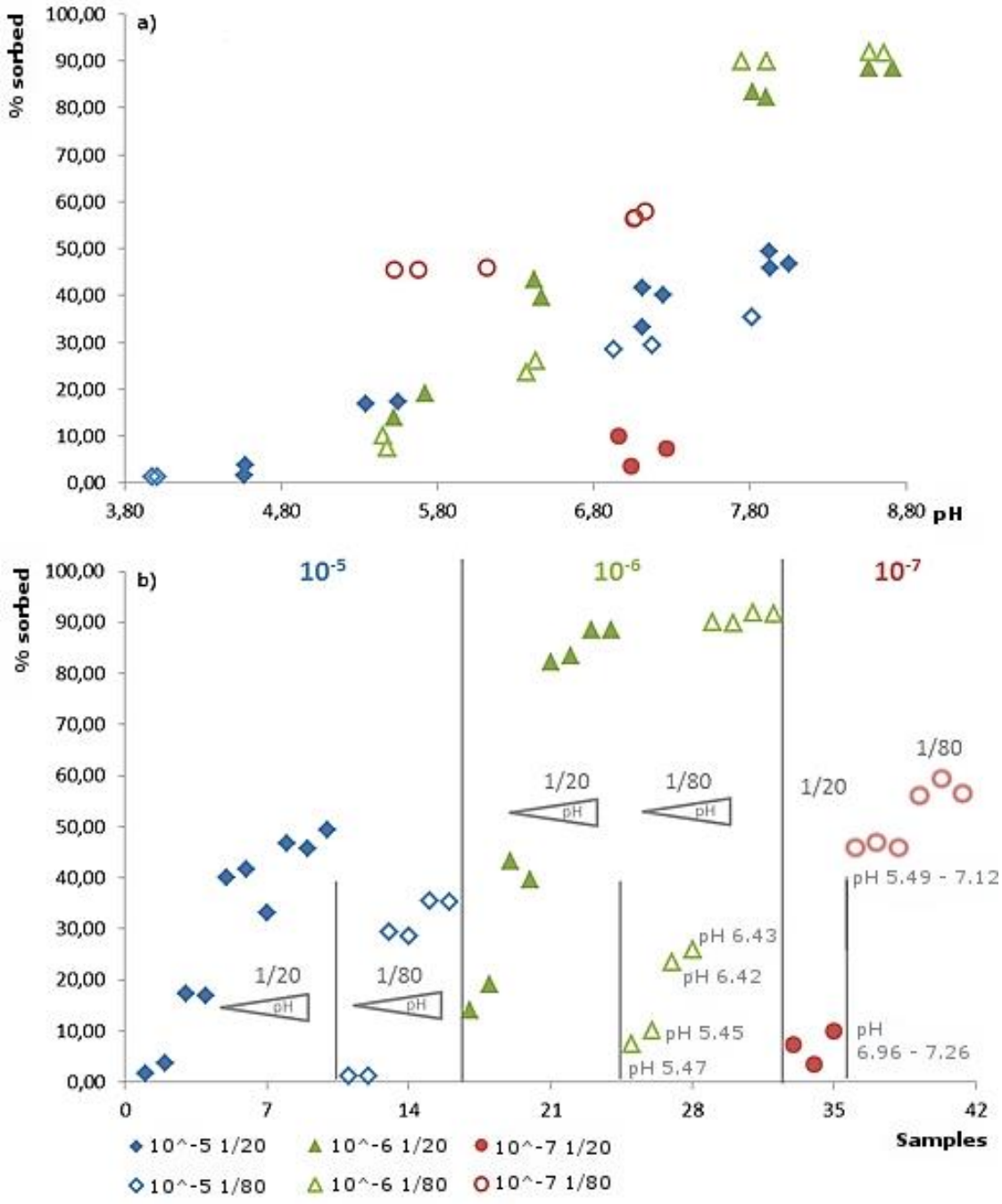

Fig. 4.6 Results of the orthoclase-Sr^{2+} batch experiment

Figure a) offers pH-dependencies, figure b) illustrates the sorbat concentration in % of each sample. Different M/V, pH-conditions, and concentrations are displayed.

However, regarding initial Sr^{2+} concentrations of 10^{-7} mol L^{-1}, measurements show an inconsistence referring to the correlation of the pH and the amount of sorbed Sr^{2+}. Comparing sorbat concentrations of 10^{-6} mol L^{-1} applied Sr^{2+} (M/V 1/80) with concentrations of 10^{-7} mol L^{-1} Sr^{2+} (M/V 1/20), it is not understood why the measurements indicate fewer surface complexes concerning the smaller element input, even though samples hold higher pH-values and a higher solid-liquid ratio. Since the measurements cannot be explained by any means, they are neglected regarding the subsequent determination of surface complexation parameters.

However, generally speaking none of the chosen conditions allowed the entire applied Sr^{2+}-concentration to be sorbed onto the minerals surface.

4.3.4 Batch experiments involving Eu^{3+}

Muscovite

Both images in Fig. 4.7 illustrate expected results. An explicit correlation between the elements in solution and the sorbat concentration in comparison with the pH and the solid-liquid ratio can be observed. This is represented on the one hand by decreasing equilibrium concentrations with increasing pH-values, and on the other hand by generally higher equilibrium concentrations, respectively lower sorbat concentrations relating to the smaller solid-liquid ratio. Detailed values of the measurements can be obtained from Tab. A.11 in the appendix.

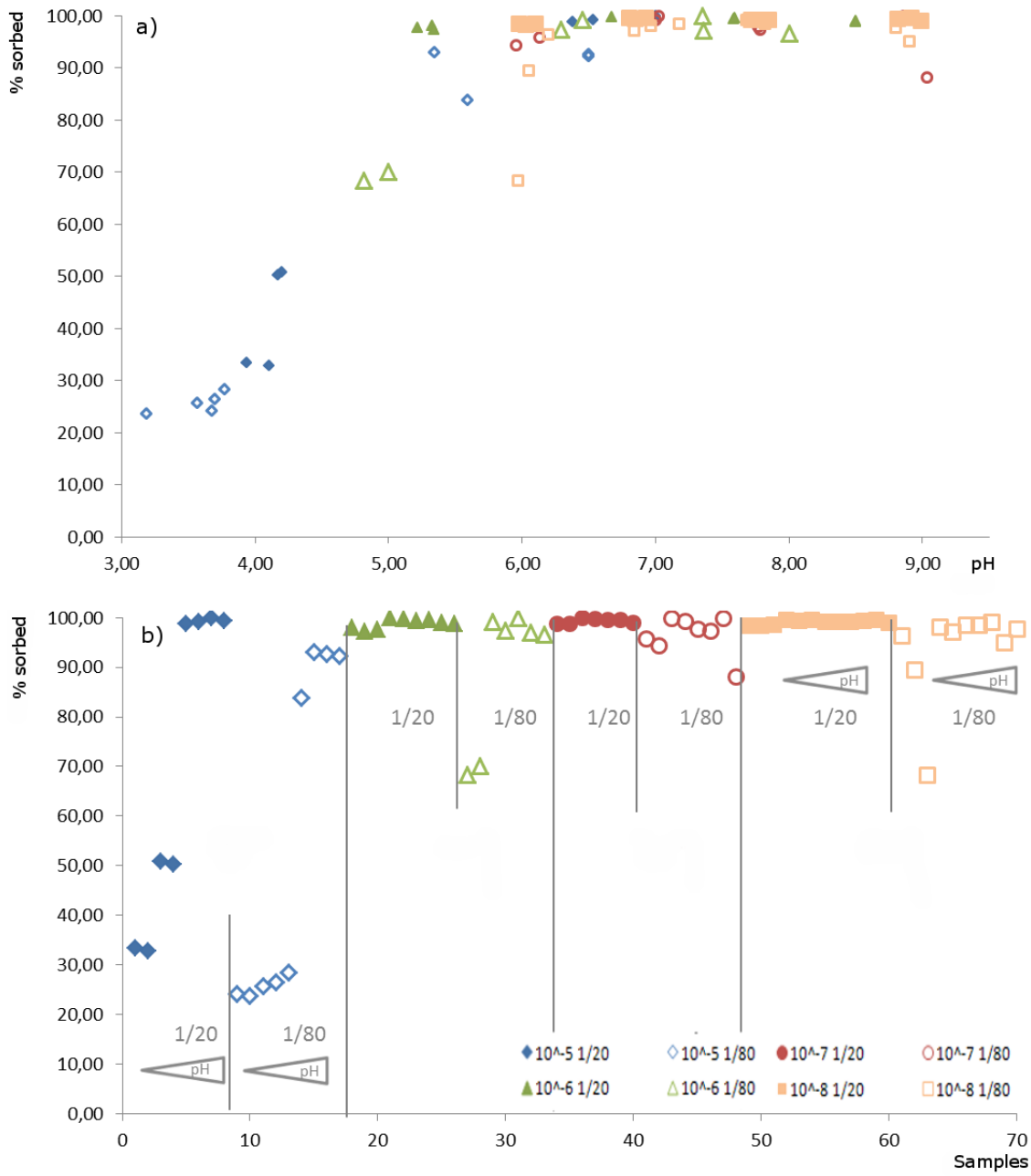

Fig. 4.7 Results of the muscovite-Eu^{3+} batch experiment

Figure a) offers pH-dependencies, figure b) illustrates the sorbat concentration in % of each sample. Different M/V, pH-conditions, and concentrations are displayed.

Examining sorption results of pH 8 and 9, especially for low Eu^{3+} concentrations it is noticeable that equilibrium concentrations rise even though a decreasing tendency would be assumed. A similar observation is reported by /BRA 05b/ who ascribe this behavior to peptisation processes in basic solutions with low ionic strength resulting in smaller specific surface areas which is correlated with smaller sorbat concentrations. However, this is only an explanatory approach since no further information concerning

this behavior has been available, yet. However, here the influence of precipitated Eu^{3+} hydroxo- and carbonato- compounds can be ruled out since molarities range approximately around 10^{-14} molkg^{-1} to 10^{-21} molkg^{-1} according to PHREEQC calculations.

Orthoclase

Results obtained from batch experiments that implement orthoclase and Eu^{3+} are comparable to the described observations regarding muscovite. Fig. 4.8 illustrates clear correlations between the employed pH-values, equilibrium concentrations in the samples as well as the different solid-liquid ratios and initial Eu^{3+} concentrations. Sorption exceeds 99 % concerning initial element concentrations of 10^{-7} mol L^{-1} and 10^{-8} mol L^{-1}. However, the expected relationships are explicitly detectable referring to higher initial Eu^{3+} concentrations as illustrated in Fig. 4.8. It is shown that aqueous Eu^{3+} concentrations decrease with increasing pH and smaller initial concentrations. Furthermore, higher sorbat concentrations are detected referring to the higher solid-liquid ratio.

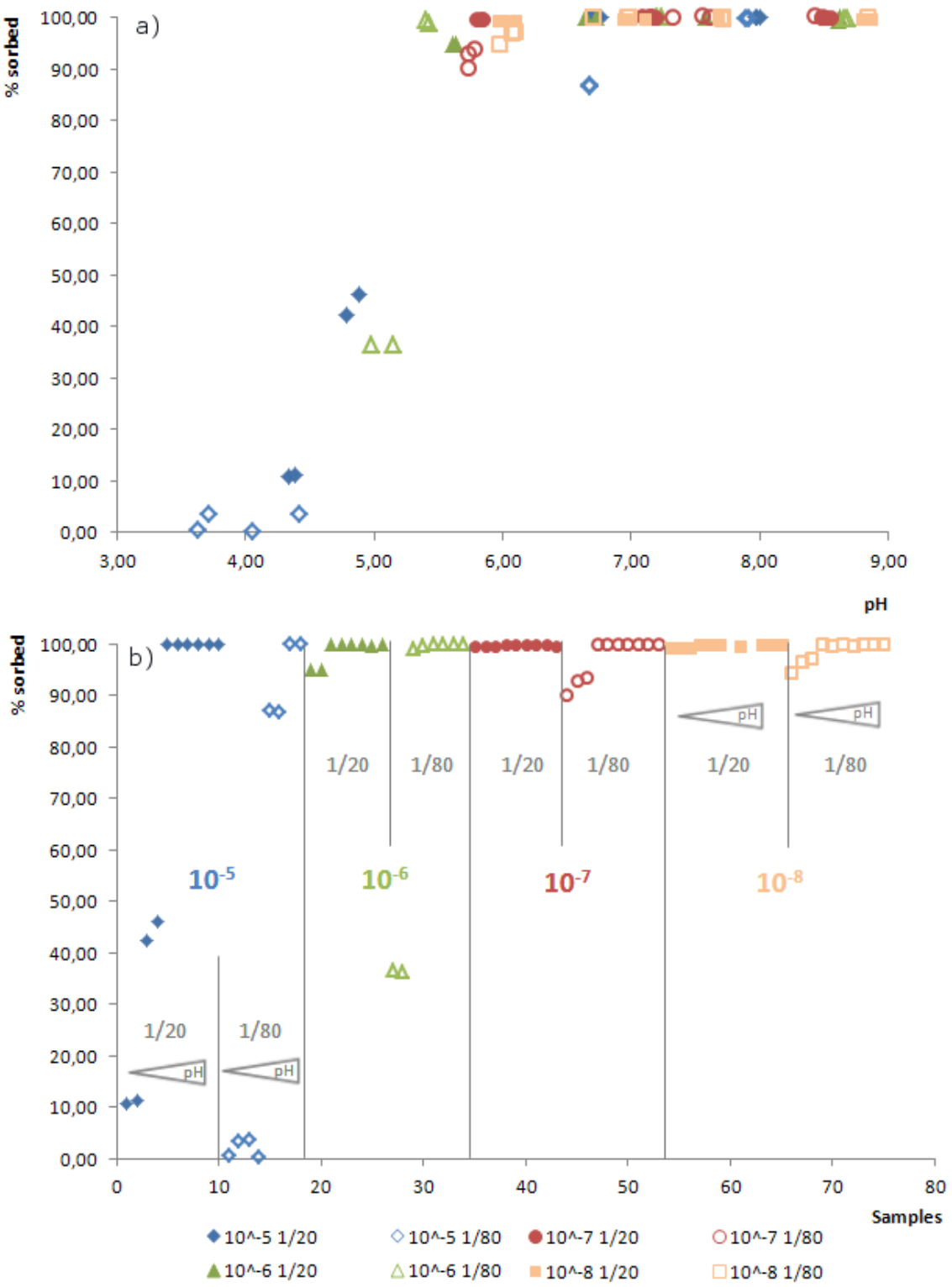

Fig. 4.8 Results of the main batch experiment applying orthoclase and Eu^{3+}

Figure a) offers pH-dependencies, figure b) illustrates the sorbat concentration in % of each sample. Different M/V, pH-conditions, and concentrations are displayed.

4.4 Computer-based analysis and discussion

The focus of this section lies upon fit results, determined surface complexation parameters (SCP), and modeled data sets by means of PHREEQC and UCODE. However, developed surface complexation models (SCM) as well as the iterative approach to asses according SCP and formation constants are described in detail in /BRI 11/.

Following, SCP relates to all determined mineral-specific surface complexation parameters, i. e. surface site area (SSA), surface site density (SSD), and protolysis as well as stability constants for surface complexation and exchange reactions. Models determining SSA, SSD, and protolysis constants are referred to as titration models (TM) and hence relate to the conducted titration experiments, whereas models implemented to determine stability constants (log K-values), i. e. from fits employing data sets obtained from the final batch experiments, are mentioned as the final SCM. Since two minerals are employed in this study, consequently there are two TM and two final SCM each dealing with muscovite and orthoclase, respectively.

Briefly, the stepwise development of the final SCM can be structured in intermediate modeling steps. First, input files are written for the geochemical speciation code PHREEQC in order to iteratively determine SSA, SSD, and protolysis constants of the according minerals. These codes refer to the priorly introduced TM. Here, it is important that the SSD and the SSA are fitted one after another preventing the parameters to influence each other, hence biasing the resulting SCP-values. The following step comprises the further development of the TM by means of program-code adaptation to assess stability constants of surface complexation and exchange reactions. These advanced files represent the actual final SCM of muscovite and orthoclase. However, within the final SCM priorly determined SSA, SSD, and protolysis constants are applied as fix values, whereas stability constants are iteratively determined.

In order to be able to evaluate the correctness of the final SCM and hence the robustness of all assessed SCP, a combination of both final SCM is applied to a synthetic sediment (section 6.3.1). Simulating measured data-sets through the application of the final SCP offers a means to evaluate the determined SCP on the one hand, but also holds the opportunity to verify the bottom-up approach chosen for this study. More detailed information regarding the synthetic sediment, its composition, as well as the model can be obtained from section 6.3.1 and /BRI 11/. Tab. 4.3 offers an overview of the determined SCP and stability constants obtained from titration curve fits, where pK-

values represent protolysis constants according to the following deprotonation and protonation reaction: $SOH = SO^- + H^+$, $SOH + H^+ = SOH_2^+$, and S stands for the mineral surface.

Tab. 4.3 Mineral-specific SCP obtained from titration-curve fits for muscovite and orthoclase

SCP	Muscovite	Orthoclase
SSA [m^2g^{-1}]	5.96	15.2
SSD [sites nm^{-1}]	1.73	7.18
pK1	8.13	8.04
pK2	-6.7	-6.8
R	0.944	0.992

Tab. 4.4 summarizes SCP estimated by applying the final SCM and according fitting procedures to the collected experimental data set. SCP given in Tab. 4.3 are applied as fix values for these fitting procedures.

In Tab. 4.4 “X” indicates parameters applied to specify ion exchange reactions. Exchange species and related log K-values (e. g. LogK_KX) are obtained from literature and determined via implemented half reactions. In contrast, values relating to LogK-EX (E stands for each applied element in the batch experiments) are determined by applying PhreeqC in combination with UCODE. R symbolizes the correlation coefficients for each fit. Eu^{3+} fits are adapted manually; hence no R-values are available. Regarding orthoclase no ion exchange and only one sorption site (logK a) is incorporated in the model. Stabilitiy constants logK a and b stand, e. g., for the S_aOEu2+, S_bOEu2+ strong and weak surface complexes, respectively (section 4.4.2.1).

Tab. 4.4 Mineral-specific stability constants estimated by fitting experimental batch data sets

SCP	**Muscovite**			**Orthoclase**	
	Cs^{+}	Sr^{2+}	Eu^{3+}	Sr^{2+}	Eu^{3+}
logK a	1.12	-4.1	3.5	-4.8	1.95
logK b	-5.66	-6.6	1.6		
SSD (K a/K b)	1/690	1/151	1/100		
EX	0.0				
logK_EX	-1.23	-0.9	-0.6		
KX	$1.64*10^{-2}$ (M/V 1/20), $2.18*10^{-3}$ (M/V 1/80)				
logK_KX	1.3				
NaX	$4.32*10^{-3}$ (M/V 1/20), $3.01*10^{-3}$ (M/V 1/80)				
logK_NaX	0.6				
HX	0.0				
logK_HX	1.26				
R	0.9512	0.8558		0.9123	

4.4.1 Titration model fits

Fig. 4.9 offers a comparison between the measured and fitted data set regarding muscovite a) and orthoclase b) titration curves. Major characteristics of both graphs are well reproduced even though small differences between the measured and the fitted data sets are apparent. According to /HIL 98/ results offered in Tab. 4.3 show fairly good fits referring to the correlation coefficient R (R > 0.9 in both fits). Orthoclase shows only small offsets, while muscovite is represented perfectly except for slight differences relating to higher pH-value.

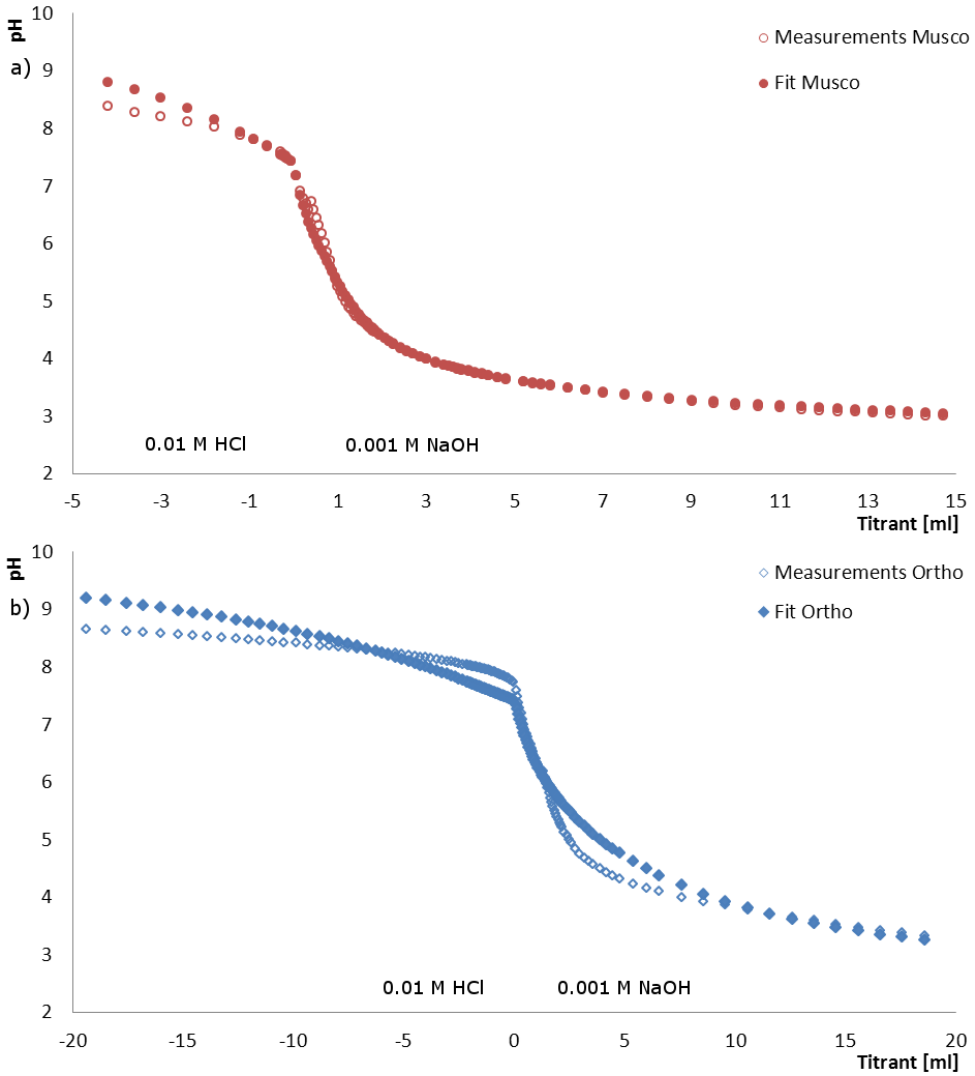

Fig. 4.9 Comparison between the fitted and the measured, experimental data set of the titration experiment applying a) muscovite b) and orthoclase

a) correlation coefficient R = 0.944, b) R = 0.992. Derived SCP are provided in Tab. 4.3.

For comparison, fitted final SCP and SCP-values derived from literature are provided in Tab. 4.5.

To some extent, determined SSD and SSA-values particularly for orthoclase seem to be quite high in relation to typically applied values, e. g. SSD 2.31 sites nm^2 /DAV 90/. However, the preconditioning processes of the minerals by the retailer have to be taken into account in order to put the assessed values into proportion. Especially applicable for orthoclase, where the retailer claims the application of hydrofluoric acid throughout the conditioning process at some point which affects mineral lattice traits such as the SSA and hence SSD /BRI 11/. Furthermore, applied BET measurements hold a fairly

high error according to /OCH 11/, which also needs consideration. Despite, generally speaking, comparable parameter values can be found in literature as Tab. 4.5 shows. Due to similar applied preconditioning techniques of the minerals and comparable experimental set ups a direct comparison is justified. However, since data is lacking, albite is chosen as a close enough equivalent for orthoclase in order to at least estimate the correctness of the assessed parameter dimensions.

Tab. 4.5 Summary of relevant literature parameter sets/values to verify assessed SCP. See also Tab. 4.3 for reasons of comparison

	Mineral	**SSA [m^2g^{-1}]**	**SSD [sites nm^{-1}]**	**pK 1**	**pK 2**
/ARN 01/	Muscovite	1.4	2.61	7.76	-6.11
/TIC 93/	Muscovite	5.2			
/ARN 99c/	Albite		3.1	7.74	-6.47
/ARN 98/	Albite	0.2			
/WAL 05/	Albite	21.6			
/HEG 84/	Orthoclase	15.2			

Hence, determined pK-values refer well to literature as illustrated in Tab. 4.3. Concerning stability constants of surface exchange reactions (Tab. 4.4, LogK_EX) no relevant data is available regarding muscovite and orthoclase. Hence, at this point a verification of these parameters is not possible.

4.4.2 SCM fits

The TM of muscovite and orthoclase offer SCP that are applied as fix parameters in both final SCM to assess the remaining required SCP, i. e. stability constants for surface complexation and ion exchange reactions of muscovite and orthoclase. Priorly assessed and now subsequently employed parameters can be obtained from Tab. 4.3. All final models (muscovite and orthoclase) apply the same surface complexes. Hence, comparing results with one another is reasonable.

In the following figures measured experimental data is represented by colored symbols and simulated ones by black characters. Assessed log K-values are provided in Tab. 4.4. Verifications of the fitted log K-values to literature data sets are not possible since there are no stability constants available regarding relevant surface complexation

reactions and exchange reactions for the applied elements on muscovite and orthoclase surfaces.

4.4.2.1 Fitting approach

In general, the determination of pending stability constants is iteratively approached starting out with the application of initial values obtained from varying data bases. Conducting numerous simulation runs offers the possibility to get an insight of the interaction of the CEC, stability constants and possible varying sorption affinities of the employed elements towards special sorption sites on the minerals' surfaces. Since mica minerals hold more complex surfaces compared to feldspar minerals, both silica surfaces are implemented differently into the geochemical speciation code PHREEQC. Orthoclase, on the one hand, employs only one sorption site (a), while muscovite, on the other hand, is described by strong and weak sorption sites (a and b).

Intending to develop a simple, widely applicable model which is capable to reporduce experimental data as good as possible lead to the implementation of the common monodentate surface complexes S_aOCs^{+}, S_aOSr^{+}, and S_aOEu^{2+}, where S stands for the surface of the according mineral, 'a' and 'b' for the sorption sites, respectively. For reasons of comparability these complexes are applied in all fits.

Obtained fits generally match collected data sufficiently. However, regarding Cs^{+} and Sr^{2+} offsets between the measurements and the estimated data are evident regarding both minerals (section 4.4.2.2 and 4.4.2.3). Hence, in order to improve correlations between the fitted and experimental data, the muscovite-Sr^{+} data set is chosen to adapt PHREEQC codes by means of introducing further, partially more complex surface reactions, exemplarily. Therefore, the monodentate surface complex S_aSr(OH) and the bidentate $(S\_aO)_2Sr$ complex are implemented into the codes.

Fig. 4.10 illustrates results obtained from the application of varying surface complexes. The different graphs are meannually adapted to offer a better overview of the assessed data. The graps highlight mean values of sorbat cocentrations regarding the two employed solid liquid ratios, where each color represents the fit of one surface complex. Here, black characters illustrate the collected experimental data as well as the final fitted data set (x) as a means for comparison. The values for the according stability constants of each complex combination can be obtained from Tab. 4.6. For

further information regarding the final calculated data set of the muscovite-Sr^+ batch experiment see section 4.4.2.2.

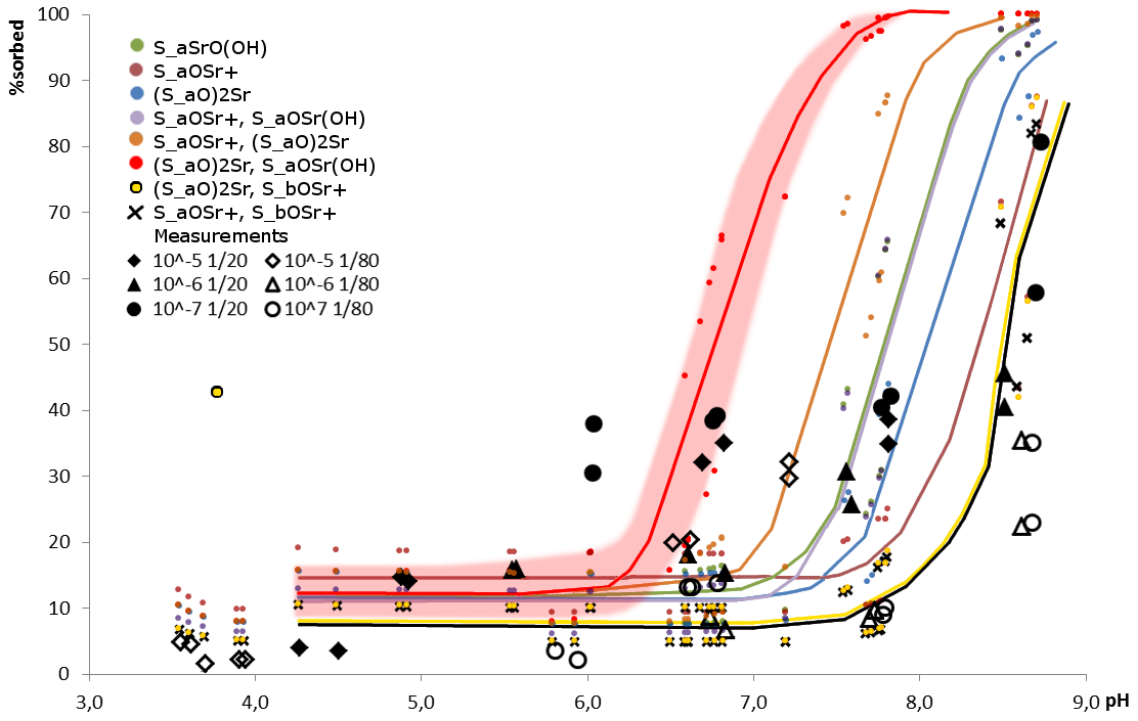

Fig. 4.10 Comparison of fitted results based on different sets of surface species. The graphs represent manually adapted sorption isotherms

The red shadow exemplarily illustrates the range of the measurements for the species set $(S\_aO)_2Sr$, S_aOSr(OH). The final fitted data set is symbolized with black crosses.

Tab. 4.6 List of applied surface complexes and according log K-values. a and b refer to strong and weak sorption sites

Complex	**Site**		**CEC**
	Log K a	Log K b	
S_aSrO(OH)	-12.0		-0.7
S_aOSr^+	-12.0		-0.7
$(S\_aO)_2Sr$	-12.0		-0.7
S_aOSr^+, S_aSr(OH)	-6.9, -12.0		
S_aOSr^+, $(S\_aO)_2Sr$	-4.0, -12.0		
$(S\_aO)_2Sr$, S_aOSr(OH)	-12.0, -10.1		
$(S\_aO)_2Sr$, S_bOSr^+	-11.0, -19.0	-19.0	-0.9
S_aOSr^+, S_bSr^+	-4.1	-6.6	-0.9

As illustrated in Fig. 4.10, so far it is not possible to determine a fit that correlates satisfactorily over the entire data set. Sorbat concentrations ranging between 25 % and 55 % are difficult to estimate. Fig. 4.10 highlights that no matter which complex or complex-combination is applied the steepness of the sorption isotherm is not affected resulting in low correlations regarding the mentioned sorbat-concentration range. So far it is only possible to shift the curve longitudinally by applying varying surface complexes, and vertically by introducing different values for the stability constant of exchangeable cations.

As shown in Fig. 4.10 the bidentate complex-combination $(S\_aO)_2Sr$ – S_bOSr^+ (strong a, weak b sites) produces similar results compared to the final fitted data set that employs the fairly simple, monodentate, two-sites' complex S_aOSr^+ - Sr_bOSr^+. Since it is the aim to produce a simple, broadly applicable model, the implementation of the model associated with the single monodentate surface complex is favored over the surface-complex combination regarding all fits.

However, further research is needed to fully understand the according surface reactions and geochemical processes, in order to be able to reproduce experimental data more precisely.

4.4.2.2 Muscovite SCM

Cesium

Fig. 4.11 offers a comparison between the measured experimental data and the calculated data set. Differences are obvious, even though the illustrated results offer the best fit obtained after applying PHREEQC in combination with UCODE. Obtained SCP are illustrated in Fig. 4.11 a).

Sorbat concentrations resulting from higher initial element input of 10^{-5} mol L^{-1} are estimated satisfactorily. In comparison, the fitted data set representing 10^{-6} mol L^{-1} Cs^+ shows major deficits. Similar differences can be observed regarding smaller element concentrations.

As indicated in section 4.3.2 sorbat concentrations resulting from initial element concentrations of 10^{-6} to 10^{-8} mol L^{-1} Cs^+ could represent sorption maxima referring to the

maximum amount of effective sorbat concentration. Unfortunately, so far it is not possible to estimate data sets that display the experimental data and hence the sorption plateau of Cs^+ on muscovite surfaces more accurately. However, the developed PHREEQC codes undergo constant reevaluation and improvement. It is likely that a better adapted input file for PHREEQC results in an enhancement of the fit's properties, which is planned to be achieved throughout an upcoming research project.

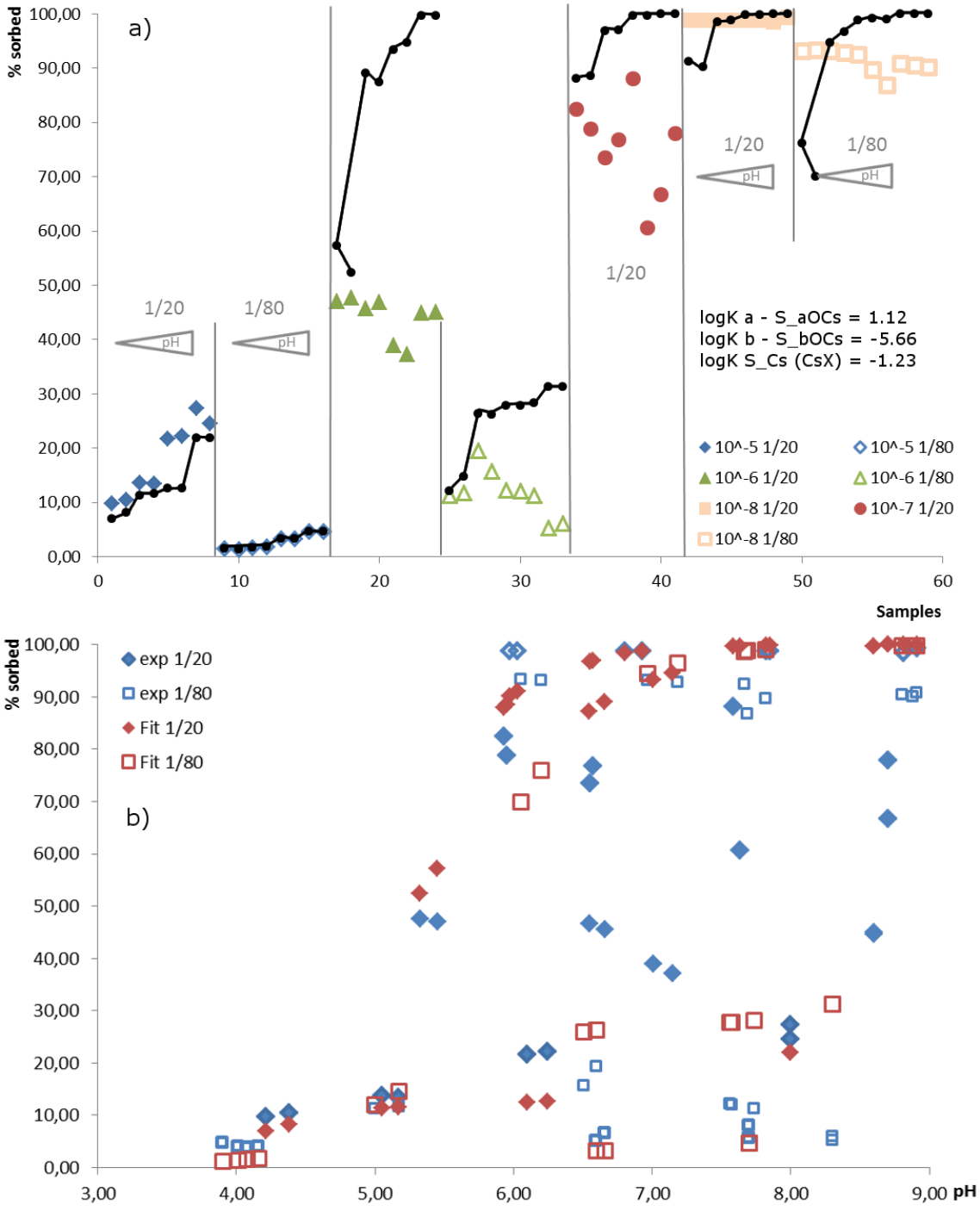

Fig. 4.11 Results of the muscovite-Cs^+ fit: a) black characters represent the fitted data set, b) gives pH-dependencies

Strontium

Generally speaking, data illustrated in Fig. 4.12 a) represents sufficient correlations between measurements and experiments.

However, significant discrepancies are still apparent regarding initial Sr^{2+} concentrations of 10^{-5} mol L^{-1}. Here, the pronounced relation between increasing sorbat concentrations and increasing pH-values is unsatisfactorily displayed. Regarding smaller element concentrations offsets are smaller; hence the fitted data set describes major sorption trends more precisely.

In Fig. 4.12 b) both data sets (calculations and measurements) are plotted against the pH. It becomes obvious, that even though sorption tendencies are sufficiently represented regarding initial Sr^{2+} concentrations of 10^{-6} mol L^{-1} to 10^{-8} mol L^{-1} sorption edges are estimated slightly too steep compared to experimental values.

However, since the focus of this study lies on trace element concentrations the assessed SCP parameters display the collected experimental data satisfactorily and may be obtained from Fig. 4.12 a) or Tab. 4.4.

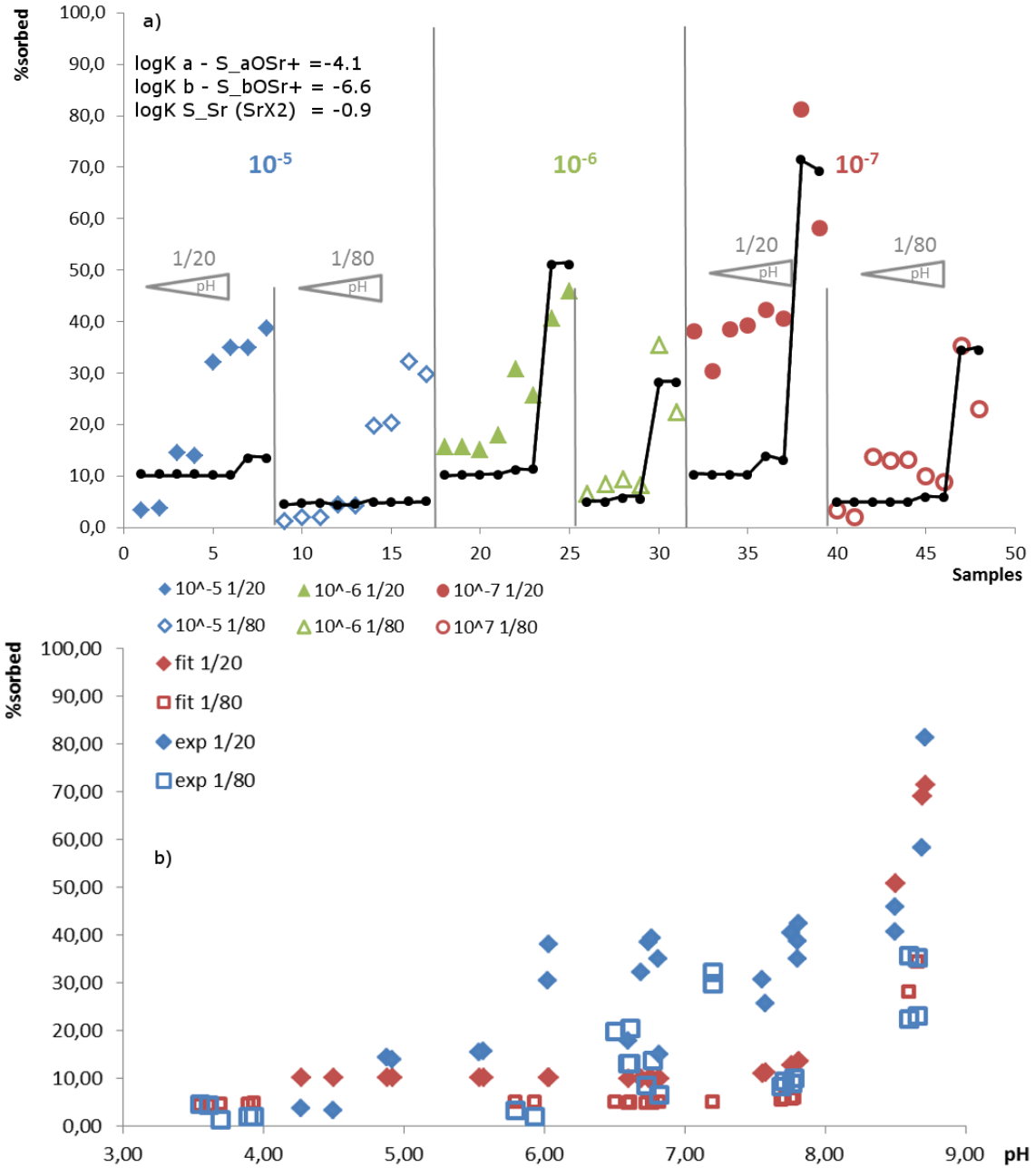

Fig. 4.12 Results of the muscovite-Sr^{2+} fit: a) black characters represent the fitted data set, b) gives pH-dependencies

Europium

As shown in Fig. 4.13 a) and b) simulated data generally offers a good fit of the muscovite-Eu^{+} measurements.

However, the estimated data shows a slightly better correspondence concerning low element concentrations: Fitted Eu^{+} amounts of 10^{-5} mol L^{-1} and 10^{-6} mol L^{-1} show minor

deficits. Whereas in comparison, sorbat concentrations representing initial 10^{-7} mol L^{-1} to 10^{-8} mol L^{-1} Eu^{3+} are adequately simulated regarding all pH-values. However, overall major sorption trends as well as sorption edges are satisfactorily represented whereat, i. e. different amounts of sorbed Eu^{+} correlate well with the applied M/V as well as increasing sorbat percentages involve decreasing Eu^{+} concentrations.

Plotting the pH against sorbed relative Eu^{+} percentages (Fig. 4.13 b)) illustrates the influence of the CEC regarding the mica mineral: Due to element and crystal-lattice interactions lowest observed relative sorbed Eu^{+} concentrations do not fall below 20 %. Hence, the implementation of CEC reactions regarding muscovite is reinforced.

Furthermore, Fig. 4.13 b) underlines slight offsets between the fitted and measured data set in the range of pH 4.5 and 6. As shown, calculated concentrations underestimate measured ones which has already been indicated in Fig. 4.13 a). However, interactions between sorption processes and pH conditions are still satisfactorily displayed by means of correctly fitted sorption edges in Fig. 4.13 a) and b).

According assessed stability constants are given in Fig. 4.13 as well as in Tab. 4.3 and Tab. 4.4. Due to the good correlation between the experimental data and the fit the derived SCP are assumed to hold a high accuracy. The application of the SCM to a synthetic sediment also backs up this statement (section 6.3.1).

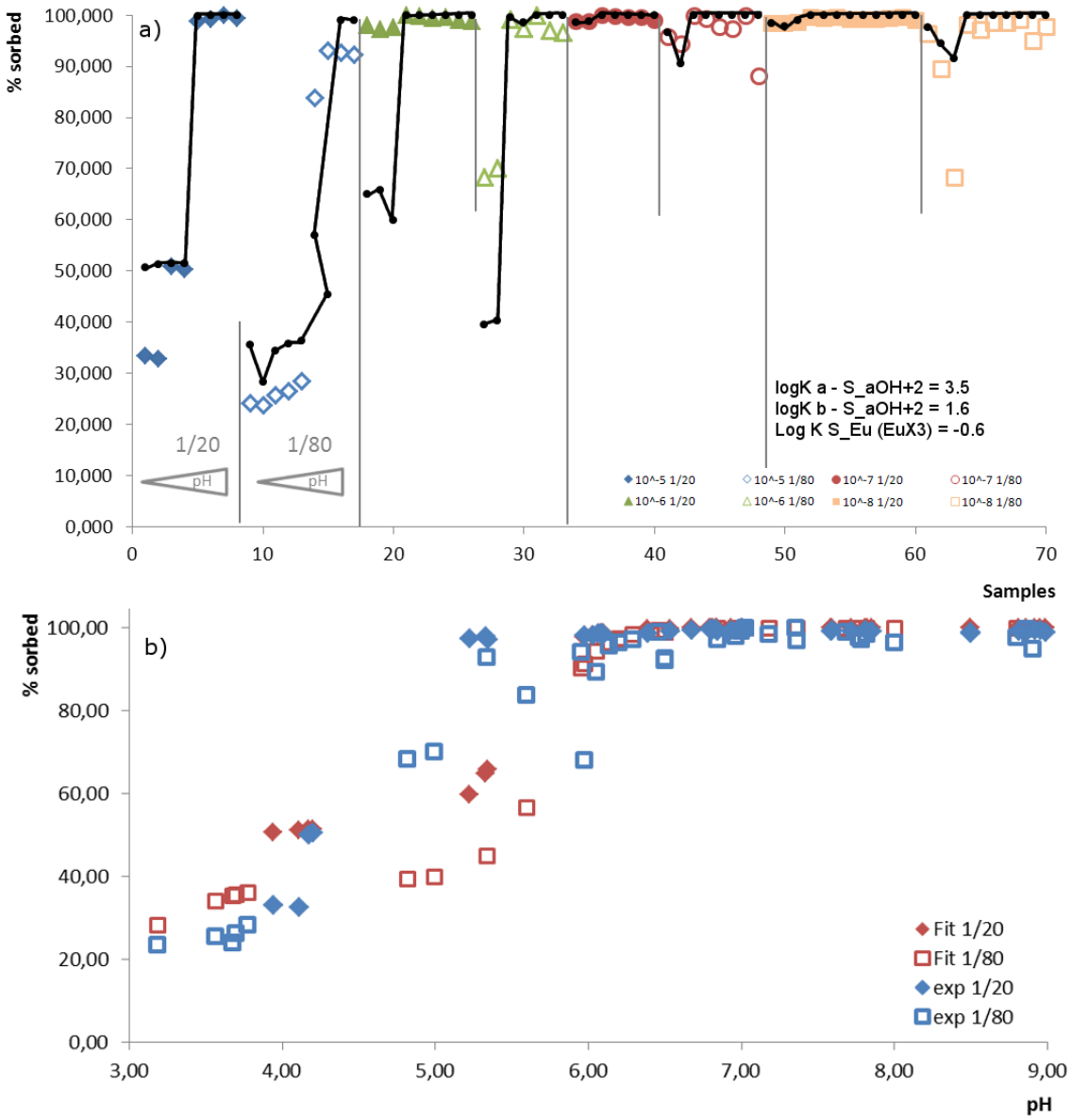

Fig. 4.13 Results of the muscovite-Eu^{3+} fit: a) black characters represent the fitted data set, b) gives pH-dependencies

4.4.2.3 Orthoclase SCM

Analogue to muscovite the experimental data of orthoclase is simulated. In comparison, the only difference lies in the application of different SCP obtained from the TM (Tab. 4.3) and in the exclusion of the CEC since generally K-feldspars are no major cation exchangers. Hence, the only outstanding parameter to be assessed for orthoclase is the surface stability constant for surface complexes where no difference is

made between strong and weak sorption sites due to the orthoclase's straightforward crystal lattice structure.

Strontium

As indicated in section 4.3.3 measurements regarding initial element concentrations of 10^{-7} mol L^{-1} are neglected from further data processing. Hence, Fig. 4.14 only illustrates fitted data referring to higher initial element Sr^{2+} concentrations.

In general, the estimated data set represents measurements sufficiently since major sorption trends are successfully represented. However, similar to muscovite-Sr^{2+} fit experimental data regarding sorbat concentrations in the range of 20 % to 50 % are difficult to calculate (Fig. 4.14 b)). Here, estimated sorption percentages associated with initial Sr^{2+} concentrations of 10^{-6} mol L^{-1} are too low at the pH of 6.4. In contrast, sorbat concentrations resulting from initial Sr^{2+} input of 10^{-5} mol L^{-1} and pH conditions of 7.8 are significantly overestimated (Fig. 4.14 a)).

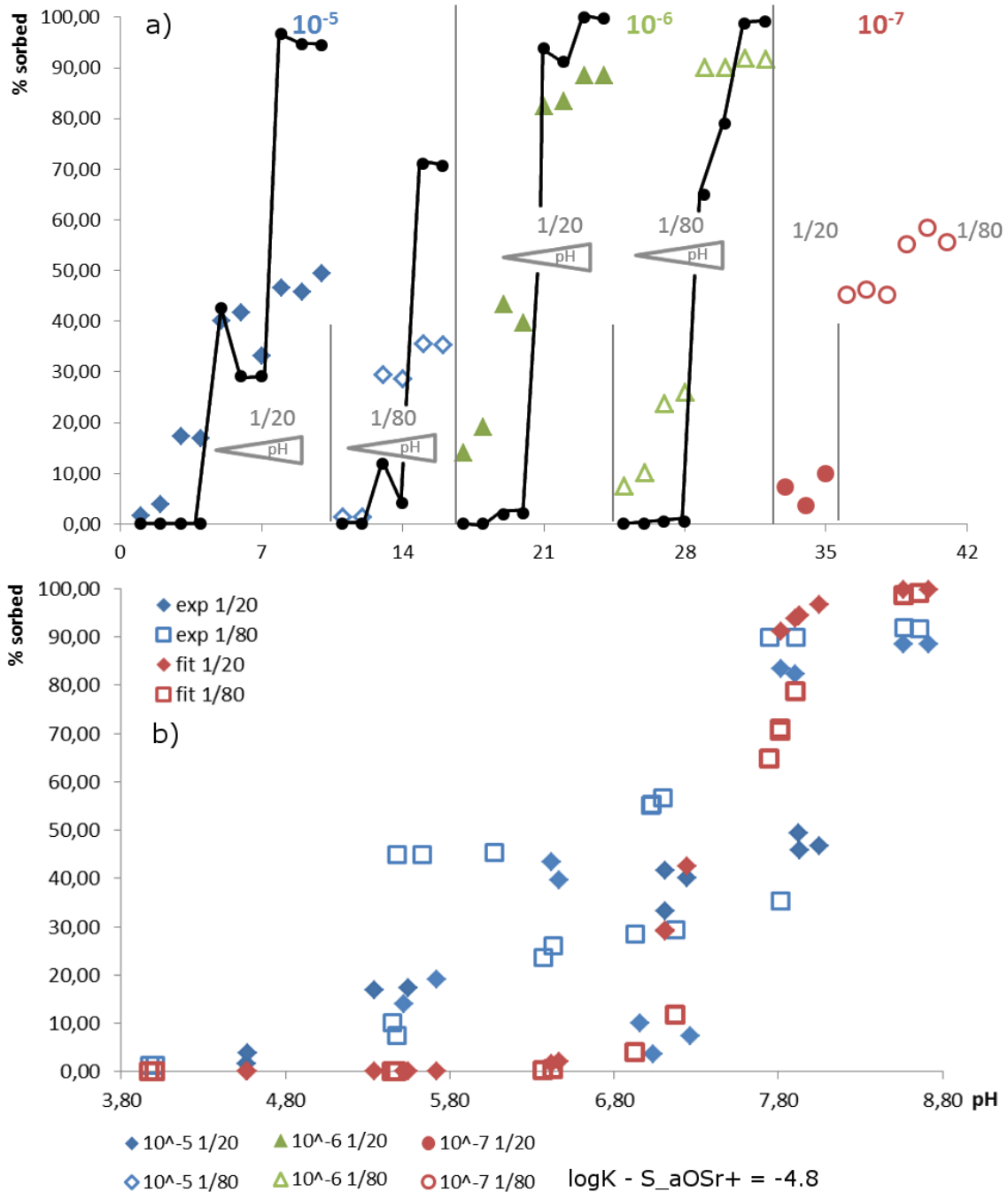

Fig. 4.14 Results of the orthoclase-Sr^{2+} fit: a) black characters represent the fitted data set, b) gives pH-dependencies

Europium

Fig. 4.15 illustrates the fit of the measurements from Eu^{3+} batch experiments. The determined Eu^{3+} surface complex stability constant equals 1.95.

As illustrated, both data sets correspond very well. All major sorption trends regarding all pH conditions and element concentrations are represented. Simulated sorption edges express measured ones satisfactorily. However, minor discrepancies between the fit and the measured data can be observed regarding Eu^{+} concentrations ranging between 10^{-5} mol L^{-1} and 10^{-6} mol L^{-1} which is similarly reported for muscovite.

Here again, the application of the developed SCM to a synthetic sediment (section 6.3.1) and the successfully modeled results support the robustness of the assessed data set regarding the batch experiment orthoclase-Eu^{3+}.

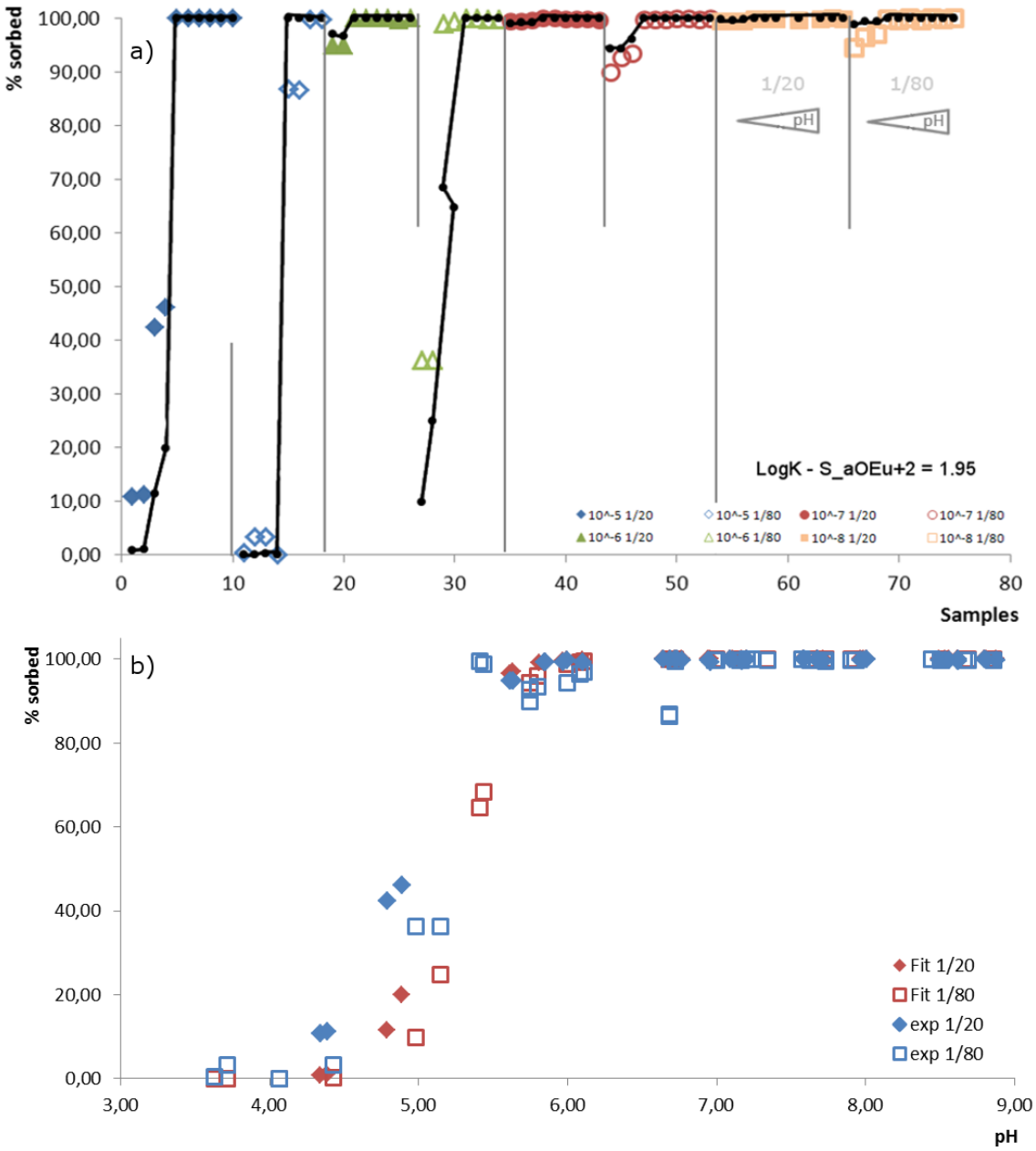

Fig. 4.15 Results of the orthoclase-Eu^{3+} fit: a) black characters represent the fitted data set, b) gives pH-dependencies

4.5 Future perspectives

Concluding, the conducted measurements and obtained SCP embody reliable data sets offering the possibility to closer analyze sorption behavior of sediments. Furthermore, the generally good correlation between the experimental data and each fit emphasizes the robustness of the determined SCP. The exemplarily application of the

Eu^{3+} SCM to a synthetic sediment (section 6.3.1) further backs up the assessed SCP and approves the chosen bottom-up approach of this study.

However, difficulties lie in the execution of the extensive experimental set-up. The correct application of the geochemical speciation code PHREEQC also demands solid background knowledge regarding the code and is hence under constant improvement.

Further research will be conducted as part of an upcoming project in order to gain a better insight into the chemistry of radionuclides crucial for long-term safety analysis. Within this following research the Cs^{+}-orthoclase system is planned to be repeated and PHREEQC input files are intended to be improved. More detailed geochemical conditions will be applied, e. g. incorporating elevated saline conditions as well as competing cations and ligands in order to obtain robust, reliable data complementing sorption data bases that are applied in chemical transport scenarios.

5 Identification and selection of governing environmental parameters E_i

The sorption of radionuclides onto the relevant mineral phases (section 2.1) is governed by environmental parameters such as pH, dissolved inorganic carbon (DIC), temperature, ionic strength (salt concentration) and concentration of complexing and competing ions.

5.1 Environmental parameters

To keep the complexity and the CPU time to a minimum, the number of environmental parameters was limited and only those were selected having an important influence onto sorption processes. The selected environmental parameters E_1 – E_6 are listed below, one should, however, keep in mind that factors such as pH and DIC or Ca and IS are correlated.

1. E_1: pH
2. E_2: DIC
3. E_3: Ionic strength IS
4. E_4: Total concentration of Al
5. E_5: Total concentration of Ca
6. E_6: Total radionuclide concentration

Obviously, there are more complexing and competing ions than considered as environmental parameters; the most important representatives amongst them are silicon and iron. The concentration of the ions SiO_3^{2-} and Fe^{3+} is primarily determined by equilibria with solubility limiting mineral phases (suitable phases would be quartz and hematite, respectively), and the input parameters already established above. Thus these concentrations can be considered as “secondary” environmental parameters whose value can be derived from the already established values for E_1 to E_6. This provides two alternatives of handling them: It can be incorporated into r³t or it can become part of the computation scheme to generate the multi-dimensional K_d-cloud. To keep the chemical speciation calculations with r³t at a minimum, the second alternative has

been selected within this project. A final criterion for establishing the K_d-matrix is the relevance and concentration of repository-specific radionuclides. The following elements are selected (section 2.4): Am, Cm, Cs, Ni, Np, Pu, Ra, Se, Th, and U (with Am and Th also used as chemical analogues for Cm and Pu).

Beside these chosen parameters, there are further environmental parameters at the Gorleben site, such as organic material which is ubiquitous in these sediments and might impact the sorption of the radionuclides. However, to keep the system simple it is decided to not consider further parameters like the organic ligands at this stage. This organic material is only included as a carbon source due to metabolistic activities, see section A.7.

5.2 Best estimation of minimum and maximum concentrations

Based on the site-specific environmental conditions in the sedimentary overburden of the Gorleben salt dome as well as the maximum element concentrations of repository-relevant radionuclides the following minimum and maximum concentrations of relevant environmental parameters $E_1 – E_6$ are proposed for the calculation of the K_d-matrices for each sedimentary unit (UAF, AT, LAF, section 2.2) in Tab. 5.1. Our reasons and arguments for the variation of these environmental parameters are taken from various documents as explained below.

As a basis for the estimation of the minimum and maximum values of pH, DIC, Ionic Strength [IS], [Al] and [Ca] the chemical data for groundwater in the sedimentary overburden of the Gorleben salt dome was used /KLI 04/ (Tab. A.2 to Tab. A.4 in appendix). Additionally, the soluble Al and Ca contents in the most important mineral phases in the Gorleben sediments are considered for the maximum values. Based on the mass percentage of the relevant Al-minerals (gibbsite, anorthite, muscovite), Ca-minerals (calcite, anorthite) and carbonates (calcite) their soluble Al-, Ca- and DIC-content were calculated by PHREEQC and added to the maximum values. Also on basis of /KLI 04/ the different error distribution functions (EDF) for $E_1 – E_6$ were estimated.

In order to determine the maximum radionuclide concentrations [RN], which are needed to establish the K_d-matrix, far-field calculations for a scenario with relatively high radionuclide release rates from the near field was regarded (brine intrusion scenario). The calculations have been performed with a two-dimensional model described in de-

tail in /KEE 05/. The selection of the maximum radionuclide concentrations is described in section 2.4.1.

Tab. 5.1 Proposed minimum and maximum values of environmental parameters (concentrations in mol L^{-1})

Environmental parameter		UAF		AT		LAF		EDF
		Min	Max	Min	Max	Min	Max	
E_1:	pH	6.40	8.68	6.73	9.26	6.36	8.69	Uniform
E_2:	DIC	3.53E-04	9.05E-03	7.78E-04	8.03E-03	1.32E-03	1.35E-02	log-Uniform
E_3:	IS	9.58E-04	1.77E-02	3.86E-04	4.55E-02	6.14E-03	5.00E-01	log-Uniform
E_4:	[Al]	7.68E-07	4.29E-06	1.20E-07	8.83E-04	5.10E-07	8.54E-05	log-Uniform
E_5:	[Ca]	2.40E-04	4.84E-03	2.64E-05	1.02E-03	8.77E-05	1.67E-01	log-Uniform
E_6:	[RN]							
	Am	1.00E-14	1.00E-08	1.00E-14	1.00E-08	1.00E-14	1.00E-08	log-Uniform
	Cm	1.00E-14	1.00E-08	1.00E-14	1.00E-08	1.00E-14	1.00E-08	log-Uniform
	Cs	1.00E-12	1.00E-06	1.00E-12	1.00E-06	1.00E-12	1.00E-06	log-Uniform
	Ni	1.00E-12	1.00E-06	1.00E-12	1.00E-06	1.00E-12	1.00E-06	log-Uniform
	Np	1.00E-13	1.00E-07	1.00E-13	1.00E-07	1.00E-13	1.00E-07	log-Uniform
	Pu	1.00E-13	1.00E-07	1.00E-13	1.00E-07	1.00E-13	1.00E-07	log-Uniform
	Ra	1.00E-13	1.00E-07	1.00E-13	1.00E-07	1.00E-13	1.00E-07	log-Uniform
	Se	1.00E-12	1.00E-06	1.00E-12	1.00E-06	1.00E-12	1.00E-06	log-Uniform
	Th	1.00E-14	1.00E-08	1.00E-14	1.00E-08	1.00E-14	1.00E-08	log-Uniform
	U	1.00E-12	1.00E-06	1.00E-12	1.00E-06	1.00E-12	1.00E-06	log-Uniform

5.3 Temperature

In Northern Germany, the average temperature of the near surface groundwater is 8 °C /KAP 61/. The geothermal gradient in Northern Germany amounts to 0.03 °C m^{-1} /LEG 04/. Therefore the temperature for a model representing a sedimentary overburden in Northern Germany would vary in the range between 8 °C and 20 °C for a depth between 0 and 400 m below ground surface (bgs). Presuming this temperature field, the solubility of rock salt lies in the range of c (T = 8 °C) = 358.85 g L^{-1} and c (T = 20 °C) = 360.54 g L^{-1} with a difference of 2.22 g L^{-1} or 0.62 % solely[2] (Tab. 5.2). Due to this marginal impact, the dependence of the salt solubility on the temperature is not regarded in groundwater flow simulations.

Tab. 5.2 Equilibrium solubility c of rock salt (NaCl) /DAN 67/ in water depending on the temperature T

Temperature *T*	**0 °C**	**10 °C**	**20 °C**
Concentration c [g L^{-1}]	356.85	358.70	360.54

To this end, the code used for groundwater flow simulations only regards the dependency of the dynamic viscosity μ and the density ρ on the temperature /FEI 99/. Heat transport or the influence of the temperature on the environmental parameters is not regarded in the flow and transport codes used in this project. The influence of the temperature on the groundwater density and therefore on the flow field is marginal compared to the influence of the salt concentration on the density (Tab. 5.3). However, the influence of the temperature on the dynamic viscosity of the groundwater is not insignificant and should be considered in flow simulations.

Tab. 5.3 Viscosity and density of water depending on the temperature T and the salt concentration c, calculated after /FEI 99/

Temperature *T*	**8 °C**	**8 °C**	**20 °C**	**20 °C**
c	minimum	maximum	minimum	maximum
μ (c,T) [kg m^{-1} s^{-1}]	$1.41 \cdot 10^{-3}$	$2.79 \cdot 10^{-3}$	$1.00 \cdot 10^{-3}$	$2.03 \cdot 10^{-3}$
ρ (c,T) [kg m^{-3}]	999.68	1198.98	998.20	1197.20

[2] c (T = 8 °C) interpolated linearly between c (T = 0 °C) and c (T = 10 °C).

This work focusses on the geochemical interactions whose dependency on the temperature in the above mentioned range is negligible (section 3.2). A constant temperature for the entire model domain enables us to identify the effects of geochemical changes isolated from the effects of the temperature-dependent changes in the dynamic viscosity. As a consequence, a constant temperature for the entire model domain was defined, neglecting the effects of the temperature on the viscosity of the groundwater. The temperature increase at the contact to the salt dome is also not considered in our model.

The disposal of radioactive waste in a salt dome will increase the temperature at the top of the salt dome with a maximum after a few thousands of years. Approx. 10,000 a after the closure of the repository the initial temperature conditions will be met due to the decreasing heat production and the subsequent cooling. Considering a time span of one million years, the temperature increase during the thermal phase has no significant influence on the subrosion or the groundwater flow through the sedimentary overburden of the salt dome /BUH 08/. Radionuclide release into the overburden will only occur in case of an altered evolution of the repository system. Current investigations show that such scenarios are typically dominated by diffusive transport in the repository with radionuclide releases several 10,000 a after the closure of the repository /BUH 10/, i. e. at a point in time, when the temperature effect of the repository in the overburden is no more existent.

Thus a constant temperature field of 14 °C for the entire model area is assumed as a mean value between 8 °C at the surface and 20 °C in 400 m depth. For future simulations, the need to apply a realistic temperature field should be checked.

6 Calculation and evaluation of smart K_d-values

6.1 Methodology

The sorption of radionuclides onto the relevant mineral phases is modeled in the geochemical speciation program PHREEQC /PAR 99/ as a function of important environmental parameters. For each sedimentary unit UAF, AT and LAF a specific geochemical model was defined, containing the mineral phases as defined in section 2.2. Various important geochemical influence parameters (section 5.1) are also specific for each unit. Here, it should be noted, that the calculated smart K_d-values for LAF were not implemented in r³t due to the high ionic strength in these sedimentary unit. This will be done in the follow-up project by using the PITZER.

Some restrictions to be obeyed are:

1. A gas phase must be defined in the data base but without specifying a respective partial pressure in the PHREEQC input file. In such a way CO_2 is a know component but will not define the carbonate content (and thus overrule the settings for DIC passed on by UCODE).

2. The pH as defined by UCODE is automatically preserved only through the first reaction step in PHREEQC (initial solution calculation). Further steps (equilibrium with mineral phases and the actual sorption step) require a specific coding to keep the pH at the wanted value.

3. The charge balance is kept by varying the content of calcium, for unknown reasons the more natural choice of sodium (as the highest concentrated ion) caused convergence problems.

4. The mineral phases Calcite and Anorthite that are part of the chemical calculations within r³t are defined as not undergoing dissolution/precipitation reactions. Otherwise their content would be changed and thus differ from the r³t results.

5. The mineral phases Quartz and Goethite are considered as being available indefinitely. They can partly dissolve and precipitate and thus define the Si- and Fe-content within the aqueous solution, which in turn may affect the speciation of the radionuclides.

6. The mineral phases Gibbsite, Muscovite, Kaolinite, and Illite are only required as sorbing phases and thus need not to be defined within the mineral assemblage.

6.1.1 Calculation of K_d-values in PHREEQC

The smart K_d-values are based on mechanistic surface complexation models (SCM), vary in time and space depending on the actual geochemical conditions and can be used as predictive values within the conventional paradigm of distribution coefficients (K_d).

Generally, all calculations of K_d-values are performed as batch reactions in PHREEQC with the project-specific thermodynamic data base ESTRAL.dat see section 3 for details of its setup or the attached CD. The following sequence in the PHREEQC input file, which based on description by /PAR 99/, /APP 05/ and /MER 08/, forms the basis:

1. First, the groundwater solution is defined (by the SOLUTION keyword) describing also all important environmental parameters (E_i) that are variable.

2. Second, the present site-specific mineral phases (section 2.2) are equilibrated with the groundwater solution, this utilizes the EQUILIBRIUM_PHASES keyword.

3. Third, all relevant surfaces parameter (binding sites in sites m^{-2}, specific surface area in $m^2\ g^{-1}$, mass of solid in g kgw^{-1}, SCM type) are defined with the SURFACE keyword. However, the explicit diffuse_layer calculation is excluding for being consistent with the used SCM parameter sets.

The nomenclature of the different surfaces can be chosen freely. Here, the surfaces are named according the mineral abbreviation after /KRE 83/ (e. g. Gt for goethite). In this project, the generalized two-layer model described by /DZO 90/ was used for modeling surface complexation reactions. All necessary SCM parameters (pK_1/pK_2-values, log K-values, reaction equations) are selected as explained in section 3.3 and were implemented as SURFACE_MASTER_SPECIES and SURFACE_SPECIES in the ESTRAL.dat data base (in attachment).

Finally, the distribution coefficients (K_d) for every radionuclide in each sedimentary unit (UAF, AT, LAF) were calculated under specified groundwater chemistry conditions. Based on Component Additivity Methodology /DAV 98/, which relies on the principle that the radionuclide sorption in a particular medium can be determined based on the

additive radionuclide sorption effect from the individual minerals, the K_ds were calculated as presented in following equation and exported in a separate file.

$$K_d\ (L/g\ or\ m^3/kg) = \frac{mol_{sorb} / g_{tot}}{mol_{aq} / L} = \sum_{i=1}^{n} K_{d,i}\phi_{m,i} \qquad (6.1)$$

$mol_{sorb}\ g_{tot}^{-1}$= the adsorbed amount per unit mass of solid [mol g^{-1}]

$mol_{aq}\ L^{-1}$ = the equilibrium concentration of [RN] [mol L^{-1}]

$K_{d,i}$ = distribution coefficient [L g^{-1}] for the individual mineral *i*

Φ_m = mass fraction of mineral *i* with respect to the bulk medium

After these batch reactions, it is important to save the resulting solution composition after equilibration with the SAVE keyword. After it, the saved new solution is used in subsequent surface simulations through the USE keyword.

6.1.2 Variation of environmental parameters in UCODE

The sorption of radionuclides is modeled as a function of the selected geochemical influence parameters $E_1 – E_6$ (section 5). Parameter variation is performed by UCODE (version 1.024 /POE 05/) and assembling of K_d-matrices by a separate program, paste.exe, a freeware port of the respective linux command to windows. The information flow between UCODE and PHREEQC is shown in Fig. 6.1.

For the simultaneous transmission of multiple K_d-values for the same space-time point of r^3t (multi-element-sediment combinations), it is definitely advantageous if K_d-values have identical coordinates (E_i) for all element sediment combinations. Then only one next-neighbor search is necessary. However, the approach to calculate separate K_d-matrices for each element-sediment combination only works with excluded competitive effects between different sorptives and sorbates.

To enable a highly automated calculation, the following approach is proposed:

1. Deployment of the vector E of the parameters and the associated ranges of values (+ if necessary error distribution functions - EDFs). This depends on whether an equidistant grid is necessary or arbitrarily populated grids can be used.

2. Generating a matrix of all the realizations of E and storing in a separate file.

3. Line-by-line reading of this matrix and substitution of the concrete realization of E_i into a template file for the PHREEQC input. For this purpose, UCODE is used.

4. Calculation of each $K_{d,i}$ by PHREEQC, extraction of this value via batch-file and storage together with E_i.

Building the combined PHREEQC/UCODE model (see also Fig. 6.1) is performed stepwise in the following order.

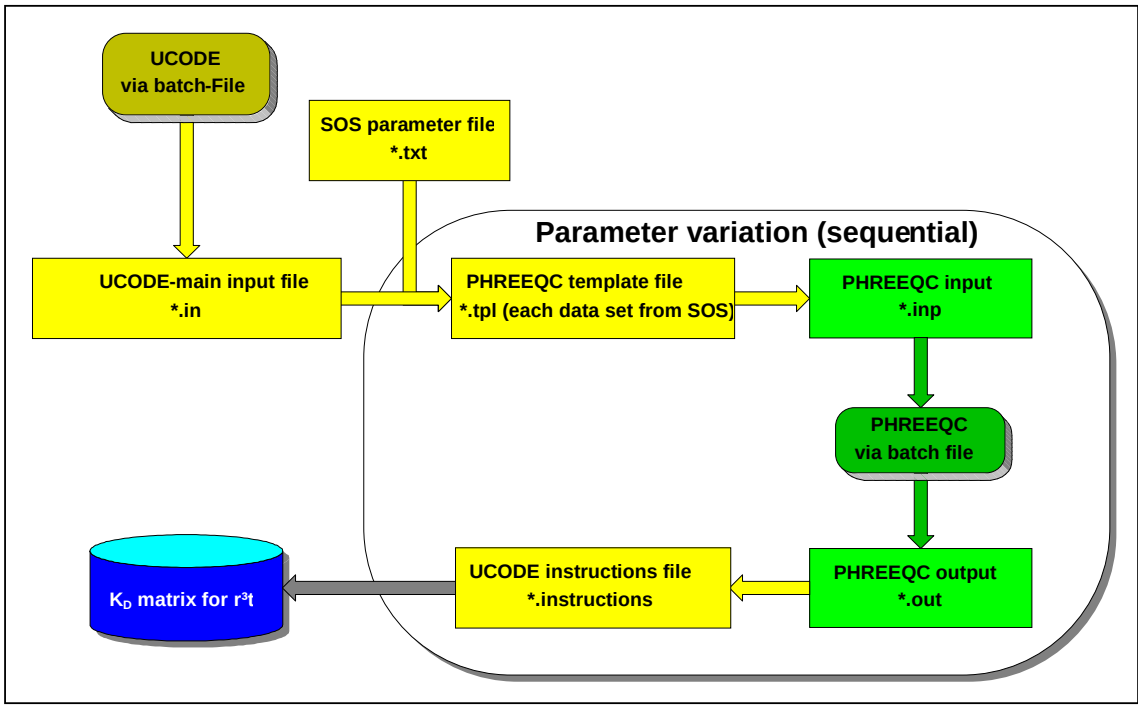

Fig. 6.1 Information flow between UCODE and PHREEQC

1. Creating and implementing the PHREEQC model (as the inner computation routine). The program must be run from a batch file so that it can later be launched from the UCODE main input file. This is attained by using a batch version of PHREEQC instead of the common version with graphical user interface. It is necessary for each radionuclide to combine the K_d-values obtained for several minerals into one specific for the chosen sediment.

2. Creating the files associated with running UCODE:

   a. The *main input file* (filename.in) controls the iteration process: It tells UCODE which models to execute, which parameters to substitute, and how to extract the PHREEQC-simulated values. Here, there is also a chance to modify input parameters by some simple arithmetic and logic. This is, e. g., required to cor-

relate the ionic strength with the content of a variety of ions. Moreover, new parameters can be defined that are computed from the original ones.

b. The *template file* (filename.tpl) is a modified PHREEQC input file, in which UCODE inserts test values of parameters given by the SOS file. It should be noted here that an input parameter provided by UCODE can be substituted simultaneously on several occurrences within the template.

c. The *instruction file* (filename.instructions) tells UCODE which values from the PHREEQC-selected output file will be extracted.

d. So-called “observations” have to be defined in the main input file, here only as place-holders (dummies) to allow a proper output processing by UCODE.

e. The *SOSFile* (filename.txt) provides all parameters for the variable geochemical environment to UCODE to determine the corresponding K_d-values. It is created separately with the help of an EXCEL macro.

f. It must be taken care of that failed computations of K_d-values within the inner (PHREEQC) routine must be signaled to UCODE without causing a premature stop of the overall computation cycle. Such failures may happen for extreme combinations of varied input parameters. In such case K_d shall be assigned a value of -1 (negative values cannot be computed by “normal” geochemical speciation calculation). This is achieved by replacing in a PHREEQC selected output file from a normal run the K_d-values with -1. Thus modified file is saved as *dummy.txt*. Before every execution of PHREEQC this *dummy.txt* is copied and renamed to the actual chosen filename for the selected output (*filename.txt*). PHREEQC produces only a selected output file, and thus overrides the dummy, if the simulation was terminated normally. If PHREEQC was terminated normally UCODE reads the computed K_d-value otherwise it reads a -1.

3. Intermediate test step: Execution of UCODE in forward mode (usually also as batch file) to verify the accuracy of the PHREEQC input file and its derived PHREEQC outputs.

4. The parameter variation (provided by the SOSFile) will then be extended to all parameters.

5. Finally, each extracted K_d-value has to be combined with its originating parameter combination to be stored in a special matrix (for details see below).

The computation of the K_d-values was planned for a total of six variable input parameters, namely the pH-value, the total concentration of dissolved inorganic carbon (DIC), the ionic strength IS, the total concentration of dissolved aluminum [Al], the total concentration of dissolved calcium [Ca], and the total concentration of (one) dissolved radionuclide [RN]. Currently, [Al] is not treated as varying environmental parameter due to difficulties in the conceptual model. However, Al is still considered as geochemical element (equilibrium phase). To minimize efforts for both computing K_d-values and retrieving them within the modified r³t code (requiring just one next-neighbor search), K_d-values for all eight radionuclides (Cs, Ra, Ni, Am, Th, Np, U, Se) will be stored inside the same vector of a unique input parameter combination. This means identical coordinates (E_i) for all element-mineral combinations, which implies that the concentration range of each radionuclide has to extend over the same order of magnitude. Then, scaling factors can be introduced to map the concentration range for all radionuclides onto the same basic range. In addition, the approach to calculate simultaneously K_d-matrices for each element-mineral combination only works with excluded competitive effects between different sorptives and sorbates. This assumption must be verified by investigating the sensitivity analyses with respect to all radionuclide concentrations.

Moreover, as the concentration ranges span several orders of magnitude the respective parameter variation should be done rather on a logarithmic scale than on a linear one. Generally, a logarithmic EDF may of course also be true for other input parameters.

The distribution of the various input parameters, as determined in section 5, will be used to generate the *SOSFile*.

6.1.3 Possible types of K_d-clouds

As a first approximation an equidistant grid (implying a uniform parameter distribution) is generated, just taking the expected minimum and maximum values for each input parameter and dividing this range by the number of steps. This has the advantage of requiring only very simple (and consequently very fast) interpolation algorithms inside the modified r³t code. As starting point for the number of steps, the pH as most sensi-

tive input parameter has 15 steps, the radionuclide concentration [RN], the DIC, the ionic strength and the calcium concentration have 8 steps each. As a next step, the results from the sensitivity analyses shall serve as guidance for how many steps per input parameter are optimal. However, the total number of steps directly scales the size of the resulting K_d-cloud, where restrictions have to be taken into account, see end of next section.

Later, more realistic EDFs will be used eventually resulting in K_d-cloud with a higher density in the center and fewer points at the edges. This can again be realized in (at least) two different ways.

As an intermediate step to at least roughly mapping the real EDFs of the input parameters onto an equidistant grid one could enlarge the grid and populate all knots in the region of high probability, but populate only every 2^{nd}, 3^{rd}, or 4^{th} knot in the tailing regions. Then (i. e. before storing the K_d-cloud and delivering it to r³t) advanced interpolation algorithms can be used to assign also K_d-values to all unpopulated knots. This will save computational efforts within the modified r³t as this interpolation has only to be done once.

The most advanced version, unfortunately also requiring the largest computational efforts within the modified r³t code (and thus slowing down computation) will be the usage of real EDFs, necessarily leading to a K_d-cloud with an arbitrary distance between each point in all dimensions of the grid.

6.1.4 Storage structure of the K_d-cloud

The K_d-cloud has to obey a well-defined formal structure, which is outlined below. It consists of two parts. First, a header provides all information to define type and dimension of the K_d-cloud. Second, the actual K_d-cloud follows optionally including the corresponding input parameter values. The overall cloud file then obtains an MD5 checksum to allow for identifications of later data manipulations which will be stored in a separate file. A simple UNIX program capable of doing of is `md5sum`. Each cloud file obtains a unique file name composed of the following elements (which are all connected by underscore characters). The file name ends with ".dat" in case of the cloud and with ".md5" in case of the associated MD5 checksum file.

1. Project title (up to 8 characters)
2. Site/experiment name (up to 8 characters)
3. Sediment name (up to 4 characters)
4. Running number or final version (up to 5 characters)

Example for this naming convention: `ESTRAL_GORLEBEN_UAF_final.dat`

Part A: Header

1. 0th line: a magic word to distinguish the equidistant case from the real distribution: EQUI or DIST
2. 1st line: description of the problem /task (up to 255 characters)
3. 2nd line: date and time of creation (Format: yyyy-mm-dd; hh:mm)
4. 3rd line: name and institution (in parentheses) of creator, different names are separated by semicolon (up to 255 characters)
5. 4th line: number of distinct input parameters (including the generic radionuclide concentration) and number of radionuclides (Format: two integers separated by space)
6. 5th line: Abbreviations of all input parameters (Format: strings with a maximum length of six characters each, separated by space), to be selected from a predefined pool at the moment consisting of pH, DIC, IS, [Ca], [RN]. This defines the order of input parameter variations used for the K_d-cloud matrix.
7. 6th line: Specification which dimensions are actually logarithmic ones (will stay as empty line if there are no logarithmic scales used)
8. 7th line: In case of an equidistant K_d-cloud, this specifies start value, step size and numbers of steps for each input parameter, all separated by space. The start values for DIC, [Ca], and [RN] are given in mol m^{-3}, for IS in mol L^{-1}. In case of a matrix population based on a real EDF, only the number of steps is given. The actual values for each input parameter are then part of the tupels within the K_d-cloud.

9. 8th line: Chemical symbols for each radionuclide considered (Format: strings with a length of one or two characters as defined by the IUPAC, separated by space). This defines the order of specific K_d-values within each line of the K_d-cloud matrix.

10. 9th line: Factors to be multiplied with the generic radionuclide concentration [RN] to obtain the real concentration for each radionuclide.

An example for such a header is presented below:

```
EQUI
Final Kd_cloud for UAF (upper aquifer; Cs, Ra, Ni, Am, …)
2012-03-26; 17:00
Madlen Stockmann; Johannes Schikora (HZDR)
5 8
pH DIC IS [Ca] [RN]
2 3 4 5
6.4 0.17 15 -3.5 0.21 8 -3.02 0.19 8 -3.62 0.19 8 -12 0.86 8
Cs Ra Ni Am Th Np U Se
1 10 1 100 100 10 1 1
```

Part B: Actual multi-dimensional matrix for the K_d-cloud (in a linearized form).

The specific format of this part has to be defined in a way that primarily allows for a fast access by the r³t code.

For the equidistant case it will contain vectors of the K_d-values for each radionuclide, i. e. comprising of as many numbers as specified by the second parameter of the 4th header line – and in exactly the order as induced by the 7th line of the header. No further information is required since the coordinates of the associated input parameters for each vector can be derived directly from the position of the vector in the cloud. This requires that the order of vectors follows the sequence of the indices of a multidimensional matrix. There, the left-most parameter listed in the 5th header line will be varied most frequently whereas the right-most parameter will be the one varied at last.

In case of real EDFs for the K_d-cloud input parameters, the coordinates of each dimension must be stored together with the K_d-vector. Thus each vector consists of as many parameters as given by the sum of the first and second parameter of the 4th header line, again following the order specified in the 5th and 7th line of the header, respectively.

There are some boundary conditions to be kept in mind, however, to avoid too long computing times (as the K_d-cloud has to be surveyed rather often within one r³t run).

Ideally the whole cloud should be small enough to fit into the memory of a CPU (in case of parallel computing this holds for each core), which currently sets an upper limit of ca. 2 GByte. Example: If six dimensions (E_1 – E_6) were practiced, with 20 points per dimension. This gives $20^6 = 6.4\times10^7$ points. As K_d-values for all 8 radionuclides of interest will be stored together for each point, it results in 5.12×10^8 floating point (such a precision should suffice, requires 4 Bytes per value) numbers. This in turn equals 2.048 GByte – thus there is not any safety margin here.

6.2 Uncertainty analyses and sensitivity analyses

The sensitivity and uncertainty analyses of the so-called smart K_d-values are done by coupling a third computer code as outer shell to the two above mentioned codes PHREEQC and UCODE. This third code is SimLab, a software package for uncertainty and (global) sensitivity analysis, which is developed at the JRC Ispra. The most recent version of SimLab may be obtained from http://simlab.jrc.ec.europa.eu/.

The information flow between SimLab and the existing combined model UCODE/PHREEQC is visualized in Fig. 6.2. The inner routines are identical to those presented in Fig. 6.1. They are coupled via batch-files. A detailed description of the coupling of these codes can be found in /SCH 11/.

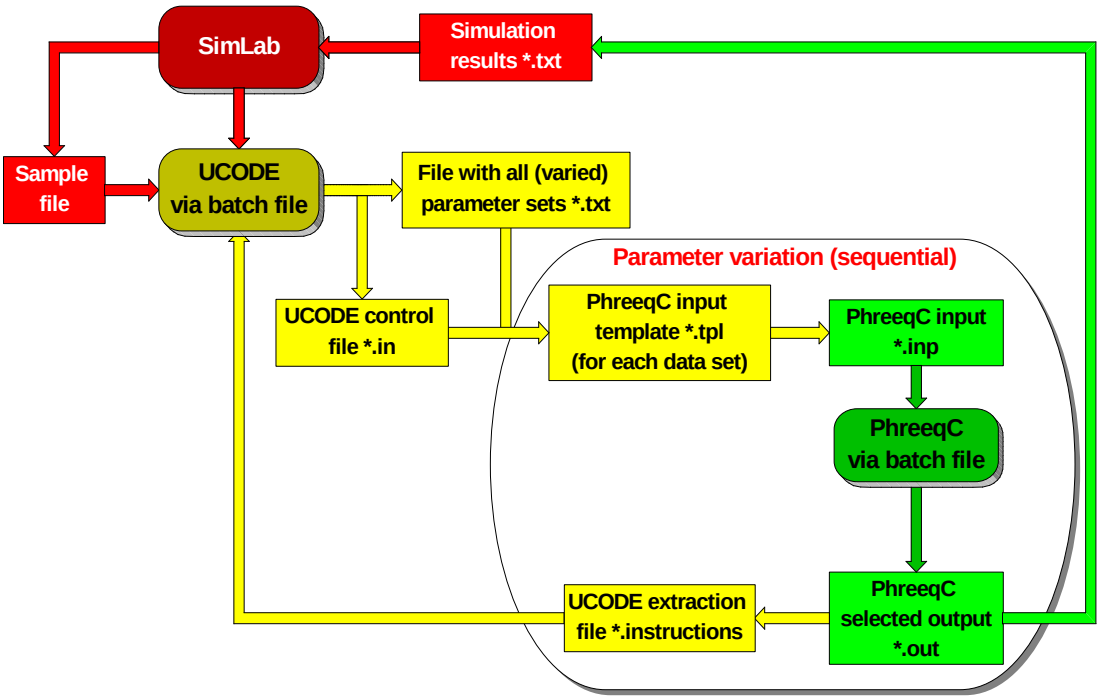

Fig. 6.2 Information flow between SimLab, UCODE and PHREEQC

According to /SCH 05/ variance-based methods are a subset of sampling-based methods. Generally, Monte-Carlo methods (sampling-based methods) are performed in the following way /HEL 00/, /SCH 05/:

1. Determination of the probability distributions for the input variables,
2. Creation of multiple samples for the input variables from these distributions,
3. Evaluation of the model for the samples,
4. Analysis of the resulting model output distribution function (uncertainty analysis), and
5. Sensitivity analysis.

6.2.1 Sensitivity analysis and results

SimLab provides in contrast to UCODE also methods for global variance-based sensitivity analysis (SA). So it is possible to investigate the behavior of the considered system over the full range of its input parameters. In the framework of a local SA one only investigates the system response to small perturbations of the current input parameter values. This type of analysis is useful for systems that already operate in a defined

point, for example in an optimum. In this case a local sensitivity analysis shows how the system responses to (small) disturbances. Sensitivity indices which are calculated with local SA methods are only valid for the point in the parameter space defined by the used input parameters. This is especially important for nonlinear problems like that considered here. Furthermore local SA methods aren't capable to quantify interactions between parameters.

Global SA methods don't have these disadvantages. Their indices are valid for the whole parameter space and they are able to quantify interactions between the input parameters. Variance-based global SA methods also have the advantages that they are model independent and that their indices are easy to understand. Because of these reasons it is decided to switch from local methods (UCODE) to global methods (SimLab).

In detail, the use of the extend Fourier Amplitude Sensitivity Test (eFAST) as SA method is favored. Details about this method are given below. The classical FAST method was already developed in the 70's by /CUK 73/, /CUK 75/, /CUK 78/ and /SCH 73/. In 1998 /SAL 98/ improved the classical FAST method and in 1999 /SAL 99/ extended the version towards a calculation formula for the total sensitivity index (eFAST).

The basic idea of FAST is the transformation of the multi-dimensional parameter space spanned by $y = f(x_1, x_2, ..., x_n)$ into a one-dimensional parameter space. That way the multi-dimensional integral, which would be necessary to calculate the variance of the output V(y), can be calculated by a one-dimensional integral. The transformation of the original function is done by a 'search curve' which explores the parameter space. This curve depends only on the variable s and is described by a set of equations G_i. Using these equations, the original parameters x_i are replaced. /SAL 99/ propose the following transformation function $G_i(\sin[\omega_i \cdot s])$

$$x_i = \frac{1}{2} \cdot \frac{1}{\pi} \arcsin(\sin(\omega_i \cdot s)) \qquad (6.2)$$

with ω_i as different, properly chosen, integer angular frequencies assigned to the individual parameters x_i.

After this transformation y depends only on s and all the parameters x_i will change along the specified search curve when s is varied. The multidimensional integral for the variance simplifies to one-dimensional integral, which is easier to compute.

The extended Fourier Amplitude Sensitivity Test provides two indices for the evaluation of the importance of an input parameter – S_1 the first-order sensitivity index and S_T the total sensitivity index.

The first-order sensitivity index is calculated as follows

$$S_{1,i} = \frac{D_i}{D} = \frac{V[E(y \mid x_i)]}{V(y)} \tag{6.3}$$

$V[E(y|x_i)]$ is the amount by which the total variance of the model output would be reduced if it would be possible to determine the true value of x_i within its range of variation. $S_{1,i}$ is therefore a measure (in percent) of the relative importance of the parameter x_i. A sensitivity index of $S_{1,1} = 0.5$ means that 50 % of the output variance is caused by parameter x_1. So if one knows the true value of x_1, one could reduce the total variance of the model output by 50 %. In principle it is very unlikely that the true value of a parameter can be determined. Nevertheless the first-order sensitivity index helps to make a reasonable decision about the parameter on which further research should be concentrated and thus to reduce the uncertainty associated with this parameter. The parameter with the largest S_1 offers the greatest potential to reduce the output variance.

The total sensitivity index is defined as follows

$$S_{T,i} = 1 - \frac{D_{(-i)}}{D} = \frac{E[V(y \mid x_{-i})]}{V(y)} \tag{6.4}$$

$E[V(y|x_{-i})]$ is the amount of the total variance that would remain if all parameters except x_i had been fixed to their true value and x_i is the only parameter which can vary according to its distribution. The total sensitivity indices can be used for model simplification. A parameter with $S_T = 0$ would not affect the model output alone (main effect) or via interactions and thus can be fixed to any value within its parameter range.

The K_d-values and their UA/SA are calculated as a function of important environmental parameters (section 5). As a result of the sensitivity analysis, the importance of the environmental parameters can be identified. In the following, the results exemplary for the sorption of U(VI) in the upper aquifer (UAF) at the Gorleben site are presented. Fig. 6.3 shows the 3-D plot for the K_d-matrix for U(VI) as a function of pH, [Ca], and [DIC] (logarithmic scale).

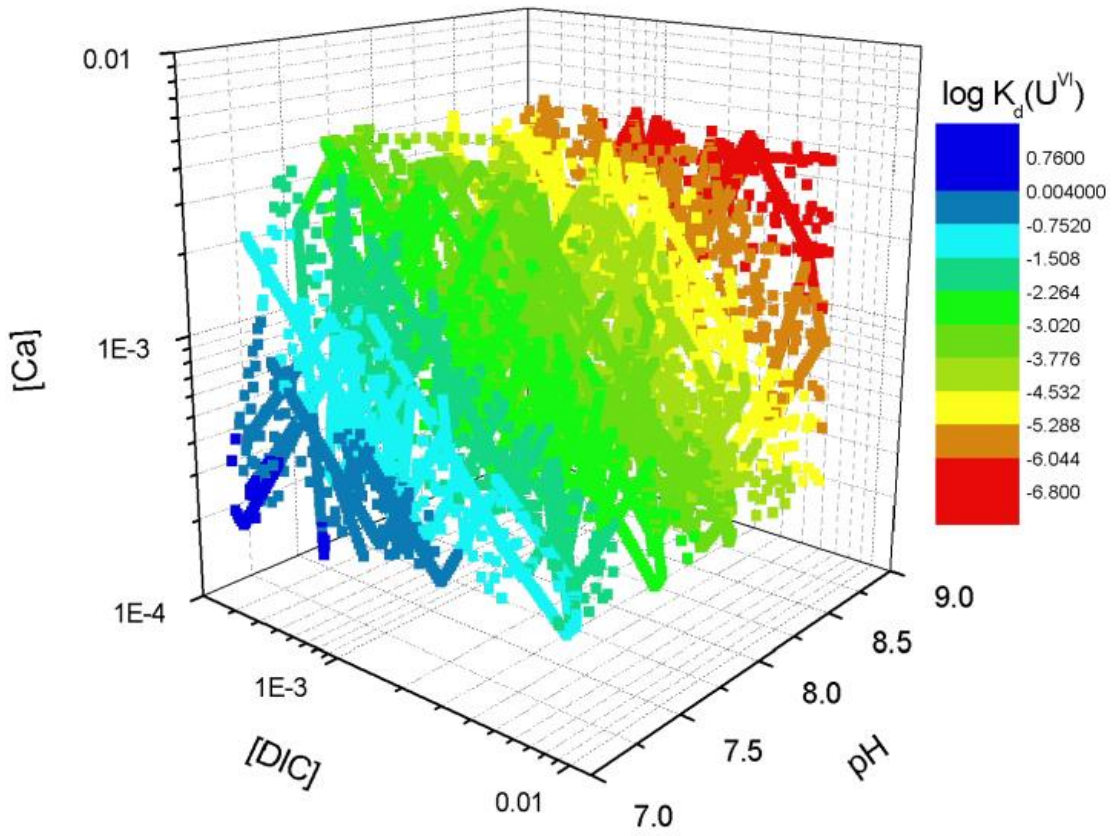

Fig. 6.3 Multidimensional K_d-matrix for U(VI) as a function of pH, [Ca], and [DIC] (K_d in $m^3\ kg^{-1}$, logarithmic scale)

The ranking list of sensitivity indices for U(VI) in UAF is presented in Tab. 6.1. and for all other radionuclides in Tab. 6.2 to Tab. 6.4. Indices ranked highest are the most sensitive parameters. It is obvious that pH mainly influences the sorption of radionuclides, followed by [Ca], and [DIC].

Tab. 6.1 Sensitivity indices for log K_d-values for U(VI) in UAF calculated with eFAST (25 000 parameter samples)

E_i	$S_{1,i}$	$S_{T,i}$	$S_{T,i} - S_{1,i}$	Rank
pH	0.779	0.788	0.009	1
[Ca]	0.146	0.152	0.006	2
[DIC]	0.067	0.075	0.008	3
[U]	0.0004	0.003	0.003	4
IS	0.0002	0.003	0.003	5

The difference between the total sensitivity index and the first-order sensitivity index is an indicator for the level of interaction of the respective parameter. A difference of zero would mean that a parameter doesn't contribute to the output variance via interactions, but solely via the main effect (first-order sensitivity index). So for the sorption of U(VI) in the UAF the most important parameters show little interaction. They contribute mostly direct to the model output variance. The fact that the other radionuclides have very little first-order sensitivity indices supports our assumption that the radionuclides do not influence each other and can thus be calculated simultaneously.

Tab. 6.2 Sensitivity indices first order for log K_d-values for radionuclides in UAF calculated with eFAST (25 000 parameter samples)

E_i	Cs	Ra	Ni	Am	Th	Np	U	Se
pH	0.993	0.746	0.987	0.787	0.049	0.884	0.779	0.962
DIC	0.000	0.000	0.009	0.155	0.942	0.064	0.067	0.000
IS	0.000	0.005	0.001	0.001	0.000	0.000	0.000	0.012
[Ca]	0.000	0.219	0.005	0.014	0.001	0.001	0.146	0.002
[Cs]	0.000	0.000	0.000	0.000	0.000	0.000	0.000	0.000
[Ra]	0.000	0.000	0.000	0.000	0.000	0.000	0.000	0.000
[Ni]	0.000	0.000	0.000	0.000	0.000	0.000	0.000	0.000
[Am]	0.000	0.000	0.000	0.000	0.000	0.000	0.000	0.000
[Th]	0.000	0.000	0.000	0.000	0.000	0.000	0.000	0.000
[Np]	0.000	0.000	0.000	0.000	0.000	0.000	0.000	0.000
[U]	0.000	0.000	0.000	0.000	0.000	0.000	0.000	0.000
[Se]	0.000	0.000	0.000	0.000	0.000	0.000	0.000	0.008

Tab. 6.3 Sensitivity indices first order for log K_d-values for radionuclides in AT calculated with eFAST (25 000 parameter samples)

E_i	Cs	Ra	Ni	Am	Th	Np	U	Se
pH	0.996	0.989	0.974	0.214	0.034	0.374	0.895	0.994
DIC	0.000	0.000	0.011	0.721	0.957	0.476	0.091	0.000
IS	0.001	0.006	0.004	0.007	0.000	0.001	0.002	0.001
[Ca]	0.000	0.000	0.000	0.000	0.000	0.000	0.000	0.000
[Cs]	0.000	0.000	0.000	0.000	0.000	0.000	0.000	0.000
[Ra]	0.000	0.000	0.000	0.000	0.000	0.000	0.000	0.000
[Ni]	0.000	0.000	0.000	0.000	0.000	0.000	0.000	0.000
[Am]	0.000	0.000	0.000	0.000	0.000	0.000	0.000	0.000
[Th]	0.000	0.000	0.000	0.000	0.000	0.000	0.000	0.000
[Np]	0.000	0.000	0.000	0.000	0.000	0.000	0.000	0.000
[U]	0.000	0.000	0.000	0.000	0.000	0.000	0.000	0.000
[Se]	0.000	0.000	0.000	0.000	0.000	0.000	0.000	0.000

Tab. 6.4 Sensitivity indices first order for log K_d-values for radionuclides in LAF calculated with eFAST (25 000 parameter samples)

E_i	Cs	Ra	Ni	Am	Th	Np	U	Se
pH	0.992	0.413	0.965	0.820	0.061	0.854	0.446	0.790
DIC	0.000	0.000	0.000	0.110	0.868	0.096	0.029	0.000
IS	0.002	0.047	0.011	0.012	0.003	0.001	0.001	0.107
[Ca]	0.001	0.457	0.015	0.012	0.046	0.002	0.498	0.044
[Cs]	0.000	0.000	0.000	0.000	0.000	0.000	0.000	0.000
[Ra]	0.000	0.000	0.000	0.000	0.000	0.000	0.000	0.000
[Ni]	0.000	0.000	0.000	0.000	0.000	0.000	0.000	0.000
[Am]	0.000	0.000	0.000	0.000	0.000	0.000	0.000	0.000
[Th]	0.000	0.000	0.000	0.000	0.000	0.000	0.000	0.000
[Np]	0.000	0.000	0.000	0.000	0.000	0.000	0.000	0.000
[U]	0.000	0.000	0.000	0.000	0.000	0.000	0.000	0.000
[Se]	0.000	0.000	0.000	0.000	0.000	0.000	0.000	0.003

6.2.2 Uncertainty analysis and results

Another benefit from the use of SimLab as an extra shell is that it is also possible to perform uncertainty analysis (UA) within SimLab. So both analyses, SA and UA, can be done inside one program and it is not necessary to switch the interface. SimLab provides for the purpose of UA histograms, cumulative distribution functions and inverse cumulative distribution functions. It also calculates statistical descriptors like mean, variance, standard deviation or skewness of the distribution of the simulation results.

All mean smart K_d-values for UAF, AT and LAF and their minimum, maximum and standard deviation (2σ) are summarized in Tab. 6.5.

Tab. 6.5 Mean smart K_d-values for UAF, AT and LAF and their minimum, maximum and standard deviation 2σ (K_d in $m^3\ kg^{-1}$, logarithmic)

	Mean	Min	Max	SD (2σ)
UAF				
log K_d (Cs)	0.76	-0.46	2.32	0.74
log K_d (Ra)	-0.13	-1.49	1.38	0.60
log K_d (Ni)	-2.01	-3.99	0.08	1.06
log K_d (Am)	0.63	-1.29	3.45	0.98
log K_d (Th)	0.24	-0.76	1.32	0.51
log K_d (Np)	-3.54	-4.48	-2.36	0.49
log K_d (U)	-2.98	-7.02	0.90	1.88
log K_d (Se)	-2.58	-5.07	-0.06	1.16
AT				
log K_d (Cs)	2.00	0.67	3.46	0.76
log K_d (Ra)	3.64	1.45	5.65	1.10
log K_d (Ni)	0.40	-1.75	1.92	0.99
log K_d (Am)	3.90	1.94	5.92	0.93
log K_d (Th)	0.71	-0.80	2.40	0.84
log K_d (Np)	0.02	-0.87	1.13	0.47
log K_d (U)	-1.29	-5.95	2.48	2.17
log K_d (Se)	-4.41	-7.52	-1.44	1.63
LAF				
log K_d (Cs)	0.74	-0.51	2.40	0.74
log K_d (Ra)	-0.67	-2.33	2.36	0.90
log K_d (Ni)	-2.27	-4.45	0.16	1.10
log K_d (Am)	0.11	-2.02	2.85	0.99
log K_d (Th)	0.02	-0.96	1.40	0.47
log K_d (Np)	-3.58	-4.46	-2.25	0.43
log K_d (U)	-4.06	-7.92	0.82	2.09
log K_d (Se)	-3.10	-4.99	-0.25	0.93

A suitable tool for the description of the resulting total variance is the frequency distribution function. This allows to determine the probability of the parameters to fall in a certain interval.

In Fig. 6.4. the frequency distribution of the pre-calculated log K_d-values exemplary for the sorption of U(VI) in UAF based on eFAST over all environmental parameters (section 5) is shown. The remaining frequency distributions for all investigated radionuclides in UAF, AT and LAF are given in appendix A.5.

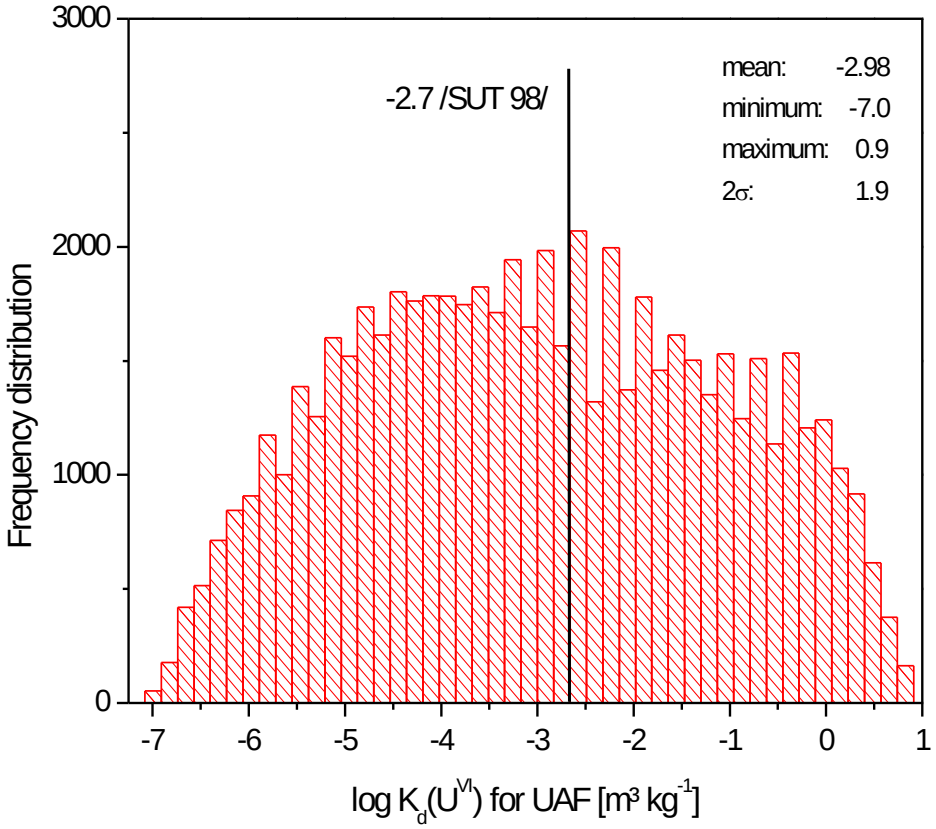

Fig. 6.4 Frequency distribution of 25 000 pre-calculated logK_d-values for U(VI) in UAF (logK_d in $m^3\ kg^{-1}$)

As shown in Fig. 6.4, the log K_d-values for the sorption of U(VI) onto mineral surfaces in UAF range from -7.0 to 0.9 with a mean smart K_d-value of -2.98. Comparing to the temporally constant conservative K_d-value of -2.7 from /SUT 98/, which was previously used in r³t for the retention of radionuclides in UAF at Gorleben site, the resulting mean K_ds show good agreement, but accounts now for geochemical variations. Thereby, freshwater conditions are assumed for UAF and saltwater conditions for AT and LAF.

Comparing to assimilable literature K_d-values (Fig. 6.5), such as from /ZAV 04/, /BRA 03/, /BRA 08/, /ARC 08/ and /JOS 11/, mainly good correlations between modelled smart K_d-values and published K_d-values are obtained. Apparently the sorption of Cs, Ra and Am in AT is overestimated, which has to be clarified in further modelling.

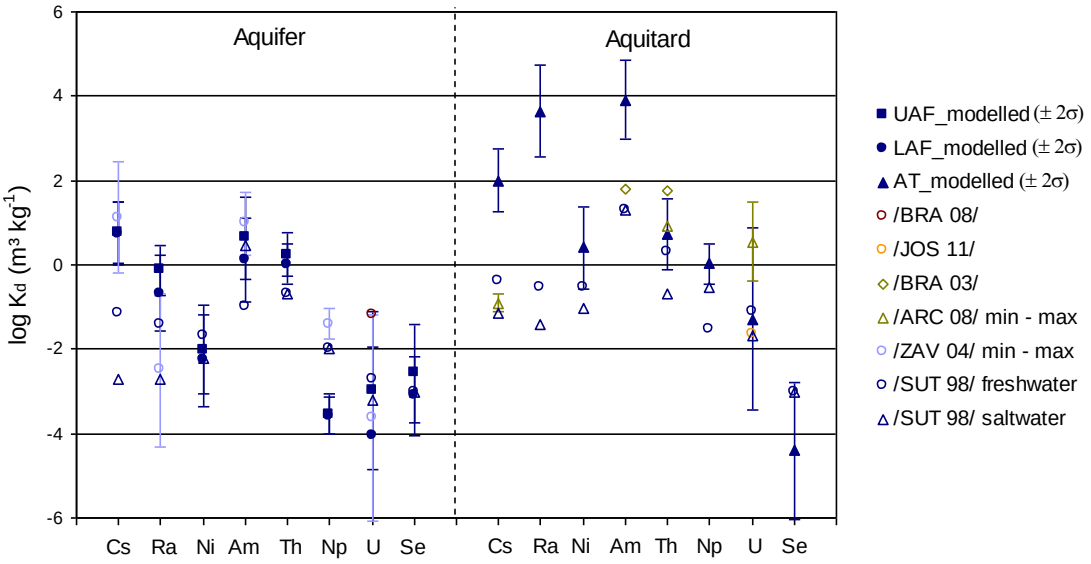

Fig. 6.5 Modelled mean smart K_d-values compared to literature values

6.3 Evaluation of K_d-values for defined batch systems

In order to check the bottom-up approach, i. e. the calculation of K_d-values as a function of the environmental parameters for sediments containing several minerals by considering the sorption on each mineral phase, two approaches were applied. On the one hand it was decided to perform additional batch sorption experiments for a specific mineral mixture (“synthetic sediment”), particularly to check the new surface complexation parameters for orthoclase and muscovite derived by sorption experiments with Eu (section 4). On the other hand batch experiments from literature were applied to check, whether the sorption models and parameters as well as the modeling approach used are adequately describing the sorption behavior of uranium on synthetic and natural sands. And therewith back-up the data sets used to describe the sorption of U(VI) on quartz, muscovite and iron oxides.

6.3.1 Sorption of Eu on a synthetic sediment

The application of a surface complexation model to a synthetic sediment further backs up the assessed parameters and approves the chosen bottom-up approach of this study. Hence, representing naturally occurring sediments by means of their constituents is proven to offer robust and trustworthy data sets.

The composition of the synthetic sediment was defined as 10 wt% orthoclase, 10 wt% muscovite and 80 wt% quartz, related to the sedimentary composition of the upper aquifer. It was decided to perform these experiments with Eu for three pH-values ranging between 3 and 8), two different V/M ratios (1/80 and 1/320) and for three different element concentrations (10^{-5}, $5 \cdot 10^{-6}$ and 10^{-6} mol L^{-1}). It is the aim to check whether the applied surface complexation models with the respective parameters for all minerals are able to describe the K_d-values for the sorption of Eu^{3+} under different environmental conditions for this synthetic sediment. The results from the batch experiment are shown in Fig. 6.6.

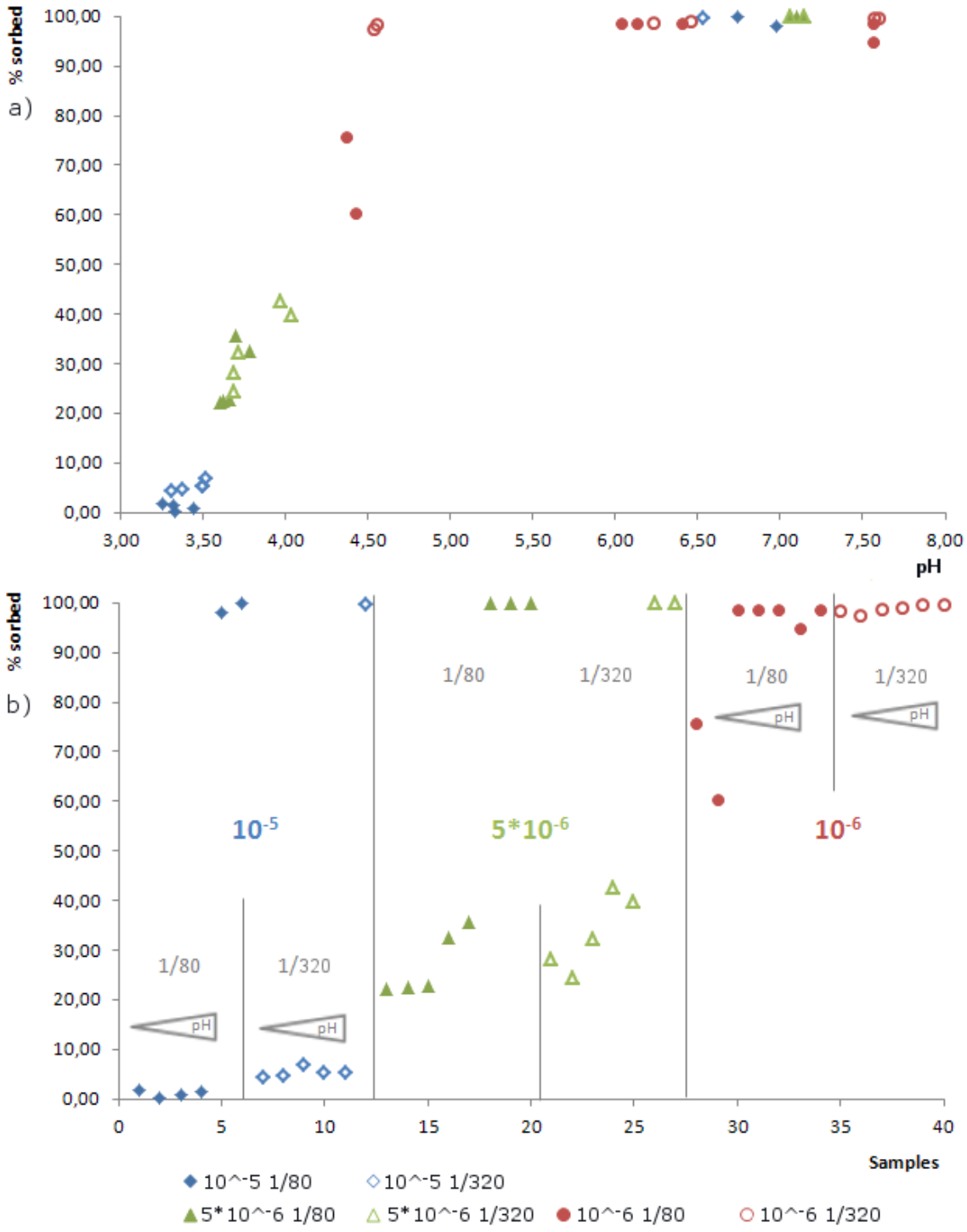

Fig. 6.6 Results of the batch experiment with Eu^{3+} applying the synthetic sediment

In figure a) % Eu^{3+} sorbed is plotted against the pH. Figure b) illustrates the sorbate concentrations in % of each sample for different V/M ratios and initial Eu^{3+} concentrations.

Through the application of our surface complexation model for Eu^{3+} of the according sediment constituents muscovite and orthoclase, and by employing a literature data set for quartz the simulation is conducted. Therefore, the surface complexation parameters

for quartz (introduced by /KIT 99/) that comprise the specific surface area (SSA), the surface site density (SSD), as well as the Eu^{3+} stability constant are applied. The here conducted experimental set up and developed final surface complexation model show similarities compared to the procedure chosen in /KIT 99/, which backs up the implementation of the according model with its parameters. However, a drawback embodies the assumption that /KIT 99/ applies a quartz mineral holding a comparable, good purity since unfortunately, no explicit information concerning the employed Mt. Myoken quartz can be obtained from /KIT 99/ or other literature.

Fig. 6.7 illustrates the results of the applied SCM where colored characters symbolize measured and black ones simulated data sets. The application yields a satisfying simulation of the measured data regarding all sorption trends without limitations for all ranges of element concentrations.

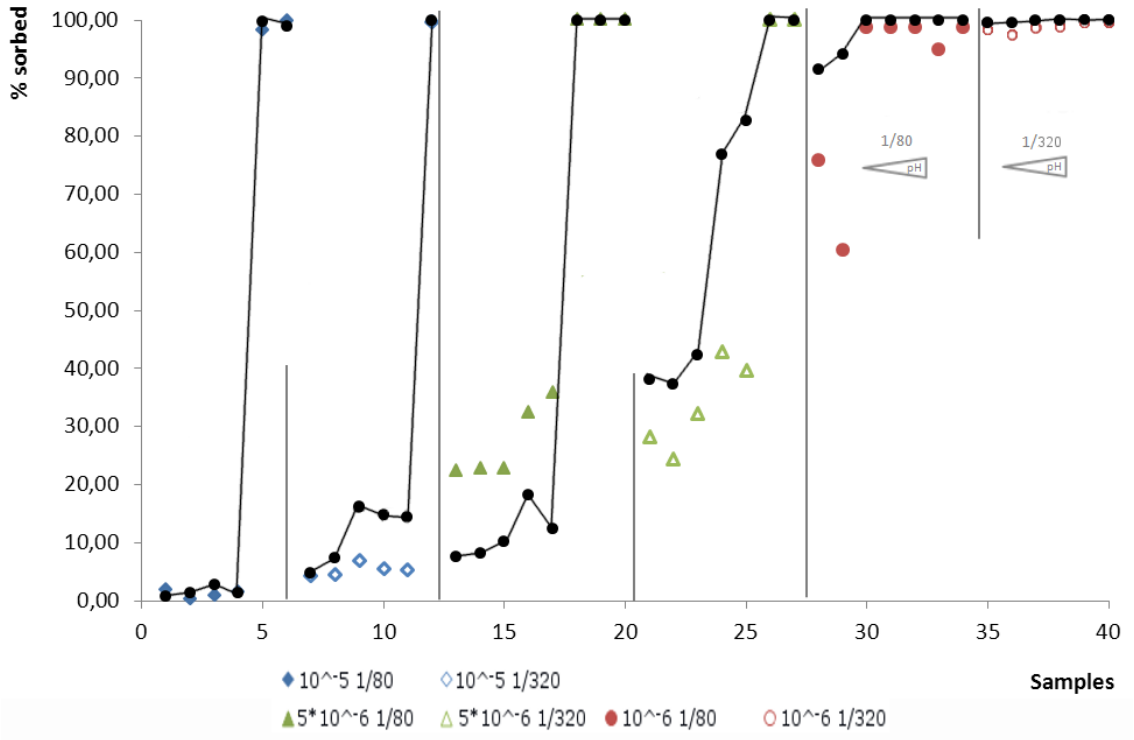

Fig. 6.7 Presentation of fitted results regarding the synthetic sediment which are obtained by applying the final SCM

Colored characters symbolize the measured experimental data. Black symbols and graphs stand for the fitted data and relate to the according V/M, pH, and Eu^{3+} concentration.

The good description of the experimental data of the synthetic sediment reinforces the conclusions concerning the robustness of the assessed parameters regarding both minerals. Furthermore, the successful application of the surface complexation model

also affirms that the simulation of sediments by means of their mineral constituents is feasible, thus backing up the chosen bottom-up approach of this study. A detailed description of this work can be found in /BRI 11/.

Sorption results obtained from the batch experiment employing the synthetic sediment illustrate that other than assumed, here, quartz holds the major influence concerning sorption processes under the examined conditions. Only relatively high element applications of 10^{-5} mol L^{-1} and 10^{-6} mol L^{-1} Eu^{3+} result in significant fraction bound by surface complexation regarding muscovite and orthoclase. Hence, at the Gorleben site the percolation and possible breakthrough of potential contaminants comparable to Eu^{3+} (such as Am^{3+}) at trace element concentrations are here mostly governed by the presence of quartz and maybe by other sediment fractions where studies are still pending.

6.3.2 Sorption of U on synthetic and natural sands

Further, experimental results from another experimental and modeling study published in /BRA 08/ have been selected to qualify our models as well as the bottom-up approach. Experimental data from batch experiments with uranium on natural and synthetic sands performed by HZDR have been used.

For simulation all protolysis constants and log K-values for the sorption reactions of uranium on quartz, muscovite and goethite from the RES³T data base as described in section 3.3.3 have been applied. For the specific surface area, the values given in /BRA 08/ were used. The synthetic sand consists of 95 % quartz and 5 % muscovite with specific surface areas of 0.047 m^2 g^{-1}, and 0.88 m^2 g^{-1}, respectively. The results of the simulation are shown as green curve in Fig. 6.8. The simulation significantly underestimates the experimental curve.

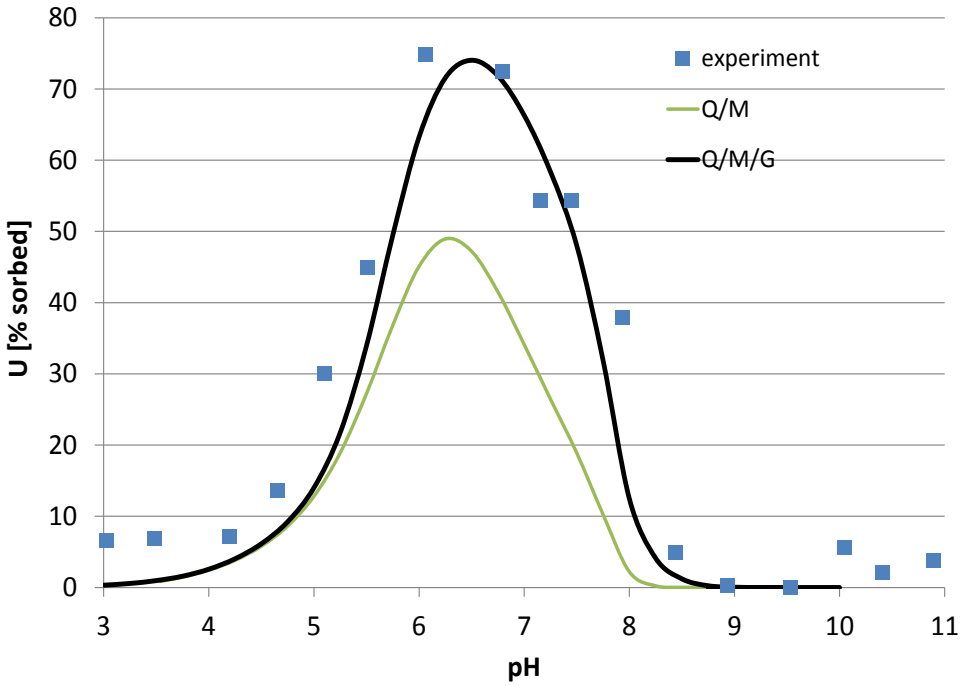

Fig. 6.8 U(VI) sorption on synthetic sand. Experimental data (/BRA 08/) compared to simulation results for a mixture of quartz and muscovite (Q/M) and quartz, muscovite and goethite (Q/M/G) (see text for details)

The reason for that is probably an additional iron content of about 5 % in the mineral muscovite, which was shown by digestion and ICP-MS analysis in /BRA 08/. As in this study it is also assumed here that muscovite contains an iron oxide with an average specific surface of 10 $m^2\ g^{-1}$. For this oxide the data listed in the ESTRAL.dat data base for goethite are applied. With the assumption that muscovite contains 6 % of this iron oxide a quite good agreement between experimental and simulated curve is reached. These results give further confidence in the models and the approach used. Further calculations with natural sand including the dependence on the initial uranium concentration will be performed and documented in the final report.

The relevance of the different surface species is shown in Fig. 6.9. For pH-values < 6 the most important complex is $QzOUO_2^+$. For pH-values > 6 the species $QzOUO_2OH$ and $GtOH_2(UO_2)_2CO_3(OH)_3$ are the most dominating ones, i. e. due to the high amount of quartz in the mixture it is important over the whole pH-range, whereas sorption of U on muscovite only plays a minor role. Although only available in accessory amounts the iron oxides are quite important for the description of the system.

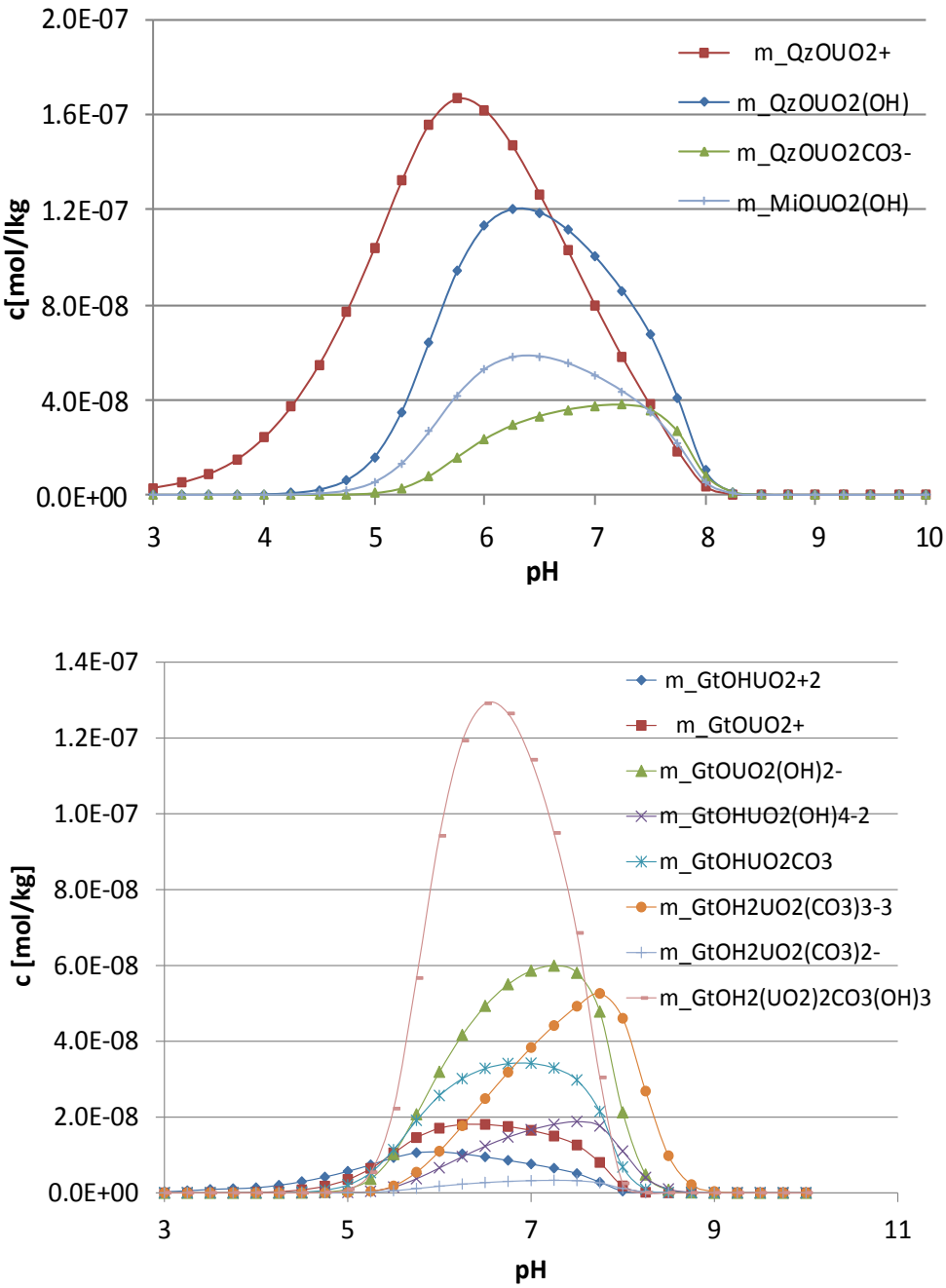

Fig. 6.9 Distribution of uranium on different sorbed species of quartz, mica (top) and goethite (bottom) for the system U – synthetic sand

As a second system uranium soprtion on a natural sand was selected. The pH dependent sorption curve measured in /BRA 08/ is shown in Fig. 6.10. Due to the investigations in /BRA 08/ the natural sand is characterized by 90 % quarz, 5 % muscovite and 5 % iron oxide. For the simulation this mineral ratio and the same parameters as used for the synthetic sand are applied. The resulting curve in comparison to the experimental values is shown in Fig. 6.10. As expected sorption on goethite plays a more important role than for the synthetic sand because of the higher

content of this mineral in the mixture. The simulated curve shows a quite good agreement for the plateau of the sorption curve in the pH range between 5 and 8. However, the sorption edge at low pH-values (between 3.5 and 5 is significantly underestimated by the simulated curve. The reason for that might be an additional mineral phase or even organic material, which are not considered in the simplified bottom-up approach using three minerals only.

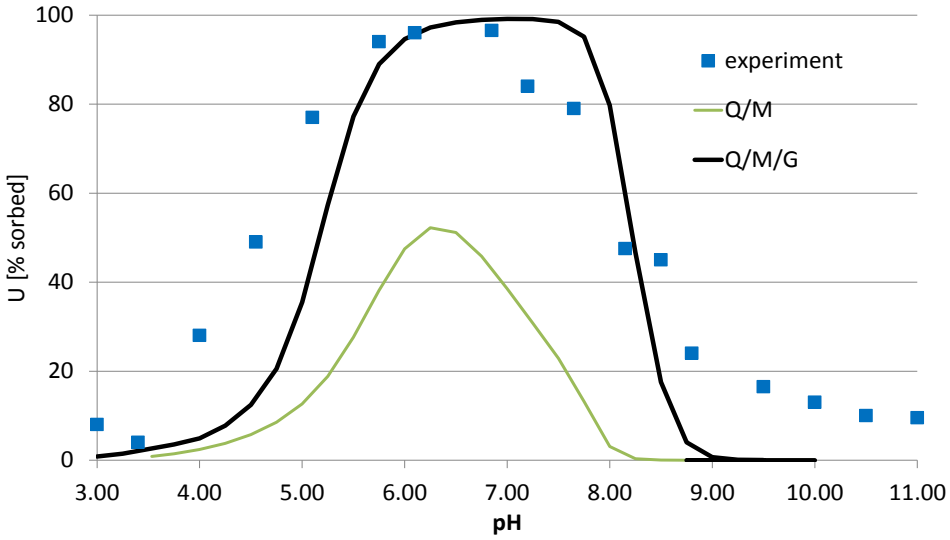

Fig. 6.10 U(VI) sorption on natural sand

Experimental data (/BRA 08/) compared to simulation results for a mixture of quartz and muscovite (Q/M) and quartz, muscovite and goethite (Q/M/G). See text for details.

The role of the single surface complexes is shown in Fig. 6.11. It illustrates that the uranium surface complexes with goethite are dominating over the whole pH range. Only in the pH range 3 to 5 the complex on quartz, $QzOUO_2^+$ contributes in a similar order of magnitude as the hydroxo-complex on goethite $GtOHUO_2^{+2}$. In the pH range 5.5 to 9 the sorption is firstly controlled by the hydroxo-complex $GtOHUO_2(OH)_2^-$ and above pH 6.5 clearly by the carbonato-complex $GtOH_2UO_2(CO_3)_3^{-3}$.

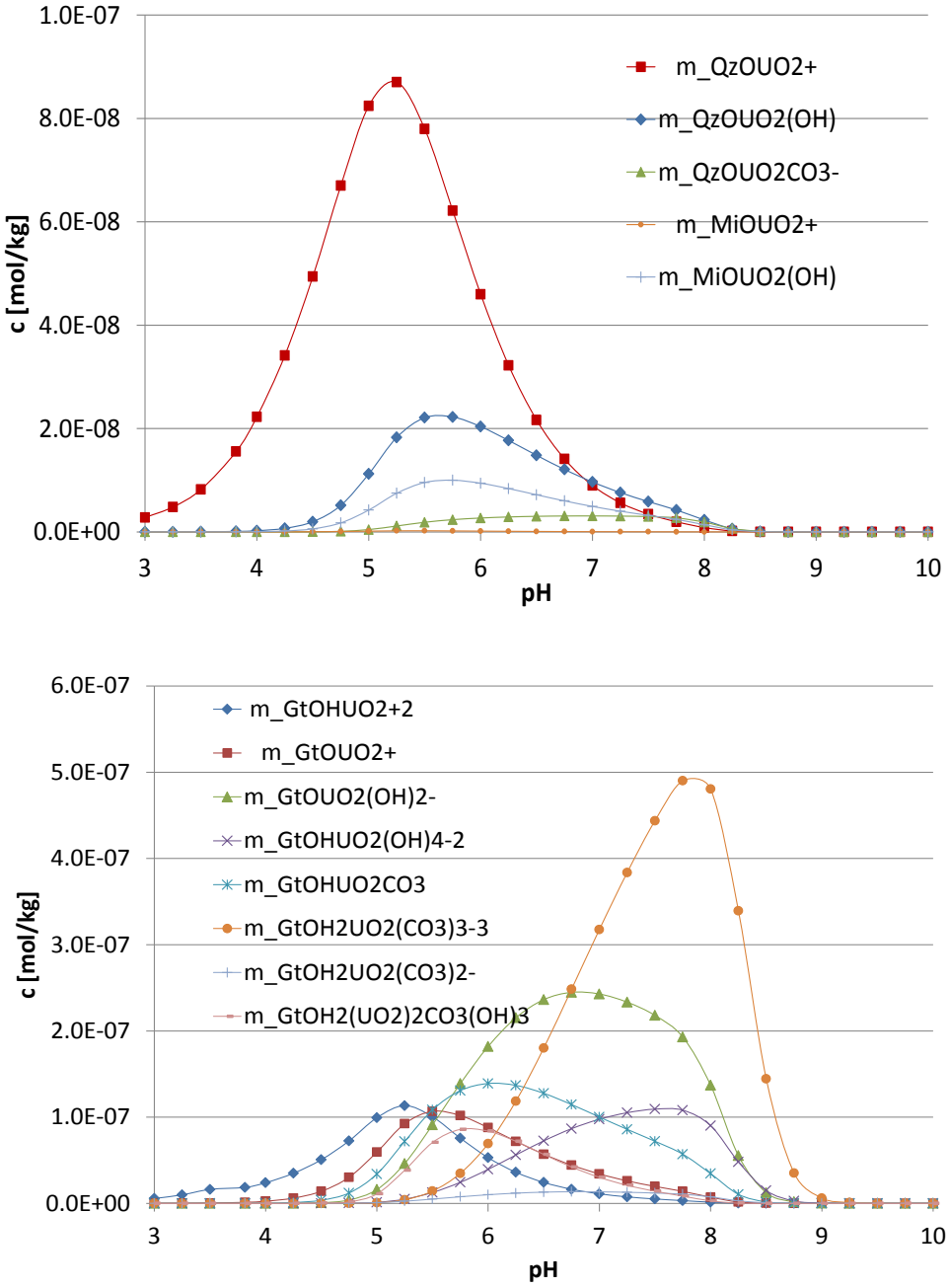

Fig. 6.11 Distribution of uranium on different sorbed species of quartz, mica (top) and goethite (bottom) for the system U – natural sand

Finally sorption of uranium on granite was simulated. The experimental data stem also from /BRA 08/. As discussed there a mixture of orthoclase of 35 % quartz, 33 % muscovite, 31 % albite und 1 % goethite was assumed for the simulations. For the specific surface areas of the minerals quartz and muscovite the same values as applied for the sand have been selected. For albite and goethite 1.4 $m^2 g^{-1}$, and 1.2 $m^2 g^{-1}$ have been used, respectively /ARN 99c/. Log K-values have been taken from the ESTRAL.dat data base for albite are taken from /ARN 99c/. For all other minerals the values from

RES³T data base as described in section 3.3.3 have been applied. The results of the simulation are shown in Fig. 6.12. The simulated curve very well fits the experimental data. It can also be seen that all the mineral phases contribute to some extent and no single phase can be neglected. Nevertheless, the main contributor to uranium sorption is albite. In this case, where quartz and muscovite are present roughly in the same amount, sorption on muscovite plays a more important role than sorption on quartz.

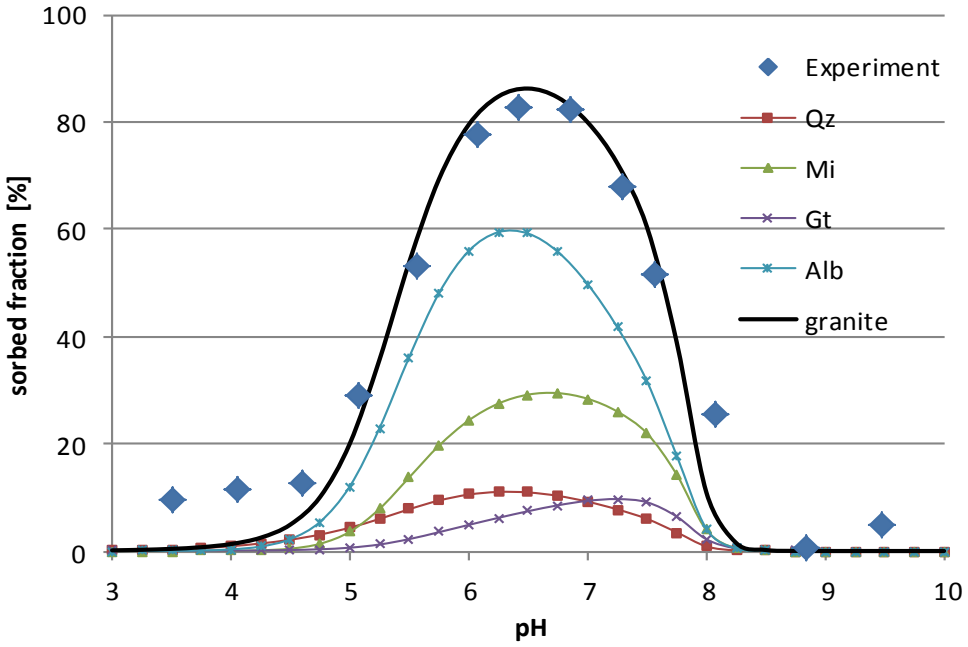

Fig. 6.12 U(VI) sorption on granite. Experimental data (/BRA 08/) compared to simulation results

Granite was assumed as a mixture of quartz (Qz), muscovite (Mi), goethite (Gt) and albite (Alb). The contribution of each mineral is shown (see text for details).

In general the results from all applications of the bottom-up approach give quite good results for the sorption of europium and uranium, respectively, underpinning the concept developed here. In a follow on project application cases for additional elements will be included broadening the basis for the bottom-up approach.

7 Conceptual model for the consideration of spatial and temporal changes of geochemical conditions

The transport code r^3t is used so far to consider the transport of radionuclides in large model areas over long periods in time. The previous version of r^3t used linear and non-linear isotherms to describe retardation proceses of contaminants. It was also possible to describe the sorption parameters as a function of the concentration of another element, whose transport is considered in r^3t. However, it was not possible so far to describe the sorption of a contaminant as a function of the concentration of several environmental parameters, and particularly not to describe the pH value as a function of both, proton transport and chemical reactions with mineral phases.

7.1 Conceptual model for variable chemistry

A key part of the whole project is the conceptual model for implementation of the relevant chemical processes into the transport code. As described in section 6.1.2 five environmental parameters have been selected, pH, ionic strength and concentration of DIC, Ca, and the selected radionuclides. An important assumption is that the interaction between the radionuclides is neglected. Further it is assumed that radionuclides generally do not impact the geochemical conditions. Therefore, major effort needs to be put on the other five environmental parameters.

A crucial aspect of our concept is that the pH-value is affected by proton transport and by chemical reactions with the dissolved ions (preferably DIC and Ca) and mineral phases of the sediments. According to the results from site investigation main reactions in the Gorleben aquifers are calcite dissolution (mainly in the upper aquifer), microbial SOC degradation causing enhanced CO_2 partial pressures (DIC source) and dissolution of feldspars /KLI 07/ (section 2). Ion exchange processes, which might occur in the aquitard and at the interface to the upper aquifer, have not been regarded to keep the system not too complex and clearly represented.

7.1.1 Strategy

In general the concept comprises the following steps, which are described in more detail in the following sections:

1. Calculation of the changed concentrations for Ca and DIC, as well as for the pH-value on the basis of transport calculation and possible sources (e. g. microbial DIC formation). The resulting concentrations/pH are denoted [Ca]T, DICT and pHT.

2. Examination, whether the solution is under- or oversaturated with respect to calcite (section 7.1.6). At this stage of development it is assumed that there will be always enough calcite in the system. However, a mass balance for calcite is performed, because it will be needed for the further improvement of the model.

3.a) In case of undersaturation of calcite it will be precipitated. The amount of precipitated calcite, the resulting concentrations for Ca and DIC as well as the new pH-value are then iteratively calculated as described in section 7.1.7.

3.b) In case of oversaturation of calcite it will be dissolved. The amount of dissolved calcite the resulting concentrations for Ca and DIC as well as the new pH-value are then iteratively calculated as described in section 7.1.8.

4. The concentrations and the pH-value resulting from step 3.a) or 3.b) are denoted as [Ca]*, DIC* and pH*.

5. The new equilibrium concentrations together with the current radionuclide concentration will be used to select the Kd-value for each radionuclide for this time step.

6. Calculation of proton and hydroxyl ion concentrations from the equilibrium pH-value pH*.

7.1.2 General terms

In order to get a consistent calculation the following aspects and assumptions need to be adhered.

1. For each sediment (hydrogeological unit) the initial conditions need to be fixed:

2. The conditions all over the sediment are the same (future option: a gradient)

3. The mineral composition of each sediment

4. The initial concentrations of DIC and Ca in solution as well as the pH-value are fixed and are derived from equilibrium calculations with PHREEQC. Initial concen-

trations for Si, Fe and Al are not needed, since their transport is not considered. Their concentration is determined by the pH-value and the mineral phases quartz, goethite and gibbsite, respectively.

5. For some elements sources might exist. One example is DIC, which is known to be produced by microbial degradation of organic material via sulphate reduction. Volume or plane sources can be defined as time dependent functions in [mol $(m^3\ s)^{-1}$].

6. Initial concentrations for Na and Cl are taken from the relative salt concentrations calculated with d³f, (section 7.1.4). Concentrations for K, Mg and SO_4 are calculated from the NaCl concentration via scaling factors (corresponding to the composition of seawater /LAN 02/). The scaling factors are as follows:

   $f_K = 0.017$
   $f_{Mg} = 0.097$
   $f_{SO4} = 0.053.$

   These values are not constant and might change for example in the case of seawater transgression or subrosion of the salt dome. However, at this stage the factors are considered to be constant.

Inflow concentrations:

7. Concentrations need to be given for Ca, DIC, Na, Cl, K, Mg, SO_4 and “pH”.

8. For radionuclides temporal dependent mass flows, which might be derived from near-field calculations, are used as input. For the radionuclide release from a salt dome – as considered here – it is assumed that the radionuclide inflow occurs via a point source.

9. In this concept it is assumed that the radionuclides do not influence each other and also do not influence the geochemical conditions in general.

10. All thermodynamic data are taken from the ESTRAL.dat data base.

11. It has to be denoted that all concentrations for r^3t need to be given and are handled by the code in [mol m^{-3}]. Therefore all concentrations in the formulas in this section are given in this unit, if not stated otherwise.

7.1.3 Temperature

The temperature is considered to be spatially and temporally isotropic. For the depth range of 0 – 400 m considered in this project a value of 15 °C is assumed. The thermodynamic data, which are documented for 25 °C, do not need to be re-calculated. The ΔH-values for the relevant mineral phases (calcite, gibbsite and anorthite) have been investigated and show that changes in the solubilities are within the range of the data uncertainties. A more detailed description and explanation for the use of a constant temperature is given in section 5.3.

7.1.4 Ionic strength

The ionic strength is derived from the calculations of the code d^{3}f for density driven flow. Beside the flow field d^{3}f calculates the distribution of the relative concentration of sodium chloride, $c_{rel,NaCl}$ [3] (value between 0 and 1). This value has to be transferred to r^{3}t for each point in space. This need to be done for selected points in time, depending on the problem considered.

The ionic strength I is calculated from the relative concentration of sodium chloride as follows. The concentration for the saturated NaCl solution $c_{sat,NaCl}$ is calculated via the mass fraction, density and molar weight of NaCl as

$$c_{sat,NaCl} = m_{NaCl} \cdot \rho_{NaCl} / M_{NaCl} = 5428.78 \text{ [mol m}^{-3}\text{]}$$

with the mass fraction m_{NaCl} = 0.265 /DAN 67/ and the density ρ_{NaCl} = 1197.2 kg m^{-3} of saturated NaCl solution at 20°C and the molar weight M_{NaCl} = 0.05844 kg mol^{-1}. The sodium chloride concentration is then calculated as $c_{NaCl} = c_{rel,NaCl} \cdot c_{sat,NaCl}$.

The ionic strength is defined as

$$I = 0.5 \cdot \sum_i [i] z_i^2$$

with the concentration of the dissolved ions $[i]$ in [mol L^{-1}] and their corresponding charges z_i.

[3] Please note that $c_{rel,NaCl}$ = f(T). This is important, if in a later stage a temperature field is considered

A simple approach is then

$$I = 0.5([Cl^-] + [Na^+])/10^3 = c_{NaCl}/10^3.$$

In a slightly extended approach additionally the ions K, Mg and SO_4 are considered using the scaling factors (see above) and a corrected sodium concentration:

$$I = 0.5([Cl^-]+[Na^+]+[K^+]+4\cdot[Mg^+]+4\cdot[SO_4^{2-}])/10^3$$
$$= [Cl^-]\cdot 0.5(1+0.859+0.017+4\cdot 0.097+4\cdot 0.053)/10^3$$

resulting in

$$I = 1.24\cdot[Cl^-]/10^3.$$

The activity coefficients are derived from the Specific Ion Interaction Theory (SIT) /CIA 80/. For the relevant ions the single activity coefficients are formulated according to SIT:

$$\log \gamma_{Ca^{2+}} = -4D + \varepsilon_{Ca,Cl} \cdot m_{Cl^-} \quad mit\ \varepsilon_{Ca,Cl} = 0.14$$
$$\log \gamma_{Al^{3+}} = -9D + \varepsilon_{Al,Cl} \cdot m_{Cl^-} \quad mit\ \varepsilon_{Al,Cl} = 0.33$$
$$\log \gamma_{H^+} = -D + \varepsilon_{H,Cl} \cdot m_{Cl^-} \quad mit\ \varepsilon_{H,Cl} = 0.12$$
$$\log \gamma_{HCO_3^-} = -D + \varepsilon_{HCO3,Na} \cdot m_{Na^+} \quad mit\ \varepsilon_{HCO3,Na} = 0.0$$

with an extended Debye-Hückel-Term $D = \frac{0.5012\sqrt{I}}{1+1.5\sqrt{I}}$ and the interaction coefficients ε_i.

The data are taken from /RAN 08/.

7.1.5 Transport of the relevant components

The transport of Ca, DIC and protons (and hydroxyl ions) is considered in r^{3}t. Calcite ($CaCO_3$ – Cc) need to be balanced, since it is the sink/source for Ca and DIC. It is assumed that the concentration of free calcium ions [Ca^{2+}] equals the total concentration of calcium $[Ca]_{tot}$. The impact of further solution species as $Ca(HCO_3)^+$, $CaCO_3^0$ und $Ca(OH)^+$ is in the considered pH range between 3 and 9 always below 2 % and is therefore neglected here. The initial concentrations of Ca and DIC as well as the initial pH-value are usually derived from equilibrium calculations (section 7.1.2).

Since the pH-value is a function of the ionic strength I, the activity correction need to be performed by $pH = -\log([H^+]_{korr} \cdot \gamma_{H+})$, as described in section 7.1.4. The activity coefficient for H^+ is derived by

$$\log \gamma_{H+} = -z^2 D + \sum \varepsilon_{H+,k}[k]/10^3$$

with the concentration of the most relevant anions (Cl^-, HCO_3^-; SO_4^{2-}) *[k]*, and the SIT interaction coefficients ε_i. For H^+ only the interaction coefficient $\varepsilon_{H+,Cl-}$ = 0.12 is available. The interaction coefficients of other monovalent cations Na^+ and Li^+ with the relevant anions $\varepsilon_{Na+,HCO3-}$ = 0.0 and $\varepsilon_{Li+,SO42-}$ = -0.03 show that these interactions are low. Considering typical SO_4 concentrations this contribution is always below 1 % of the interaction of H^+ with Cl^-. Then it is

$$\log \gamma_{H+} = -D + 0.12[Cl^-]/10^3$$

and for hydroxyl ions

$$\log \gamma_{OH^-} = -D\,.$$

After a transport step of protons and hydroxyl ions the pH-values is calculated from their concentrations as

$$pH^T = [H^+]^{korr} \gamma_{H^+}$$

with

$$[H^+]/10^3 - x = [H^+]^{korr}\ ,$$

$$x = \frac{[H^+]^T/10^3 + [OH^-]^T/10^3}{2} - \sqrt{\left(\frac{[H^+]^T/10^3 + [OH^-]^T/10^3}{2}\right)^2 - [H^+]^T[OH^-]^T/10^6 + \frac{K_W}{\gamma_{H^+}\gamma_{OH^-}}} \quad (7.1)$$

and the ionic product of water $K_W = 10^{-14}$ mol^2L^6.

7.1.6 Determination of over-/undersaturation of calcite

In the first step the ionic activity product (*IAP*) is calculated with the following equation

$$\log IAP = \log \frac{[DIC]^T}{10^3} + pH^T + \log \frac{[Ca]^T}{10^3} - \log(1 + 10^{6,35-D} + 10^{pH-10,329+D}) - 5D + 0{,}14\frac{[Cl]^T}{10^3} \quad (7.2)$$

The saturation index S_i shows, whether the solution is over- or undersaturated

$S_i = 10^{\log IAP - \log K_{CaCO3}}$.

For S_i > 1 the system is oversaturated, calcite precipitates (section 7.1.6). For Si < 1 the system is undersaturated, calcite becomes dissolved (section 7.1.8).

7.1.7 Precipitation of calcite

Firstly a correction factor is defined

$$F_{Korr} = \sqrt{S_i} .$$

Then it is estimated, which amounts of [Ca] und [DIC] theoretically would fulfill the solution equilibrium

$$[Ca]^{korr} = \frac{[Ca]^T}{F_{Korr}} \quad \text{and} \quad [DIC]^{korr} = \frac{[DIC]^T}{F_{Korr}} .$$

Afterwards the corresponding concentration differences are determined. The according to amount lower concentration change has to be applied to both components. The following concentration of calcite precipitates

$$\Delta[C_i] = Min([C_i]^T - [C_i]^{korr}) F_D$$

With a damping factor F_D, which can be defined by the user and index i describing the component (Ca or DIC). Therewith the new equilibrium concentrations of Ca and DIC are calculated

$$[C_i]^* = [C_i]^T - \Delta[C_i]$$

The proton concentration in equilibrium is the iteratively calculated. For the first step of the outer iteration the initial value for the inner iteration is

$$\left[H^+\right]_0^* = \left[H^+\right]^T$$

and for the following steps of the inner iteration

$$\left[H^+\right]^*_{n+1} = \left[H^+\right]^*_0 + F_{DIC}\left([DIC]^* - \left[HCO_3^-\right]^*_n\right) \quad (7.3)$$

with $F_{DIC} = \frac{[DIC]^T - [DIC]^*}{[DIC]^T}$ is applied.

For further steps of the outer iteration the starting value of the inner iteration is

- for the case $F_{Korr} < 0$ $\left[H^+\right]^*_0$ from the last outer iteration where $F_{Korr} > 0$,
- for the case $F_{Korr} > 0$ $\left[H^+\right]^*_{n-end}$, i. e. the proton concentration derived in the last outer (and inner) iteration loop.

For the following steps equation (7.3) is applied.

For the concentration of HCO_3^- holds

$$\left[HCO_3^-\right]^*_n = \frac{[DIC]^*}{\left(\frac{K_{s1}}{[H^+]^*_n/10^3} + 1\right)} \quad (7.4)$$

with K_{s1} = 4,689·10^{-11} mol L^{-1}.

Convergence of this inner iteration is assumed, when the change in pH-value is below 10^{-3}. With the new pH-value and the new concentrations of Ca and DIC in equilibrium the ionic activity product (IAP, equation (7.2)) is calculated again. This outer iteration is repeated until the difference between the correction factor and 1 is below 10^{-3}.

For this iteration an oscillation between precipitation and dissolution should be avoided by reducing the damping factor for the case that the saturation index < 1 occurs by a defined factor and repetition of the calculation until a saturation index > 1 is achieved.

7.1.8 Dissolution of calcite

In analogy to the procedure for the precipitation of calcite the dissolved calcite concentration is calculated by

$$\Delta[C_i] = Min([C_i]^T - [C_i]^{korr})F_D$$

From that the new equilibrium concentrations for Ca and DIC in solution are determined:

$$[C_i]^* = [C_i]^T + \Delta[C_i]$$

The concentration of protons and hydroxiyl ions are calculated by

$$\frac{[H]}{10^3} = \frac{pH}{\gamma_{H^+}}$$

$$\frac{[OH^-]}{10^3} = \frac{10^{pH-14}}{\log \gamma_{OH^-}} - \frac{K_B}{2} + \sqrt{\frac{K_B^2}{4} + K_B \frac{\Delta C_i}{10^3}} \qquad (7.5)$$

with K_B = 2,133·10^{-4} mol L^{-1}. The concentration of protons has to be corrected in the same way as after a transport step by the following equation

$$([H^+]/10^3 - x) = [H^+]^{korr}$$

with

$$x = \frac{[H^+]/10^3 + [OH^-]/10^3}{2} - \sqrt{\left(\frac{[H^+]/10^3 + [OH^-]/10^3}{2}\right)^2 - [H^+][OH^-]/10^6 + \frac{K_W}{\gamma_{H^+}\gamma_{OH^-}}} \qquad (7.6)$$

The equilibrium pH-value is then

$$pH^* = [H^+]^{korr} \gamma_{H^+}.$$

The new equilibrium constants are used to calculate the new ionic activity product (log IAP) and from that the new concentrations of Ca and DIC as well as the equilibrium pH-value. The iteration is continued until the difference between correction factor and 1 is lower than 10^{-3}.

Within the iteration an oscillation between dissolution and precipitation need to be avoided. This is realized by reducing the damping factor – for the case the saturation index exceeds 1 – by a defined value and repetition of the calculation until the saturation index is <1.

After termination of the iteration the proton concentration, which is needed for the transport step has to be back-calculated from the pH-value by an activity correction via

$$[H^+]/10^3 = 10^{-pH} / \gamma_{H^+} .$$

Afterwards the hydroxyl ion concentration is updated by

$$[OH^-]/10^3 = 10^{-(\log K_W /10^6 - pH)} / \gamma_{OH^-} .$$

7.2 Implementation of the conceptual model

In the following, the extensions made to r^{3}t in order to implement the conceptual model described in section 7.1 are described using a simple 1D test case. This test case consists of a vertical column that is saturated with a first mixture in a state of equilibrium with respect to the environmental parameters denoted as Estral agents in the programme files. In a first phase, fluid consisting of this same mixture plus a contaminant is injected at the bottom of the column with a constant inflow velocity. In a second phase the inflowing fluid is replaced by another mixture of different composition with regard to the environmental parameters but without any contaminant. How to setup this problem with r^{3}t's configuration files and standard script is now described, thereby also showing the concrete values used for this numerical experiment.

Fig. 7.1 shows the content of the file “pollutant”. Here, *RN-001* denotes the contaminant; the next four lines introduce the Estral agents. They must all be present and named exactly like this to get proper treatment after each time step.

```
pollutant

model estral
version version_1

RN-001

agent eCa
agent eDIC
agent eH
agent eOH

pollutant end
```

Fig. 7.1 Content of the programme file “pollutant”

Programme file “initial” shown in Fig. 7.2 contains the initial conditions for all Estral agents and the contaminants. For convenience, there are functions *I_H_from_pH* and *I_OH_from_pH* that compute the initial concentrations of protons, *[eH]* and hydroxyl ions, *[eOH]* from a prescribed pH and the ionic strength taken from flow code d^3f.

```
initial

model estral
version version_1

liquid

validity all

global const 0.0

validity all end

validity eCa
############

global const 25.02

validity eCa end
```

Fig. 7.2 Content of the programme file “initial”

```
validity eDIC
#############

global const 1

validity eDic end

validity eH
###########

global function I_H_from_pH 7

validity eH end

validity eOH
############

global function I_OH_from_pH 7

validity eOH end

validity RN-001
###############

global const 1e-9

validity RN-001 end

liquid end

initial end
```

Fig. 7.2 (cont.) Content of the programme file “initial”

The file “boundary, shown in Fig. 7.3, defines values at the inflow boundary for the two phases (time ≤ 10000 s and time > 10000 s) for the contaminant and all Estral agents. Again, there are several convenience functions for specifying *[eH]* and *[eOH]* in terms of a pH and the ionic strength from d[3]f. *B_H_from_pH_2* e. g. has the length of the first phase in seconds, the pH for phase one, and the pH for phase two as arguments.

```
boundary

model estral
version version_1

validity all
############

time independent

surface 2 inout 0.0

time independent end

validity all end

validity eCa
############

time dependent
surface 0  time     0  level const 25.02
                   time 10000  level const 25.02
                   time 10001  level const  0.24394
                   time 99999  level const  0.24394
                   time end

time dependent end

validity eCa end

validity eDIC
#############

time dependent

        surface 0  time     0  level const 1.0
                   time 10000  level const 1.0
                   time 10001  level const 3.14394
                   time 99999  level const 3.14394
                   time end

time dependent end
```

Fig. 7.3 Content of the programme file “boundary”

```
validity eDIC end

validity eH
############

time dependent

        surface 0  level function B_H_from_pH_2 10000 7 8.05518

time dependent end

validity eH end

validity eOH
############

time dependent

        surface 0  level function B_OH_from_pH_2 10000 7 8.05518

time dependent end

validity eOH end

validity RN-001
#############

time dependent

        surface 0  time     0  level const 1e-5
                   time 10000  level const 1e-5
                   time 10001  level const 0
                   time 99999  level const 0
                   time end

time dependent end

validity RN-001 end

boundary end
```

Fig. 7.3 (cont.) Content of the programme file “boundary”

In the programme file “retention” (Fig. 7.4), the function *Estral_Kd* implements the smart K_d-concept. Arguments are (strictly speaking) the concentrations of protons, DIC, Ca and the corresponding radionuclide, i. e. *[eH]*, *[eDIC]*, *[eCa]*, and *[RN-001]*, respectively. Ionic strength from d^{3}f is implicit, and the last argument ('6' in this case) selects which smart K_d-value (indexing starts with zero) from the ones associated with the given point in the smart K_d-cloud is returned. The smart K_d-cloud itself is loaded into the memory from a file in the “config”-Folder called “cloud” on the first invocation of this function. The format of this file has to follow the description in section 6.1.4.

```
retention

model estral
version version_1

hydrogeo2mat

   MATERIAL1: UNIT1

hydrogeo2mat end

MATERIAL1

  rock_density 700 porosity 0.2 porosity_im 0.0 g 1.0
  diffusion 1e-9 alpha_L 0.2 alpha_T 0.0

  RN
    mobile
      equilibrium Henry function Estral_Kd eH eDIC eCa RN-001 6
    mobile end
  RN end

MATERIAL1 end

retention end
```

Fig. 7.4 Content of the programme file “retention”

Fluid velocity and salt concentration are precomputed by the flow code d^{3}f. The programme file “flow” (see Fig. 7.5) directs r^{3}t to the respective files provided by d^{3}f. In the stationary case (referring to both velocity and salt concentration) a single input file is read before the first timestep. In this case, r^{3}t can use its own timestep control. In the

instationary case, r^{3}t reads an input file before each timestep. Timesteps in r^{3}t will be automatically in sync with those used in d^{3}f.

```
flow


model estral
version version_1


velocity instationary path "$(HOME)/ESTRAL/rnt/estral4/input/"


fluid_density const 1000.0


flow end
```

Fig. 7.5 Content of the programme file “flow”

The parameters listed in file “defaults.scr” (Fig. 7.6) are damping factors and error bounds for the postprocessing after each timestep (see section 7.1 for description) for precipitation ('1') and dissolution ('2') of calcite, respectively. Experience with how to choose these values is rather limited yet, but the values shown work reasonably well with this example.

```
...
ESTRAL_DAMP1 = 0.05;
ESTRAL_DAMP2 = 0.2;
ESTRAL_EPS1  = 0.005;
ESTRAL_EPS2  = 0.005;


...
```

Fig. 7.6 Content of the programme file “defaults.scr”

The purpose of this test case is to illustrate the extensions made to r^{3}t and to verify that the implemented concepts basically work and produce plausible results. The following remarks are therefore only of a qualitative nature. During phase two, solution 1 being in equilibrium with calcite at pH 7 is replaced by a second solution of pH 8. Chemical reactions occur starting from the inflow zone and propagating through the column, see Fig. 7.7. As a consequence of calcite precipitation the pH of the inflowing solution decreases from 8 to about 7.5 in accordance with the conceptual model.

The retrieved smart K_d-values show their highly nonlinear dependence on the environmental parameters and the concentration of the respective radionuclide. Examplarily the spatial distribution of the smart K_d-value for uranium in the column is depicted in Fig. 7.8, which roughly shows that smart K_d-values are larger towards the bottom of the

column (inflow) and smaller towards the top. This is the result of an increasing pH and a decreasing Ca concentration at the bottom of the column in phase 2. The radionuclide uranium injected in phase one should therefore show a larger retardation towards the bottom of the column at this point in time, which is in accordance with Fig. 7.9. The decreasing retardation with increasing column length leads to a faster uranium transport at the top of the column, therewith causing an asymmetric spatial distribution with a flatter slope to the top of the column.

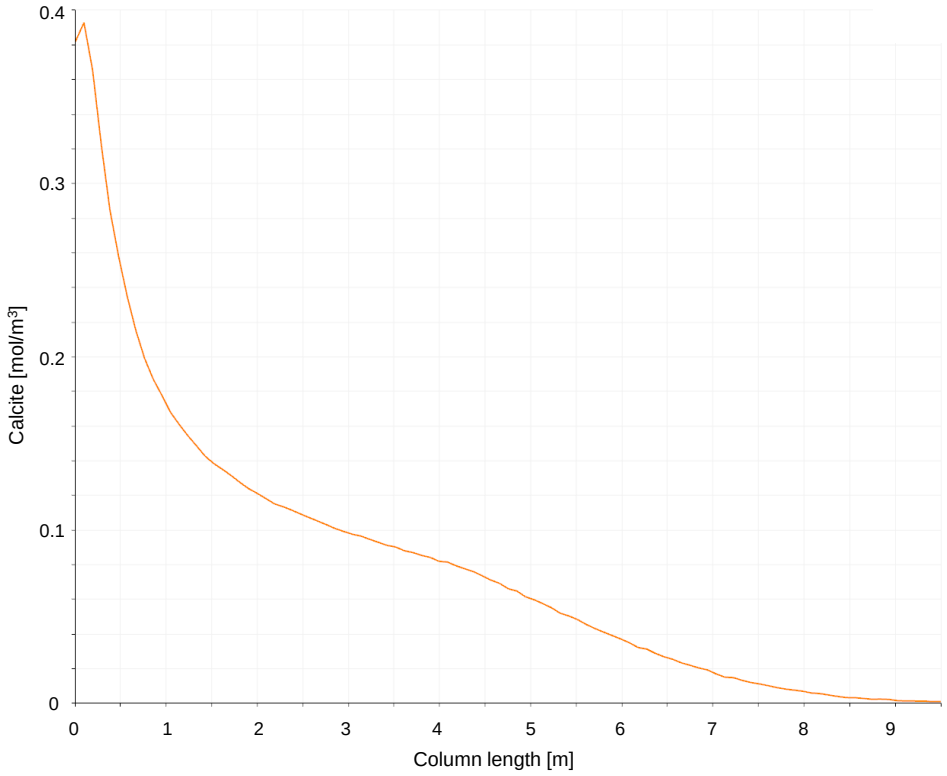

Fig. 7.7 Calcite precipitation over length of column (middle of phase two)

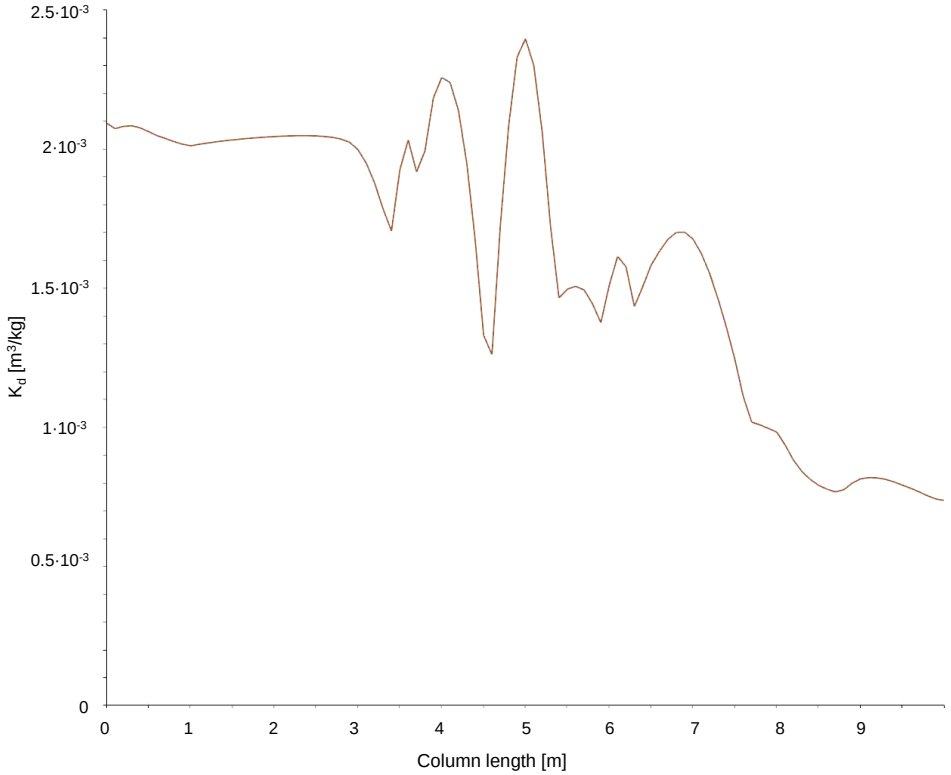

Fig. 7.8 Smart K_d-values for uranium retrieved as a function of the environmental parameters over column length (middle of phase two)

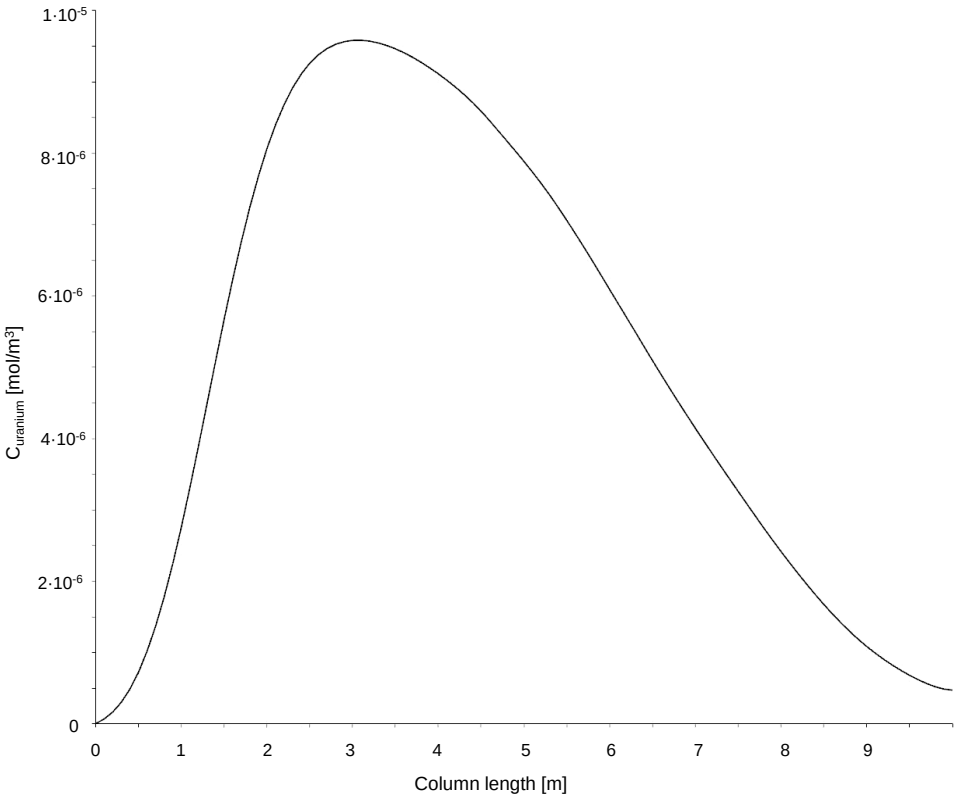

Fig. 7.9 Uranium concentration over column length (middle of phase two)

8 Applied simulation of selected processes

Applied simulations were conducted for the Gorleben reference site. An overview of the geology and hydrogeology is given in section 2.3. Possible future climate transitions are a seawater trans- and regression and the freezing and thawing of permafrost, amongst others. These two climate transitions are described in the following with a focus on respective past climate transitions in Northern Germany and the potential future climatic evolution of the reference site. Model simulations were only conducted for a seawater trans- and regression (in the following denoted as “seawater transgression”). Results of these applied simulations are given in sections 8.3.4 and 8.4.4.

8.1 Climate transitions

Possible future climate transitions can be derived from the geological past. The Quaternary period is characterized by extreme climate changes, i. e. the repeated advance and retreat of inland ice sheets, and the transgression of the North Sea in Northern Germany due to a global sea level rise /BEN 95/. With the knowledge about past climate and its driving forces, possible future climate states can be simulated.

Several studies investigate the possibility of a future sea level rise due to global warming. Ganopolski /GAN 07/ assumes a sea level rise of 20 m to 30 m within the next 50,000 a. Taking the thermal expansion and density changes of seawater into account, the melting of the global ice volume can be calculated. Therefore, a sea level rise of up to 80 m is possible /WIL 93/, but is not regarded as a realistic scenario /MEY 06/. According to different publications, the next cold stage may be expected in ca. 20,000 a /EMI 57/, not earlier than 50,000 a /LOU 00/ or even not earlier than 170,000 a to 500,000 a /ARC 05/. Values are based on different methods, such as the evaluation of oxygen isotopes of foraminifers from deep-sea cores or of the orbital parameters, and on different assumptions, e. g. regarding the future CO_2 emissions.

All in all, a repetition of past interglacial and glacial cycles is most probable on a time scale of one million years, so that a future cold stage or a sea level rise have to be considered for the long-term future. In this project, the Holstein Warm Stage is used as a reference for warm stage model simulations and the Weichsel Cold Stage as a reference for cold stage model simulations.

8.1.1 Seawater Transgression

Quaternary sea level oscillations can be regarded as a result of the Milankovitch cycles and hence are dependent on the global ice volume /IMB 84/. In Northern Germany, the sea level variations amounted to several dekameters up to ca. 120 m in the course of the last 18,000 a /STR 04/. Several Quaternary North Sea transgressions are recorded for Northern Germany. In the geological past, periods of seawater inundation in Northern Germany persisted for about a few thousand years only /STR 04/. The maximum extension of the Quaternary marine transgressions occurred during the Holstein Warm Stage (Fig. 8.1), which lasted from 335,000 until 330,000 a before present (BP). The marine transgression occurred in form of a single, uninterrupted sea-level rise with an average rising rate of 1 m per 100 a /STR 04/. This led to a local sea level rise of more than 50 m /STR 04/ up to ca. 65 m /LIN 85/, while the global sea-level rise amounted to more than 100 m /ROH 98/. The sea-level high stand persisted for the time of ca. 5,000 a.

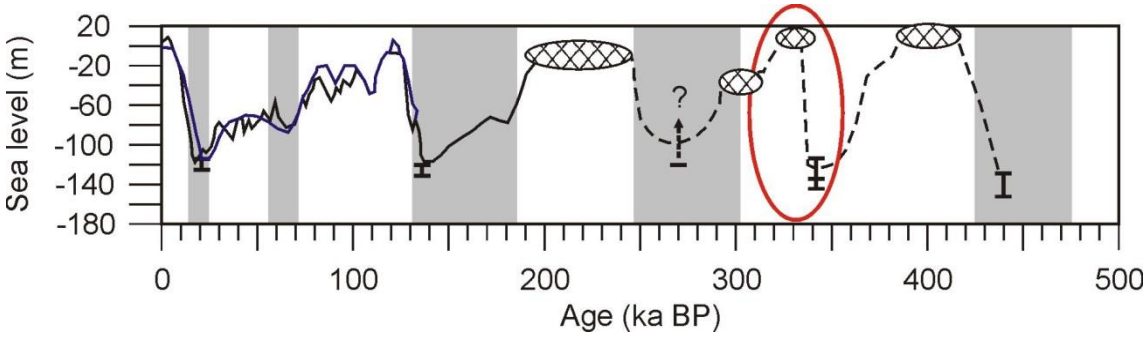

Fig. 8.1 Global sea level record of the past 500,000 a modified from /ROH 98/

Solid lines are based on different climate proxies. The dashed line shows schematic sea-level fluctuations sketched through the control points following the main trends in the oxygen isotope record. Cross-hatched ovals show ranges of interglacial sea-level highstands. Error bars represent ranges of glacial sea-level lowstands according to the model presented in /ROH 98/. The red oval shows the Holstein interglacial.

8.1.2 Permafrost

In the geological past, climate states with the formation of permafrost occurred periodically at the Gorleben site. According to model calculations, permafrost during the Weichsel Cold Stage in the Gorleben area reached thicknesses between 40 m and 140 m /KLI 07/. Here, periods with and without permafrost alternated with a periodicity

of ca. 10,000 to 30,000 a. The permafrost growth and decay can be simulated for a time of 40,000 a according to Fig. 8.2.

Completely unfrozen zones – so-called taliks – could have been formed in areas beneath rivers and lakes due to their thermal influence /DEL 98, KEL 98/. In case of a future glacial it has to be assumed that there will be, similar to that of the last glacial (Weichselian), an inland ice sheet north or northeast of the Gorleben area. During the maximum extension of the Weichselian ice sheet ca. 16,000 to 20,000 a BP /STR 04/, the ice margin was located in the immediate vicinity of the investigation area in less than 50 km distance /KOE 00/. Permafrost areas melt in case of a glacial overriding because of a subglacial thermal disequilibrium /BOU 04/. Therefore, the permafrost decays below the glacier. Glacial meltwater is forced into the subglacial aquifer, and will rise to the free surface beyond the permafrost areas in front of the ice sheet. In this case, large volumes of meltwater could infiltrate into the underground and flow into the lower aquifer of the model domain. According to Boulton /BOU 93/ unfrozen zones in the permafrost may concentrate discharge and produce exceptionally high upward water fluxes. The river Elbe, which served as a glacial valley with a talik during the Weichselian, is expected to persist and, due to the high meltwater volumes from the ice sheet, have a larger width than today /KOE 00/. Another talik is assumed to have been formed beneath the River Seege further south. During rainfall or flood events, these taliks serve as infiltration areas for groundwater recharge. At the same time, groundwater could be discharged due to high inflow from the north into the lower aquifer, through the taliks of the upper aquifer, up to the surface.

The climate transition between the present climate and the permafrost conditions is only theoretically discussed in this report and is not modeled. Therefore, only results of model simulations of the constant climate and the seawater trans- and regression are presented in the following.

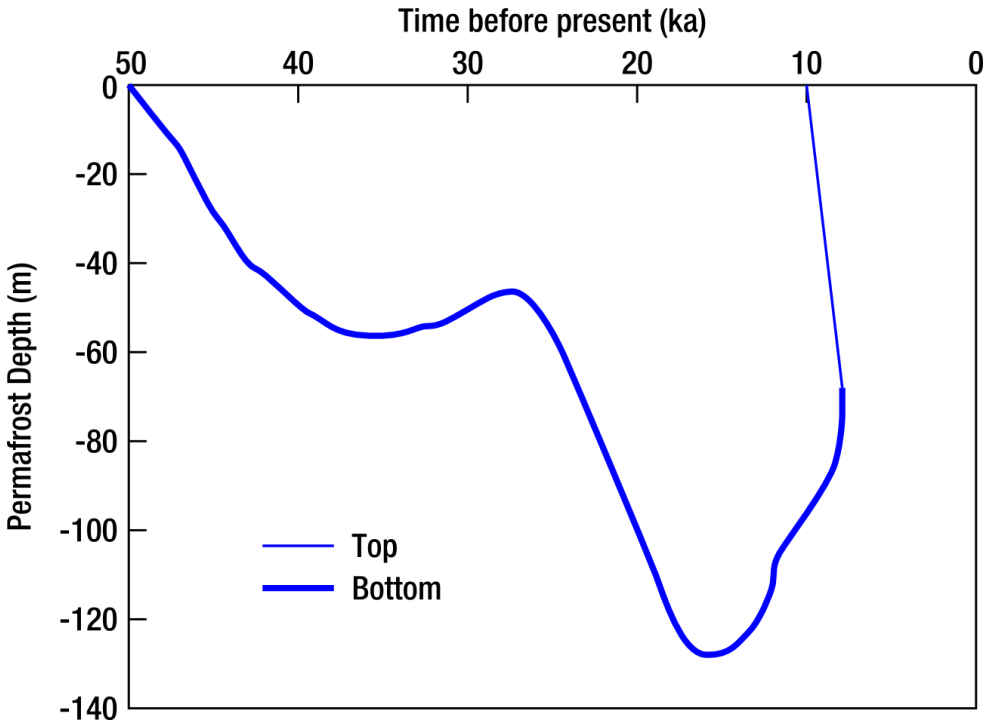

Fig. 8.2 Calculated permafrost depth depending on the surface temperature for the past 50,000 a, modified from /DEL 98/

8.2 Groundwater flow and transport model

Flow and transport were simulated using the codes d³f for groundwater flow and r³t for radionuclide transport, which were developed under the auspices of GRS /FEI 04, FEI 99/. Main characteristic of d³f is the possibility to calculate the transient, density-driven transport of salt, which is the most important process influencing the groundwater flow in the model area /KLI 07/. Transport calculations with r³t are based on the flow field calculated by d³f. The most important feature of r³t is the possibility to simulate pollutant transport in very large model domains for long periods in time. The smart K_d-concept was implemented in the transport code r^3t (section 7).

8.2.1 Model set-up

The model is based on a schematic cross section through the Gorleben area, which summarizes all main geological and hydrogeological characteristics (section 2.3) of the site under present conditions (Fig. 8.3). It comprises three geological units, representing the lower aquifer, the aquitard, and the upper aquifer. The lower aquifer is characterized by high salt concentrations of the groundwater, resulting from the contact to the

salt dome in the lower aquifer and leaching of salt, while the upper aquifer is characterized by low salt concentrations. Groundwater recharge takes place at the surface. Part of this water is drained to the lowlands of the river Elbe, while the other part may infiltrate through the hydraulic windows of the aquitard down to the lower aquifer. At the contact to the salt dome within the lower aquifer, salt can be dissolved rising the salt concentration and the density of the groundwater. From the contact to the salt dome, the water flows to the north and sinks down in the northwestern rim syncline. Apart from that it can rise up into the upper aquifer through the hydraulic windows or through the aquitard, resulting in locally elevated layers of salt water underlain by less saline water and in salt water areas at the surface.

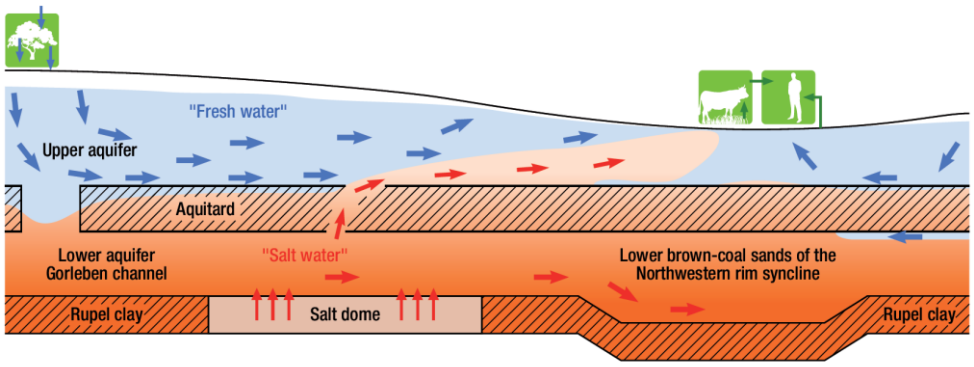

Fig. 8.3 Schematic cross section of the hydrogeological system at the Gorleben reference site, modified from /KLI 02/

8.2.2 Model geometry

A two-dimensional model was set up based on the schematic cross section (Fig. 8.3) and the geological and hydrogeological information given by numerous publications (e. g. /KLI 07/, /KLI 02, /LUD 02/). The two-dimensional model has a length of 16.4 km and a maximum depth of 400 m (Fig. 8.4). It consists of three different units representing a lower and an upper aquifer with an intercalated aquitard. In the model, both aquifers have a thickness of 100 m. The northwestern rim syncline is realized in the model with an additional thickness of the lower aquifer of 150 m. The aquitard has a thickness of 50 m. Both, the Hamburg Clay and the Lauenburg Clay Complex, are locally interrupted by hydraulic windows, i. e. local absence of the aquitard. One hydraulic window with a width of 500 m is realized close to the southern boundary of the model and a second hydraulic window at the northern boundary of the northwestern rim syncline. The contact of the lower aquifer to the cap rock of the Gorleben salt dome is marked in

red in Fig. 8.4. All figures of the model and results of the simulations are exaggerated by a factor of 10.

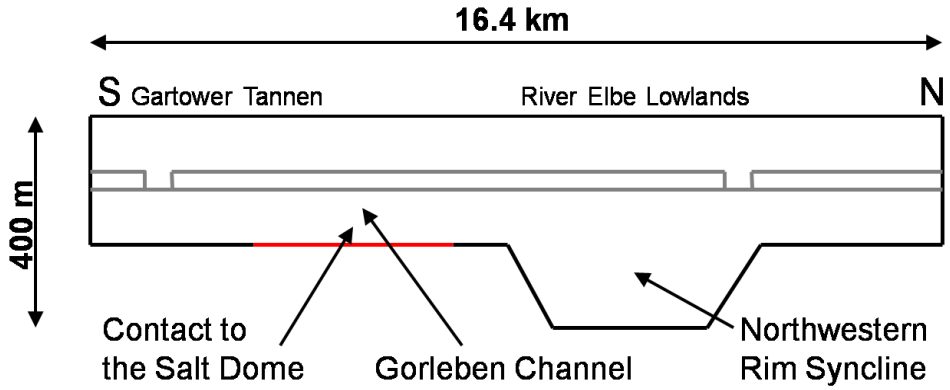

Fig. 8.4 Geometry of the groundwater flow and transport model with two aquifers and an intercalated aquitard

8.3 Flow simulations

Values for the hydraulic parameters were taken from different publications about the Gorleben aquifer system (cited in /FLU 09/ and /NOS 09/). The permeability k is $1 \cdot 10^{-12}$ m^2 for the aquifers and $1 \cdot 10^{-16}$ m^2 for the aquitard. The porosity φ is 0.2 (aquifers), and 0.05 (aquitard). A uniform longitudinal dispersion length α_L of 10 m, a transversal dispersion length α_T of 1 m and a molecular diffusion coefficient D_m of $1 \cdot 10^{-9}$ m^2 s^{-1} are set for the entire model domain (Tab. 8.1).

Tab. 8.1 Hydaulic parameters for the three hydrogeological units upper aquifer (UAF), aquitard (AT) and lower aquifer (LAF)

Parameter	Notation	UAF	AT	LAF
Permeability	k [m^2]	$1 \cdot 10^{-12}$	$1 \cdot 10^{-16}$	$1 \cdot 10^{-12}$
Porosity	φ [-]	0.2	0.05	0.2
Longitudinal dispersion length	α_L [m]	10		
Transversal dispersion length	α_T [m]	1		
Molecular diffusion coefficient	D_m [m^2 s^{-1}]	$1 \cdot 10^{-9}$		

As an initial condition, the temperature rises linearly from 8 °C at the surface to 20 °C at the bottom of the model. Heat transport is not calculated in the simulations.

The salt concentration is given in form of a relative concentration /FEI 99/:

$$c_{rel} = \frac{c_{abs}}{c_{abs,\max}} \text{ with } c_{abs} = \frac{m_{tracer}}{m_{tracer} + m_{H_2O}}$$

and

c_{rel} = relative salt concentration = relative salt mass fraction [-]
c_{abs} = absolute salt mass fraction [-]
$c_{abs,max}$ = maximum absolute salt mass frcation [-]
m_{tracer} = mass of salt [kg]
m_{H_2O} = mass of water [kg].

The expected salt concentrations range between fresh water (minimum absolute salt mass fraction = 0.0) to saturated brines (maximum absolute salt mass fraction = 0.265, equivalent to 360.54 g L^{-1}).

Initial and boundary conditions as well as changes in the hydraulic parameters for each climate transition are described in the following.

8.3.1 Present state and constant boundary conditions

The model simulation starts with the present climate state. Therefore, present conditions need to be simulated first. Initial conditions for the salt concentration are set according to the presumed salt distribution in the Gorleben area after the end of the Weichsel Cold Stage and the beginning of the Holocene at 11,500 a BP /STR 07, KLI 07/. Therefore, the upper 70 m of the model domain show fresh water conditions (c_{rel} = 0). The salt concentration rises linearly from c_{rel} = 0 to 1 within the lower 30 m of the upper aquifer. The aquitard and the lower aquifer show salt water conditions (c_{rel} = 1). Boundary conditions are defined according to different publications /KLI 07, KLI 02, LUD 02/. In the Gorleben Channel, where the lower aquifer has contact to the salt dome, salt can be dissolved. Therefore, the salt concentration at this location is set to c_{rel} = 1 at a length of 4 km (red line in Fig. 8.4). At the southern and the northern part of the model surface, groundwater recharge of 160 mm a^{-1} is defined in form of an inflow of freshwater with a velocity of $5.1 \cdot 10^{-9}$ m s^{-1} with a salt concentration of c_{rel} = 0. In

the center of the surface, a hydrostatic pressure is given. Here, fresh water may infiltrate (c_{rel} = 0) or groundwater of different salinity may be discharged (in- and outflow boundary condition). At the northern boundary, an inflow of groundwater into the lower aquifer is defined with a velocity of $6.3 \cdot 10^{-8}$ m s^{-1} and a salt concentration of c_{rel} = 0. After 11,500 a model time, the present climate state is reached.

8.3.2 Seawater Transgression

The simulation of permafrost conditions starts after 161,500 a of model time (11,500 a until reaching the present state and another 150,000 a of constant conditions). Then the lateral boundaries are closed and a time-dependent pressure boundary condition is defined at the surface representing a transgression for 5,000 a, a sea-level high-stand at 50 m for another 5,000 a, and a regression for 5,000 a. The salt concentration of the seawater is set to c_{rel} = 0.13. At the contact to the salt dome, the boundary condition of c_{rel} = 1 remains.

8.3.3 Permafrost

Starting from the present state, the model is run for another 150,000 a model time. In the model, permafrost regions in the upper aquifer are realized by a reduction of the permeability of $k = 1 \cdot 10^{-12}$ m^2 to $k = 1 \cdot 10^{-20}$ m^2. The permafrost extends over the entire thickness of the upper aquifer of 100 m. A large unfrozen zone with a width of 5 km is located in the area of the Elbe lowlands above the northwestern rim syncline. Another smaller unfrozen zone is located below the River Seege at 450 m to 550 m north of the southern boundary (south of the southern hydraulic window). All other hydrogeological parameters remain unchanged from the present climate state. At the model surface, a Dirichlet condition is defined representing a hydrostatic pressure. Similar to the present climate state, an in- and outflow boundary condition is set for the salt mass flow. For the southern boundary of the lower aquifer, a hydrostatic pressure for the total mass flow and an in- and outflow boundary condition for the salt mass flow are defined. At the northern boundary of the lower aquifer, a maximum inflow of meltwater is assumed which is given in form of a head gradient of 0.1 /KOE 00/. The inflow boundary condition for the northern boundary of the lower aquifer is then defined as time-dependent function, where the inflow rate is interpolated depending on the permafrost thickness, and the salt concentration of the inflowing water is c_{rel} = 0.

8.3.4 Results of the flow simulations

Three different points in time are discussed in detail: The present state (11,500 a model time), the point in time after the time frame of 150,000 a with constant boundary conditions (161,500 a), and the point in time after the seawater trans- and regression (176,500 a).

8.3.4.1 Present state (11,500 a)

The hydrogeological system, as presented by /KLI 07/, /KLI 02/ and /LUD 02/ can be quite well described with this model /FLU 09/. After 11,500 a model time, the present stage is met (Fig. 8.5). At the surface, groundwater recharge takes place leading to low salt conentrations in the upper aquifer. Adjacent to the areas of groundwater recharge at the surface, groundwater is discharged. In the center of the surface, where the hydrostatic pressure is set, the groundwater flow is directed downward. At the hydraulic windows, groundwater from the upper and the lower aquifer can mix. In the vicinity of these areas, numerous changes in the flow direction can be observed. Part of the groundwater is drained to the surface while another part descends into the lower aquifer. In the upper part of the lower aquifer, the groundwater flow is directed from the hydraulic windows to the center of the aquifer. The inflow of formation water from the north into the lower aquifer leads to a decrease of the salt concentration in the lower aquifer. At the contact to the salt dome, salt is dissolved and transported to the rim syncline according to the flow direction. There, the saline groundwater descends due to its higher density. These opposing flow directions in the upper and lower part of the lower aquifer are forming a convection cell within the lower aquifer. The model shows a clear density stratification. Highest salt concentrations up to $c_{rel} = 1$ are found in the northwestern rim syncline and at the contact to the salt dome, while in the upper part of the lower aquifer lower salt concentrations of $c_{rel} = 0.4 – 0.6$ can be observed. The areas of groundwater inflow are characterized by the lowest salt concentrations. Fresh water conditions (< 1 g L^{-1} of total dissolved solids (TDS), classification after /DAV 67/) are found in these areas as well as at the center of the surface. The dominant process for the salt transport is advection.

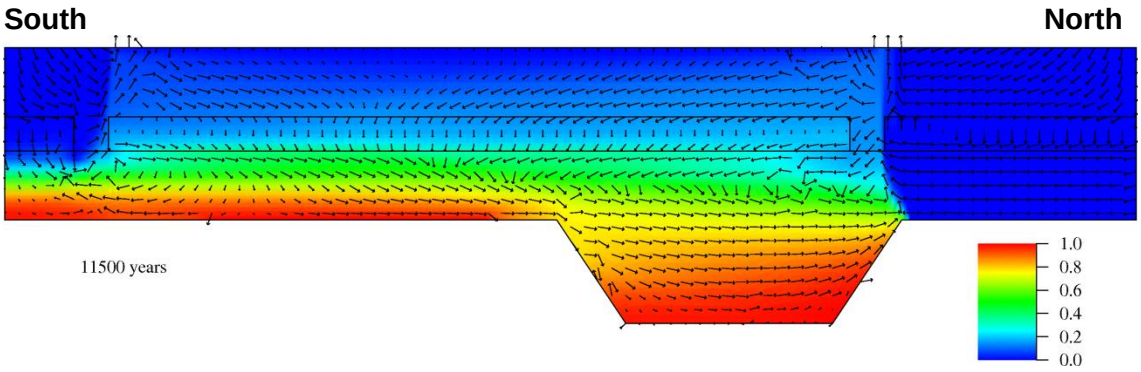

Fig. 8.5 Salt concentration and velocity field for the present state at 11,500 a (length of velocity vectors proportional to velocity)

8.3.4.2 Constant boundary conditions (161,500 a)

The model shows a clear decrease in salt concentrations compared to the present state in particular in the lower aquifer and the northwestern rim syncline (Fig. 8.6). Salt concentrations of c_{rel} = 1.0 only remain at the contact to the salt dome, where salt is constantly dissolved. In the northwestern rim syncline, the salt concentration is reduced to about c_{rel} = 0.4 – 0.6. This reduction results from the inflow of fresh water into the lower aquifer which dilutes the salt water in the rim syncline and transports it up to the surface. The areas of groundwater discharge at the surface are broadened. General flow directions are preserved. The flow velocity is slightly reduced, especially in the upper aquifer. After 160,000 a model time, the salt concentration and the groundwater flow almost meet steady-state conditions. The dominant process for the transport of the salt is, as for the present state, advection due to the high flow velocities.

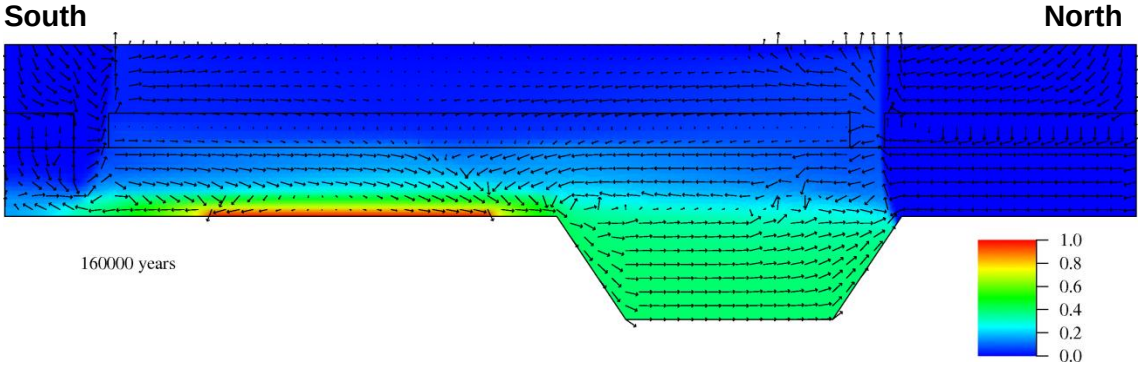

Fig. 8.6 Salt concentration and velocity field for constant boundary conditions at 160,000 a (length of velocity vectors proportional to velocity)

8.3.4.3 Seawater transgression

During the seawater inundation, no inflow of fresh water is defined. Therefore, the advective groundwater flow ceases and convection is the dominant process for the mixing of differently mineralized water and the transport of salt. In the aquitard, where a lower permeability is set, the dominant transport process for the salt is diffusion.

A clear change in the flow field can already be seen shortly after the boundary conditions have changed. In the lower aquifer, the flow directions roughly remain unchanged apart from the missing inflow of fresh water into the lower aquifer. In the southern part the flow is still directed to the north towards the contact to the salt dome and the rim syncline. After the passage of the rim syncline, the groundwater partly flows further in northward direction and then partly flows back to the contact to the salt dome due to the formation of a convection cell above the rim syncline. In the aquitard, the flow velocity decreases due to the missing groundwater recharge. Slight formation of fingering structures occur in the upper aquifer which result from infiltration of seawater with higher salt concentration (c_{rel} = 0.13) into the upper aquifer (Fig. 8.7).

An almost horizontal density stratification of the groundwater occurs with increasing density with depth and a more abrupt increase of salt concentrations within the lower aquifer. The entire upper aquifer shows a salt concentration equal to that of the seawater of c_{rel} = 0.13 after the time of the inundation. Particularly in the upper aquifer, the salt concentration is elevated compared to the salt concentration at 160,000 a.

An inundation time of only a few thousands of years has a clear influence on the salt concentration and the groundwater flow in the upper aquifer and in the aquitard. During this period, the salt concentration and flow directions of the lower aquifer are hardly affected by the changed boundary conditions. Steady-state groundwater flow and salt concentration distributions are not met after an inundation time of 15,000 a.

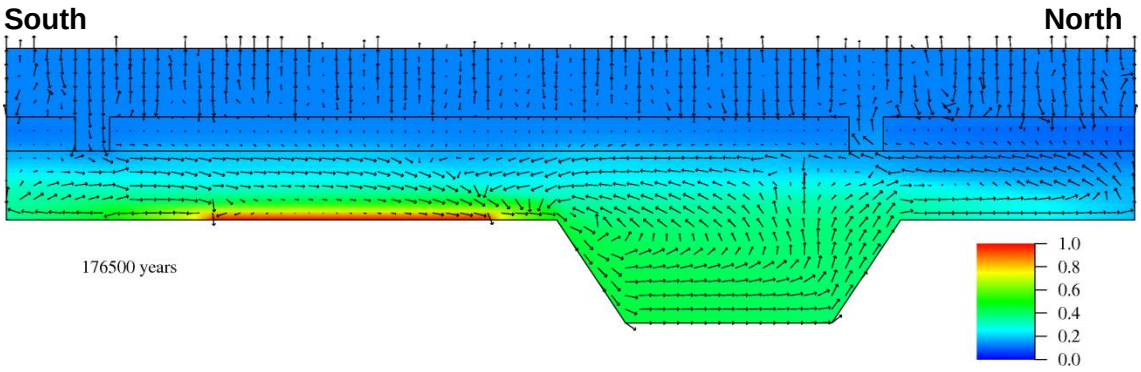

Fig. 8.7 Salt concentration and velocity field for the seawater transgression at 176,500 a (length of velocity vectors proportional to velocity)

8.4 Transport simulations

In the transport simulations, the following singles nuclides as well as decay series are regarded:

- Single nuclides: Cs-135, Se-79, Ni-59, Np-237
- Americium decay series: Am-243, Pu-239, U-235
- Uranium decay series: U-238, U-234, Th-230, Ra-226.

Additionally, in each of the three model simulations, the transport of an inert tracer was regarded in order to be able to compare the transport of the radionuclides, which are subject to radioactive decay and sorption, to the transport of an inert substance.

In the case of an altered evolution of the repository, radionuclides can be released from the near field into the far field, be transported through the overburden, and reach the biosphere. In the model, the radionuclides are released into the model area at the center of the contact to the salt dome in form of a stylized inflow function derived from formerly conducted model simulations for the Gorleben site (Fig. 8.8, after /KEE 05/). For each of the considered radionuclides, the maximum of the respective source term is identified. All of the source terms have their maximum between 1,000 a to 100,000 a after the closure of the repository. In the model simulations, a straightforward approach to simplify these source terms is realized in order to better interpret and compare the results. Thus, the source terms are defined as stylized, constant release rates in the amount of the maximum concentration of the respective radionuclide as determined by /KEE 05/ for a time of $9.9 \cdot 10^4$ a (Fig. 8.9, Tab. 8.2). For the inert tracer, the source term was set to the source terms of Cs-135, U-238 and Am-243, respectively. In this study,

the impact of altering geochemical conditions in the hydrogeologic system due to climatic changes is to be identified. In order to observe these impacts in the entire model domain and to keep the interpretation simple, the inflow of radionuclides is assumed to start at 1,000 a after the present state (12,500 a model time).

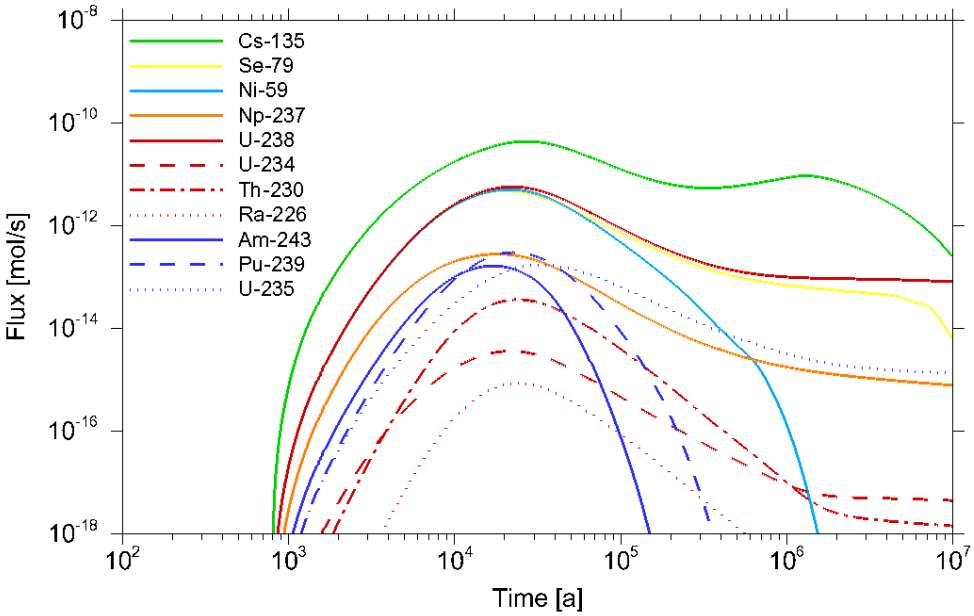

Fig. 8.8 Source terms from the near to the far field for considered radionuclides as determined by /KEE 05/

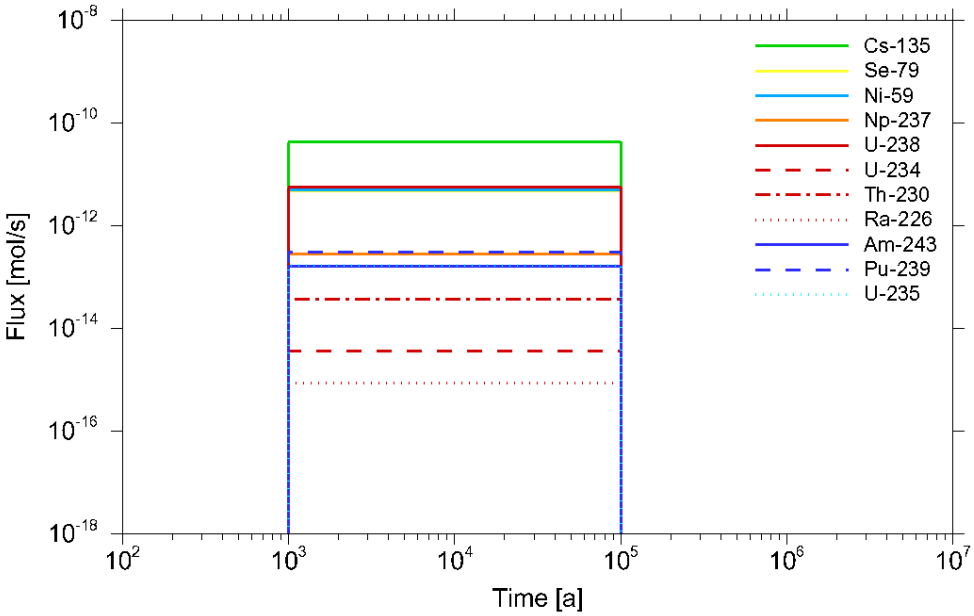

Fig. 8.9 Stylized, constant source terms from the near to the far field for considered radionuclides as applied in the model simulations

Tab. 8.2 Source terms for the considered radionuclides

The asterisk indicates that an inert tracer was modeled with the same source term as the marked radionuclide. Indented radionuclide names indicate the considered daughter nuclides of the radionuclide named above them.

Nuclide	**Flux [mol s^{-1}]**
Cs-135*	$4.35 \cdot 10^{-11}$
Np-237	$2.78 \cdot 10^{-13}$
Se-79	$4.73 \cdot 10^{-12}$
Ni-59	$5.03 \cdot 10^{-12}$
Am-243*	$1.64 \cdot 10^{-13}$
Pu-239	$2.98 \cdot 10^{-13}$
U-235	$1.71 \cdot 10^{-13}$
U-238*	$5.68 \cdot 10^{-12}$
U-234	$3.59 \cdot 10^{-15}$
Th-230	$3.63 \cdot 10^{-14}$
Ra-226	$8.50 \cdot 10^{-16}$

An inflow of radionuclides is only given at the center of the salt dome. For all other boundaries, inflowing water always has a radionuclide concentration c_{rn} of 0 mol m^{-3}, while for an outflow, c_{rn} is set equal to the concentration in the outflowing groundwater (in- and outflow boundary condition). The half-lives of all considered radionuclides are taken from /MAG 06/ and given in Tab. 8.3.

For transport simulations, the environmental parameters have to be quantified for the initial and boundary conditions. /KLI 04/ gives a comprehensive overview of groundwater chemical data for the Gorleben area as described in section 2.4.3.1 and given for the three hydrogeological units in Tab. 2.7. For the transport simulations, only the parameters pH, Ca, and DIC are required (Tab. 8.4). The salt concentration for each time step is provided by d^3f simulations, and r^3t calculates the required ionic strength from the salt concentration as described in section 7.1.4. Based on the environmental parameters and the ionic strength, r^3t selects the according smart K_d-value from the K_d-cloud. The assignment of smart K_d-values is only applied to the aquitard and the upper aquifer, for the lower aquifer, conventional K_d-values are set.

The mineral composition of the hydrogeological units is accounted for during the calculation of the smart K_d-clouds (section 2.3) and does not have to be specified in the r^3t calculations.

Tab. 8.3 Half-lives (HL) /MAG 06/ and K_d-values /SUT 98/ of the regarded radionuclides

Limit between fresh water and saline water is at TDS = 10 g L^{-1}. Indented radionuclide names indicate the considered daughter nuclides of the radionuclide named above them.

Radionuclide	**HL [a]**	**K_d, sand (aquifer) [m^3 kg^{-1}]**		**K_d, silt, clay (aquitard) [m^3 kg^{-1}]**
		Fresh	**Saline**	**Saline**
Cs-135	$2 \cdot 10^6$	0.07	0.002	0.07
Np-237	$2.144 \cdot 10^6$	0.01	0.01	0.3
Se-79	$4.8 \cdot 10^5$	0.001	0.001	0.001
Ni-59	$7.5 \cdot 10^4$	0.02	0.006	0.09
Am-243	$7.37 \cdot 10^3$	0.1	3	20
Pu-239	$2.411 \cdot 10^4$	0.1	0.1	3
U-235	$7.038 \cdot 10^8$	0.002	0.0006	0.02
U-238	$4.47 \cdot 10^9$	0.002	0.0006	0.02
U-234	$2.46 \cdot 10^5$	0.002	0.0006	0.02
Th-230	$7.54 \cdot 10^4$	0.2	0.2	0.2
Ra-226	$1.6 \cdot 10^3$	0.04	0.002	0.04

Tab. 8.4 Initial pH-value and initial concentration of the components Ca and DIC for the three hydrogeological units upper aquifer (UAF), aquitard (AT) and lower aquifer (LAF)

Parameter	Unit	UAF	AT	LAF
pH	[-]	7.5	8.0	7.2
Ca	[mol m^3]	1.21	0.24	22.28
DIC	[mol m^3]	2.70	3.57	4.75

Comparative calculations were conducted neglecting the smart K_d-concept and using constant K_d-values for each hydrogeological unit. The sorption coefficients used here were gained from a study evaluating sediment and groundwater samples from the Gorleben region. Here, the K_d-values were differentiated with respect to the concentration of total dissolved solids in the water. “Saline water” is defined by a TDS content higher than 10 g L^{-1}, “fresh water” shows a TDS content lower than 10 g L^{-1}, hence the limit between fresh and saline water is given by a relative salt concentration of c_{rel} = 0.0375. For every radionuclide the constant K_d-values, which depend on the groundwater salinity and the sediment type, are stated in Tab. 8.3 /SUT 98/.

Since transport calculations are based on transient flow fields, the salt concentration is not constant in time. The assignment of the appropriate conventional K_d-values was performed taking the evolution of the isoline of the salt concentration c_{rel} = 0.0375 and of the flow field into account (Fig. 8.10). For zones with salt concentrations of c_{rel} > 0.0375, the K_d-value for saline groundwater is assumed. This is the case for the lower aquifer and the aquitard for all three points in time. However, mainly in the upper aquifer this cannot always be clearly determined and has to be based on personal judgement. The assignment of the K_d-values then depends on the flow direction. In the beginning of the inflow of radionuclides at 12,500 a model time, the salt concentration in the upper aquifer is mainly above c_{rel} = 0.0375. During the time of the constant boundary conditions, the salt concentration decreases and shows fresh water conditions in almost the entire upper aquifer after 161,500 a model time. After ca. 50,000 a to 60,000 a the isoline meets the upper limit of the aquitard, and after ca. 90,000 a it is in a steady-state (both not depicted). Although the upper aquifer does not show fresh water conditions for the entire time of the constant boundary conditions, the K_d-values are assigned assuming fresh water conditions. This is due to the fact that most of the regarded radionuclides are only reaching the upper aquifer at a later stage of the model simulations, when fresh water conditions in the upper aquifer are dominating. For the

seawater transgression, the K_d-value for the upper aquifer is set for saline groundwater conditions according to the quickly established elevated salt concentration (Fig. 8.10). Tab. 8.5 gives a matrix for the assignment of the conventional K_d-values for the different time frames of the transport simulations.

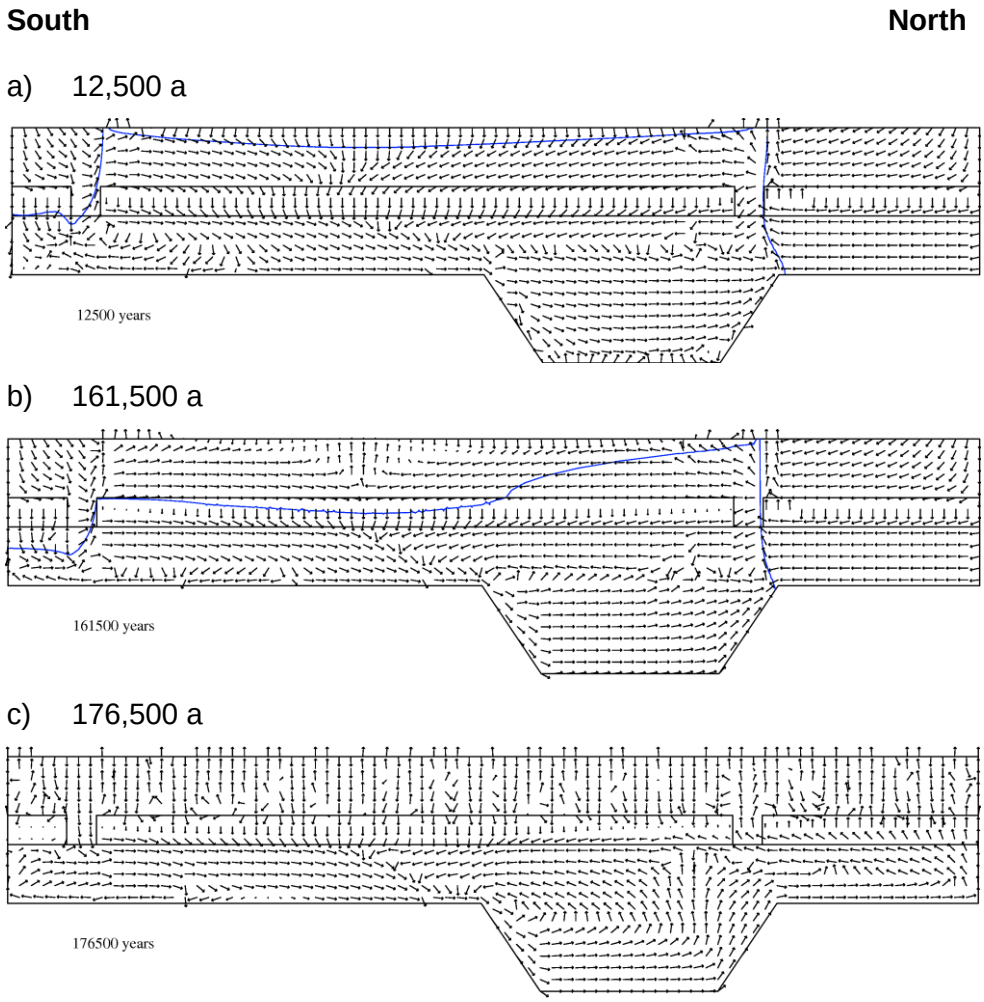

Fig. 8.10 Isolines for c_{rel} = 0.0375 (10 g L^{-1} TDS) and flow fields for different stages of the simulations

Arrows indicate the flow direction. For the seawater inundation, the isoline crel = 0.0375 does not exist.

Tab. 8.5 Matrix for the assignment of conventional K_d-values for the different time frames of the transport simulations and for the three hydrogeological units

	UAF	AT	LAF
Present state	fresh	saline	saline
Constant boundary conditions	fresh	saline	saline
Seawater transgression	saline	saline	saline

8.4.1 Present state

For the present state and the constant boundary conditions, a Dirichlet condition is set for the inflow into the lower aquifer. The inflowing groundwater is assumed to have a chemical composition according to the formation water of the lower aquifer (Tab. 8.4). An in- and outflow boundary condition is stated for the model surface, depending on the flow direction, which was determined in the d³f calculations. The chemical composition of the outflowing water at the surface equals the calculated actual chemical composition of the groundwater. In case of an inflow, the chemical composition is defined equal to the composition of the precipitation water /MAT 94/, which is described in section 2.4.3.3 and given in Tab. 8.6.

Tab. 8.6 pH-value and concentration of the components Ca and DIC for the precipitation water /MAT 94/

Parameter	Unit	Precipitation water
pH	[-]	5.6
Ca	[mol m^3]	0.025
DIC	[mol m^3]	0.002

8.4.2 Seawater Transgression

For the marine transgression, the water composition at the model surface is dependent on the flow direction. An in- and outflow boundary condition is set for the surface with a seawater chemistry according to /LAN 02/, which is described in section 2.4.3.2 and given in Tab. 8.7. For the sea water transgression, the lateral boundaries of the model are defined as impermeable.

Tab. 8.7 pH-value and concentration of the components Ca and DIC for the seawater after /LAN 02/

Parameter	Unit	Seawater
pH	[-]	5.6
Ca	[mol m^3]	0.025
DIC	[mol m^3]	0.002

8.4.3 Permafrost

For the Permafrost state, the in- and outflow boundary conditions at the model surface for the present state apply. At the southern boundary a hydrostatic pressure is defined in the flow simulations. Here, formation water may enter the model area, while for an outfow the chemical composition of the water is calculated by r^3t. From the north, glacial meltwater is flowing into the lower aquifer. The composition of glacial water is derived from the composition of an Antarctic ice core /LEG 88/ (appendix, section A.2) and described in Tab. 2.10. The DIC concentration was taken from /MAT 94/ assuming that the effects of increased solubility in precipitation and decreased atmospheric CO_2 concentration during glacial compensate each other. pH-value and Ca and DIC concentrations considered in model simulations are summarized in Tab. 8.8.

Tab. 8.8 pH-value and concentration of the p Ca and DIC for the glacial meltwater after /LEG 88/ and /MAT 94/

Parameter	Unit	Glacial meltwater
pH	[-]	5.7
Ca	[mol m^3]	0.005
DIC	[mol m^3]	0.002

For the transition between permafrost and the present climate (and vice versa) the boundary condition for the model surface is maintained. The southern boundary of the lower aquifer is impermeable in case it is impermeable in d^3f. An in- and outflow boundary condition is defined in case the boundary is not impermeable in d^3f. A stepwise function is used to define the chemical composition of the inflowing groundwater from the north.

In case the velocity of the inflowing groundwater is

$$v_{in} \leq \frac{v_{in}\left(permafrost\right) - v_{in}\left(present\right)}{10} + v_{in}\left(present\right),$$

the chemical composition of the formation water (Tab. 8.4) is used, while in case

$$v_{in} > \frac{v_{in}\left(permafrost\right) - v_{in}\left(present\right)}{10} + v_{in}\left(present\right),$$

the chemical composition of glacial meltwater is used (Tab. 8.8).

8.4.4 Results of the transport simulations

The results of the transport simulations with the smart K_d-concept comprise the concentration distributions of calcium and DIC as well as the pH-values in the model area. Furthermore, the calcite concentration and the ionic strength are calculated by r^3t. The temporal evolution of these environmental parameters is described in section 8.4.4.1.

The transport of the inert tracer is described in section 8.4.4.2. Transport simulations were summarized to three model runs. Single nuclides were modeled in one model run, while the radionuclides of the americium decay series and of the uranium decay series were each calculated in two separate model runs. Therefore, the calculated smart K_d-values and the radionuclide concentration distributions of each of the respective group of radionuclides are described in separate sections 8.4.4.3 to 8.4.4.5.

Many results of the transport simulations cannot be depicted in this report. Smart K_d-values and radionuclide (and tracer) concentration distributions for the described points in time, which are not depicted in sections 8.4.4.2 to 8.4.4.5, can be found in the appendix (section A.9).

8.4.4.1 Environmental parameters

In the following, the evolution of the Ca and DIC concentration as well as the pH-value as calculated by r^3t are described. Additionally, r^3t stores the calcite concentration in

the model area in form of an integrated calcite concentration, i. e. the given values for one time step are the sum of the calcite concentrations of all time steps. Negative values indicate the calcite concentration is lower than initially defined, positive values indicate the calcite concentration is higher than initially defined. The distribution of the ionic strength is derived from the salt distribution calculated by d^3f according to the conceptual model (section 7.1.4).

The values of the environmental parameters at 0 a (Fig. 8.11) are conform to the initial conditions as described in section 8.4.1. In the first time step the calcite concentration is still 0 mol m^{-3}. The distribution of the ionic strength is consistent with the initial conditions of the relative salt concentration in the d^3f simulations.

South **North**

a) Ca [mol m^{-3}]

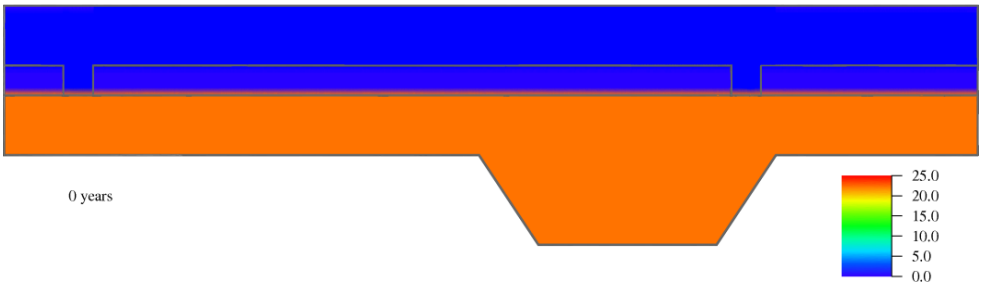

b) DIC [mol m^{-3}]

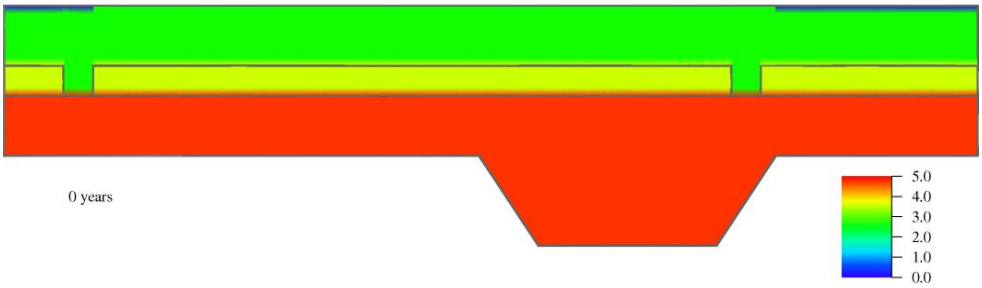

c) pH [-]

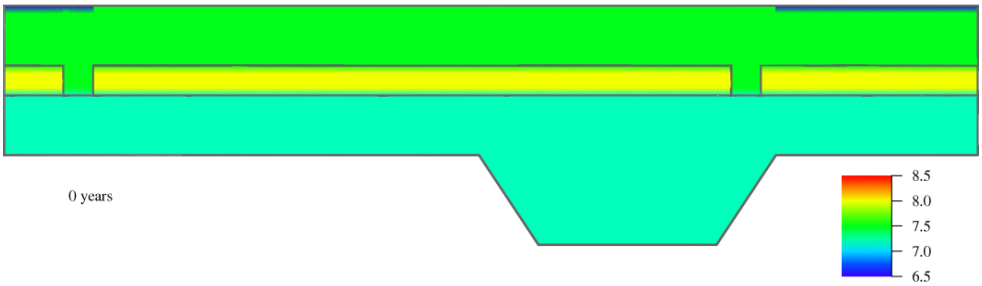

d) Calcite [mol m^{-3}]

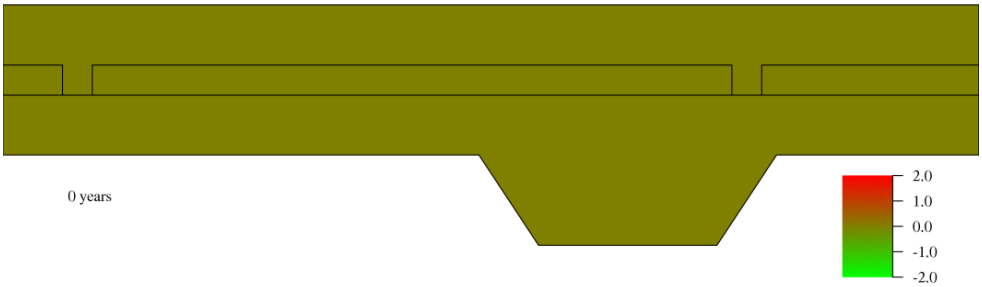

e) Ionic strength [mol L^{-3}]

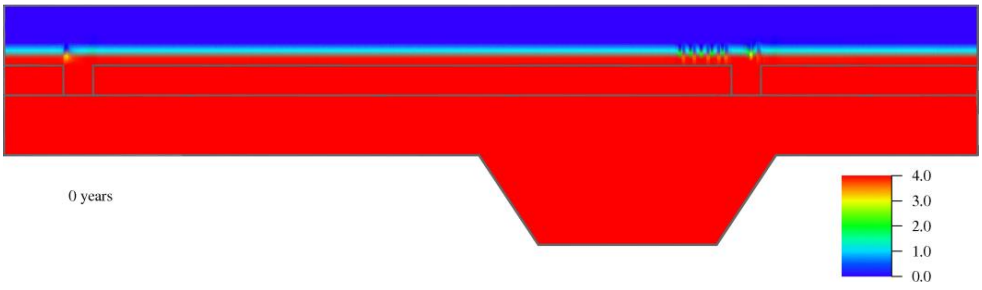

Fig. 8.11 Distribution of environmental parameters at the beginning of the model simulations at 0 a

After 11,500 a model time, the distribution of the environmental parameters has changed according to the flow field, the boundary conditions and the geochemical interactions of the environmental parameters (Fig. 8.12).

In the northern and southern part of the upper aquifer, groundwater recharge takes place. The rainwater has a low pH-value of 5.6, while the formation water in the upper aquifer had a pH-value of 7.5 at the beginning of the simulation. Additionally, the rainwater has a low content of [Ca] = 0.025 mol m^{-3} and [DIC] = 0.002 mol m^{-3} compared to the initial Ca and DIC concentrations in the upper aquifer of [Ca] = 1.21 mol m^{-3} and [DIC] = 2.70 mol m^{-3}. Due to the influence of the lowly mineralized rainwater, the Ca and DIC concentrations in the recharge areas decrease compared to the formation water of the upper aquifer. As a consequence of the low concentration of Ca and DIC, calcite dissolves causing an increase of the pH-value to above the initial value of the formation water. The evolution of the ionic strength follows the trend of the relative salt concentration (section 8.3.4.1) with highest concentrations in the Gorleben Channel and the northwestern rim syncline. In the center of the upper aquifer, the groundwater is still affected by the groundwater recharge in the south and in the north. Calcite is dissolved, the pH-value increases, and the Ca and DIC concentrations are decreased.

The aquitard has a low permeability, and therefore low flow velocities are to be observed here (section 8.3.4.1). Changes of the environmental parameters in the aquitard are mainly caused by diffusion from the lower and the upper aquifer into the aquitard. As a consequence, trends of the changes in the two aquifers can be traced into the aquitard.

The lower aquifer shows different zones of the geochemical environment: The region of formation water inflow north of the northwestern rim syncline, the region of influence of the hydraulic windows with complex groundwater flow, and the region with the high salinities at the contact to the salt dome and in the northwestern rim syncline.

Initially, the formation water is not at equilibrium with calcite. Initial environmental parameters were defined according to /KLI 07/ without equilibrating them prior to the simulations. Therefore, calcite precipitates in the lower aquifer. After 11,500 a, this effect is most evident in the northern part of the lower aquifer, where formation water is entering the model area. As a consequence, the pH-value as well as the Ca and DIC concentrations of the inflowing formation water are decreasing after entering the model area.

In the vicinity of the northern hydraulic window, part of the groundwater flow from the lower aquifer is directed through the hydraulic window to the upper aquifer and from there to the south. At the same time, part of the groundwater from the upper aquifer descends through the hydraulic window, mixes with the groundwater from the lower aquifer and is then directed to the south. Thus in the lower aquifer, the alteration of the geochemical parameters can be traced from the northern part, where the groundwater inflow takes place, to the upper parts of the lower aquifer south of the northern hydraulic window. The complex flow patterns additionally result in a plume with higher Ca and DIC concentrations in the upper aquifer south of the hydraulic window. In this region, the pH-value is lower than given by the initial conditions and is also lower than in the others parts of the upper aquifer. Calcite dissolution and precipitation can only be vaguely distinguished.

The area in the vicinity of the contact to the salt dome and the northwestern rim syncline is characterized by a high salinity i. e. a high ionic strength. It is important to note that the smart K_d-concept is so far not designed for dealing with very high ionic strengths as featured by saturated brines. Therefore, results for the environmental parameters in this area have to be handled with care, since at this stage the Pitzer formalism is not implemented in our model. Ca and DIC concentrations decrease compared to the initial conditions. This is a result of the inflow of recharging rainwater, which mainly enters the lower aquifer through the southern hydraulic window. Relatively high DIC concentrations are remaining in the lower parts of the lower aquifer. At the same time, the mentioned region shows a considerable decrease of the pH-value.

South **North**

a) Ca [mol m^{-3}]

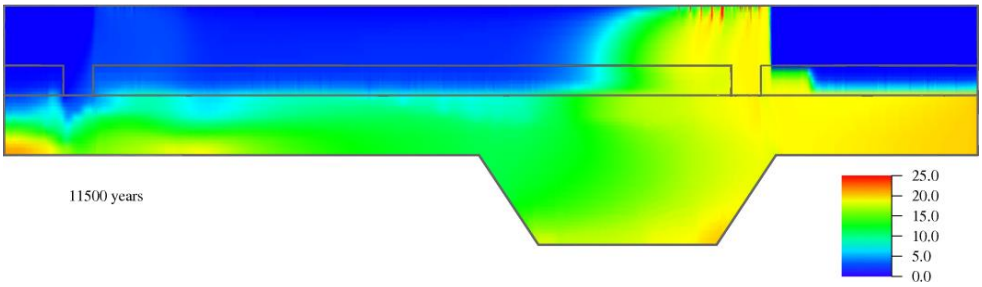

b) DIC [mol m^{-3}]

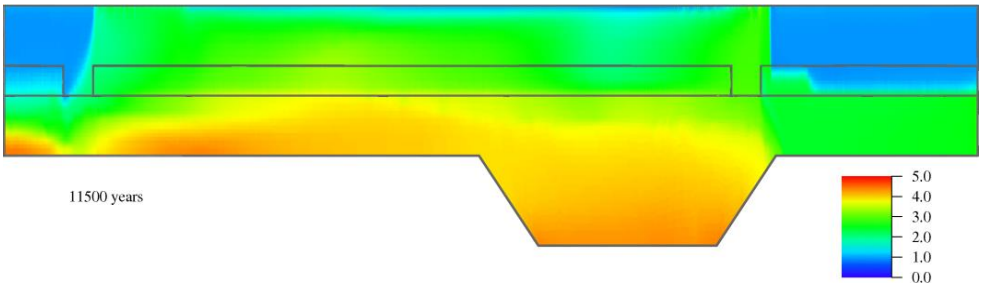

c) pH [-]

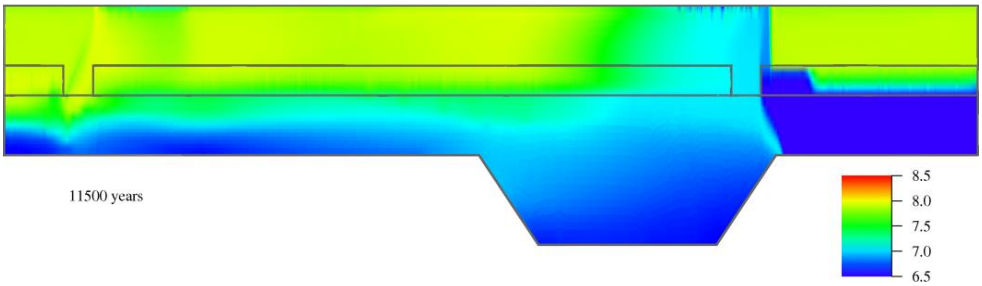

d) Calcite [mol m^{-3}]

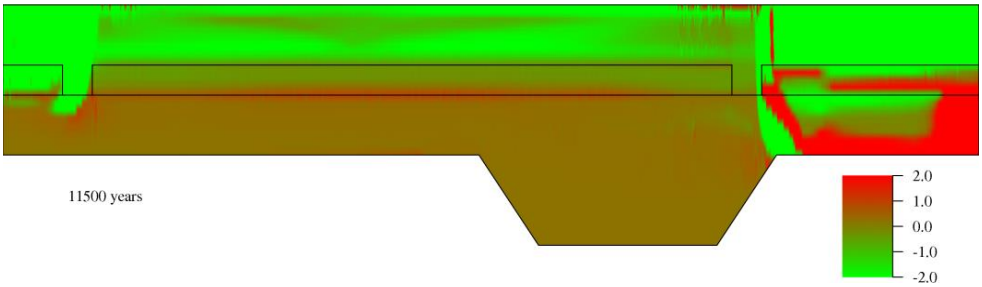

e) Ionic strength [mol L^{-3}]

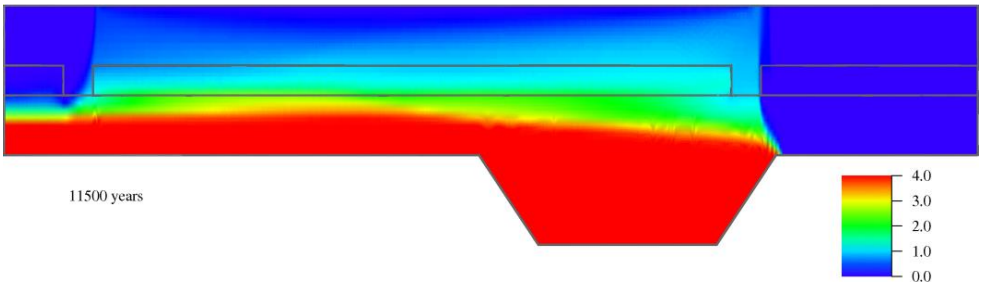

Fig. 8.12 Environmental parameters for the present state at 11,500 a

Following up the evolution of the environmental parameters during the time of constant boundary conditions until just shortly before the marine transgression occurs (Fig. 8.13 at 160,000 a), the trend of the geochemical changes and thus the alteration of the environmental parameters can be traced as described above.

The influence of the ascending groundwater in the upper aquifer becomes more distinct, which can most clearly be observed for the Ca concentration. At the same time, the recharged rainwater maintains its influence on the upper aquifer, which is demonstrated by the decreasing DIC concentration. The pH-value increases in the southern and northernmost region, where there is a strong influence of the recharge, while it decreases in the region of the northern hydraulic window, which is influenced by the ascending formation water from the lower aquifer. In the center of the upper aquifer, the different types of groundwater mix. Calcite is still being dissolved in the upper aquifer.

In parts of the lower aquifer, mainly the southern region, calcite is dissolved, which leads to an increase of the pH-value. At the bottom of the lower aquifer, i. e. at the contact to the salt dome, calcite precipitates. This is the region of high ionic strength. There is no calcite dissolution in the northwestern rim syncline, so the pH-value is lower than in the southern region. The Ca concentration distribution is mainly affected by the groundwater recharge with lowly mineralized rainwater in the south. The DIC concentration strongly decreases in the entire model domain, while the DIC distribution roughly stays the same. In the northern part of the lower aquifer the process observed after 11,500 a continues, i. e. the amount of precipitated calcite is further increased accompanied by lower pH-values and lower Ca and DIC concentrations compared to the formation water.

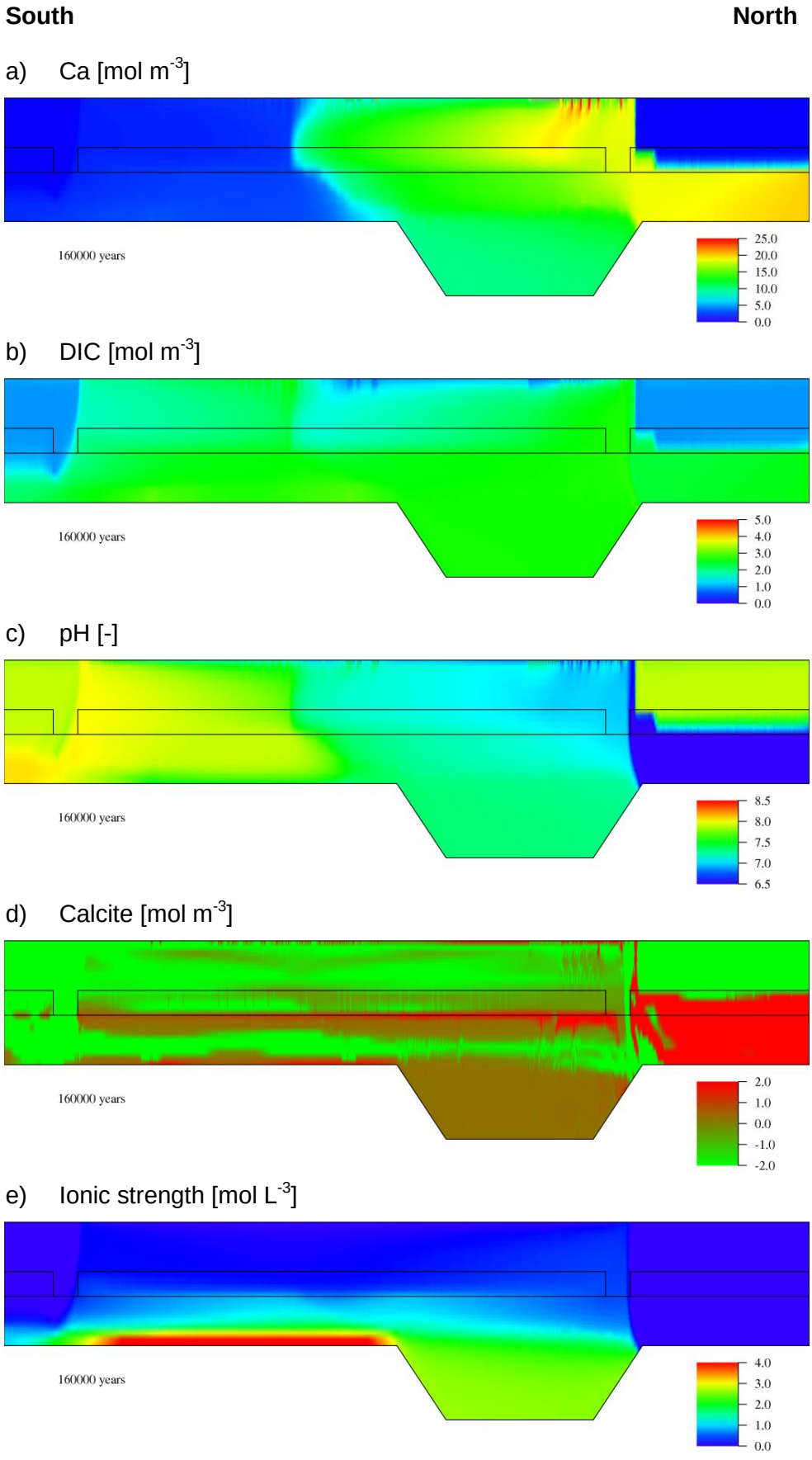

Fig. 8.13 Environmental parameters for constant boundary conditions at 160,000 a

A seawater inundation of 15,000 a drastically influences the distribution and concentration of all environmental parameters (Fig. 8.14). The inflow of formation water into the lower aquifer terminates with the onset of the marine transgression. A horizontal layering of the groundwater can be observed, where the salt concentration and the density are increasing with depth. The advective groundwater flow ceases and diffusion becomes the main transport process for the salt. The upper aquifer is affected by the overlying seawater, resulting in an elevated salt concentration (section 8.3.4.3) and ionic strength. With the onset of the transgression, fingering structures occur in the upper aquifer, which result from infiltration of seawater with higher salt concentration (c_{rel} = 0.13) into the upper aquifer.

The pH-value levels out over the entire model domain but stays below the pH-value of seawater of 8.2. In most of the model domain calcite precipitates, which is leading to the mentioned decrease of the pH-value compared to seawater.

South **North**

a) Ca [mol m^{-3}]

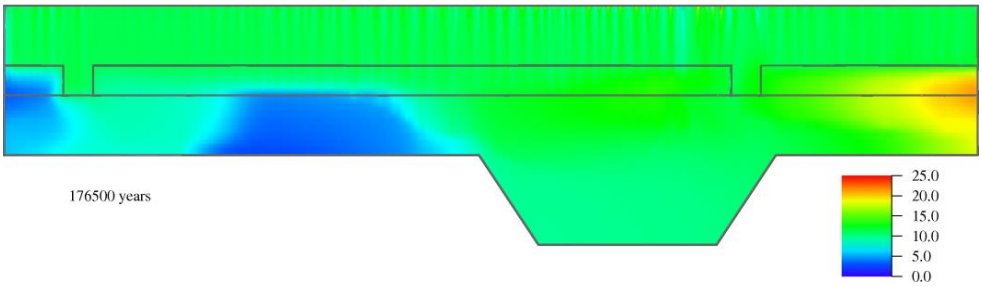

b) DIC [mol m^{-3}]

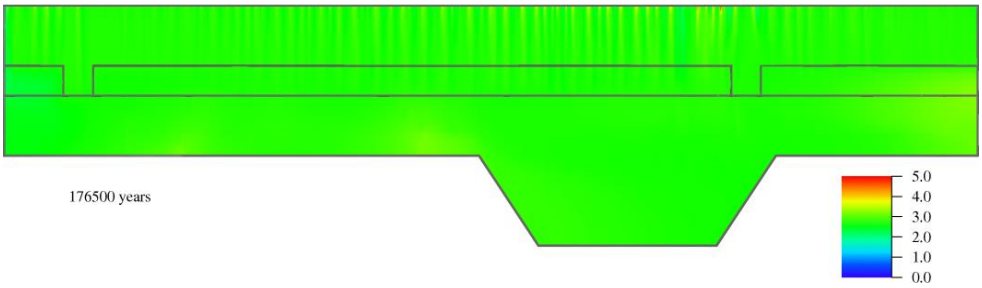

c) pH [-]

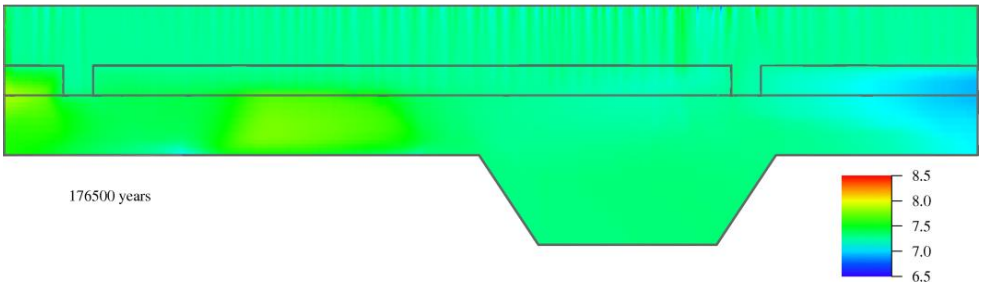

d) Calcite [mol m^{-3}]

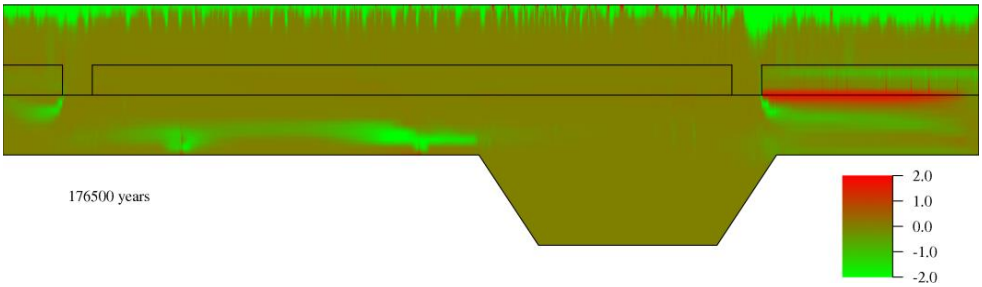

e) Ionic strength [mol L^{-3}]

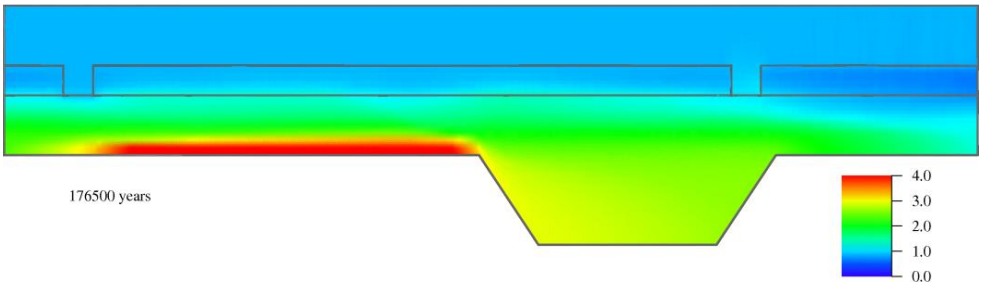

Fig. 8.14 Environmental parameters after the seawater inundation at 176,500 a

8.4.4.2 Transport of an inert tracer

The inert tracer is not subject to sorption or radioactive decay, so transport simulations should feature the widest concentration distributions and the highest concentrations compared to the considered radionuclides. Three transport simulations were conducted with different source terms for the tracer, for which the source terms of Cs-135, Am-243 and U-238 are employed.

The dominant transport process is advection; diffusion is of subordinate importance for the present and constant boundary conditions until 161,500 a model time. Therefore, the tracer is transported from the contact to the salt dome to the north and into the lower aquifer according to the flow direction (Fig. 8.15; figures for the tracer distribution employing the U-238 source term can be found in the appendix, section A.9, Fig. A.22). Then it rises up to the upper aquifer by passing the aquitard in the model center as well as the northern hydraulic window. Smaller tracer concentrations are found south of the contact to the salt dome in both aquifers and the aquitard. Here, diffusion drives the tracer distribution. After 160,000 a model time, the tracer can be observed almost in the entire model domain except from the northernmost area, where inflow boundary conditions are set causing a flow from north to south. The results of the three model simulations only differ slightly in the tracer concentration, the areas of tracer distribution are identical.

During the sea water inundation, the advection ceases and diffusion gains influence. After 176,500 a fingering structures are observed in the upper aquifer. At the end of the model simulations, the tracer distribution extends over the entire model domain with highest concentrations in the central and northern part and lowest concentrations in the southern part of the upper aquifer.

South **North**

a) 160,000 a, source term according to the Am-243 source term, logarithmic scale [mol m^{-3}]

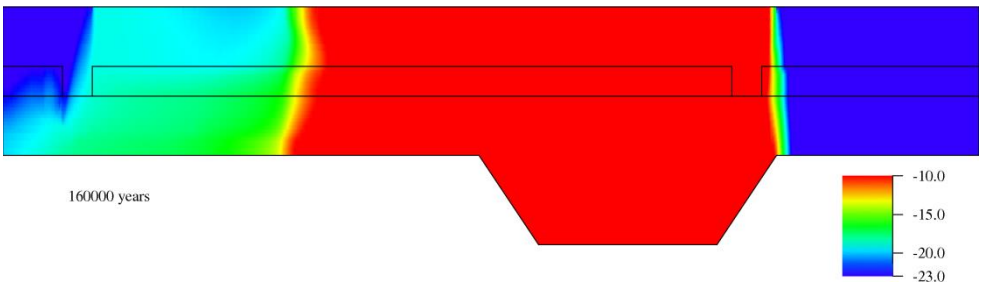

b) 176,500 a, source term according to the Am-243 source term, logarithmic scale [mol m^{-3}]

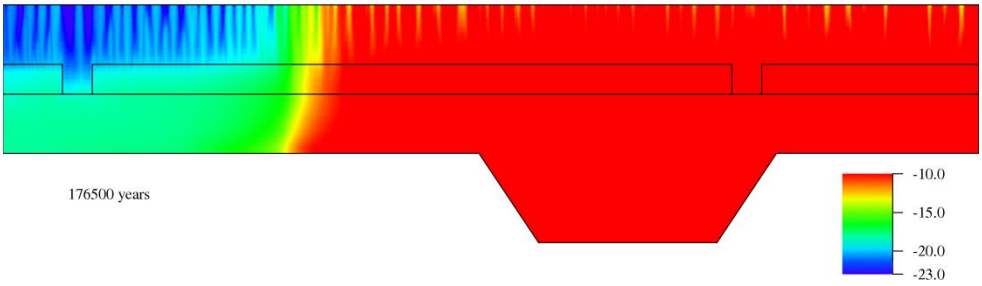

c) 160,000 a, source term according to the Cs-135 source term, logarithmic scale [mol m^{-3}]

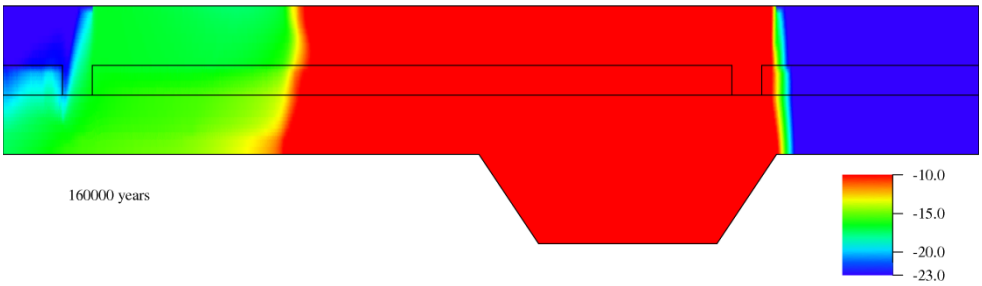

d) 176,500 a, source term according to the Cs-135 source term, logarithmic scale [mol m^{-3}]

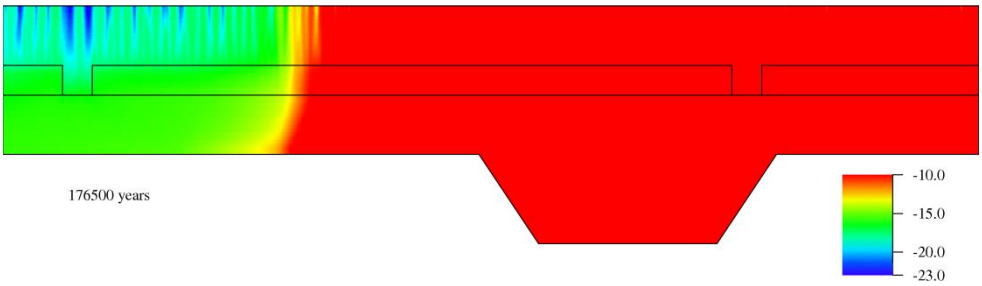

Fig. 8.15 Distribution of the inert tracer after the constant boundary conditions (160,000 a) and after the seawater transgression (176,500 a) for the source terms in accordance to the source term of Am-243 and Cs-135

8.4.4.3 Transport of selected single nuclides

Generally, calculated smart K_d-values are higher than those given by /SUT 98/. Average calculated smart K_d-values are compiled in Tab. 6.5 and Fig. 6.5. The smart K_d-values for Cs-135 are about three orders of magnitude higher than the corresponding conventional K_d-values. For Se-79 the smart K_d-values fit quite well to the conventional K_d-values. For the aquitard they are slightly higher, for the upper aquifer slightly lower than the conventional values. The smart K_d-values of Np-237 and Ni-59 are in the same order of magnitude as the conventional K_d-values. Generally the trends and the development of the environmental parameters can be traced in the evolution of the smart K_d-values. The pH-value is the environmental parameter with the by far strongest influence on the smart K_d-value of the selected single nuclides as discussed in section 6.2. The K_d-values of the cations Cs-135, Ni-59, and Np-237 increase, whereas the K_d-value of Se-79, occurring in anionic form, decrease with increasing pH.

The distribution of radionuclides is in good agreement with the calculated smart K_d-values. Many of the radionuclides are retarded within the aquitard and do not reach the upper aquifer. Se-79 is the only anion of all regarded single nuclides. Therefore its smart K_d-values follow the opposite trend than the smart K_d-values for Cs-135, Np-237 and Ni-59. This leads to an increased transport of Se-79 in areas, where the other single nuclides are increasingly retarded and the other way around.

Exemplarily the transport of Cs-135 and Se-79 is described in detail in the following (sections 8.4.4.3.1 and 8.4.4.3.2), the transport of Np-237 and Ni-59 is only described briefly (section 8.4.4.3.3).

8.4.4.3.1 Cs-135

Calculated smart K_d-values are generally higher than K_d-values given in /SUT 98/. For Cs-135 (Fig. 8.16), the conventional K_d-value is 0.07 $m^3\ kg^{-1}$ for the aquitard under salt water conditions as well as for the upper aquifer with fresh water conditions. The smart K_d-value of Cs-135 after the first time step is calculated to be 84.6 $m^3\ kg^{-1}$ in the aquitard. In the upper aquifer, the smart K_d-value is 4.4 $m^3\ kg^{-1}$ for the lower part and 4.8 $m^3\ kg^{-1}$ for the upper part of the aquifer.

During the first 11,500 a model time the smart K_d-value very well follows the evolution of the environmental parameters, in the upper aquifer as well as in the aquitard. Since

the pH-value is the most important parameter, the smart K_d-value is higher in area with higher pH and vice versa. Additionally the higher content of clay minerals causes the higher smart K_d-values in the aquitard.

For constant boundary conditions, the trends in the evolution of the environmental parameters and the calculated smart K_d-value persist. The smart K_d-value in the aquitard continues to decrease, especially above the northwestern rim syncline, where the pH-value is the lowest. Where groundwater from the lower aquifer rises to the upper aquifer and is transported to the south, lowest smart K_d-values of 1 – 2 $m^3 kg^{-1}$ in the upper aquifer are found. Elevated smart K_d-values of ca. 12 $m^3 kg^{-1}$ can be observed in the areas of groundwater recharge. Highest smart K_d-values of up to ca. 14 $m^3 kg^{-1}$ are found in the vicinity of the southern hydraulic window according to the highest pH-values found there.

Under the influence of the reduced flow velocities and the missing inflow of lowly mineralized water during the seawater transgression, the system equilibrates and shows a more uniform distribution of the environmental parameters and smart K_d-values. In the aquitard, the smart K_d-values range from ca. 55 $m^3 kg^{-1}$ in the southern part to ca. 6 $m^3 kg^{-1}$ in the northern part according to the distribution of the pH-value. In the upper aquifer, the smart K_d-values show an even more uniform distribution with values of 1 – 8 $m^3 kg^{-1}$. Where the pH-value is decreasing, the smart K_d-value descreases as well. The fingering structures, caused by the mixing of higher mineralized seawater at the surface with the lower mineralized groundwater in the upper aquifer, can be observed for all environmental parameters as well as for the smart K_d-values.

The inflow of radionuclides starts at 12,500 a model time. Therefore, no radionuclide concentration is to be observed at the start of the simulations or at the present stage after 11,500 a model time. Therefore, the concentration distributions after 160,000 a and after 176,500 a model time are only discussed here.

After 160,000 a Cs-135 is transported mainly in the lower aquifer (Fig. 8.17). Here, the K_d-value is set to 0.002 $m^3 kg^{-1}$. The transport calculations are based on the same flow simulations, therefore the concentration distribution in the lower aquifer is identical for both implementations. According to the flow direction, Cs-135 is transported from the contact to the salt dome to the north. In the aquitard, the smart K_d-values and the conventional K_d-value differ by three orders of magnitude. Therefore, Cs-135 is retarded strongly and does not reach the upper aquifer when employing the smart K_d-value. In

contrast to that, Cs-135 concentrations can be observed in the upper aquifer up to half of the vertical extent in case the conventional K_d-value is employed.

During the seawater transgression the dominant horizontal flow components in the upper aquifer recede and the vertical components become more important. The upper aquifer shows saline conditions, therefore the conventional K_d-value is strongly reduced to 0.002 $m^3\ kg^{-1}$. Cs-135 is transported through the upper aquifer and reaches the surface vertically above the contact to the salt dome. In contrast to that, the smart K_d-value is still strongly elevated in the aquitard with values between 6 $m^3\ kg^{-1}$ and 55 $m^3\ kg^{-1}$. Cs-135 does not reach the upper part of the aquitard or the upper aquifer during the simulation employing the smart K_d-values.

South **North**

a) Smart K_d-value, logarithmic scale [m^3 kg^{-1}], 0 a

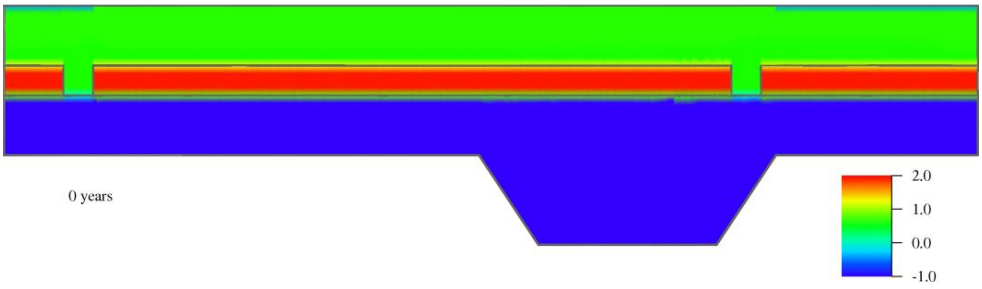

b) Smart K_d-value, logarithmic scale [m^3 kg^{-1}], 11,500 a

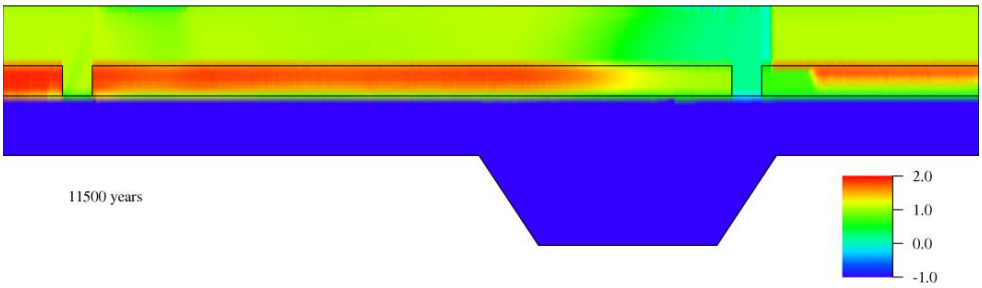

c) Smart K_d-value, logarithmic scale [m^3 kg^{-1}], 160,000 a

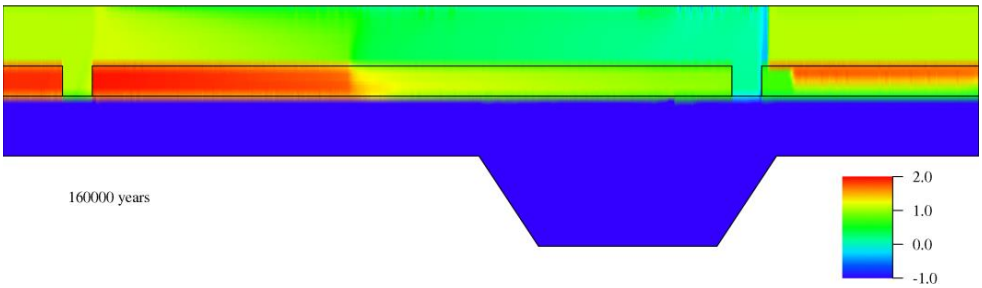

d) Smart K_d-value, logarithmic scale [m^3 kg^{-1}], 176,500 a

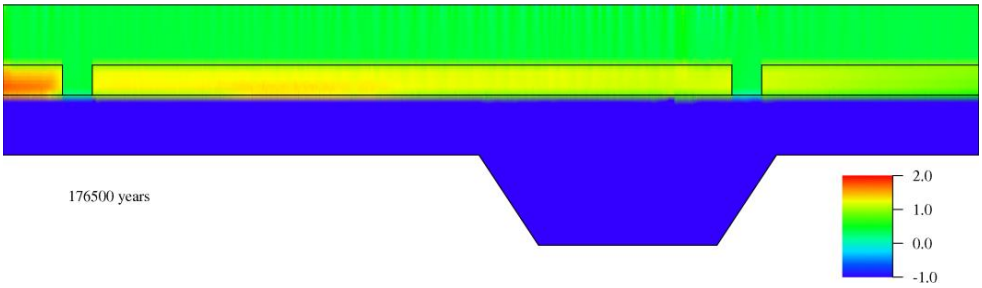

Fig. 8.16 Smart K_d-values for Cs-135 for different points in time

South **North**

a) Conventional K_d-value, 160,000 a, logarithmic scale [mol m^{-3}]

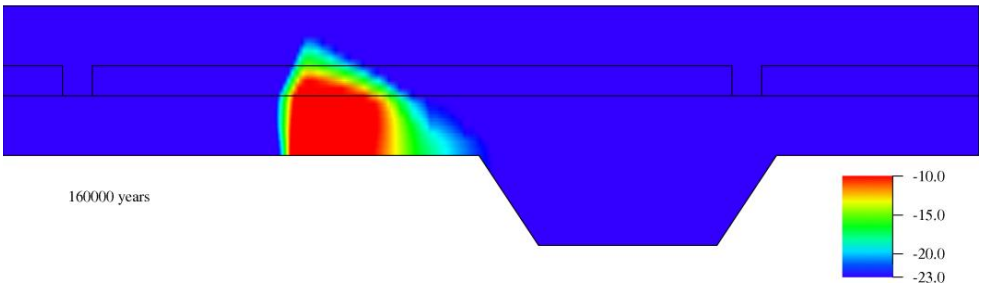

b) Smart K_d-value, 160,000 a, logarithmic scale [mol m^{-3}]

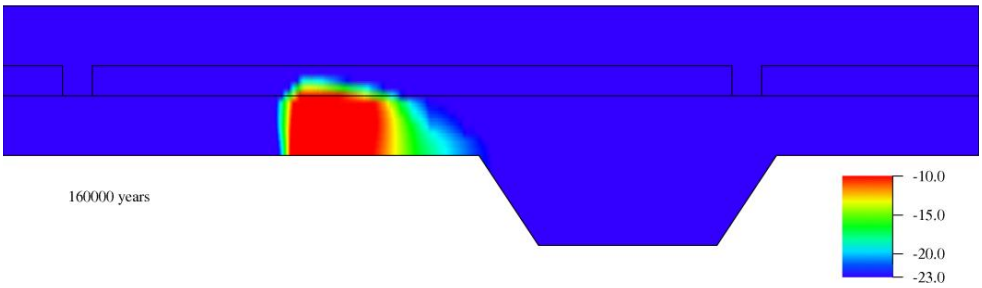

c) Conventional K_d-value, 176,500 a, logarithmic scale [mol m^{-3}]

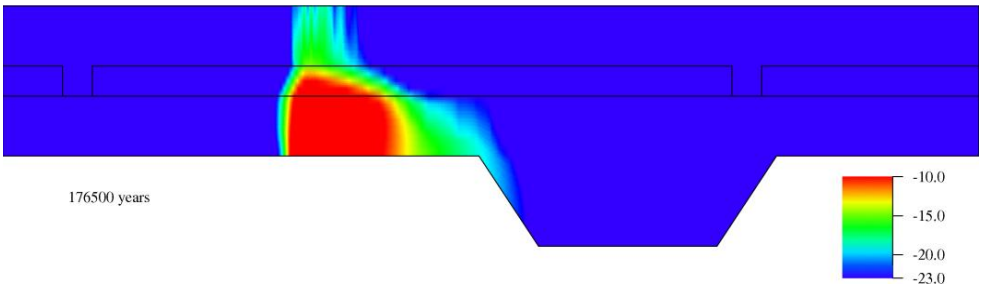

d) Smart K_d-value, 176,500 a, logarithmic scale [mol m^{-3}]

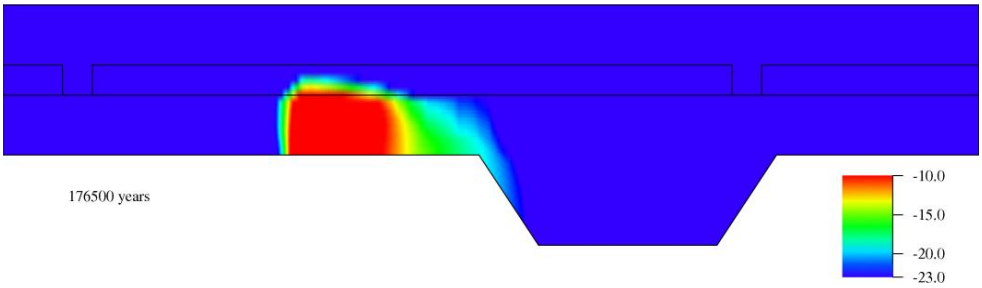

Fig. 8.17 Distribution of Cs-135 after the constant boundary conditions (160,000 a) and after the seawater transgression (176,500 a) employing the conventional K_d-value /SUT 98/ and the smart K_d-value

8.4.4.3.2 Se-79

For Se-79 the pH-value is the most important environmental parameter, too. Since SeO_3^{2-} is the basic species considered here, its trend is opposite to that of the cations, Cs^+, Ni^{2+} and NpO_2^+. Its smart K_d-value decreases with increasing pH-value. For Se-79, the smart K_d-value and the conventional K_d-value are not differing as much as the values for Cs-135 (Fig. 8.18). The conventional K_d-value is $1 \cdot 10^{-3}$ m^3 kg^{-1} in the entire model domain. At the beginning of the simulation, the smart K_d-value is $4 \cdot 10^{-5}$ m^3 kg^{-1} in the aquitard. The lower part of the upper aquifer shows a higher smart Kd-value of $3 \cdot 10^{-3}$ m^3 kg^{-1}, while the upper part shows the highest smart K_d-value of $8 \cdot 10^{-3}$ m^3 kg^{-1}.

In general the smart K_d-value follows the distribution of the pH-value. At the present state (11,500 a), the smart K_d-value is slightly elevated in the aquitard compared to the beginning of the simulation and shows values between $5 \cdot 10^{-5}$ m^3 kg^{-1} in the southern part and $3 \cdot 10^{-2}$ m^3 kg^{-1} in the northern part. In the upper aquifer, the smart K_d-value is reduced compared to the beginning of the simulations. In the areas of groundwater recharge, where the pH is relatively high, the smart K_d-value is ca. $1.7 \cdot 10^{-3}$ m^3 kg^{-1}, while in the central part it is in the range of $6 \cdot 10^{-4} – 1 \cdot 10^{-3}$ m^3 kg^{-1}. Above the northern hydraulic window, highest smart K_d-values in the upper aquifer are observed with maximum values of ca. $1 \cdot 10^{-2}$ m^3 kg^{-1}. Therefore a broader distribution of Se-79 is expected in the aquitard and a higher retention of Se-79 in the upper aquifer compared to the simulations employing the conventional K_d-value by /SUT 98/.

Assuming constant boundary conditions, the influence of the northern hydraulic window on the smart K_d-value in the upper aquifer increases. Where the groundwater from the lower aquifer ascends, mixes with water from the upper aquifer and flows southward, the smart K_d-value rises, due to decreased pH-values there. The central part of the upper aquifer now shows smart K_d-values of $1 \cdot 10^{-2}$ m^3 kg^{-1}. Within a small range above the northern hydraulic window, smart K_d-values of up to $1 \cdot 10^{-1}$ m^3 kg^{-1} are reached. The smart K_d-values within the aquitard are only sparsely altered.

The overlying seawater has a balancing effect on the smart K_d-values in the upper aquifer and the aquitard. While the smart K_d-value of Cs-135 decreases in the aquitard after a seawater transgression, the smart K_d-value of Se-79 rises, again caused by a decrease of pH. In the upper aquifer, a broad distribution of a smart K_d-value of ca. $6 \cdot 10^{-3}$ m^3 kg^{-1} can be observed for Se-79. Maximum smart K_d-values of ca. $1 \cdot 10^{-2}$ m^3 kg^{-1} are reached in the fingering structures.

Se-79 generally shows a lower K_d-value (both for the conventional K_d-value and the smart K_d-value) than Cs-135. Therefore after 160,000 a model time, a wider distribution of Se-79 can be observed (Fig. 8.19). Se-79 is transported into the northwestern rim syncline and even reaches the model surface approximately vertically above the salt dome for both K_d-implementations. Resulting from the lower smart K_d-values in the aquitard compared to the conventional K_d-values, Se-79 is less retarded in the aquitard when employing the smart K_d-concept. Therefore a larger amount of Se-79 reaches the upper aquifer. In the upper aquifer the smart K_d-value is lower than the conventional K_d-value south of the location of the radionuclide inflow and higher in the area north of the inflow location. The general groundwater flow in the area, where Se-79 enters the upper aquifer, is directed to the north. Therefore, a wider distribution of Se-79 is observed for the conventional K_d-value after 160,000 a model time. In contrast to that, higher concentrations of Se-79 are observed for the smart K_d-value. Due to the higher smart K_d-values, the distribution of Se-79 is spatially limited and Se-79 accumulates. This would result in an elevated radiation exposure at the surface although the retention is elevated.

The seawater transgression does not have an explicit influence on the Se-79 distribution in the model domain. Se-79 is transported further through the northwestern rim syncline and through the aquitard to the north. This applies for the conventional K_d-value as well as for the smart K_d-value. Only in the upper aquifer, a broader distribution of Se-79 can be observed for the conventional K_d-value due to its broader distribution at the beginning of the seawater transgression. Additionally the smart K_d-value is considerably elevated leading to a smaller spatial distribution and hence higher concentration of Se-79.

South **North**

a) Smart K_d-value, logarithmic scale [m^3 kg^{-1}], 0 a

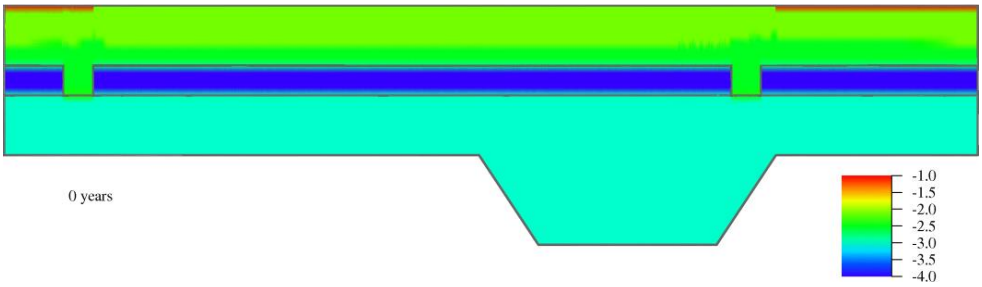

b) Smart K_d-value, logarithmic scale [m^3 kg^{-1}], 11,500 a

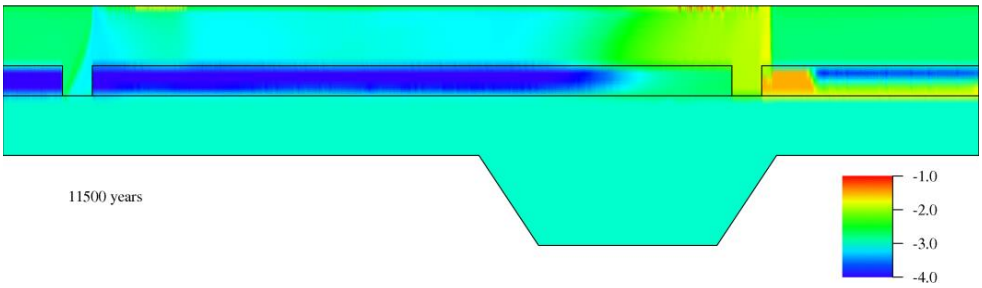

c) Smart K_d-value, logarithmic scale [m^3 kg^{-1}], 160,000 a

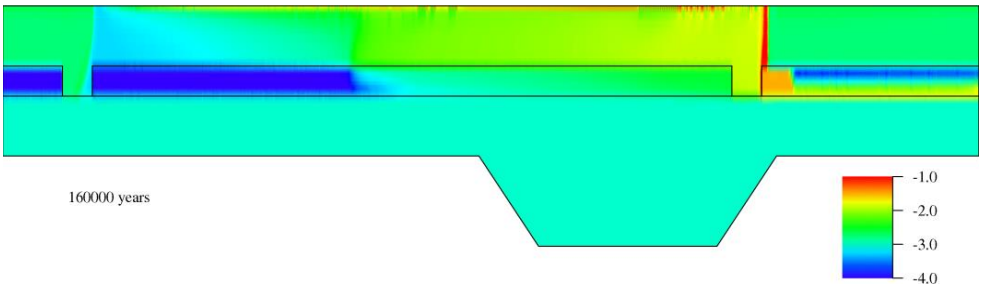

d) Smart K_d-value, logarithmic scale [m kg^{-1}], 176,500 a

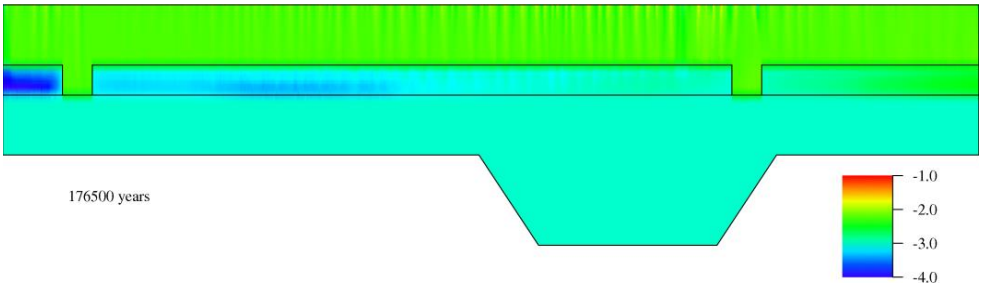

Fig. 8.18 Smart K_d-values for Se-79 for different points in time

South **North**

a) Conventional K_d-value, 160,000 a, logarithmic scale [mol m^{-3}]

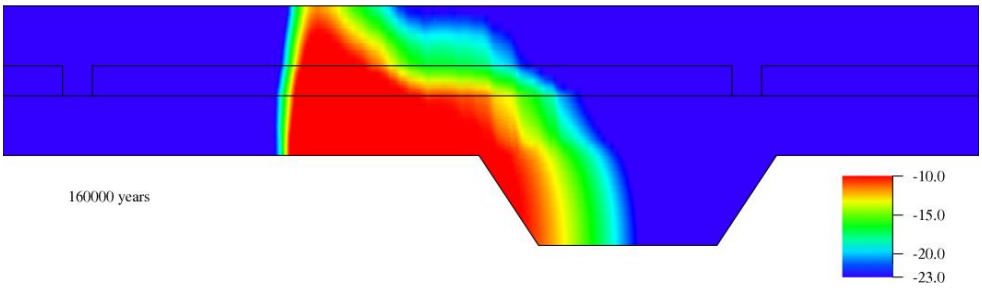

b) Smart K_d-value, 160,000 a, logarithmic scale [mol m^{-3}]

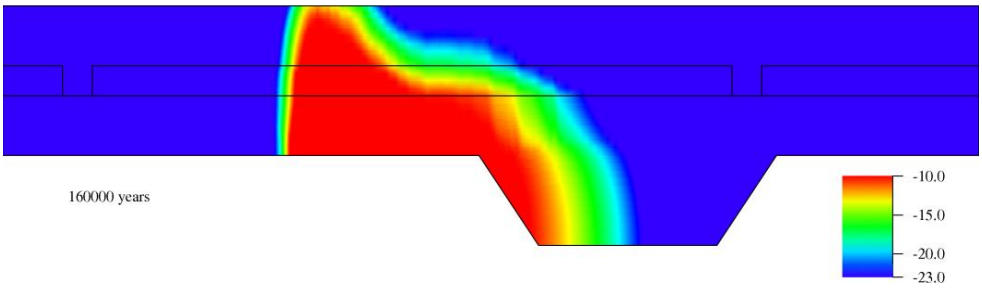

c) Conventional K_d-value, 176,500 a, logarithmic scale [mol m^{-3}]

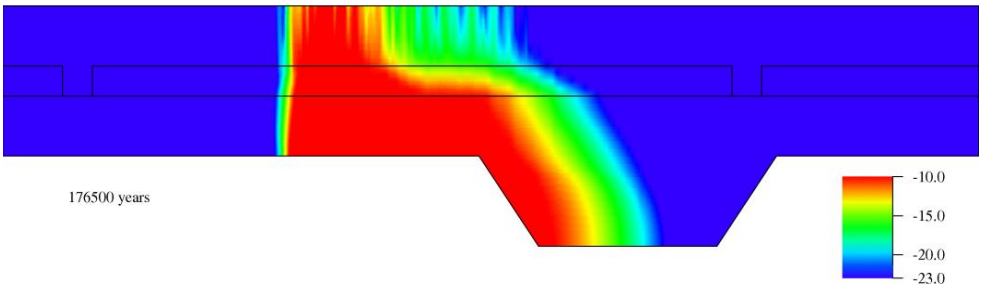

d) Smart K_d-value, 176,500 a, logarithmic scale [mol m^{-3}]

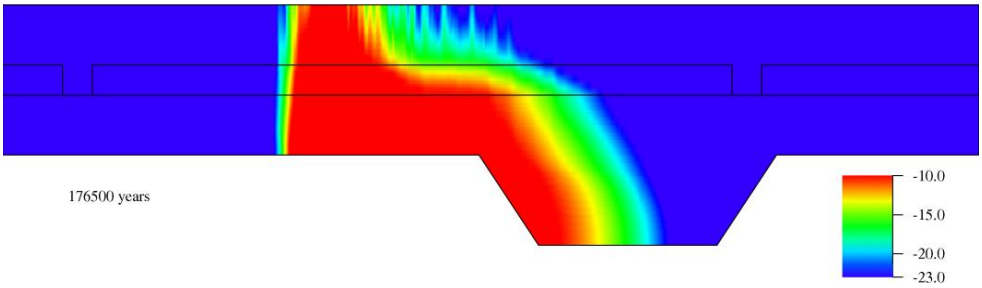

Fig. 8.19 Distribution of Se-79 after the constant boundary conditions (160,000 a) and after the seawater transgression (176,500 a) employing the conventional K_d-value /SUT 98/ and the smart K_d-value

8.4.4.3.3 Np-237 and Ni-59

The smart K_d-values for Np-237 and Ni-59 are generally in in the same order of magnitude as those given by /SUT 98/. For both the trend in the spatial and temporal development of the smart K_d-value (appendix, Fig. A.23) is comparable to that of Cs-135, since both elements have increasing smart K_d-values with increasing pH-values. For the pentavalent Np-237 the conventional K_d-value in the lower aquifer is $1 \cdot 10^{-2}$ m^3 kg^{-1}, therefore it is strongly retarded in the lower aquifer and only reaches the aquitard after 160,000 a. There the conventional K_d-value by /SUT 98/ is $3 \cdot 10^{-1}$ m^3 kg^{-1}, while the smart K_d-value is in the range of 0.2 – 3 m^3 kg^{-1}. After the seawater transgression Np-237 has still not reached the upper aquifer in either of the simulations (appendix, Fig. A.24).

For Ni-59, the smart K_d-values are in the same range as those of Np-237, thus the distribution of Ni-59 and Np-237 is very similar after each regarded point in time. Employing the smart K_d-concept, Ni-59 does not reach the upper aquifer. Setting a conventional K_d-value a small Ni-59 distribution can be found in the upper aquifer (appendix, Fig. A.26). Ni-59 does not reach the model surface after 176,500 a model time.

8.4.4.4 Transport of the radionuclides of the americium decay series

For all considered radionuclides of the Am-243 decay series, a separate input function was defined (section 8.4). Pu-239 and U-235 are therefore not only generated by radioactive decay, but are released into the model area as well. For these simulations the focus is on the transport of U-235 (section 8.4.4.4.3). Am-243 (section 8.4.4.4.1) and Pu-239 (section 8.4.4.4.2) feature high smart K_d-values, so the transport is restricted to the lower aquifer. The smart K_d-values and transport of these two radionuclides is only evaluated briefly, the corresponding figures can be found in the appendix (Fig. A.27 to Fig. A.30). In general all three radionuclides are in a different way affected by the environmental parameters. Am-243 follows the trend of Cs-135, Ni-59 and Np-237, i. e. the smart K_d-values are increasing with increasing pH. For Pu-239 the DIC concentration is the dominant environmental parameter but pH also plays an important role. With an increase in DIC smart K_d-values decrease due to the formation of mobile carbonate complexes. For uranium the major effect in the upper aquifer and aquitard is a decrease of the smart K_d-values with increasing pH. The sorption plateau is around a

pH-value of 6 with decreasing smart K_d-values at higher pH, caused by enhanced formation of carbonato and calcium-carbonato complexes.

8.4.4.4.1 Am-243

For Am-243 all the observed effects described in the following can be explained by the dependence of the smart K_d-value on the pH-value. At the beginning of the simulation, the smart K_d-value for Am-243 is ca. $2 \cdot 10^4$ m^3 kg^{-1} for the aquitard, 2 m^3 kg^{-1} in the upper part of the upper aquifer and 1.8 m^3 kg^{-1} in the lower part of the upper aquifer (appendix, Fig. A.27). The conventional K_d-value is 20 m^3 kg^{-1} for the aquitard and 0.1 m^3 kg^{-1} for the upper aquifer. The smart K_d-values are in good agreement with the pH-value. Until reaching the present state, the smart K_d-value in the aquitard stays in the range of ca. $2 \cdot 10^4$ m^3 kg^{-1}, while in the upper aquifer the influence of infiltrating rainwater becomes visible. In the southern and northern part of the upper aquifer, the smart K_d-value is ca. 20 m^3 kg^{-1}, while in the central part it is between 0 – 10 m^3 kg^{-1}. During the evolution with constant boundary conditions, the smart K_d-value even rises and reaches values of up to ca. $9 \cdot 10^4$ m^3 kg^{-1} in the southern part and of ca. $3 \cdot 10^4$ – $5 \cdot 10^4$ m^3 kg^{-1} in the northern part. Close to the northern hydraulic window, the smart K_d-value decreases to ca. $2 \cdot 10^3$ m^3 kg^{-1}. In the upper aquifer, the upflowing groundwater from the lower aquifer leads to a further decrease of the smart K_d-value in the central part of the aquifer. After the seawater transgression, the smart K_d-value in the upper aquifer is roughly between 0.5 – 2 m^3 kg^{-1}, showing higher values in the salt water fingering structures with higher pH-values and lower values in the areas with a lower ionic strength and lower pH-values.

Conventional K_d-values were set for the lower aquifer for both simulations. The K_d-value is 3 m^3 kg^{-1}. Am-243 is sorbed to the sediment within the lower aquifer and does not reach the aquitard until the end of the model simulations. Therefore the results for the two implementations employing either the conventional or the smart K_d-value are identical (appendix, Fig. A.28).

8.4.4.4.2 Pu-239

For Pu-239 as well the smart K_d-values are in good agreement with the evolution of the DIC concentration, which is also correlated to the pH-value (appendix, Fig. A.29). The smart K_d-value stays in the range of 0 – 5 m^3 kg^{-1} in the upper aquifer, while in the aqui-

tard it rises during the constant boundary conditions. In the vicinity of the northern hydraulic window, it even reaches ca. 100 $m^3 kg^{-1}$. During the seawater inundation it descends to ca. 10 – 15 $m^3 kg^{-1}$ in the aquitard. In the upper aquifer the smart K_d-value is 1 – 2 $m^3 kg^{-1}$. Likewise Am-243, Pu-239 is strongly retarded within the lower aquifer and only reaches the lower border of the aquitard within the model time (appendix, Fig. A.30).

8.4.4.4.3 U-235

At the start of the simulation, the smart K_d-value of U-235 is $8 \cdot 10^{-2}$ $m^3 kg^{-1}$ in the aquitard, $2 \cdot 10^{-3}$ $m^3 kg^{-1}$ in the lower part of the upper aquifer and $1 \cdot 10^{-3}$ $m^3 kg^{-1}$ in the upper part of the upper aquifer. As discussed above the smart K_d-value of U-235 is negatively correlated with the pH-value. Where low pH-values occur at the start of the simulation, e. g. in the areas of groundwater recharge, higher smart K_d-values are calculated (Fig. 8.20). In the same way the increased smart K_d-values at the top and the bottom of the aquitard correspond negatively to the lower pH-value.

This effect becomes even more obvious after the simulation of the constant boundary conditions. While the smart K_d-value is in the range of $1 \cdot 10^{-5}$ – $1 \cdot 10^{-3}$ $m^3 kg^{-1}$ in the upper aquifer for the present state, it rises to $1 \cdot 10^{-5}$ – $1 \cdot 10^{-2}$ $m^3 kg^{-1}$ for the constant boundary conditions. The smart K_d-value for the aquitard rises from the south to the north and shows values from ca. 1 $m^3 kg^{-1}$ to ca. 250 $m^3 kg^{-1}$. The ascending groundwater from the lower aquifer has a lower pH-value than the rest of the upper aquifer causing elevated smart K_d-values for U-235.

After the seawater transgression, the smart K_d-value is harmonized in the upper aquifer and the fingering structures are the only areas, where the smart K_d-value is elevated, again with higher values for lower pH-values and vice versa.

Most of the U-235 is transported from the contact to the salt dome to the north according to the flow direction (Fig. 8.21). North of the contact to the salt dome, the higher saline groundwater sinks down into the northwestern rim syncline, thus U-235 concentrations can be found here. The U-235 distribution in the lower aquifer is identical in both simulations. Compared to Am-243 and Pu-239, the K_d-value of U-235 is very low in the lower aquifer ($6 \cdot 10^{-4}$ $m^3 kg^{-1}$). Therefore, the U-235 distribution is the highest in this model run. The conventional K_d-value in the aquitard and the upper aquifer is a few or-

ders of magnitude smaller than the smart K_d-values. After 160,000 a U-235 has reached the model surface when employing the conventional K_d-value, but it only reaches the model surface during the seawater transgression when employing the smart K_d-value. A much wider spatial distribution of U-235 can be observed in the aquitard and the upper aquifer for the implementations of the conventional K_d-value.

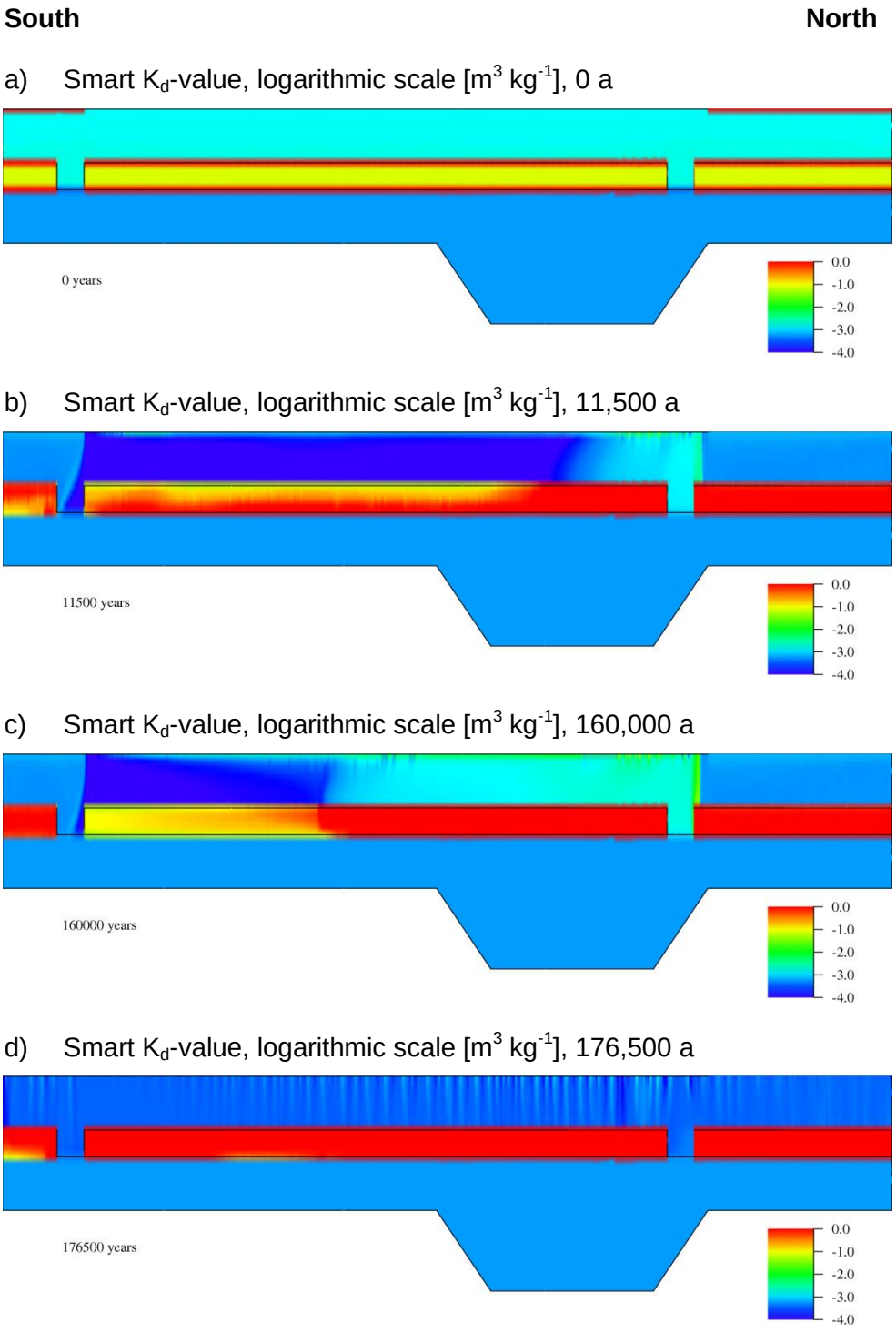

Fig. 8.20 Smart K_d-values for U-235 for different points in time

South **North**

a) Conventional K_d-value, 160,000 a, logarithmic scale [mol m^{-3}]

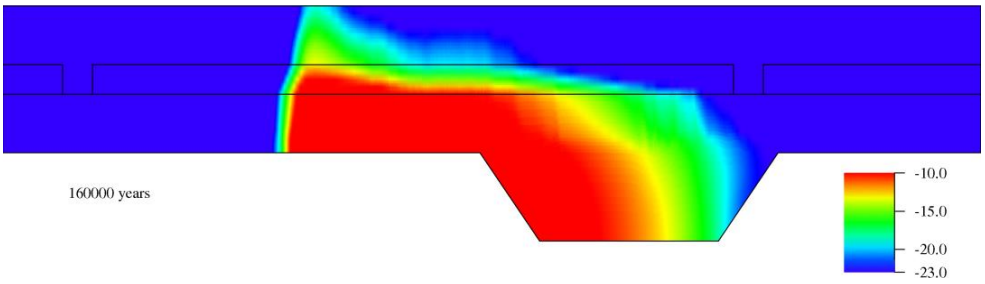

b) Smart K_d-value, 160,000 a, logarithmic scale [mol m^{-3}]

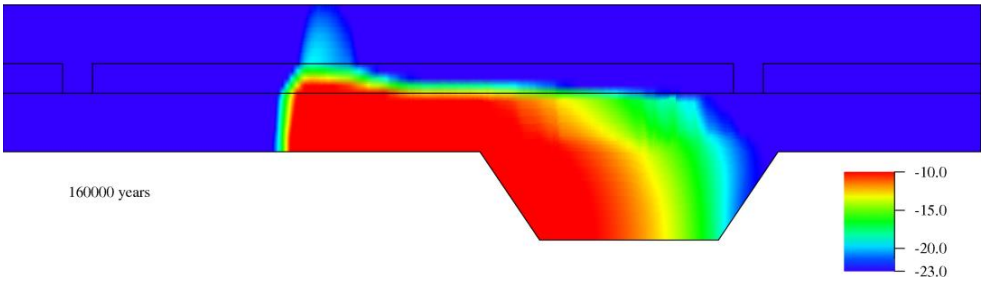

c) Conventional K_d-value, 176,500 a, logarithmic scale [mol m^{-3}]

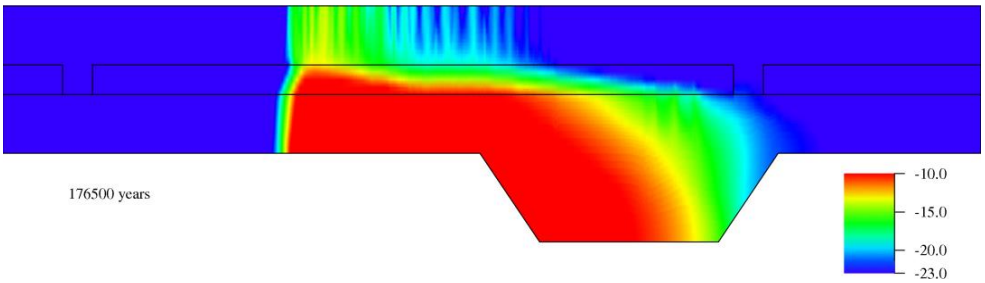

d) Smart K_d-value, 176,500 a, logarithmic scale [mol m^{-3}]

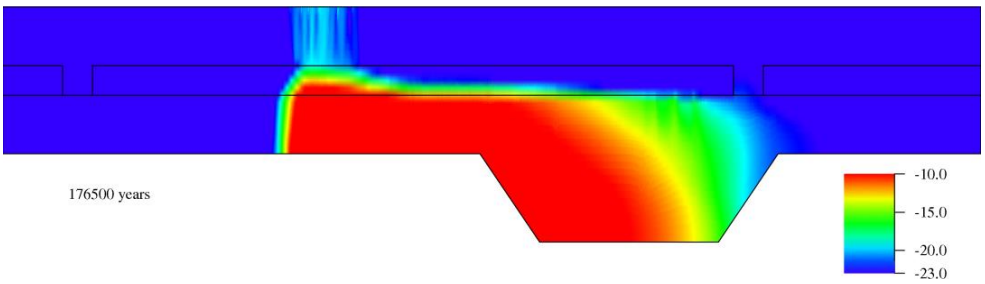

Fig. 8.21 Distribution of U-235 after the constant boundary conditions (160,000 a) and after the seawater transgression (176,500 a) employing the conventional K_d-value /SUT 98/ and the smart K_d-value

8.4.4.5 Transport of the radionuclides of the uranium decay series

Uranium, which is assumed to exist in the hexavalent state, shows the lowest conventional K_d-values and smart K_d-values, therefore highest radionuclide distributions can be found for all radionuclides of the uranium decay series. Since Th-230 is one of the considered radionuclides, for which the DIC is the most important environmental parameter, results for Th-230 will be discussed in detail in this chapter. As for Pu-239 its pH-value decreases with increasing DIC content. The smart K_d-values of uranium and Ra-226 are predominantly dependent on the pH-value.

8.4.4.5.1 U-234 and U-238

Smart K_d-values for uranium are discussed in section 8.4.4.4.3 and depicted in Fig. 8.20. Due to the very low K_d-values in the lower aquifer, uranium is transported to the north and into the northwestern rim syncline according to the flow direction (appendix, Fig. A.31). After 160,000 a uranium has reached the model surface for both the conventional K_d-value and the smart K_d-value. U-234 shows a lower concentration at the surface than U-238 due to the smaller source term (appendix, Fig. A.32). The smart K_d-value of U-234 is higher than the conventional K_d-value in the aquitard. Thus, U-234 is mainly retarded in the aquitard and only very low concentrations of U-234 can be observed in the upper aquifer. In some parts of the upper aquifer, the smart K_d-value is smaller than the conventional K_d-value. Here, the transport of uranium should be facilitated due to the reduced sorption. However this does not apply, because a smaller amount of U-238 and U-234 is released from the aquitard to the upper aquifer in the first place. Therefore smaller uranium concentrations are observed in the upper aquifer employing the smart K_d-value. After 176,500 a U-238 and U-234 show the largest concentration distribution at the surface of all the considered radionuclides except for Se-79.

8.4.4.5.2 Th-230

The smart K_d-value of Th-230 is not primarily dependent on the pH-value but on the DIC concentration (section 6.2). The development of the smart K_d-value is negatively correlated to the development of the DIC concentration, because mobile carbonato complexes are formed at the pH conditions considered here resulting in a reduction of the smart K_d-values (Fig. 8.11 to Fig. 8.14). For example in the area of the upper aqui-

fer, where low saline groundwater from the lower aquifer rises through the northern hydraulic window, the DIC concentration is elevated and the smart K_d-value of Th-230 is reduced (Fig. 8.22). Highest smart K_d-values can be observed in the northern and southern part of the aquitard of up to ca. 10^2 m^3 kg^{-1}. During the seawater transgression, the DIC concentration in the model area levels out. At the same time the smart K_d-value of Th-230 harmonizes and shows a value of 10 – 15 m^3 kg^{-1} in the aquitard and of ca. 1 m^3 kg^{-1} in the upper aquifer. The conventional K_d-value is 0.2 m^3 kg^{-1} for all formations. After 160,000 a there are only slight differences in the distribution of Th-230 for the different K_d-implementations (Fig. 8.23).

South **North**

a) Smart K_d-value, logarithmic scale [m^3 kg^{-1}], 0 a

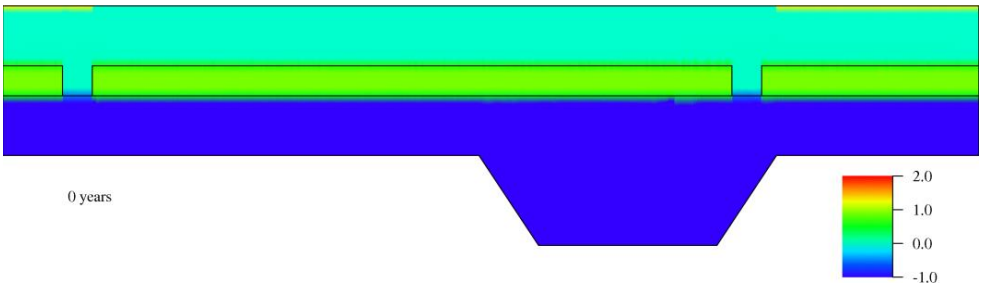

b) Smart K_d-value, logarithmic scale [m^3 kg^{-1}], 11,500 a

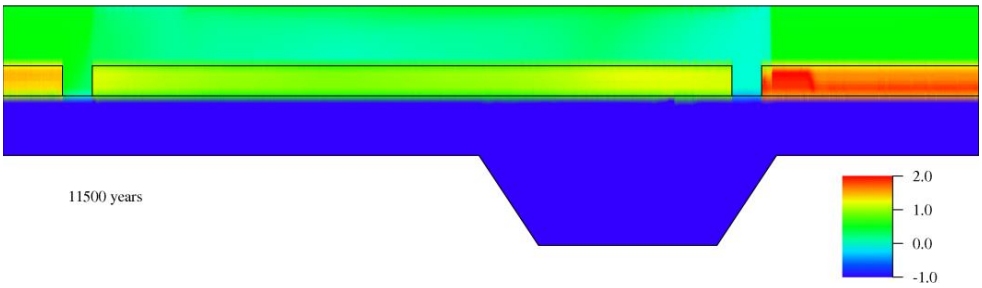

c) Smart K_d-value, logarithmic scale [m^3 kg^{-1}], 160,000 a

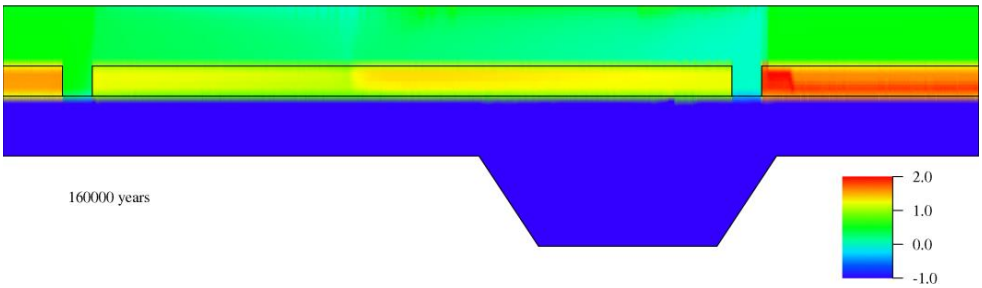

d) Smart K_d-value, logarithmic scale [m^3 kg^{-1}], 176,500 a

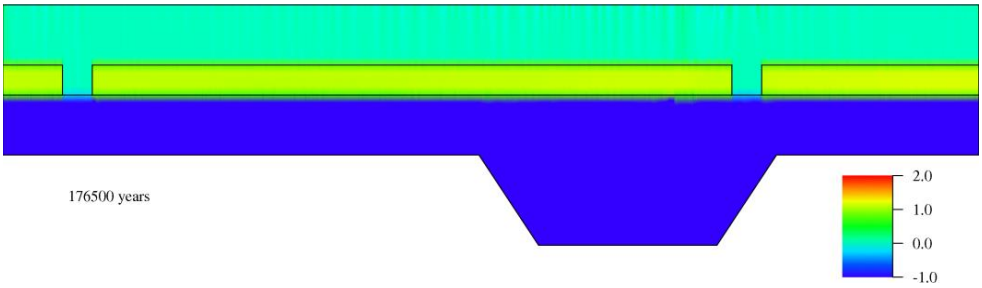

Fig. 8.22 Smart K_d-values for Th-230 for different points in time

South **North**

a) Conventional K_d-value, 160,000 a, logarithmic scale [mol m^{-3}]

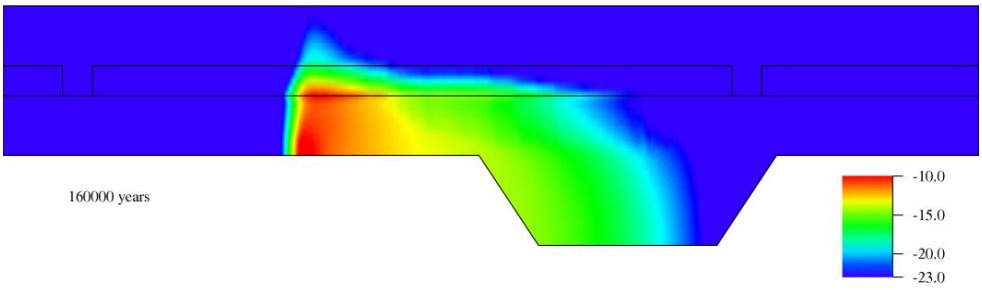

b) Smart K_d-value, 160,000 a, logarithmic scale [mol m^{-3}]

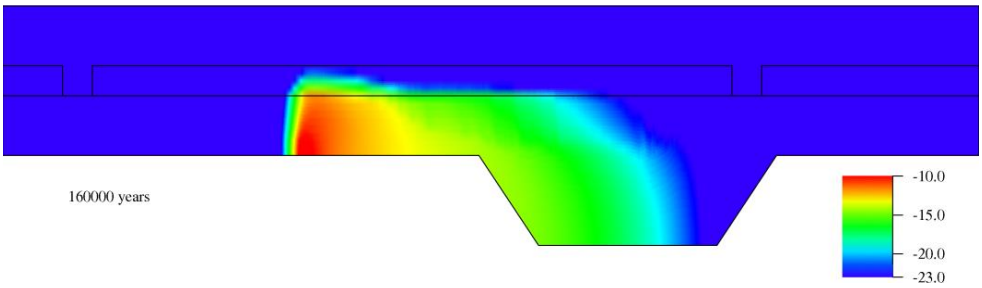

Fig. 8.23 Distribution of Th-230 after the constant boundary conditions (160,000 a) employing the conventional K_d-value /SUT 98/ and the smart K_d-value

8.4.4.5.3 Ra-226

Ra-226 shows the highest smart K_d-values of the regarded radionuclides of the uranium decay series (appendix, Fig. A.33). Again, maximum values can be observed in the northern and southern part of the aquitard of up to ca. $4 \cdot 10^3$ m^3 kg^{-1}. After the seawater transgression, the aquitard shows a smart K_d-value of $10^2 – 10^3$ m^3 kg^{-1} and the upper aquifer a value of ca. $2 \cdot 10^{-1}$ m^3 kg^{-1}. The conventional K_d-value is much lower with a value of $4 \cdot 10^{-2}$ m^3 kg^{-1} for the aquitard and the freshwater upper aquifer (during present and constant boundary conditions) and of $2 \cdot 10^{-3}$ m^3 kg^{-1} for the saline upper aquifer (during the seawater transgression).

As a consequence, only very small Ra-226 concentrations are found in the lowest part of the aquitard after 160,000 a regarding the smart K_d-value, while regarding the conventional K_d-value Ra-226 is transported half-way through the upper aquifer (appendix, Fig. A.34). During the seawater transgression, the transport is even facilitated, because of the higher salinity of the seawater.

8.5 Conclusions for transport simulations

Transport calculations have been performed to test the modified code, which includes the implementation of the transport of different components and of the smart K_d-concept. The results of the transport simulations were verified quantitatively for specific points in time and space and the correlation between the single environmental parameters and the smart K_d-values was analyzed. The results show that

- the implementation of the concept for transport of the geochemical components works well. The changes in pH, ionic strecngth, concentrations of Ca and DIC, and dissolution/precipitation of calcite are plausible and can be explained according to the concept for the different states of climate changes.
- the smart K_d-concept also works well showing the major dependencies and trends of all selected elements identified in sensitivity analysis, i. e. the dominant effect of the pH-value on the smart K_d-values for most of the regarded cations. The smart K_d-values of Cs-135, Ni-59, Am-243 and Np-237 increase, those of Se-79 and uranium decrease with increasing pH-values, under the conditions considered here. For Pu-239 and Th-230 the DIC concentration has the strongest impact, leading to a decrease of smart K_d-values with increasing DIC concentrations. These dependencies can be observed at different points in time, for which different flow and transport patterns are dominant. These result from the different boundary conditions for the regarded climate states and transitions.

Calculated smart K_d-value are mostly higher than the conventional K_d-values, some even exceed the K_d-values given by /SUT 98/ in several orders of magnitude. K_d-values by /SUT 98/ were determined by sorption experiments on Gorleben groundwater and sediment samples, which can contain more minerals and elements than considered in our calculations of the smart K_d-values. Thus, results cannot easily be compared to results of simulations employing the conventional K_d-values. Nevertheless, some of the smart K_d-value calculated on the basis of available thermodynamic sorption data (e. g. for Cs and Ra) seem to be very high. This observation need to be verified in future studies.

For the present climate and the constant boundary conditions, the transport of the radionuclides is dominated by advection. The environmental parameters reflect well the interaction of the initial and boundary conditions as well as the mixing processes and thus the changes of the geochemical environment. The weaker sorbing nuclides are

transported to the north and the northwestern rim syncline, while the stronger sorbing radionuclides mostly stay within the vicinity of the source. In the lower aquifer, conventional K_d-values are defined for both implementations, therefore the results of the radionuclide distributions are identical. The weaker sorbing radionuclides, such as uranium, reach the aquitard and eventually the upper aquifer after 160,000 a model time. The smart K_d-concept features higher smart K_d-values than the conventional K_d-values, especially in the aquitard. Therefore the radionuclide distribution is spatially restricted and smaller for the smart K_d-concept.

For a seawater transgression, the flow velocity is considerably reduced and diffusion dominates both the mixing process between fresh water and saline water and the migration of radionuclides. The environmental parameters level out over the entire model domain, just as the smart K_d-values. In the upper aquifer, fingering structures can be observed due to the overlying seawater. Radionuclide distributions are still mainly bound to the lower aquifer. The elevated ionic strength in the upper aquifer and the aquitard leads to decreased smart K_d-values. A broader distribution of most radionuclides is the consequence of the altered geochemical conditions and smart K_d-values, especially for Cs-135, Se-79 and uranium. The difference in the radionuclide concentrations for the two implementations can most clearly be observed for Cs-135, Se-79 and all the considered radionuclides of the uranium decay series.

Generally, the climate states determine the groundwater flow field and thus the flow direction and the dominant transport process (advection or diffusion). In addition to that the hydrogeochemical changes strongly impact the sorption of the radionuclides. Accordingly, the results for the radionuclide transport show considerable differences. The different climate states have a lower influence on the strongly sorbing radionuclides, e. g. Am-243, while for the weaker sorbing radionuclides, the retardation is strongly influenced by the flow direction and velocity, the dominant transport process and the mineralization of the groundwater. Therefore, introducing a temporally and spatially variable K_d-value, which takes the hydrogeochemistry into account, is a crucial step towards a more realistic treatment of the sorption in long-term safety assessments.

The transport simulations employing the conventional K_d-value were run for a model time of ca. 33 – 35 h. The simulations employing the smart K_d-concept took ca. 100 – 110 h. For the given model set-up and geochemical problem, the needed CPU time to run the transport model regarding the smart K_d-concept and the geochemical environment is only exceeded by a factor of 3 – 3.5 compared to employing the con-

ventional K_d-values. This ratio will vary for other models depending on the specific geological and hydrogeochemical conditions defined in the respective model.

9 Summary and conclusions

In this work an approach to implement the smart K_d-concept into the transport program r^3t, which is applied to large model areas and very long time scales in long-term safety assessment, is introduced. So-called smart K_d-values are based on mechanistic surface complexation models (SCM), vary in time and space and depend on the actual geochemical conditions. Therefore, the concept introduced here is based on an appropriate treatment of the most relevant environmental parameters in the transport code and smart K_d-values calculated in dependence on these parameters.

In the first stage this approach has been developed for a typical sedimentary system covering rock salt and clay formations in Northern Germany. Such a system can roughly be divided into three different hydrogeological units: an upper aquifer, an aquitard and a lower aquifer. The upper and lower aquifers are hydraulically connected by hydraulic windows in the intercalated aquitard. Each hydrogeological unit is characterized by a specific composition of single minerals. In our study a bottom-up approach is used, i. e. sorption for each element is described as the sum of the sorption of the element on every single mineral fraction. In order to keep the number of sorbates manageable the considered minerals and elements was constrained. The selection of the mineral phases was mainly based on reports about the petrography of samples from a number of different drill cores from the Gorleben site and their relevance for sorption or influencing of geochemical conditions. As most relevant quartz, feldspar, muscovite, gibbsite, goethite, calcite, kaolinite and illite have been determined. For the elements three groups have been considered: elements occurring as radionuclides, elements acting as competing cations and complexing ligands. The selection of the first group was based on their relevance for long-term safety, on the question whether they are sorbing at all and on the availability of comprehensive and reliable thermodynamic data. For the second and third group the ones with highest impact and high probability of occurrence in the natural system or released from the repository have been included. As a result Ni, Se, Cs, Cm, Am, Pu, U, Th, Np, Ra, Ca, Fe, Al, CO_3^{2-}, and SiO_3^{2-} have been selected for the calculations.

For the investigations and calculations within this project, a separate thermodynamic data base had to be created containing (i) the thermodynamic data for the aqueous element species and for solid mineral phases as well as (ii) the thermodynamic sorption data for the representative sorbates (pair of element and mineral). Therefore, the ther-

modynamic data for the representative elements and mineral phases were identified and extensively reviewed. Since for some of the relevant mineral phases, particularly feldspars and mica almost no sorption parameters for surface complexation models were available, batch sorption experiments with cesium (Cs^+), strontium (Sr^{2+}), and europium (Eu^{3+}) on orthoclase and muscovite, which are representative minerals for the Gorleben site, have been performed. From titration curves for both minerals and the results of the batch experiments thermodynamic data have been determined and included into the ESTRAL.dat data base.

The sorption of radionuclides to the relevant mineral phases is governed by environmental parameters such as pH, temperature, ionic strength (salt concentration) and concentration of complexing and competing ions. To keep the complexity and the CPU time to a minimum, the number of such parameters was limited and only those were selected having an important influence onto sorption processes. The selected environmental parameters are pH-value, DIC, Ionic strength, total concentration of Ca and total concentration of the considered radionuclide (element). In addition the most important complexing and competing ions silicon, aluminum and iron have been considered by the assumption that the concentration of the ions SiO_3^{2-}, Al^{3+} and Fe^{3+} is primarily determined by equilibria with solubility limiting mineral phases (quartz, gibbsite and hematite, respectively). Thus these concentrations have been calculated as part of the computation scheme to generate the multi-dimensional K_d-cloud.

For calculation of the sorption values as a function of the selected environmental parameters for each element onto the sediments (a defined mixture of relevant mineral phases) of the three hydrogeological units the geochemical speciation program PHREEQC was used. Parameter variation is performed by UCODE. The sensitivity and uncertainty analyses of the so-called smart K_d-values are done by coupling the code SimLab as outer shell to the two above mentioned codes PHREEQC and UCODE.

The results show quite good agreement of the average sorption values calculated from the K_d-cloud for the ten selected radionuclides and average sorption values derived from experimental results determined for the Gorleben sediments. Further, the sensitivity analysis indicates that for all ten radionuclides pH-value, DIC, and [Ca] are influencing the sorption coefficient most.

In order to verify the bottom-up approach two different test cases were chosen. On the one hand an additional batch sorption experiment with Eu on a specific mineral mixture

("synthetic sediment") was performed. Besides checking, whether the contributions of each mineral phase adequately describe the sorption on the sediment, the results also gave confidence in the new surface complexation parameters for orthoclase and muscovite derived by sorption experiments with Eu. On the other hand batch experiments from literature were applied to check, whether the sorption models and parameters as well as the modeling approach used are adequately describing the sorption behavior of uranium on synthetic and natural sands. In general the results from all applications of the bottom-up approach give quite good results for the sorption of europium and uranium, respectively, underpinning the concept developed here.

A key part of the whole project is the conceptual model for implementation of the relevant chemical processes into the transport code. As described above different environmental parameters, pH, ionic strength and concentration of DIC, Ca and ten radionuclides have been selected. An important assumption is that the interaction between the radionuclides and their impact on the geochemical conditions is neglected, since they only occur in trace concentrations. Therefore, major emphasis was put on the treatment of the other five environmental parameters. A crucial issue is the treatment of pH which is affected not only by proton transport but also by chemical reactions with the dissolved ions (preferably DIC and Ca) and mineral phases of the sediments. According to the results from site investigations main reactions in the Gorleben aquifers are calcite dissolution (mainly in the upper aquifer), microbial SOC degradation causing enhanced CO_2 partial pressures (DIC source) and dissolution of feldspars. Ion exchange processes, which might occur in the aquitard and at the interface to the upper aquifer, have not been regarded to keep the system not too complex and clearly represented. Except the dissolution of feldspars, which is only indirectly considered to determine the concentration of Al, all other relevant reactions are implemented. The core of the concept is the impact of calcite dissolution/precipitation on the pH-value, as observed in many natural systems.

Two kind of application cases have been selected to show the feasibility and capability of the method. Two 1D test cases have been used to check the plausibility of the development in a relatively simple system, where chemical changes cause dissolution or precipitation of calcite and these in turn affect the pH-value and DIC and Ca concentrations. In consequence the K_d-value and therewith the transport of the radionuclides is impacted. The results of the 1D calculations are plausible showing the applicability of our approach to implement the smart K_d-concept. Furthermore, one 2D test case was

regarded and results showed that the method is able to describe long-term chemical changes in large model areas and their impact on radionuclide sorption with acceptable calculation costs. Therefore the concept is applicable to fulfil the requirements of long-term safety assessments. The 2D case was derived from expected impacts of future climatic changes on the hydraulic conditions in the aquifer system in Northern Germany, therewith representing a calculation case, which might be addressed in a safety case for a potential repository in Northern Germany. Simulations show that the environmental parameters follow expected trends and major dependencies. The K_d values change accordingly to the change in environmental parameters. The pH-value has the most dominant effect on the smart K_d-values for most of the regarded elements, except for Pu and Th, where the DIC concentration has the strongest impact. The dependencies can be observed at different points in time, for which different flow and transport patterns are dominant. These result from the different boundary conditions for the regarded climate states and transitions.

The results of the concept applied here are very promising. The concept allows describing radionuclide sorption in large model areas over very long time frames in dependence of variable geochemical conditions. However, more test cases are needed to further qualify the modified transport code. Simple as well as more complex calculations should show the applicability of the approach for a larger variation of the environmental parameters and also in model geometry, heterogeneity and complexity of flow.

In the next stage of development additional processes as redox reactions and ionic exchange should be considered. The redox conditions will particularly impact sorption of redox sensitive radionuclides, which have been considered in this study to be present in an oxidised form. Further, the impact of additional competing cations as well as additional complexing ligands on radionuclide sorption should be studied in more detail and simulated by this approach. Finally, the application of the concept on highly mineralised solutions should be realised by applying the Pitzer formalism.

References

/ADE 94/ Adeleye, S.A., and Clay, P.G., Sorption of caesium, strontium and europium ions on clay minerals, Journal of Materials Science, 29 (1994) 954-958.

/APP 05/ Appelo, C.A.J., and Postma, D., Geochemistry, groundwater and pollution, 2nd edition, CRC Press (2005).

/ARC 05/ Archer, D. and Ganopolski, A., A movable trigger: Fossil fuel CO2 and the onset of the next glaciation, Geochem. Geophys. Geosyst., 6 (2005) Q05003, doi:10.1029/2004GC000891.

/ARC 08/ Arcos, D., Hernán, P., de la Cruz, B., Herbert, H.-J., Savage, D., Smart, N.R., Villar, M.V., Van Loon, L.R., NF-Pro, F16W-CT-2003-02389, Deliverable (D-N°: D2.6.4), RTDC-2 Synthesis Report (2008).

/ARN 82/ Arnórsson, S., and Sigurdsson, S., The chemistry of geothermal waters in Iceland. 1. Calculation of aqueous speciation from 0° to 370°C, Geochim. Cosmochim. Acta, 46 (1982) 1513-1532.

/ARN 98/ Arnold, T., Zorn T., Zänker, H., Bernhard, G., Nietsche H., Sorption behavior of U(IV) on phyllite, Chemical Geology, 151 (1998) 29-141.

/ARN 99a/ Arnórsson, S., and Andrésdóttir, Assessment of feldspar solubility in water in the range 0-350°C at P_{sat}., American J. Science, 299 (1999) 173-209.

/ARN 99b/ Arnórsson, S., and Andrésdóttir, The dissociation constants of Al-hydroxy complexes at 0-350°C and P_{sat}., in: The Proceedings of the Fifth International Symposium on the Geochemistry of the Earth's Surface (Ármannsson, H., ed.), Balkema Press, Rotterdam (1999) 425-428.

/ARN 99c/ Arnold, T., Zorn T., Zänker, H., Bernhard, G., Nietsche H.. Annual report 1999 – Modeling the sorption of uranium (VI) onto albite feldspar, Forschungszentrum Rossendorf e.V., Institute of Rediochemistry, Dresden (1999).

/ARN 01/ Arnold, T., Zorn, T., Zänker, H., Bernhard, G., Nitsche, H., Sorption behavior of U(IV) on phyllite: experiments and modeling, Journal of Contaminant Hydrology, 47 (2001) 219-231.

/ART 98/ Artinger, R., Kienzler, B., Schüßler, W., Kim, J.I., Effects of humic substances on the 241Am migration in a sandy aquifer: column experiments with Gorleben groundwater sediment systems, J. Cont. Hydrol., 35 (1998) 261-275.

/BAN 06/ Banta, E.R., Poeter, E.P., Doherty J.E., Hill, M.C., JUPITER: Joint Universal Parameter IdenTification and Evaluation of Reliability — An Application Programming Interface (API) for Model Analysis: US Geological Survey, Techniques and Methods 6-E1 (2006) 284 p.

/BEN 95/ Benda, L., Das Quartär Deutschlands, Gebrüder Bornträger, Berlin, Stuttgart (1995).

/BEN 44/ Bendel, 1944 (cited after /GRI XX/).

/BER 01/ Bernhard, G., Geipel, G., Reich, T., Brendler, V., Amayri, S., Nitsche, H., Uranyl(VI) carbonate complex formation: Validation of the $Ca_2UO_2(CO_3)_3$(aq.) species, Radiochimica Acta, 89 (2001) 511-518.

/BMU 10/ BMU, Sicherheitsanforderungen an die Endlagerung wärmeentwickelnder radioaktiver Abfälle, Bundesministerium für Umwelt, Naturschutz und Reaktorsicherheit, Berlin (2010).

/BOU 93/ Boulton, G. S., Slot, T., Blessing, K., Glasbergen, P., Leijnse, T., van Gijssel, K., Deep Circulation of Groundwater in Overpressured Subglacial Aquifers and its Geological Consequences, Quat. Sci. Rev., 12 (1993) 739-745.

/BOU 04/ Boulton, G. S., and Hartikainen, J., Thermo-Hydro-Mechanical Impacts of Coupling Between Glaciers and Permafrost, Coupled Thermo-Hydro-Mechanical-Chemical Processes in Geo-Systems - Fundamentals, Modelling, Experiments and Applications, 2 (2004) Elsevier Geo-Engineering Book Series, 293-298.

/BRA 03/ Bradbury, M.H., and Baeyens, B., Far field sorption data bases for performance assessment of a high-level radioactive waste repository in an undisturbed Opalinus Clay host rock, PSI Report 03-08 (2003) 1-128.

/BRA 05a/ Bradbury, M.H., and Baeyens, B., Experimental measurements and modeling of sorption competition on montmorillionite, Geo, 69 (17) (2005) 4187-4197.

/BRA 05b/ Bradbury, M.H., and Baeyens, B., Experimental and modelling investigation on Na-illite: Acide-base behavior and the sorption of strontium, nickel, europium and uranyl, Tech. Rep. 04-02, nagra, Wettingen (2005).

/BRA 08/ Brasser, T., Scherschel C., Brendler, V., Richter, A., Nebelung, C, Veerhoff, M., Klinger, C., Reichelt,C., ISDA - Ein Integriertes Sorptions-Datenbanksystem. GRS-Report 248, BMBF-02C1144/54/64/74, Gesellschaft für Anlagen- und Reaktorsicherheit (GRS) mbH, Braunschweig (2008).

/BRE 03/ Brendler, V., Vahle, A., Arnold, T., Bernhard, G., Fanghänel, T., RES³T-Rossendorf expert system for surface and sorption thermodynamics, J. Cont. Hydrol., 61 (2003) 281-291.

/BRI 11/ Britz, S., Sorption studies of Eu^{3+} on muscovite and orthoclase, Diploma thesis, available at: GRS Braunschweig, Theodor-Heuss-Sr. 4, Abt. 401, 38122 Braunschweig (2011).

/BRU 01/ Bruno, J., Cera, E., El Amrani, F. Z., Arcos, D., Duro, L.. Development and verification of the Thermo-Chimie thermodynamic data base, Major elements, Andra Report C.RP.0ENQ.01.003, Paris (2001).

/BUC 00/ Buckau, G., Artinger, R., Geyer, S., Wolf, M., Fritz, P., Kim, J.I., Groundwater in situ generation of aquatic humic and fulvic acids and the mineralization of sedimentary organic carbon, Appl. Geochem., 15 (2000) 819–832.

/BUH 91/ Buhmann, D., Nies, A., Storck, R., Analyse der Langzeitsicherheit von Endlagerkonzepten für wärmeerzeugende radioaktive Abfälle, GSF-Report 27/91. GSF - Forschungszentrum für Umwelt und Gesundheit GmbH, Braunschweig (1991).

/BUH 08/ Buhmann, D., Mönig, J., Wolf, J., Keller, S., Weber, J. R., Eberth, S., Kreienmeyer, M., Krone, J., Tholen, M., Überprüfung und Bewertung des Instrumentariums für eine sicherheitliche Bewertung von Endlagern für HAW – ISIBEL - FEP-Katalog für einen HAW-Standort im Wirtsgestein Salz. Cooperation report from DBE TECHNOLOGY GmbH, BMWi-FKZ 02E10055, BGR and GRS, Peine, Hannover, Braunschweig (2008) 564 p.

/BUH 10/ Buhmann,D., Mönig, J., Wolf, J., Keller, S., Mrugalla, S., Weber, J., Krone, J., Lommerzheim, A., ISIBEL II Bericht. Überprüfung und Bewertung des Instrumentariums für eine sicherheitliche Bewertung von Endlagern für HAW ISIBEL - Nachweis und Bewertung des Isolationszustandes "Sicherer Einschluss". Cooperation report from DBE TECHNOLOGY GmbH, BMWi-FKZ 02E10055, BGR and GRS, (2010).

/CIA 80/ Ciavatta, L., The specific interaction theory in evaluating ionic equilibria, Ann. Chim. (Rome), 70 (1980) 551-567.

/COR 03/ Cornell, R. M., and Schwertmann, U., The iron oxides - structure, properties, reactions, occurrences and uses, 2nd edition, Wiley-VCH, Weinheim (2003) 185-220.

/COX 89/ Cox, J.D., Wagman, D.D., Medvedev, V.A., CODATA Key Values for Thermodynamics, New York, Hemisphere Publishing (1989) 271p.

/CUK 73/ Cukier, R.I., Fortuin, C.M., Shuler, K.E., Petschek, A.G., Schaibly, J.H., Study of the sensitivity of coupled reaction systems to uncertainties in rate coefficients, Part I: theory, Journal of chemical physics, 59 (8) (1973) 3873-3878.

/CUK 75/ Cukier, R.I., Schaibly, J.H., Shuler, K.E., Study of the sensitivity of coupled reaction systems to uncertainties in rate coefficients, Part III: Analysis of the approximations, Journal of chemical physics, 63 (3) (1975) 1140-1149.

/CUK 78/ Cukier, R.I., Levine, H.B., Shuler, K.E., Nonlinear sensitivity analysis of multiparameter model systems, Journal of Computational Physics, 26 (1978) 1-42.

/CUR 02/ Curti, E., Wersin, P., Assessment of porewater chemistry in the bentonite backfill for the Swiss SF/HLW repository. Nagra Technical Report NTB 02-09, Wettingen, Switzerland, (2002).

/DAN 67/ d'Ans, J., Lax, E., Taschenbuch für Chemiker und Physiker. Lax, E., Synowietz, C. [Eds]. Vol. 1, Makroskopische physikalisch-chemische Eigenschaften, Springer: Berlin (1967) 1522 p.

/DAV 62/ Davies, C. W., Ion Association, Butterworths, Washington (1962).

/DAV 67/ Davies, S., de Wiest, R., Hydrogeology. John Wiley & Sons Inc., New York, London, Sydney (1967) 463 p.

/DAV 90/ Davis, J.A., and Kent, D.B., Surface complexation modeling in aqueous geochemistry, in: Mineral-Water Interface Geochemistry; Hochella MF, White AF (Ed.), Mineralogical Society of America, Washington, DC (1990).

/DAV 98/ Davis, J. A., Coston, J. A., Kent, D. B., Fuller, C. C., Environ.Sci.Technol. 32 (1998) 2820-2828.

/DAV 01/ Davis, J. A., Surface Complexation Modeling of Uranium (VI) Adsorption on Natural Mineral Assemblages, NUREG/CR-6708, U.S. Nuclear Regulatory Commission, Washington, DC (2001) 214 p.

/DEL 98/ Delisle, G., Numerical simulation of permafrost growth and decay, J. Quat. Sci., 13 (4) (1998) 325-333.

/DZO 90/ Dzombak, D.A., and Morel, F.M.M., Surface complexation modeling, Hydrous ferric oxide, Wiley, New York (1990).

/EMI 57/ Emiliani, C., Temperature and Age Analysis of Deep-Sea Cores, Science, 125 (1957) 383-387.

/FEI 99/ Fein, E., and Schneider, A., d³f – Ein Programmpaket zur Modellierung von Dichteströmungen, GRS-139, BMWi-FKZ 02C04650, Gesellschaft für Anlagen- und Reaktorsicherheit (GRS) mbH, Braunschweig (1999) 245 p.

/FEI 04/ Fein, E., Software Package r³t. Model for Transport and Retention in Porous Media, GRS-192, BMWA-FKZ 02E9148/2, Gesellschaft für Anlagen- und Reaktorsicherheit (GRS) mbH, Braunschweig (2004) 319 p.

/FLU 09/ Flügge, J., Radionuclide Transport in the Overburden of a Salt Dome – The Impact of Extreme Climate States, Verlag Dr.Hut, München (2009) 209 p.

/FOE 09/ Förster, B., and Noseck, U., Ermittlung eines realitätsnahen Radionuklid-Inventars für Abfälle aus der Wiederaufbereitung von Kernbrennstoffen – Auswahl sicherheitsrelevanter Radionuklide, GRS-Notiz 770432-03 (2009).

/GAM 05/ Gamsjäger, H., Bugajski, J., Gajda, T., Lemire, R., Preis, W., Chemical Thermodynamics of Nickel. Chemical Thermodynamics Vol. 6, OECD Nuclear Energy Agency, [Ed.], Elsevier, Amsterdam (2005).

/GAN 07/ Ganopolski, A., Personal Communication, 12 June 2007, GRS Braunschweig (2007).

/GRI XX/ GRIMM, W.-D. (1982 - 1994): Sedimentpetrographische Untersuchungen an Proben aus dem Raum Gorleben, München (BfS-Reports).

/GUI 03/ Guillaumont, R., Fanghaenel, T., Fuger, J., Grenthe, I., Neck, V., Palmer, D.A., Rand, M.H., Vol. 5. Update on the Chemical Thermodynamics of Uranium, Neptunium, Plutonium, Americium and Technetium, OECD Nuclear Energy Agency Data Bank, Ed.), North Holland Elsevier Science Publishers B.V., Amsterdam, The Netherlands (2003).

/GUN 00/ Gunnarsson, I., and Arnorsson, S., Amorphous silica solubility and the thermodynamic properties of H4SiO4 in the range of 0° to 350°C at Psat., Geochim. Cosmochim. Acta, 64 (2000) 2295-2307.

/HEG 84/ Helgeson, H. C., William, M. M., Aagaard, P., Thermodynamic and kinetic constraints on reaction rates among minerals andn aqueous solutions, II. Rate constants, effective surface area, and the hydrolysis of feldspar, Geochim. Cosmochim. Acta, 48 (1984) 2405-2432.

/HEL 00/ Helton, J.C., and Davis, F.J., Sampling-based Methods, in: Saltelli, A., Chan, K., Scott, E.M., Sensitivity Analysis, John Wiley and Sons, Chichester (2000).

/HIL 98/ Hill, M. C., Methods and guideline for effective model calibration (Water - resources investigations report), 98-4005, U.S.G.S., Denver, Colorado (1998).

/HUA 73/ Huang, C.P., and Stumm, W., Specific adsorption of cations on hydrous - Al2O3, J. Colloid and Interface Science, 43 (1973) 409-420.

/HUM 02/ Hummel, W., Berner, U., Curti, E., Pearson, F.J., Thoenen, T., Nagra/PSI Chemical Thermodynamic Data Base 01/01, (ed.) Universal Publishers/uPublish.com, Parkland, Florida (2002).

/IMB 84/ Imbrie, J., Hays, J. D., Martinson, D. G., McIntyre, A., Mix, A. C., Morley, J. J., Pisias, N. G., Prell, W. L., Shackleton, N. J., The Orbital Theory of Pleistocene Climate: Support from a Revised Chronology of the Marine δ18O Record, Milankovitch and Climate, Part 1, Berger, A. L., Imbrie, J., Hays, J., Kukla, G., and Saltzman, B. (eds), D. Reidel Publishing Company, Dordrecht (1984) 269-305.

/JOS 11/ Joseph, C., Schmeide, K.; Sachs, S.; Brendler, V.; Geipel, G.; Bernhard, G., Sorption of uranium(VI) onto Opalinus Clay in the absence and presence of humic acid in Opalinus Clay pore water, Chem. Geol., 284 (2011) 240-250.

/KAL 03/ Kallenrode, M.-B., Ozeane und Küsten, Vorlesungsskript University Osnabrück, Sommersemester 2003, Download at: http://www.sotere.uni-osnabrueck.de/Lehre/skript/ozeane_kuesten.pdf (date of access: 01/2010), (2003) 243.

/KAN 92/ Kantor, W., Krone, F., Nitsch, M., Ergebnisse zur Bestimmung der Porengrößenverteilung und begleitender physikalisch-chemischer sowie mineralogischer Untersuchungen in Lockergesteinen an Proben aus den Schächten I und II, Projekt Gorleben, BGR-Fachbericht A9G41111000 (1992).

/KAP 61/ Kappelmeier, O., and Geothermik, in: Bentz, A. [Ed.], Lehrbuch der Angewandten Geologie, Vol. 1. Enke: Stuttgart (1961) 863-889.

/KEE 05/ Keesmann, S., Noseck, U., Fein, E., Schneider, A., Buhmann, D., Modellrechnungen zur Langzeitsicherheit von Endlagern für abgebrannte Brennelemente in Salz- und Granitformationen, GRS-206, BMWA-FKZ 02E9239, Gesellschaft für Anlagen- und Reaktorsicherheit (GRS) mbH, Braunschweig (2005).

/KEL 98/ Keller, S., Permafrost in der Weichsel-Kaltzeit und Langzeitprognose der hydrogeologischen Entwicklung der Umgebung von Gorleben/NW-Deutschland, Z. Angew. Geol., 48 (1998) 111-119.

/KIT 99/ Kitamura, A., Fujiwara, K., Yamamoto, T., Nishikawa, S., Moriyama, H., Analysis of adsoption behavior of cations onto quartz surface by electrical double-layer model, Journal of Nuclear Science and Technology, 36 (12) (1999) 1167-1175.

/KLI 02/ Klinge, H., Köthe, A., Ludwig, R.-R., Zwirner, R., Geologie und Hydrogeologie des Deckgebirges über dem Salzstock Gorleben, Z. Angew. Geol., 2 (2002) 7-15.

/KLI 04/ Klinge, H., and Baharian-Shiraz, A., Projekt Gorleben, Dokumentation hydrogeologischer Basisdaten, Hannover (Bundesanstalt für Geowissenschaften und Rohstoffe), 16 (2004).

/KLI 07/ Klinge, H., Boehme, J., Grissemann, C., Houben, G., Ludwig, R.-R., Rübel, A., Schelkes, K., Schildknecht, F., Suckow, A., Standortbeschreibung Gorleben, Teil 1: Die Hydrogeologie des Deckgebirges des Salzstocks Gorleben, Geol. Jb., C 71 (2007) 199 p.

/KOE 00/ Kösters, E., Vogel, P., Schelkes, K., 2D-Modellierung der paläohydrogeologischen Entwicklung des Grundwassersystems im Elberaum zwischen Burg und Boitzenburg, BGR, Hannover (2000).

/KOE 07/ Köthe, A., Hoffmann, N., Krull, P., Zirngast, M., Zwirner, R., Standortbeschreibung Gorleben, Teil 2: Die Geologie des Deck- und Nebengebirges des Salzstocks Gorleben, Geol. Jb., C 72 (2007) 147p.

/KRE 83/ Kretz, R., Symbols for rock forming minerals, Amer. Mineralogist, 68 (1983) 277.

/KUL 02/ Kulik, D.A., Sorption modelling by Gibbs energy minimisation: Towards a uniform thermodynamic data base for surface complexes of radionuclides, Radiochim. Acta, 90 (2002) 815.

/LAN 02/ Langer, A., and Schütte, H., Geologie norddeutscher Salinare, Akad. Geowiss. Hannover, 20 (2002) 63-69.

/LEG 88/ Legrand, M. R., Lorius, C., Barkov, N. I., Petrov, V. N., Vostok (Antarctica) ice core: Atmospheric chemistry changes over the last climatic cycle (160,000 years), Atmospheric Environment, 22 (2) (1988) 317-331.

/LEG 04/ Legarth, B., Tischer, T., Huenges, E., Stimulating for productivity: Hydraulic Proppant Fracturing Treatments in Rotliegend Sandstones. In: Huenges, E., Wolfgramm, M. [Eds]: Sandsteine im In-situ-Geothermielabor Groß Schönebeck – Reservoir-Charakterisierung, Stimulation, Hydraulik und Nutzungskonzepte, Scientific Technical Report STR04/03. Potsdam (Geoforschungszentrum Potsdam (GFZ)) (2004) 93-106. Download at: http://www.gfz-potsdam.de/bib/zbstr.htm (date of access: February 2008).

/LIN 85/ Linke, G., Katzenberger, O., Grün, R., Description and ESR dating of the Holsteinian interglaciation, Quat. Sci. Rev., 4 (1985) 319-331.

/LOU 00/ Loutre, M. F., and Berger, A., Future climate changes: Are we entering an exceptionally long interglacial?, Clim. Change, 46 (2000) 61-90.

/LUD 02/ Ludwig, R., and Kösters, E., Hydrogeologisches Modell Gorleben – Entwicklung bis zum paläohydrogeologischen Ansatz, Hydrogeologische Modelle – Ein Leitfaden mit Fallbeispielen. Arbeitskreis “Hydrogeologische Modelle und Grundwassermanagement” der Fachsektion Hydrogeologie der Deutschen Geologischen Gesellschaft (eds), Schriftenreihe der Deutschen Geologischen Gesellschaft, 24 (2002) 69-77.

/MAG 06/ Magill, J., and Pfennig, G., Galy, J. ,Karlsruher Nuklidkarte, European Communities (2006).

/MAS 85/ Mason, B., and Moore, C.B., Grundzüge der Geochemie, Ferdinand Enke Verlag, Stuttgart (1985).

/MAT 94/ Mattheß, G., Die Beschaffenheit des Grundwassers, Lehrbuch der Hydrogeologie, Vol. 2, Mattheß, G. (ed.), Gebrüder Bornträger, Berlin, Stuttgart (1994).

/MER 08/ Merkel, B.J., and Planer-Friedrich, B., Grundwasserchemie – Praxisorientierter Leitfaden zur numerischen Modellierung von Beschaffenheit, Kontamination und Sanierung aquatischer Systeme, Springer-Verlag Berlin Heidelberg (2008).

/MEY 06/ Meyer, K.-D., Personal Communication, 1 June 2006, TU Braunschweig (2006).

/NOR 90/ Nordstrom, D.K., Plummer, L.N., Langmuir, D., Busenberg, E., May, H.M., Jones, B.F., Parkhurst, D.L., Revised Chemical Equilibrium Data for Major Water-Mineral Reactions and their Limitations. in: Chemical Modeling of Aqueous Systems II (Melchior, D.C., Basset, R.L. [Eds.]), Washington, D.C.: American Chemical Society, ACS Symposium Series 416 (1990) 398-413.

/NOS 09/ Noseck, U., Fahrenholz, C., Flügge, J., Fein, E., and Pröhl, G., Impact of climate change on far-field and biosphere processes for a HLW-repository in rock salt – Scientific basis for the assessment of the long-term safety of repositories, GRS-241, BMWi-FKZ 02E9954, Gesellschaft für Anlagen- und Reaktorsicherheit (GRS mbH), Braunschweig (2009).

/OCH 11/ Ochs, M., Payne, T.E., Brendler, V., NEA sorption project – Phase III: Thermodynamic sorption modeling in support of radioactive waste disposal safety cases, OECD/NEA, Paris (2011).

/OLI 05/ Olin, Å., Noläng, B., Öhman, L.-O., Osadchii, E., Rosén, E., Chemical Thermodynamics of Selenium, Chemical Thermodynamics Vol. 7 OECD Nuclear Energy Agency, [Ed.], Elsevier, Amsterdam (2005).

/PAR 99/ Parkhurst, D.L., and Appelo, C.A.J., User's guide to PHREEQC (Version 2) - A computer program for speciation, batch-reaction, one-dimensional transport, and inverse geochemical calculations: U.S. Geological Survey Water-Resources Investigations Report 99-4259 (1999) 312 p.

/PLU 82/ Plummer, L.N., and Busenberg, E., The solubilities of calcite, aragonite and vaterite in CO_2-H_2O solutions between 0 and 90°C, and an evaluation of the aqueous model for the system $CaCO_3$-CO_2-H_2O, Geochim. Cosmochim. Acta, 46 (1982) 1011-1050.

/POE 98/ Poeter, E.P., and Hill, M.C., Documentation of UCODE, a computer code for universal inverse modeling: U.S Geological Survey Water-Resources Investigations Report 98-4080 (1998) 122 p.

/POE 05/ Poeter, E.P., Hill, M.C., Banta E.R., Mehl, S., Christensen, S.,UCODE_2005 and Six Other Computer Codes for Universal Sensitivity Analysis, Calibration, and Uncertainty Evaluation, U.S Geological Survey, Techniques and Methods 6-A11 (2005) 299 p.

/RAN 08/ Rand, M., Fuger, J., Grenthe, I., Neck, V., Rai, D., Chemical Thermodynamics of Thorium, Chemical Thermodynamics Vol. 11, OECD Nuclear Energy Agency, [Ed.], Elsevier, Amsterdam (2008).

/RIC 07/ Richter, A., and Brendler, V., Blind prediction and parameter uncertainty – A sorption test case. in: Adsorption of Metals by Geomedia II. Barnett, M.O., Kent, D.B., [Eds.], Elsevier, Amsterdam (2008).

/ROH 98/ Rohling, E. J., Fenton, M., Jorissen, F. J., Bertrand, P., Ganssen, G., Caulet, J. P., Magnitudes of sea-level lowstands of the past 500,000 years, Nature, 394 (1998) 162-165.

/RUE 10/ Rübel, A., Becker, D.-A., Fein, E., Ionescu, A., Lauke, T., Mönig, J., Noseck, U., Schneider, A., Spießl, S., Wolf, J.: Development of Performance Assessment Methodologies. GRS-259, BMWi-FKZ 02E10276, Gesellschaft für Anlagen- und Reaktorsicherheit (GRS) mbH, Braunschweig (2010).

/SAL 98/ Saltelli, A., Bolando, R., An alternative way to compute Fourier Amplitude Sensitivity Test, Computational Statistics and data analysis, 26 (4) (1998) 445-460.

/SAL 99/ Saltelli, A., Tarantola, S., Chan, K., A quantitative modelindependent method for global sensitivity analysis of model output, Technometrics, 41 (1999) 39-56.

/SAM 09/ Samper, J., Lu , C., Ma, H., Montenegro, L, Cuñado, M., Cormenzana, J.L., Final report on benchmark calculations in granite Deliverable (D-N°:4.1.2), PAMINA - Performance Assessment Methodologies in Application to Guide the Development of the Safety Case (2009) .

/SCH 05/ Schwieger, V., Nicht-lineare Sensitivitätsanalyse gezeigt an Beispielen zu bewegten Objekten, Habilitation thesis, University Stuttgart, München (2005).

/SCH 08/ Schwyn, B., Geochemische Nahfeld-Daten für die sicherheitstechnischen Betrachtungen zum Sachplan geologische Tiefenlager, Etappe 1, Arbeitsbericht NAB 08-51, nagra, Wettingen (2008).

/SCH 11/ Schikora, J., Sensitivitäts- und Unsicherheitsanalysen zur Schadstoffausbreitung in der Umwelt, Report. TU Dresden. Institut für Verfahrensautomatisierung (2011).

/SCH 63/ Schindler, P., Michaelis, W., Feitknecht, W., Löslichkeitsprodukte von Metalloxiden und –hydroxiden, 8. Die Löslichkeit gealterter Eisen(III)-hydroxidfällungen, Helvetica Chimica Acta 46, (1963) 444-449.

/SCH 73/ Schaibly, J.H., and Shuler, K.E., Study of the sensitivity of coupled reaction systems to uncertainties in rate coefficients. Part II, applications, Journal of chemical physics, 59 (1973) 3879-3888.

/STR 04/ Streif, H., Sedimentary record of Pleistocene and Holocene marine inundations along the North Sea coast of Lower Saxony, Germany, Quat. Int., 112 (2004) 3-28.

/STR 07/ Streif, H., Das Quartär in Niedersachsen und benachbarten Gebieten - Gliederung, geologische Prozesse, Ablagerungen und Landschaftsformen. Download at: http://www.lbeg.niedersachsen.de/download/1015/Quartaer stratigraphie_von_Niedersachsen_und_benachbarten_Gebieten_2007_.pdf (accessed: September 2012) (2007).

/STU 70/ Stumm, W., Huang, C.P., Jenkins, S.R., Specific chemical interaction affecting the stability of dispersed systems, Croatica Chemica Acta, 42 (1970) 223-245.

/SUM 96/ Summerhayes, C.P., S.A. Thorpe, [Eds.], Oceanography – An illustrated guide, Manson Publ. Southampton Oceanography Center (1996).

/SUT 98/ Suter, D., Biehler, D., Blaser, P., Hollmann, A., Derivation of a sorption data set for the Gorleben overburden, Proceedings DisTec 98, International Conference on Radioactive Waste Disposal, Hamburg (1998) 581-584.

/SVE 96/ Sverjensky, D. A., Sahai, N., Theoretical prediction of single-site surface protonation equilibrium constants for oxides and silicates in water, Geochim. Cosmochim. Acta, 60 (1996) 3773-3797.

/TIC 93/ Ticknor, K.V., Actinide sorption by fracture-infilling minerals, Radiochim. Acta, 60 (1993) 33-42.

/TUR 96/ Turner, D.R., and Sassman, S.A., Approaches to sorption modeling for high-level waste performance assessment, J. Contam. Hydrol., 21 (1996) 311.

/WAG 69/ Wagman, D. D., Evans, W. H., Parker, V. B., Halow, I., Bailey, S. M., Schumm, R. H., Selected values of chemical thermodynamic properties. Tables for elements 35 through 53 in the standard order of arrangement. Report TN-270-4, National Bureau of Standards, Washington, D.C (1969).

/WAL 05/ Walter, M., Arnold, T., Geipel G., Scheinost, A., Bernhard, G., An EXAFS and TRLFS investigation on unranium (VI) sorption to pristine and leached albite surfaces, Journal of Colloid and interface science, 282 (2005) 293-305.

/WIL 93/ Williams, R.S., and Hall, D.K., Glaciers, Atlas of Satellite observations related to global change, Gurney, R.J., Foster, J.L., and Parkinson, C.L. (eds.), Cambridge Univ. Press, Cambridge (1993) 401-422.

/WOL 08/ Wolf, J., Rübel, A., Noseck, U., Becker, D.-A., Safety and performance indicators for repositories in clay and salt formations, BMWi-FKZ 02E9954, GRS-240, Gesellschaft für Anlagen- und Reaktorsicherheit (GRS) mbH, Braunschweig (2008).

/ZAV 04/ Zavarin, M., Carle, S.F., Maxwell, R.M., Upscaling Radionuclide Retardation - Linking the Surface Complexation and Ion Exchange Mechanistic Approach to a Linear Kd Approach, LLNL-report UCRL-TR-204713 2004.

/ZIR 03/ Zirngast, M., Zwirner, R., Bornemann, O., Fleig, S., Hoffmann, N., Köthe, A., Krull, P., Weiß, W., Schichtenfolge und Strukturbau des Deck- und Nebengebirges, Projekt Gorleben, BGR-Report 9G3411900000 (2003).

List of Figures

List of Tables

A Appendix

A.1 Data for seawater composition

The compounds of salt deposits as calculated from the composition of average seawater are shown in Tab. A.1. These data have been used to estimate seawater concentrations for the relevant elements considered here. Selected analyses of seawater can be found in /KAL 03/ (after /SUM 96/) and are presented in Fig. A.1.

Tab. A.1 Compounds of salt deposits calculated from the composition of average seawater /LAN 02/

Mineral	**wt%**
NaCl	2.73
$MgCl_2$	0.32
$MgSO_4$	0.23
$CaSO_4$	0.13
KCl	0.07
$Ca(HCO_3)_2$	0.02
Σ	3.50

Element	C [1/kg]	häufigste Verbindung
Lithium	174 µg	Li^+
Bor	4.4 mg	H_3BO_3
Kohlenstoff	27.6 mg	HCO_3^-, CO_3^{2-}
Stickstoff	420 µg	NO_3^-
Fluor	1.3 mg	F^-, MgF^+
Natrium	10.77 g	Na^+
Magnesium	1.29 g	Mg^{2+}
Aluminium	540 ng	$Al(OH)_4^-$, $Al(OH)_3$
Silizium	2.8 mg	H_4SiO_4
Phosphor	70 µg	HPO_4^{2-}, $NaHPO_4^-$, $MgHPO_4$
Schwefel	0.904 g	SO_4^{2-}, $NaSO_4^-$, $MgSO_4$
Chlor	19.354 g	Cl^-
Kalium	0.399 g	K^+
Calcium	0.412 g	Ca^{2+}
Mangan	14 ng	Mn^{2+}, $MnCl^+$
Eisen	55 ng	$Fe(OH)_3$
Nickel	0.5 µg	Ni^+, $NiCO_3$, $NiCl^+$
Kupfer	0.25 µg	$CuCO_3$, $CuOH^+$, Cu^{2+}
Zink	0.4 µg	Zn^{2+}, $ZnOH^+$, $ZnCO_3$, $ZnCl^+$
Arsen	1.7 µg	$HAsO_4^{2-}$
Brom	67 mg	Br^-
Rubidium	120 µg	Rb^+
Strontium	7.9 mg	Sr^{2+}
Cadmiun	80 ng	$CdCl_2$
Jod	50 µg	IO_3^-
Caesium	0.29+µg	Cs^+
Barium	14 µg	Ba^{2+}
Quecksilber	1 ng	$HgCl_4^{2-}$
Blei	2 ng	$PbCO_3$, $Pb(CO_3)_2^{2-}$, $PbCl^+$
Uran	3.3 µg	$[UO_2(CO_3)_3]^{4-}$

Fig. A.1 Seawater composition /KAL 03/

A.2 Data for element contents in ice cores

Data about the composition of an inland ice sheet and their meltwaters can be obtained from the analyses of ice cores. Detailed information about the ice chemistry is given by /LEG 88/. Data from the Vostok ice core are shown in Fig. A.2.

Stage	A	B	C	D	E	F	G	H
Depth (m)	0 325	350 550	575 850	875 975	1000 1475	1500 1600	1675 1850	1925 2080
Na_m^+	1.2 ± 0.5	4.5 ± 0.7	3.7 ± 0.8	3.6 ± 0.2	2.3 ± 0.6	2.1 ± 0.4	0.4 ± 0.1	3.4 ± 0.6
K^+	0.04 ± 0.01	0.22 ± 0.06	0.12 ± 0.02	0.15 ± 0.03	0.07 ± 0.02	0.06 ± 0.01	0.02 ± 0.01	0.16 ± 0.03
K^{+*}	0.01 ± 0.01	0.12 ± 0.05	0.04 ± 0.02	0.08 ± 0.02	0.02 ± 0.01	0.01 ± 0.00	0.01 ± 0.01	0.08 ± 0.02
Mg^{2+}	0.3 ± 0.1	1.6 ± 0.4	1.0 ± 0.2	1.3 ± 0.2	0.6 ± 0.2	0.5 ± 0.1	0.1 ± 0.1	1.3 ± 0.3
Mg^{2+*}	0.0 ± 0.0	0.6 ± 0.3	0.2 ± 0.1	0.5 ± 0.1	0.1 ± 0.1	0.0 ± 0.0	0.0 ± 0.0	0.5 ± 0.2
Ca^{2+}	0.1 ± 0.05	2.5 ± 0.9	0.9 ± 0.5	1.8 ± 0.5	0.4 ± 0.3	0.2 ± 0.1	0.1 ± 0.05	2.0 ± 0.6
Ca^{2+*}	0.06 ± 0.04	2.3 ± 0.8	0.8 ± 0.5	1.7 ± 0.5	0.3 ± 0.3	0.1 ± 0.1	0.08 ± 0.04	1.8 ± 0.6
NH_4^+	0.1 ± 0.05	0.23 ± 0.14	0.23 ± 0.06	0.19 ± 0.09	0.19 ± 0.07	0.11 ± 0.03	0.10 ± 0.02	0.14 ± 0.03
H^+	2.0 ± 1.3	2.5 ± 0.7	2.1 ± 0.7	2.5 ± 0.6	1.7 ± 0.8	1.4 ± 0.4	2.9 ± 0.3	2.2 ± 0.7
Cl^-	0.5 ± 0.4	5.1 ± 1.1	3.1 ± 1.1	3.9 ± 0.4	1.1 ± 0.5	1.0 ± 0.2	0.8 ± 0.2	4.2 ± 1.1
Cl^{-*}	-0.9 ± 0.6	-0.1 ± 0.5	-1.2 ± 0.8	-0.2 ± 0.2	-1.5 ± 0.7	-1.5 ± 0.2	$+0.3 \pm 0.1$	$+0.3 \pm 0.9$
NO_3^-	0.25 ± 0.05	1.4 ± 0.7	0.4 ± 0.2	0.8 ± 0.3	0.25 ± 0.1	0.25 ± 0.1	0.35 ± 0.1	1.0 ± 0.4
SO_4^{2-}	2.8 ± 0.6	5.3 ± 1.3	4.4 ± 0.8	5.2 ± 1.1	3.6 ± 0.7	2.7 ± 0.4	2.2 ± 0.2	4.2 ± 0.9
SO_4^{2-**}	2.6 ± 0.6	4.8 ± 1.2	3.9 ± 0.8	4.8 ± 1.1	3.3 ± 0.7	2.4 ± 0.3	2.1 ± 0.1	3.8 ± 0.9
SO_4^{2-*}	1.6 ± 1.0	4.5 ± 1.3	2.7 ± 1.2	4.5 ± 1.0	1.6 ± 0.9	0.9 ± 0.4	2.1 ± 0.1	3.6 ± 1.2
T	0.1 ± 0.1	2.9 ± 1.1	0.9 ± 0.6	2.2 ± 0.6	0.4 ± 0.2	0.1 ± 0.1	0.1 ± 0.1	2.4 ± 0.8
Al	3.0 ± 1.5	97 ± 37	31 ± 20	72 ± 22	14 ± 11	5 ± 3	3 ± 2	79 ± 27
Cl/Na_m	0.7 ± 0.8	1.8 ± 0.2	1.3 ± 0.4	1.7 ± 0.1	0.8 ± 0.3	0.7 ± 0.1	2.9 ± 0.6	1.9 ± 0.4
ΔC	$+0.2 \pm 0.3$	-0.2 ± 0.5	$+0.1 \pm 0.4$	-0.2 ± 0.4	$+0.4 \pm 0.2$	$+0.5 \pm 0.2$	$+0.4 \pm 0.2$	-0.2 ± 0.8
Σ	7.2 ± 2.0	23.5 ± 5.0	15.8 ± 3.3	19.6 ± 2.2	10.2 ± 1.8	8.4 ± 1.1	7.0 ± 0.7	18.7 ± 3.9

Fig. A.2 Ionic distribution (in µEq L^{-1}), Al content (in ng g^{-1}) and Cl/Na_m weight ratio for various stages along the Vostok ice core /LEG 88/

A.3 Groundwater data from Gorleben site

Groundwater geochemical data for the different groundwater types at the Gorleben site are listed in Tab. A.**2** to Tab. A.4.

Tab. A.2 Groundwater geochemical data for the **Ca-HCO_3**-type after /KLI 04/

TDS: Total Dissolved Solids; EC: Electric Conductivity

	TDS	Ion balance	pH	EC	K	log (K)	Na	log (Na)	Mg	log (Mg)	Ca	log (Ca)	Fe_{tot}	log (Fe_{tot})
	[mg L^{-1}]	[%]	[-]	[µS cm^{-1}]	[mg L^{-1}]	[mg L^{-1}]	[mg L^{-1}]	[mg L^{-1}]	[mg L^{-1}]	[mg L^{-1}]	[mg L^{-1}]	[mg L^{-1}]	[mg L^{-1}]	[mg L^{-1}]
Nr	37	37	35	36	37	37	37	37	37	37	37	37	35	35
Min	113	-12.41	6.6	117	0.27	-0.57	6.15	0.79	0.73	-0.14	19.8	1.3	0.01	-2.0
Max	471	2.27	8.1	502	5.0	0.7	21.7	1.34	10.8	1.03	77.6	1.89	3.5	0.54
Mean	272	-0.48	7.5	295	1.83	0.18	10.1	0.98	5.14	0.59	48.32	1.64	0.7	-0.43
Var	$1.36 \cdot 10^4$	5.49	0.144	$1.56 \cdot 10^4$	1.17	0.084	13	0.019	11.1	0.133	454	0.047	0.8	0.308

	Al	log (Al)	Cl	log (Cl)	SO_4^{2-}	log SO_4^{2-}	HCO_3^-	log HCO_3^-	PO_4^{3-}	SiO_2	log SiO_2
	[mg L^{-1}]	[mg L^{-1}]	[mg L^{-1}]	[mg L^{-1}]	[mg L^{-1}]	[mg L^{-1}]	[mg L^{-1}]	[mg L^{-1}]	[mg L^{-1}]	[mg L^{-1}]	[mg L^{-1}]
Nr	2	2	37	37	37	37	37	37	18	21	21
Min	0.04	-1.4	4.9	0.69	0.5	-0.3	62.85	1.8	-0.1	8.0	0.9
Max	0.06	-1.22	27	1.43	40.4	1.61	313	2.5	0.88	45	1.65
Mean	0.05	-1.31	12.47	1.05	14.3	0.99	165	2.16	0.26	21.21	1.29
Var	$2.00 \cdot 10^{-4}$	0.016	31.7	0.038	126	0.194	$6.67 \cdot 10^3$	0.055	0.117	88.9	0.039

Tab. A.3 Groundwater geochemical data for the **Na-HCO_3**-type after /KLI 04/

TDS: Total Dissolved Solids; EC: Electric Conductivity

	TDS	**Ion balance**	**pH**	**EC**	**K**	**log (K)**	**Na**	**log (Na)**	**Mg**	**log (Mg)**	**Ca**	**log (Ca)**	**Fe_{tot}**	**log (Fe_{tot})**
	[mg L^{-1}]	[%]	[-]	[µS cm^{-1}]	[mg L^{-1}]	[mg L^{-1}]	[mg L^{-1}]	[mg L^{-1}]	[mg L^{-1}]	[mg L^{-1}]	[mg L^{-1}]	[mg L^{-1}]	[mg L^{-1}]	[mg L^{-1}]
Nr	30	30	30	29	29	29	30	30	30	30	30	30	30	30
Min	189	-3.28	7.2	161	1.0	0.0	42	1.62	0.36	-0.44	2.4	0.38	0.05	-1.34
Max	8190	97.2	8.9	660	5.3	0.72	7790	3.89	9.43	0.97	64.53	1.81	2.59	0.41
Mean	611	2.91	8.0	383	2.15	0.29	337	1.94	2.13	0.12	9.72	0.85	0.40	-0.63
Var	$2.06 \cdot 10^6$	319	0.178	$2.23 \cdot 10^4$	1.23	0.038	$1.98 \cdot 10^6$	0.1.65	5.09	0.185	128	0.1	0.295	0.178

	Al	**log (Al)**	**Cl**	**log (Cl)**	**SO_4^{2-}**	**log SO_4^{2-}**	**HCO_3^-**	**log HCO_3^-**	**PO_4^{3-}**	**SiO_2**	**log SiO_2**
	[mg L^{-1}]	[mg L^{-1}]	[mg L^{-1}]	[mg L^{-1}]	[mg L^{-1}]	[mg L^{-1}]	[mg L^{-1}]	[mg L^{-1}]	[mg L^{-1}]	[mg L^{-1}]	[mg L^{-1}]
Nr	8	8	30	30	23	23	30	30	16	21	21
Min	0.01	-2.0	6.38	0.8	0.1	-1.0	104	2.02	-0.1	15.5	1.19
Max	1.10	0.04	42.48	1.63	26.91	1.43	366	2.56	4.63	59.0	1.77
Mean	0.47	-0.56	18.23	1.22	3.84	0.11	218	2.31	1.73	26.13	1.38
Var	0.139	0.416	71.4	0.038	38.9	0.522	$6.89 \cdot 10^3$	0.029	2.03	150	0.029

Tab. A.4 Groundwater geochemical data for the **Na-Cl**-type after /KLI 04/

TDS: Total Dissolved Solids; EC: Electric Conductivity

	TDS	**Ion balance**	**pH**	**EC**	**K**	**log (K)**	**Na**	**log (Na)**	**Mg**	**log (Mg)**	**Ca**	**log (Ca)**	**Fe_{tot}**	**log (Fe_{tot})**
	[mg L^{-1}]	[%]	[-]	[µS cm^{-1}]	[mg L^{-1}]	[mg L^{-1}]	[mg L^{-1}]	[mg L^{-1}]	[mg L^{-1}]	[mg L^{-1}]	[mg L^{-1}]	[mg L^{-1}]	[mg L^{-1}]	[mg L^{-1}]
Nr	655	655	623	636	639	639	655	655	655	655	655	655	597	597
Min	127	-94.99	1.1	159	1.0	0.08	47	1.67	0.2	-0.7	1.96	0.29	0.01	-1.89
Max	448250	74.96	10	383000	5100	3.71	196900	5.29	1950	3.29	4110	3.61	34.10	1.53
Mean	77990	-0.37	7.2	73000	317	2.04	27900	4.01	396.3	2.25	893	2.69	6.85	0.57
Var	$8.55 \cdot 10^9$	88.3	0.289	$5.46 \cdot 10^9$	$1.94 \cdot 10^5$	0.514	$1.19 \cdot 10^9$	0.506	$1.4 \cdot 10^5$	0.514	$5.03 \cdot 10^5$	0.371	38.5	0.34

	Al	**log (Al)**	**Cl**	**log (Cl)**	**SO_4^{2-}**	**log SO_4^{2-}**	**HCO_3^-**	**log HCO_3^-**	**PO_4^{3-}**	**SiO_2**	**log SiO_2**
	[mg L^{-1}]	[mg L^{-1}]	[mg L^{-1}]	[mg L^{-1}]	[mg L^{-1}]	[mg L^{-1}]	[mg L^{-1}]	[mg L^{-1}]	[mg L^{-1}]	[mg L^{-1}]	[mg L^{-1}]
Nr	103	102	655	655	647	647	636	636	196	432	432
Min	0.05	-1.30	18	1.25	0.15	-0.82	2.99	0.48	-2	1	0.0
Max	1.8	0.26	328300	5.52	7880	3.9	943	2.97	3640	58	1.76
Mean	0.31	-0.65	46500	4.22	1630	2.66	290	2.42	42.02	18.23	1.20
Var	0.093	0.115	$3.25 \cdot 10^9$	0.54	$2.93 \cdot 10^6$	1.03	$1.90 \cdot 10^4$	0.047	$1.21 \cdot 10^5$	81.2	0.057

A.4 Data compilation SSA from sorption data base RES³T for relevant mineral phases/-groups

Tab. A.5 Literature values for Gibbsite and recommended mean SSA

Mineral	SSA [m^2 g^{-1}]	Grain size [µm]	Measurement	References
Gibbsite	0.2		BET-N2	TYM96
Gibbsite	0.8		BET (general)	DMBC97
Gibbsite	0.9		BET-N2	TYM96
Gibbsite	1.5		BET (general)	ZDT06
Gibbsite	2.0		BET-N2	GG85
Gibbsite	3.4		BET-N2	HVB87
Gibbsite	3.5		BET (general)	CKWZ06
Gibbsite	3.5		Manufacturer's Specification	SEM99
Gibbsite	4.0		BET-Kr	JGH04
Gibbsite	4.0		BET (general)	ZRS94
Gibbsite	4.9	1.0	BET (general)	H94
Gibbsite	11.2		BET (general)	RLL98
Gibbsite	13.0		Rhodamin B Adsorption	WDA00
Gibbsite	18.0		BET-N2	HHV99
Gibbsite	19.8	0.5	BET-N2	HVB87
Gibbsite	25.0		BET-N2	SSLS98
Gibbsite	31.0		BET-N2	HPQ71
Gibbsite	38.0		Water Vapor Adsorption	PKV06
Gibbsite	38.0		BET (general)	VSAAJ07
Gibbsite	40.1		BET (general)	K97c
Gibbsite	40.3		BET-N2	HHV99
Gibbsite	40.8		BET-N2	HHV99
Gibbsite	45.0		BET-N2	PFRF77
Gibbsite	47.0		BET-N2	HPQ72
Gibbsite	50.0		BET-N2	GSB07a
Gibbsite	56.5		BET-N2	GFG96
Gibbsite	58.0		BET-N2	HPQ72
Gibbsite	65.3		BET-N2	LWCCH06
Gibbsite	96.0		BET (general)	YSS01
Mean	26.3	0.75		
$\pm 2\sigma$	9.1	0.1		

Tab. A.6 Literature values for Fe(III)-minerals and recommended mean SSA

Mineral	SSA [m^2 g^{-1}]	Grain size [µm]	Measurement	References
Goethite	1.4		BET (general)	T93
Goethite	5.5		BET-N2	TEI95
Goethite	7.5		BET (general)	MDCF93b
Goethite	9.0		BET-N2	BCHSS98
Goethite	14.7		BET-N2	MS92
Goethite	15.0		BET-N2	BALEB99
Goethite	15.1	0.25	BET-Ar	PVPGG03
Goethite	15.6		BET-N2	MD01b
Goethite	15.7		BET (general)	NS91
Goethite	17.0		BET-N2	HPQ72
Goethite	17.0		BET-N2	MRS81
Goethite	17.9	0.25	BET-N2	PVPGG03
Goethite	20.0		BET-N2	MMDDA00
Goethite	21.0		BET (general)	NS96
Goethite	21.4		BET-N2	E99
Goethite	21.8		BET-N2	SS00
Goethite	23.0		BET-N2	BLBBS01
Goethite	24.0		BET-N2	ESBK01
Goethite	24.0		BET (general)	MSHVB96
Goethite	27.0		BET-N2	RSRC99
Goethite	27.0		BET-N2	TA01b
Goethite	27.0		BET-N2	ZSP07
Goethite	27.7		BET-N2	CRCO08
Goethite	27.7		BET-N2	GM01
Goethite	27.7		BET-N2	SCRO00
Goethite	28.0		BET-N2	HPQ72
Goethite	28.0		BET (general)	S79
Goethite	30.0		BET (general)	RM01b
Goethite	31.2		BET-N2	GG85
Goethite	32.0		BET-N2	HPQ68
Goethite	32.4	0.1	BET-Ar	PVPGG03
Goethite	32.7		BET (general)	PS04c
Goethite	33.0		BET-N2	RSRC99
Goethite	33.1		BET (general)	WAABC00
Goethite	33.7		BET-N2	LMJ06
Goethite	33.7		BET-N2	RZEAA88
Goethite	33.8		BET (general)	PHBC06
Goethite	34.0		BET-N2	DLT89
Goethite	34.4		BET-N2	CRS99
Goethite	34.4		BET-N2	WT06
Goethite	35.0		BET (general)	MGM03
Goethite	35.6		BET-N2	PH97
Goethite	36.5		BET-N2	GLS94
Goethite	37.0		BET-N2	BPS00d
Goethite	37.7		BET-N2	CRCO08
Goethite	37.9		BET-N2	SCRO00
Goethite	38.0		BET (general)	HV96
Goethite	38.0	0.1	BET-N2	PVPGG03

Tab. A.6 (cont.) Literature values for Fe(III)-minerals and recommended mean SSA

Mineral	SSA [m^2 g^{-1}]	Grain size [µm]	Measurement	References
Goethite	38.2		BET-N2	SCRO00
Goethite	39.0		BET-N2	Y75
Goethite	39.1		BET-N2	PL96
Goethite	39.9		BET-N2	LSS90
Goethite	40.0		BET-N2	CHSGS08
Goethite	40.0		BET-N2	LCV99
Goethite	40.1		BET-N2	WWDPC06
Goethite	40.3		BET-N2	GAAGN02
Goethite	40.7		BET-N2	G94a
Goethite	40.7		BET-N2	SCRO00
Goethite	42.1		BET-N2	JSL06
Goethite	42.1		BET-N2	JSL06
Goethite	43.0		BET-N2	NPLS96
Goethite	43.2		BET-N2	GS93
Goethite	43.7		BET (general)	JSH75
Goethite	43.7		BET-N2	MG96b
Goethite	45.0		BET (general)	BBP97b
Goethite	45.0		BET (general)	HL85
Goethite	45.0		BET-N2	MFG98
Goethite	45.0		BET-N2	MG96b
Goethite	45.0		BET-N2	VRL94
Goethite	46.0		BET-N2	DK90
Goethite	47.5		BET-N2	CS95
Goethite	48.0		BET-N2	Y75
Goethite	48.5		BET-N2	BM79
Goethite	48.8		BET (general)	YM96
Goethite	49.0	0.3	BET-N2	JM77
Goethite	49.2		BET-N2	BC87
Goethite	49.5		BET (general)	K97c
Goethite	49.6		BET (general)	AWJ99b
Goethite	50.0		BET (general)	CCBPC92
Goethite	50.0		BET (general)	GESGA97
Goethite	50.0		BET-N2	ZB99
Goethite	51.8		BET-N2	BM81
Goethite	52.0		BET-N2	HL86a
Goethite	54.0		BET-N2	DH03
Goethite	54.0		BET-N2	Y75
Goethite	55.0		BET-N2	CHSGS08
Goethite	55.0		BET-N2	RJW93
Goethite	55.7		BET (general)	LS00
Goethite	55.9		BET (general)	ZSK95
Goethite	58.6		BET-N2	DA96
Goethite	60.0		BET-N2	CF01
Goethite	60.0		BET-N2	HPQ71
Goethite	62.0		BET-N2	CW04
Goethite	63.5			PFS99
Goethite	63.7			GFG96
Goethite	64.0			RFRG02

Tab. A.6 (cont.) Literature values for Fe(III)-minerals and recommended mean SSA

Mineral	SSA [m^2 g^{-1}]	Grain size [µm]	Measurement	References
Goethite	64.4			TEH00
Goethite	65.0			BPQ75
Goethite	66.0		BET-N2	MF92a
Goethite	66.0		BET-N2	TE02
Goethite	68.0		BET-N2	R96
Goethite	68.0		BET (general)	RGB85
Goethite	70.0		BET-N2	OTBBP00
Goethite	70.0		BET-N2	VL00
Goethite	70.9		BET-N2	APQ67
Goethite	71.0		BET (general)	KPONK00
Goethite	73.0		BET-N2	TEI95
Goethite	75.0		BET-N2	BPQ75
Goethite	75.8		BET-N2	GEB07
Goethite	76.0		BET (general)	J90
Goethite	76.0		BET-N2	RAV94
Goethite	76.0		BET (general)	WS01
Goethite	78.0		BET-N2	DH06
Goethite	78.0		BET (general)	P83a
Goethite	79.0		BET-N2	OMJCB05
Goethite	79.4		BET-N2	AD96a
Goethite	80.0		BET-N2	BPQ75
Goethite	80.5		BET-N2	GGSC98
Goethite	81.0		BET-N2	HPQ71
Goethite	81.0		BET-N2	MA86
Goethite	82.5		BET-N2	BLSP07
Goethite	84.0		BET-N2	JC04
Goethite	84.0		BET-N2	PZS06
Goethite	85.0		BET-N2	BLBBS01
Goethite	85.0		BET-N2	HV06
Goethite	86.0		BET-N2	LE94
Goethite	87.0		BET-N2	WE02
Goethite	88.0		BET-N2	OSS01
Goethite	89.0		BET-N2	FPQ74
Goethite	89.0	0.12	BET (general)	OQA06
Goethite	90.0		BET-N2	BPS00c
Goethite	90.0		BET-N2	CHSGS08
Goethite	90.0		BET-N2	OTBBP00
Goethite	93.0		BET (general)	AHCMB01
Goethite	94.0		BET-N2	NLP08
Goethite	94.0		BET-N2	VTL01
Goethite	94.0		BET-N2	WVKH06
Goethite	95.0		BET (general)	OBPP00
Goethite	95.0		BET-N2	VHV96b
Goethite	96.4		BET (general)	GHV97
Goethite	98.0		BET-N2	SHV06b
Goethite	98.6		BET-N2/He	RHV06a
Goethite	100.0		BET-N2	HDV89
Goethite	103.0		BET-N2	GEG01

Tab. A.6 (cont.) Literature values for Fe(III)-minerals and recommended mean SSA

Mineral	SSA [$m^2 g^{-1}$]	Grain size [µm]	Measurement	References
Goethite	103.0	8.77	BET (general)	LNPR06
Goethite	105.0		BET-N2	HV96
Goethite	110.0		BET-N2	CHSGS08
Goethite	117.0		BET-N2	JAR04
Goethite	148.8		BET-N2	GFG96
Goethite	149.0		BET-N2	CBRZ04
Goethite	149.0		BET-N2	RCBR07
Goethite	176.0		BET-N2	RZEAA88
Goethite	186.0		BET (general)	RZEAA88
Hematite	30.0	0.1	BET-N2	CHM83
Hematite	30.0		BET (general)	LS07a
Hematite	30.0		BET (general)	PS04c
Hematite	0.1		BET-N2	TEI95
Hematite	0.6		BET-N2	TEI95
Hematite	1.5		BET-N2	VT98
Hematite	3.1	0.3	BET (general)	HL85
Hematite	3.2		BET (general)	NS91
Hematite	4.0	2.2	BET-N2	RGKB98a
Hematite	4.5		BET-N2	TEI95
Hematite	5.6		BET-N2	TTMF99
Hematite	5.8		BET-N2	NFNTS99
Hematite	5.9		BET (general)	NS91
Hematite	6.0		BET-Kr	KILLS98
Hematite	6.0	5	BET (general)	P98
Hematite	7.9		BET-N2	YMRF81
Hematite	8.4	0.15	BET (general)	DLFJR03
Hematite	8.5		BET-N2	MDCF93a
Hematite	9.0		BET-N2	OMJCB05
Hematite	9.6		BET-N2	SVYT03
Hematite	10.1		BET (general)	GSCLM94
Hematite	10.9		BET-N2	GFG96
Hematite	11.8		BET (general)	T93
Hematite	13.3	0.125	BET (general)	KHM88
Hematite	14.0		BET-N2	PS02a
Hematite	14.4	0.078	BET-N2	KHL99
Hematite	14.7		BET (general)	BSS93
Hematite	15.9		BET-N2	TTMF99
Hematite	16.4		BET-N2	GG85
Hematite	17.0	0.765	BET (general)	KDKK07
Hematite	18.0		BET-N2	BL71
Hematite	18.0		BET-N2	MRS81
Hematite	18.1		BET-N2	LZJS06
Hematite	18.9		BET-N2	LZJS06
Hematite	19.0	0.055	BET-N2	C96
Hematite	20.0	0.12	BET (general)	CFKM91
Hematite	20.5		BET-N2	LZJS06
Hematite	21.0		BET-N2	BL71

Tab. A.6 (cont.) Literature values for Fe(III)-minerals and recommended mean SSA

Mineral	SSA [$m^2 g^{-1}$]	Grain size [µm]	Measurement	References
Hematite	21.0		BET (general)	OD66
Hematite	22.0		BET-N2	PD62
Hematite	23.0		BET-N2	APQ67
Hematite	23.0	0.05	BET-N2	PDCF02
Hematite	26.5		BET-N2	VDKB87
Hematite	28.3	0.119	BET-N2	CK99
Hematite	29.0		BET (general)	F87
Hematite	31.0		BET-N2	BL71
Hematite	31.9	0.134	BET (general)	CJ02
Hematite	32.0		BET-N2	Y75
Hematite	32.3		BET (general)	GK90
Hematite	32.8		BET (general)	BRLD00
Hematite	33.0		BET-N2	HLLH07
Hematite	34.0		BET (general)	B73
Hematite	34.0	0.12	BET-N2	HD85
Hematite	34.1		BET-N2	APQ67
Hematite	35.0	0.0015	BET-N2	BL73
Hematite	36.0		BET-N2	HPQ72
Hematite	36.0		BET (general)	JRKTM07
Hematite	36.4		BET-N2	APQ67
Hematite	43.5		BET-N2	APQ67
Hematite	44.6		BET-N2	APQ67
Hematite	46.1		BET (general)	BRLD00
Hematite	47.0		BET-N2	ID97
Hematite	47.8		BET (general)	PBKS05
Hematite	49.0		BET (general)	BBP97b
Hematite	56.0		BET-N2	B71
Hematite	80.0		BET (general)	L88
Hematite	109.3		BET-N2	LCV99
Hematite	191.6	3	BET (general)	SMK02
Mean value	47.9	0.97		
$\pm 2\sigma$	4.6	0.87		

Tab. A.7 Literature values for Mixed-layer-clay-minerals and mean SSA

Mineral	SSA [$m^2 g^{-1}$]	Grain size [µm]	Measurement	References
Montmorillonite	9.7		BET-N2	TS96
Montmorillonite	13.2		BET-N2	GG86
Montmorillonite	14.9		BET-N2/He	SH90
Montmorillonite	15.2		BET-N2	SSLS98
Montmorillonite	18.6		BET-N2	GG86
Montmorillonite	19.8		Saers' method	BG06a
Montmorillonite	21.4		BET (general)	SS93a
Montmorillonite	24.0		BET-N2	TBCLG05
Montmorillonite	29.4		BET-N2	BDP00
Montmorillonite	31.0		BET (general)	GP00
Montmorillonite	31.0	0.36	BET-N2	ZSRC92
Montmorillonite	31.5		BET (general)	WAKWW94
Montmorillonite	31.6		BET (general)	VF79
Montmorillonite	31.8		BET-N2	IWJA05a
Montmorillonite	31.8		BET-N2	UD93
Montmorillonite	31.8		BET (general)	WBCGA98
Montmorillonite	32.0		BET-N2	RPBGB05
Montmorillonite	35.0		BET-N2	BB97a
Montmorillonite	35.0		BET-N2	KDSE04
Montmorillonite	38.4		BET-N2	JB02
Montmorillonite	46.0		BET (general)	JBTMC06
Montmorillonite	52.3		Saers' method	BG06a
Montmorillonite	53.6		BET-N2	GG86
Montmorillonite	55.0		BET-N2	TKKMT98
Montmorillonite	68.9		BET-N2	G02a
Montmorillonite	70.3		BET-N2	GFG96
Montmorillonite	83.9		BET-N2	IWJA05a
Montmorillonite	83.9		BET-N2	IWJA05a
Montmorillonite	84.0		BET-N2	VF79
Montmorillonite	87.0		BET-N2	BDP00
Montmorillonite	88.7		BET-N2	BSNS97
Montmorillonite	89.0		BET-N2	DSMSB02
Montmorillonite	92.0		BET (general)	VF79
Montmorillonite	95.0		BET-N2	PH96
Montmorillonite	97.0		BET-N2	BPTA96
Montmorillonite	144.0		BET (general)	H84
Montmorillonite	213.0	2.9	BET (general)	GP00
Montmorillonite	245.0		BET-N2	CYZD06
Illite	7.9		BET-N2	KKC96
Illite	11.8		BET-N2	GG86
Illite	16.4		BET-N2	WMDV98
Illite	17.0		BET-N2	ES01
Illite	19.0		BET-N2	LSFDT99
Illite	21.5		BET-N2	GG86
Illite	22.3		BET-N2	D97c
Illite	22.6		BET-N2	G02a
Illite	23.7		BET-N2	GG86
Illite	24.2		BET-N2	MG96a

Tab. A.7 (cont.) Literature values for MIxed-layer-clay-minerals and mean SSA

Mineral	SSA [m^2 g^{-1}]	Grain size [µm]	Measurement	References
Illite	24.8		BET-N2	BBEHM95
Illite	24.9		BET-N2	GFG96
Illite	25.2		BET-N2	LSFDT99
Illite	25.6		BET-N2	JB02
Illite	26.2		BET (general)	LSFDT99
Illite	31.7		BET-N2	BBEHM95
Illite	33.5		BET-N2	BSNS97
Illite	36.5		BET-N2	JF06
Illite	41.0		BET (general)	NTTS98
Illite	49.2		BET-N2)	LSFDT99
Illite	53.4		BET (general)	LSFDT99
Illite	60.1		BET-N2	SAKW00
Illite	61.0		BET-N2	KASW00
Illite	66.8		BET-N2	GE07
Illite	77.1		BET (general)	WB91
Illite	79.2		BET (general)	WB91
Illite	97.0		BET-N2	RPBGB05
Illite	100.0		BET (general)	ML91
Illite	123.3		BET (general)	LAWJ03
Illite	141.0		BET (general)	EZEG05
Illite	200.0		BET-N2	KYSY06
Mean value	55.6	1.75		
±2σ	11.5	1.49		

A.5 Results of the uncertainty analysis

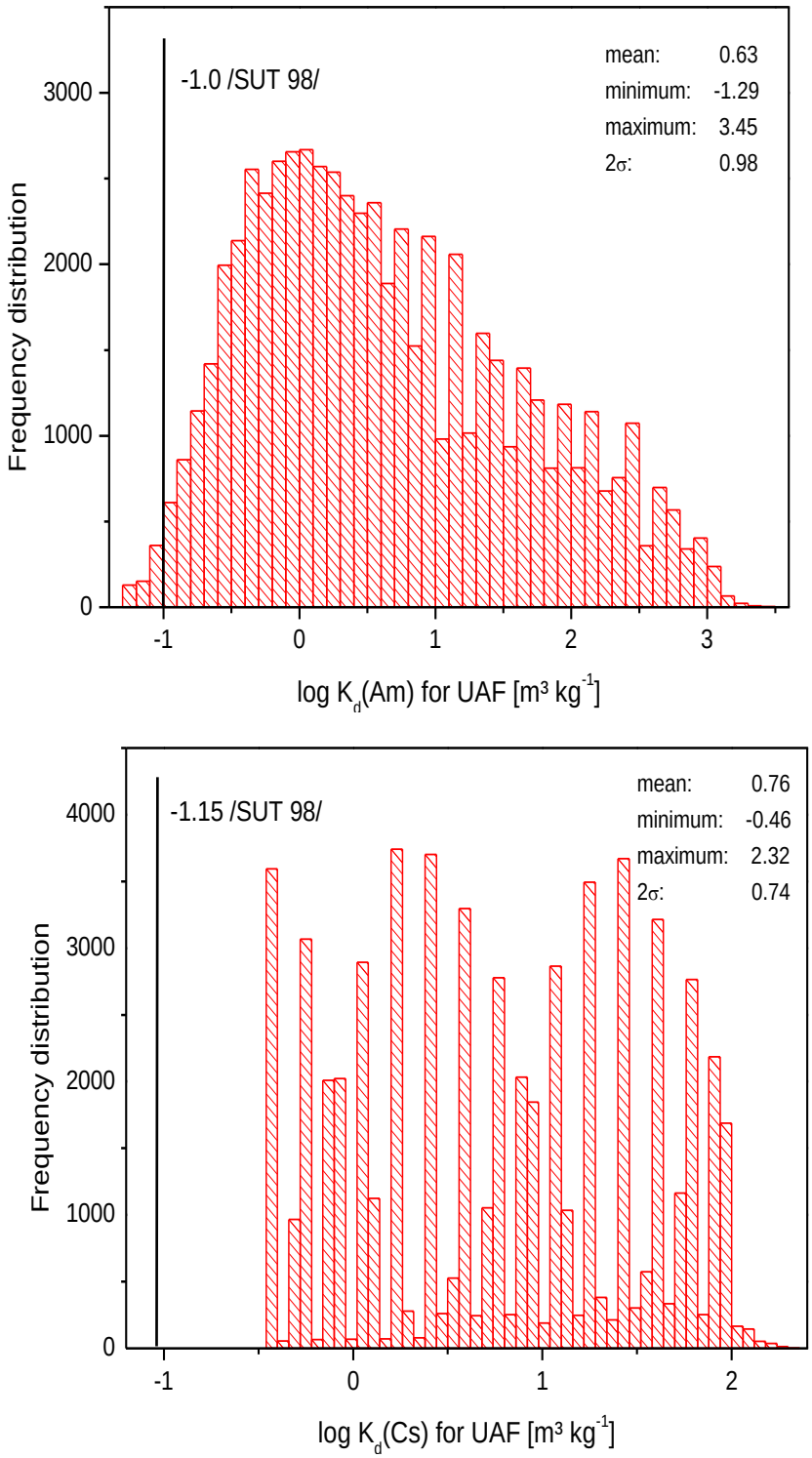

Fig. A.3 Frequency distribution of the calculated smart K_d-values for every radionuclide in UAF, and their mean, minimum, maximum and standard deviation (2σ) as well as the previously used constant K_d-values from /SUT 98/ for freshwater conditions

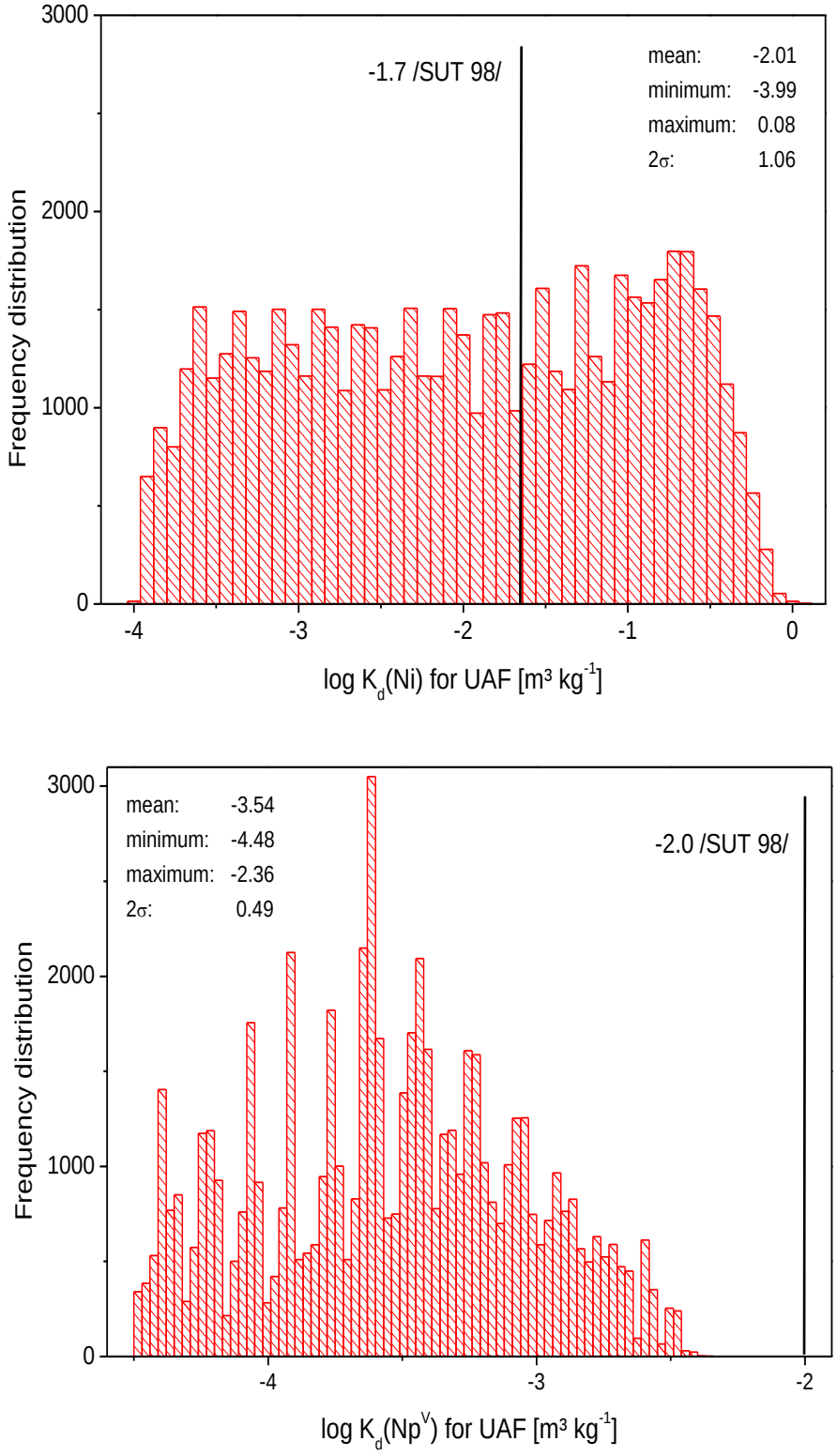

Fig. A.3 (cont.) Frequency distribution of the calculated smart K_d-values for every radionuclide in UAF, and their mean, minimum, maximum and standard deviation (2σ) as well as the previously used constant K_d-values from /SUT 98/ for freshwater conditions

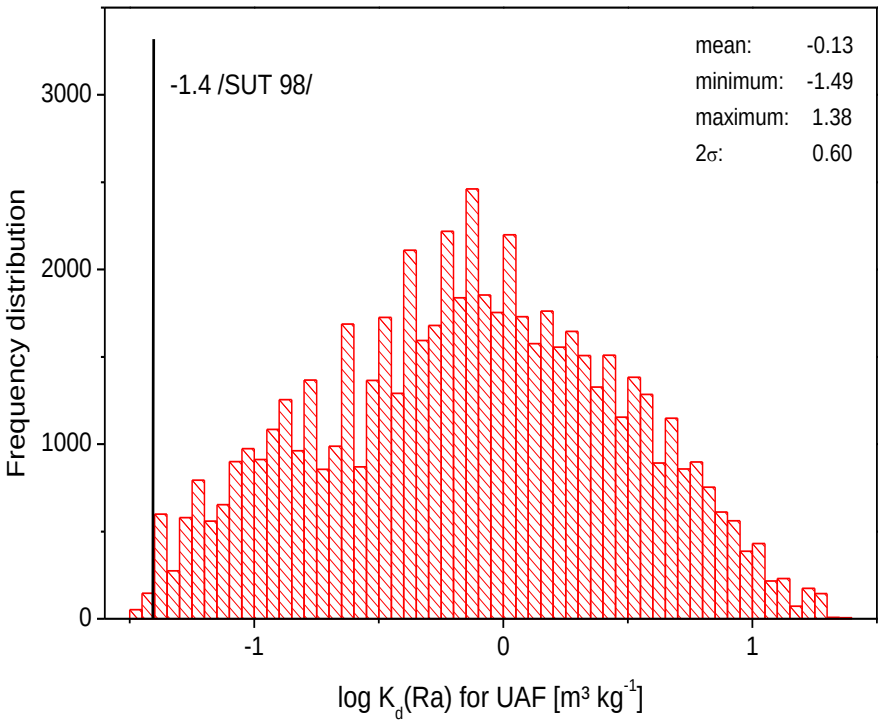

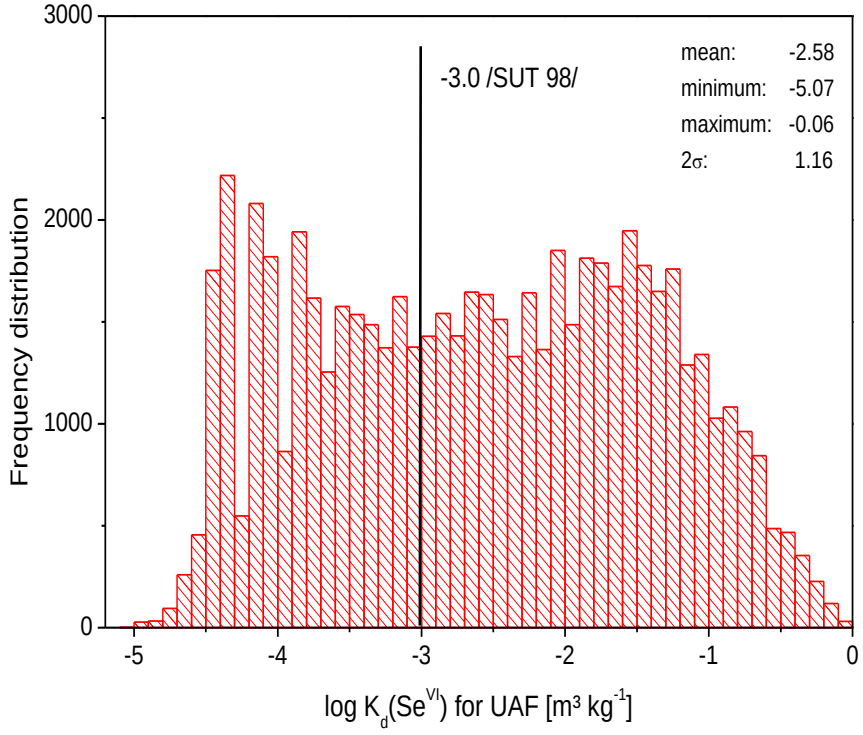

Fig. A.3 (cont.) Frequency distribution of the calculated smart K_d-values for every radionuclide in UAF, and their mean, minimum, maximum and standard deviation (2σ) as well as the previously used constant K_d-values from /SUT 98/ for freshwater conditions

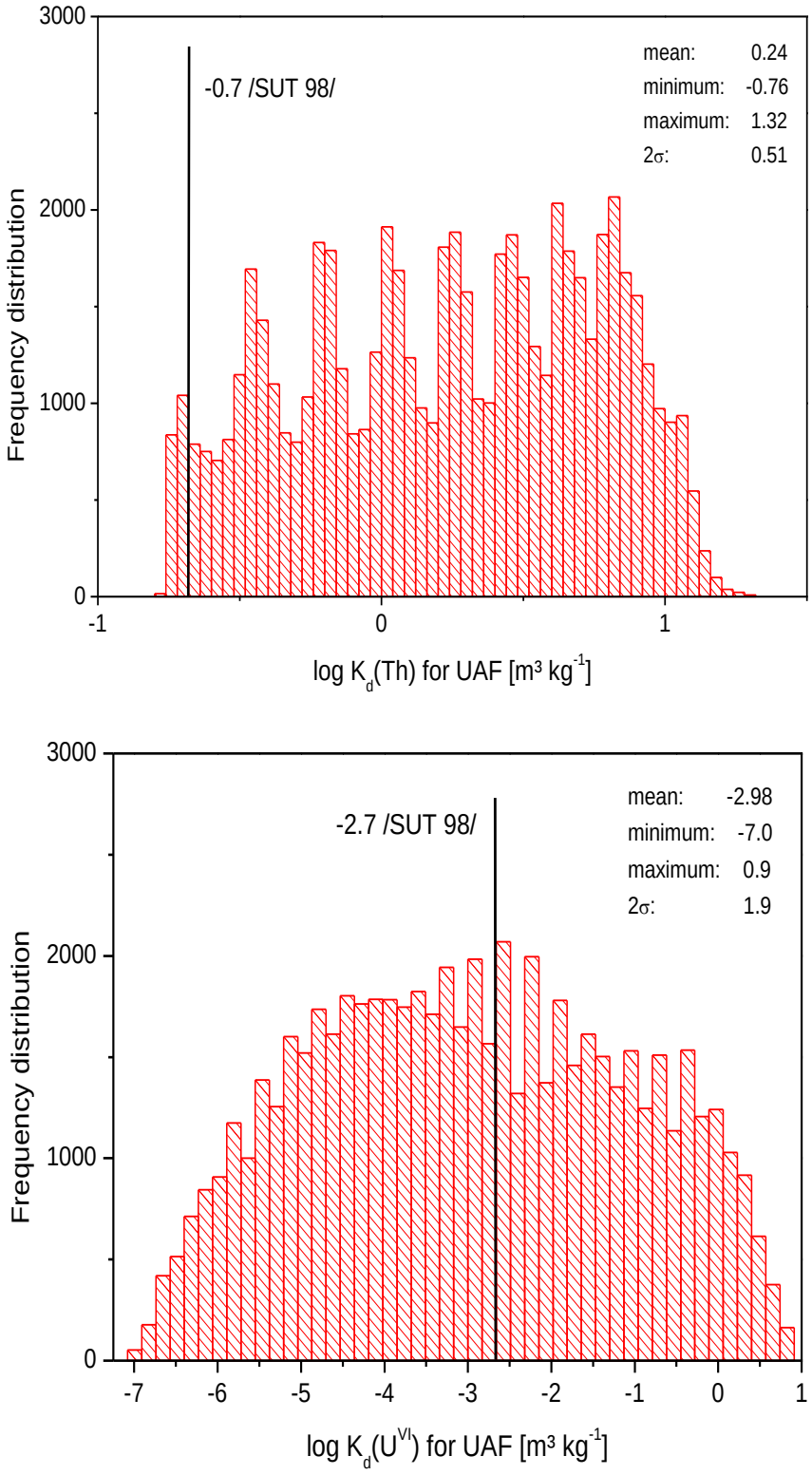

Fig. A.3 (cont.) Frequency distribution of the calculated smart K_d-values for every radionuclide in UAF, and their mean, minimum, maximum and standard deviation (2σ) as well as the previously used constant K_d-values from /SUT 98/ for freshwater conditions

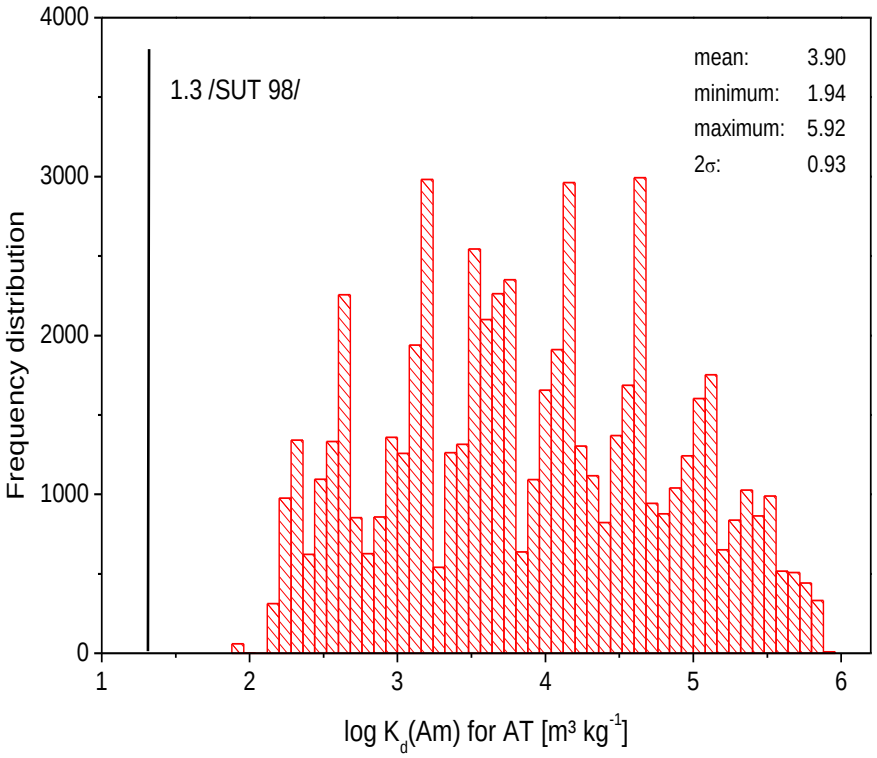

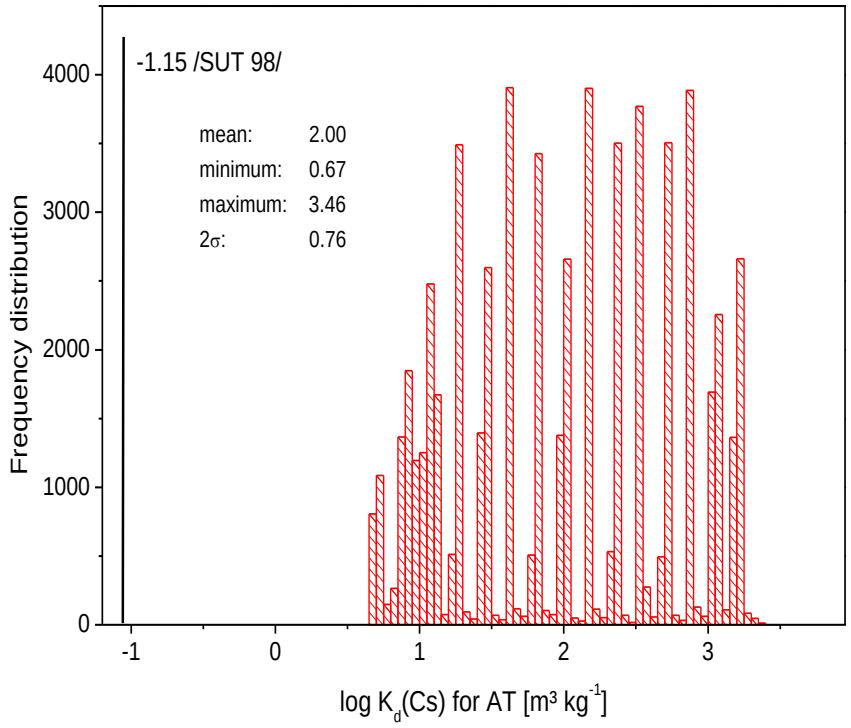

Fig. A.4 Frequency distribution of the calculated smart K_d-values for every radionuclide in AT, and their mean, minimum, maximum and standard deviation (2σ) as well as the previously used constant K_d-values from /SUT 98/ for saltwater conditions

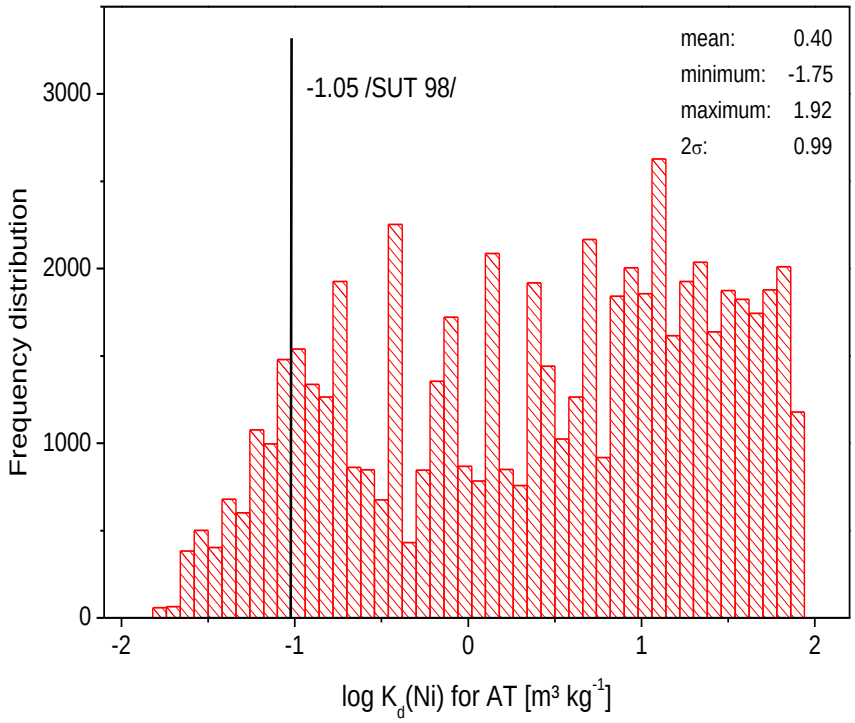

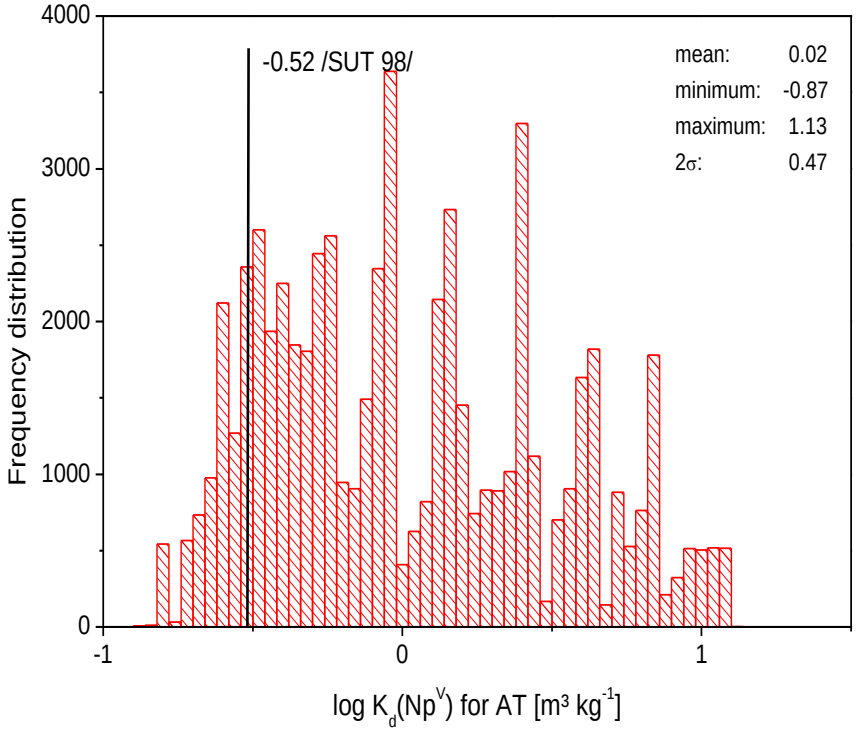

Fig. A.4 (cont.) Frequency distribution of the calculated smart K_d-values for every radionuclide in AT, and their mean, minimum, maximum and standard deviation (2σ) as well as the previously used constant K_d-values from /SUT 98/ for saltwater conditions

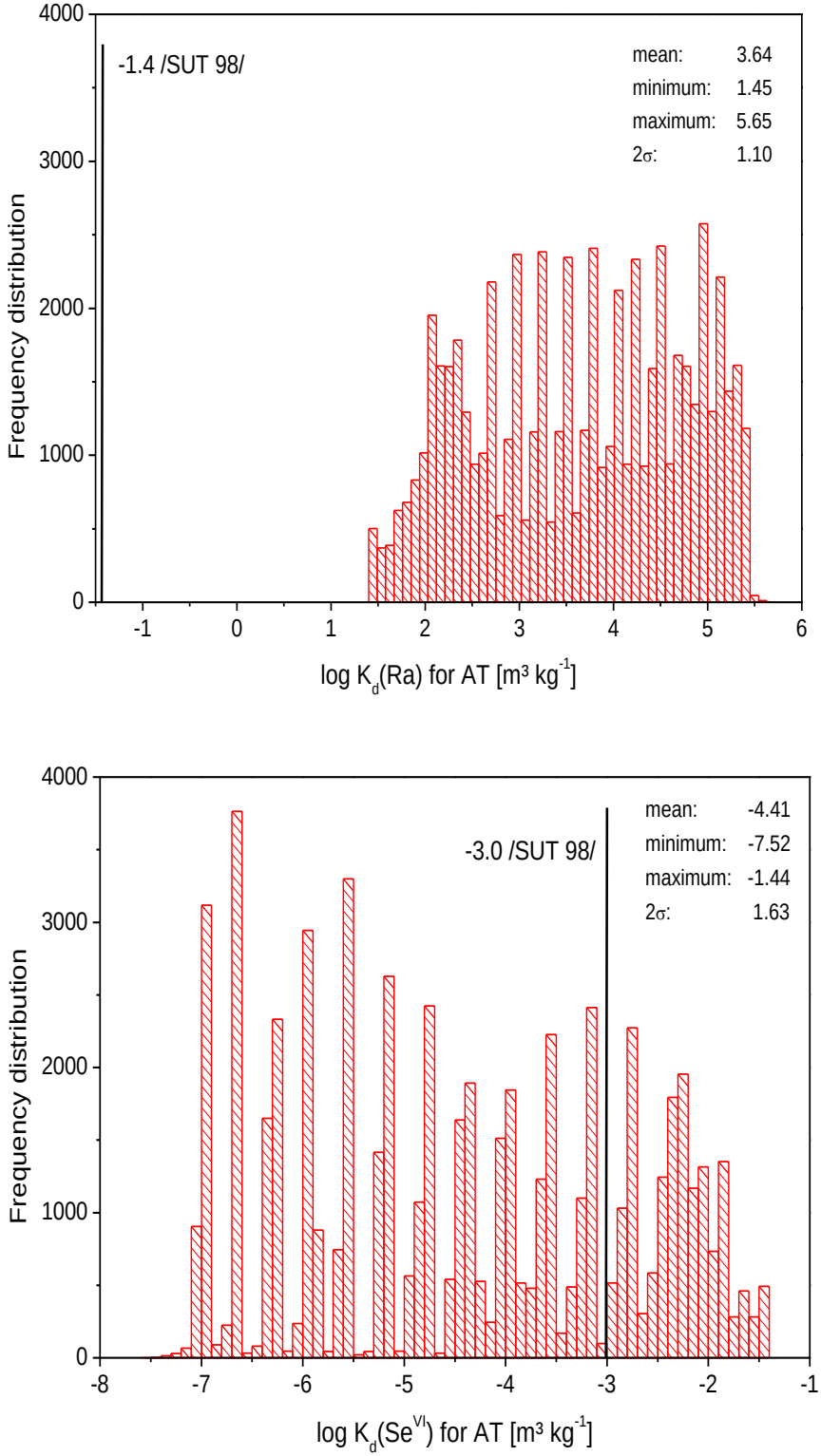

Fig. A.4 (cont.) Frequency distribution of the calculated smart K_d-values for every radionuclide in AT, and their mean, minimum, maximum and standard deviation (2σ) as well as the previously used constant K_d-values from /SUT 98/ for saltwater conditions

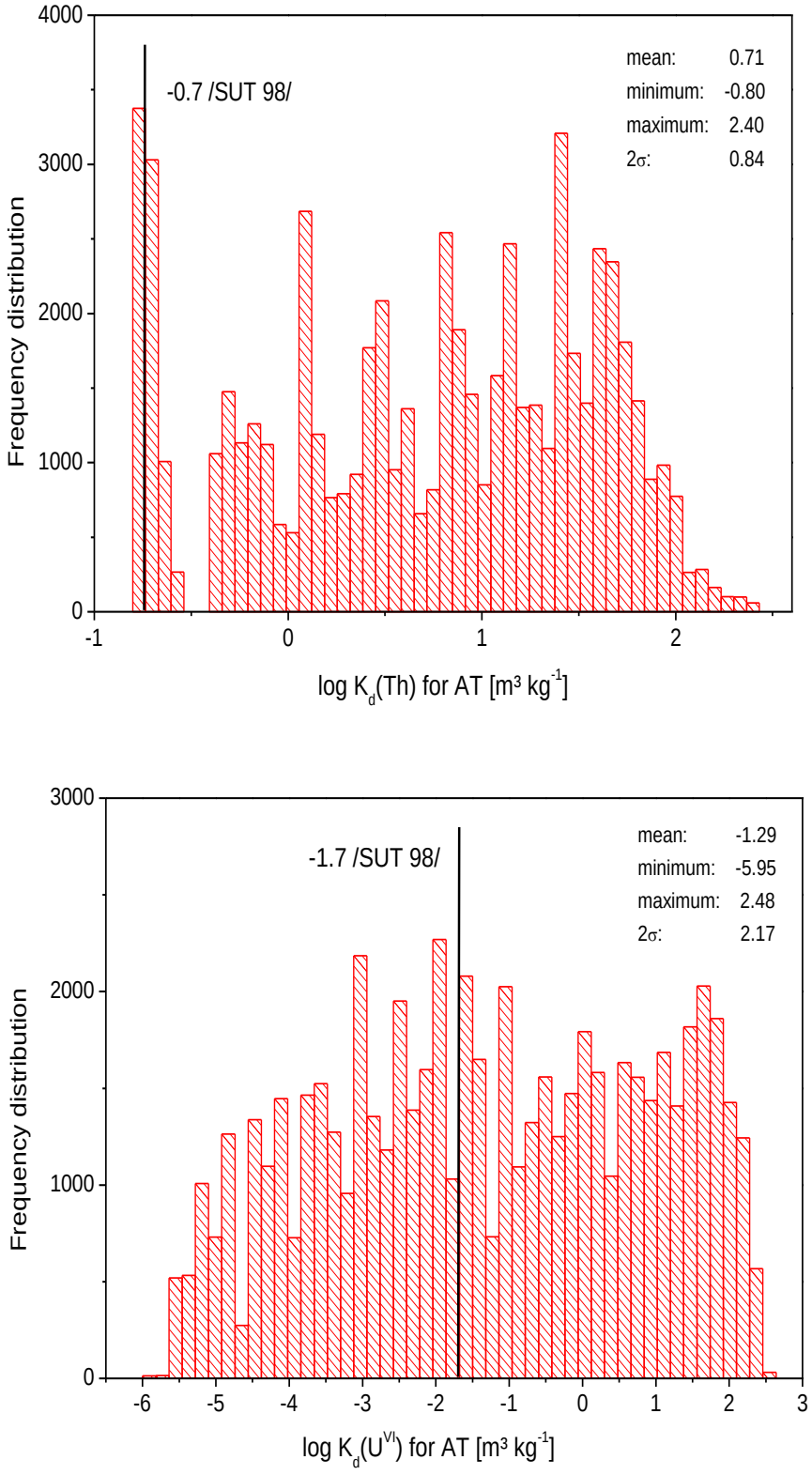

Fig. A.4 (cont.) Frequency distribution of the calculated smart K_d-values for every radionuclide in AT, and their mean, minimum, maximum and standard deviation (2σ) as well as the previously used constant K_d-values from /SUT 98/ for saltwater conditions

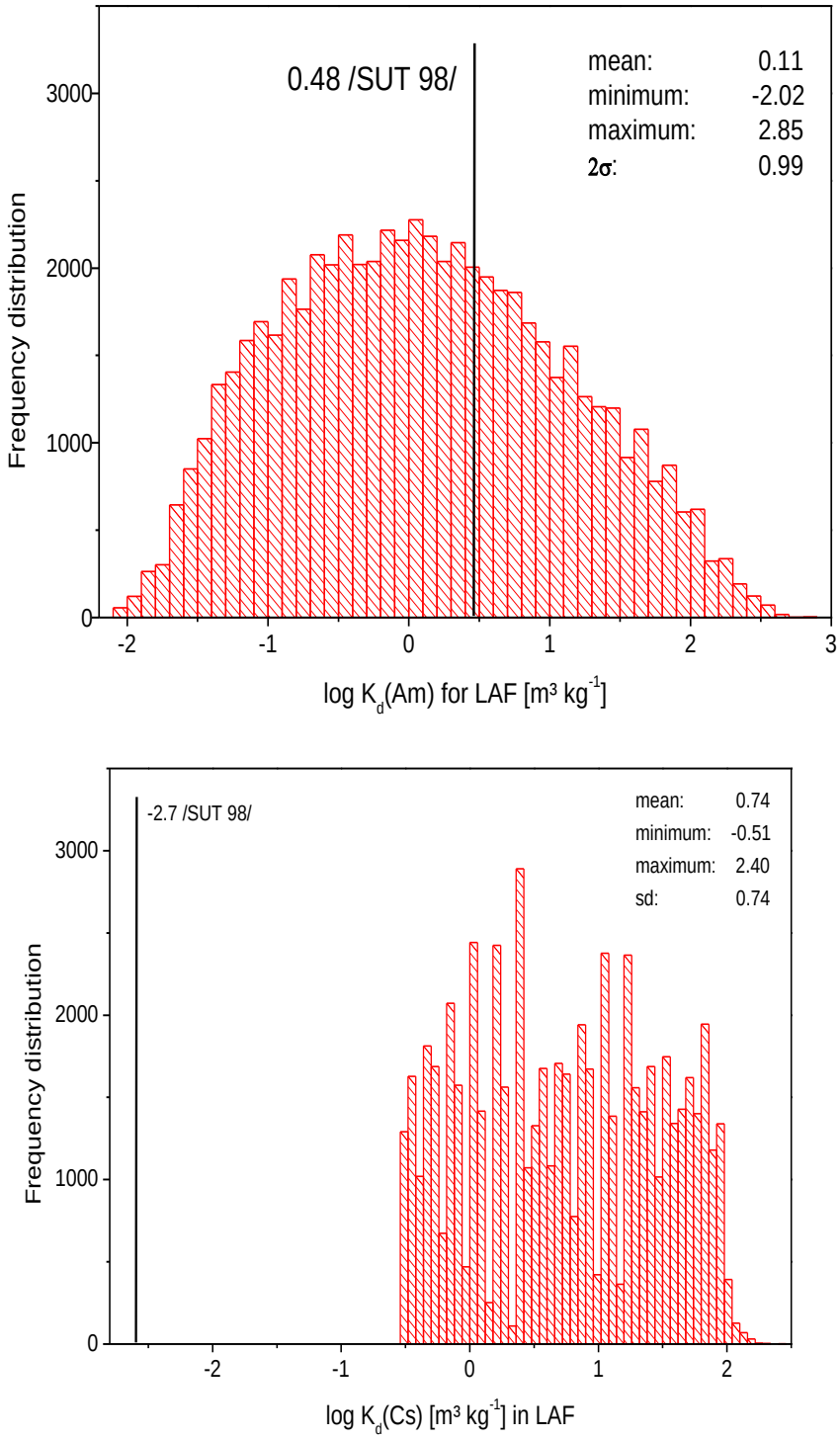

Fig. A.5 Frequency distribution of the calculated smart K_d-values for every radionuclide in LAF, and their mean, minimum, maximum and standard deviation (2σ) as well as the previously used constant K_d-values from /SUT 98/ for saltwater conditions

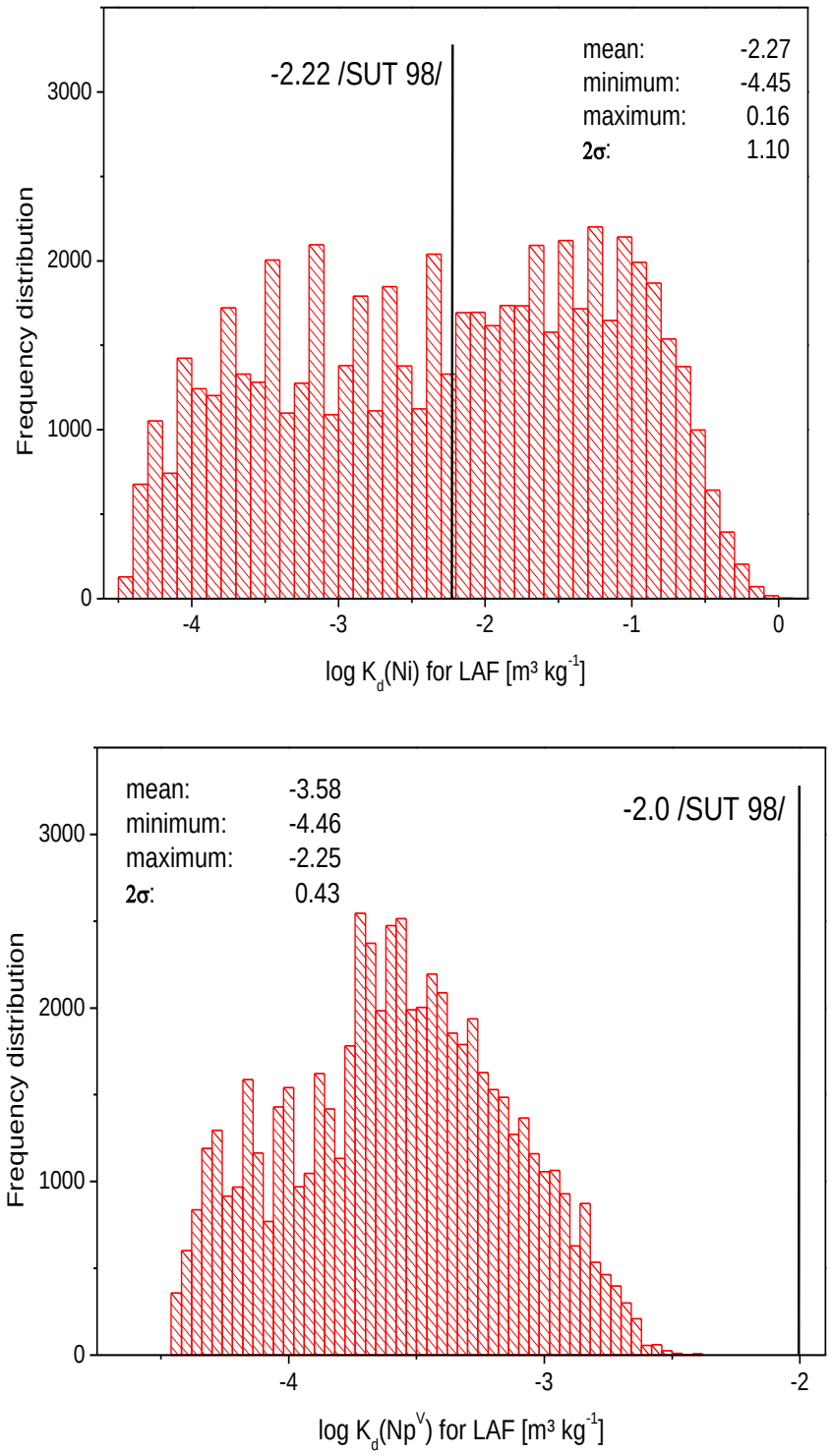

Fig. A.5 (cont.) Frequency distribution of the calculated smart K_d-values for every radionuclide in LAF, and their mean, minimum, maximum and standard deviation (2σ) as well as the previously used constant K_d-values from /SUT 98/ for saltwater conditions

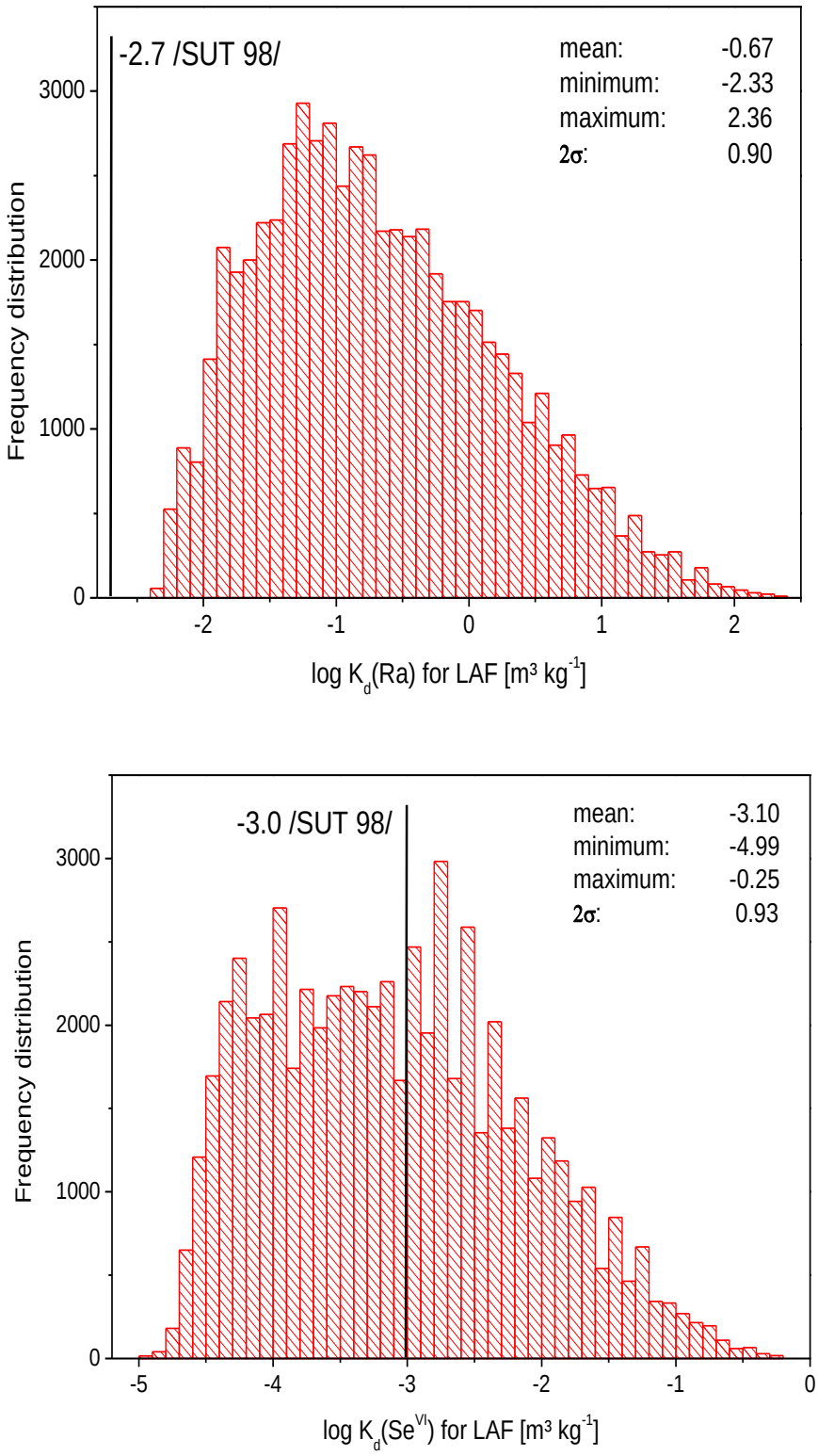

Fig. A.5 (cont.) Frequency distribution of the calculated smart K_d-values for every radionuclide in LAF, and their mean, minimum, maximum and standard deviation (2σ) as well as the previously used constant K_d-values from /SUT 98/ for saltwater conditions

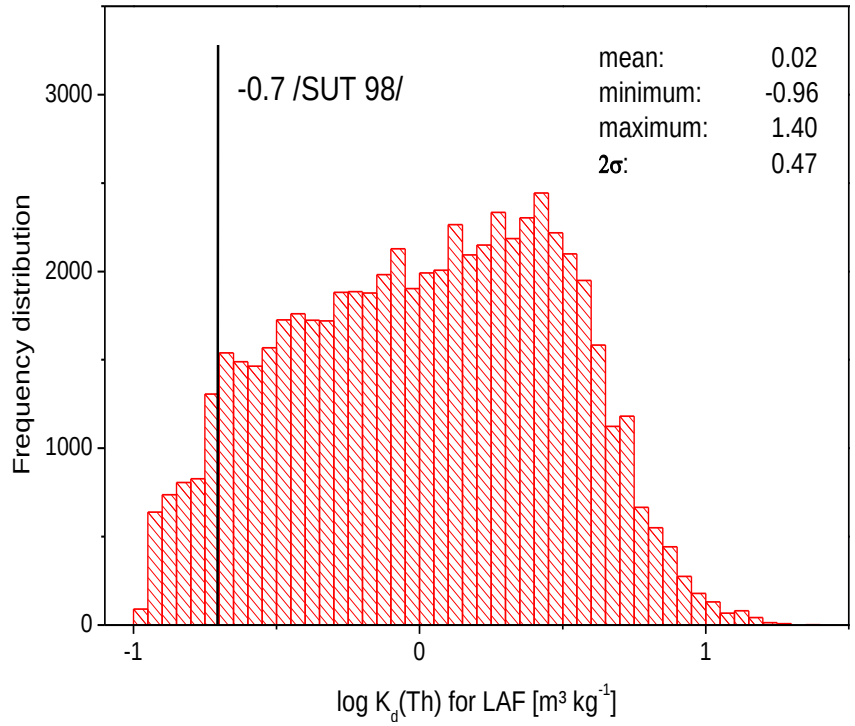

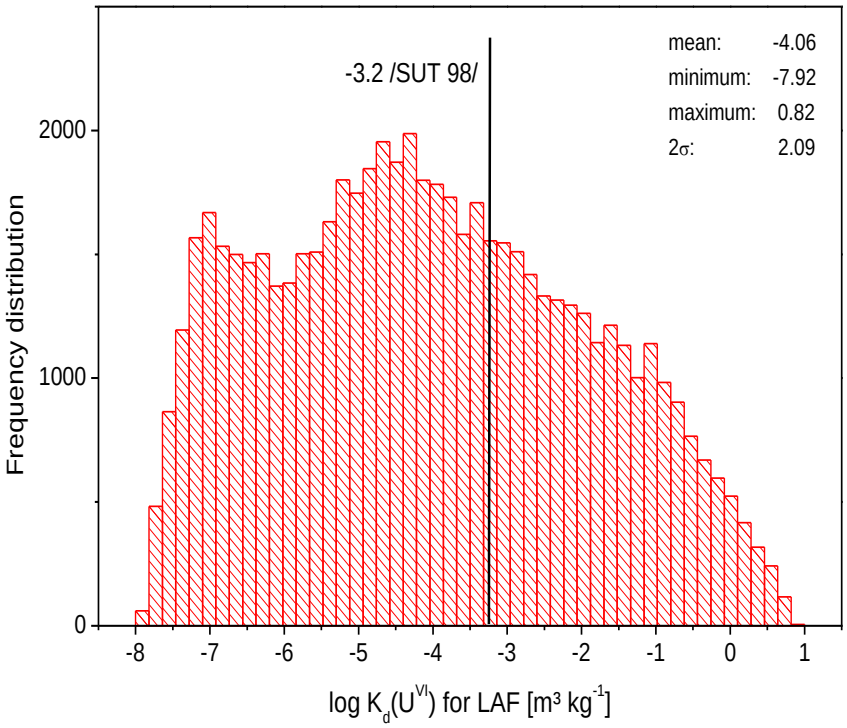

Fig. A.5 (cont.) Frequency distribution of the calculated smart K_d-values for every radionuclide in LAF, and their mean, minimum, maximum and standard deviation (2σ) as well as the previously used constant K_d-values from /SUT 98/ for saltwater conditions

A.6 Batch experiments

A.6.1 Batch experiments involving Th^{4+}

As introduced earlier all batch experiments started out with pretest. Th^{4+} pretests, however, revealed that final Th^{4+} batch experiments employing the defined chemical conditions are not feasible.

First pretests are to define a suitable solid-liquid ratio for the according Th^{4+} batch experiments. Hence, three different M/V are chosen with an initial concentration 10^{-5} mol L^{-1} Th^{4+}. The suspensions are stored in LDPE vessels with pH-values ranging between 7.55 and 7.73. According to the varying amount of applied orthoclase measurements are expected to result in different sorbat concentrations. However, collected data displays sorbed Th^{4+} concentrations ranging from 98 % to 100 % indicating the applied M/V ratios do not have a pronounced influence on the sorption behavior.

In order to analyze the monitored low equilibrium concentrations vessel-sorption experiments are conducted since sorption processes on the containers' surfaces or e. g. other side reactions are assumed to interfere with the mineral's surface complexation reactions. To already prevent possible unwanted reactions with the vessels' synthetic material the pH is set to equal 3.2. Fig. A**.6** illustrates obtained results.

Five different kinds of test tubes (PFA (Technical University of Braunschweig), PFA (Analysetechnik Helmut Feuerbacher AG), PPCO (Polypropylene Copolymer centrifuge bottles), PE, glass) hold five different Th^{4+} concentrations in 0.01 M $NaClO_4$, respectively. Concentrations range between 0.5 ppb and 2320 ppb Th^{4+}. Samples are shaken head first and analyzed after 24 hours. No additional sorbents, e. g. minerals, are added. Even though PFA and PPCO are known to be very insusceptible towards surface reactions, subsequent ICP-MS measurements reveal very low recovery rates of the initially introduced concentrations in all of the implemented containers including PFA and PPCO material. This indicates the occurrence of surface reactions on the synthetic surfaces or e. g. precipitation reactions under the chosen chemical conditions.

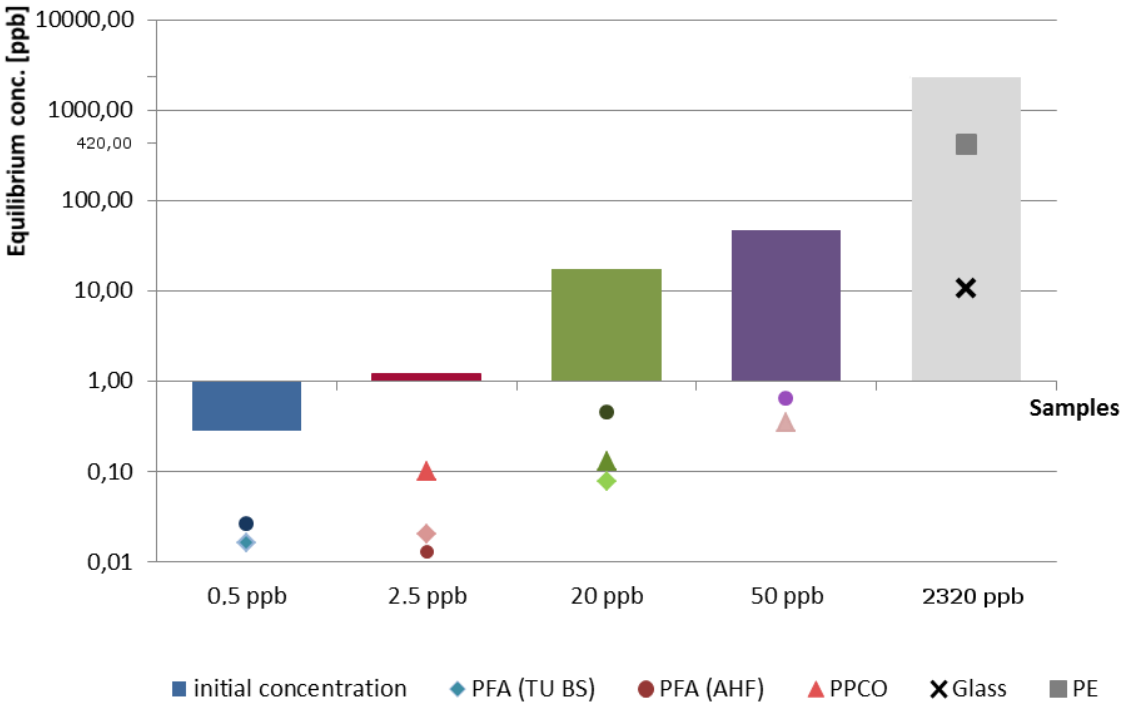

Fig. A.6 Th^{4+} equilibrium concentrations obtained from vessel-sorption experiments

Following, leaching experiments are conducted by rinsing the vessels employed for the vessel-sorption experiment with 5 % HNO_3 over 24 hours. Experiments yield that Th^{4+} interacts with all synthetic and glass surfaces resulting in high recovery rates. However, it is possible that Th^{4+} does not only interact with the vessels surfaces but also with e. g. syringes or pipette tips. Hence, it is refrained from conducting Th^{4+} batch experiments in the further course of the study since side reactions cannot be ruled out under the requested geochemical conditions.

A.6.2 Experimental data

Corrected final datasets for the different batch experiments described in section 4 are listed in Tab. A.8 to Tab. A.12.

Tab. A.8 Corrected final data set obtained from muscovite-Cs^+ batch experiments

C_o - initial concentration, C_{equil} - measured equilibrium concentration in the samples, δ f- standard deviation of each measurement, C_{sorb} - calculated sorbat concentration, LOQ/LOD - limit of quantification/determination.

		Co 1/20 = 1458,434 µg/L = 1,097*10^-5 M Co 1/80 = 1440,667 µg/L = 1,084*10^-5 M					Co 1/20 = 174,199 µg/L = 1,311*10^-6 M Co 1/80 = 151,171 µg/L = 1,137*10^-6 M					Co 1/20 = 45,776 µg/L = 3,444*10^-7 M Co 1/80 = 22,221 µg/L =1,671*10^-7 M					Co 1/20 = 32,934 µg/L =2,478*10^-7 M Co 1/80 = 9,255 µg/L =6,964*10^-8 M				
		pH	C_{equil} [ppb] MS	δ [ppb] C_{equil}	C_{sorb} [ppb]	Sorption [%]	pH	C_{equil} [ppb] MS	δ [ppb] C_{equil}	C_{sorb} [ppb]	Sorption [%]	pH	C_{equil} [ppb] MS	δ [ppb] C_{equil}	C_{sorb} [ppb]	Sorption [%]	pH	C_{equil} [ppb] MS	δ [ppb] C_{equil}	C_{sorb} [ppb]	Sorption [%]
1/20	pH6	I	4,21	**1302,000**		156,434	10,726											6,03	**0,208**	0,002	32,726	99,368
		II						5,45	**84,190**	1,247	90,010	51,670	5,93	**5,351**	0,299	40,425	88,311	5,98	**0,200**	0,003	32,734	99,393
		III	4,38	**1292,000**	16,28	166,434	11,412	5,32	**83,170**	0,716	91,030	52,256	5,95	**6,484**	0,159	39,292	85,835					
	pH7	I	5,05	**1246,000**	7,68	212,434	14,566	6,66	**86,340**	1,392	87,860	50,436						6,80	**0,208**	0,002	32,726	99,368
		II											6,55	**8,101**	0,232	37,675	82,303					
		III	5,17	**1250,000**	17,49	208,434	14,292	6,54	**84,570**	0,818	89,630	51,452	6,57	**7,098**	0,333	38,678	84,494	6,93	**0,204**	0,001	32,730	99,381
	pH8	I						7,00	**97,020**	0,789	77,180	44,305										
		II	6,10	**1130,000**	19,83	328,434	22,520						7,59	**3,650**	0,231	42,126	92,026	7,83	**0,201**	0,002	32,733	99,390
		III	6,25	**1123,000**	18,00	335,434	23,000	7,15	**99,780**	0,534	74,420	42,721	7,64	**12,050**	0,269	33,726	73,676	7,85	**0,207**	0,000	32,727	99,371
	pH9	I	8,00	**1048,000**	13,17	410,434	28,142						8,70	**10,170**	0,455	35,606	77,783	8,81	**0,274**	0,001	32,660	99,168
		II	8,00	**1090,000**	20,04	368,434	25,262	8,60	**87,770**	0,769	86,430	49,615	8,70	**6,748**	0,228	39,028	85,259	8,92	**0,119**	0,001	32,815	99,639
		III						8,60	**87,340**	0,805	86,860	49,862						8,99				
1/80	pH6	I	4,01	**1379,000**	21,34	61,667	4,280	4,99	**130,700**	1,180	20,471	13,542						6,20	**0,374**	0,003	8,881	95,959
		II																6,05	**0,365**	0,002	8,890	96,056
		III	3,90	**1367,000**	22,51	73,667	5,113	5,17	**130,100**	2,263	21,071	13,939										
	pH7	I	4,08	**1381,000**	15,25	59,667	4,142	6,59	**118,600**	1,882	32,571	21,546						6,96	**0,376**	0,002	8,879	95,937
		II	4,16	**1379,000**	13,13	61,667	4,280	6,50	**124,100**	1,213	27,071	17,908										
		III																7,18	**0,392**	0,007	8,863	95,765
	pH8	I	6,65	**1343,000**	19,22	97,667	6,779	7,56	**129,400**	1,390	21,771	14,402						7,66	**0,414**	0,002	8,841	95,527
		II						7,57	**129,600**	1,105	21,571	14,269						7,82	**0,566**	0,005	8,689	93,885
		III	6,59	**1363,000**	14,65	77,667	5,391	7,73	**130,650**	0,426	20,521	13,575						7,68	**0,728**	0,007	8,527	92,134
	pH9	I	7,70	**1321,000**	19,02	119,667	8,306											8,90	**0,501**	0,004	8,754	94,587
		II	7,70	**1356,000**	11,55	84,667	5,877	8,30	**139,600**	1,233	11,571	7,654						8,80	**0,523**	0,002	8,732	94,349
		III						8,30	**138,400**	1,041	12,771	8,448						8,88	**0,543**	0,002	8,712	94,133
LOQ				0,000					0,000					0,000					0,000			
LOD				0,000					0,000					0,000					0,000			
Sample dilution				1 / 200					1 / 20					1/20					-			

Tab. A.9 Corrected final data set obtained from muscovite-Sr^{2+} batch experiments (abbreviations correspond to Tab. A.8)

			Co 1/20 = 892,02 µg/l = 1,018*10^-5 M Co 1/80 = 880,905 µg/l = 1,005*10^-5 M					Co 1/20 = 102,54 µg/l = 1,170*10^-6 M Co 1/80 = 91,425 µg/l = 1,043*10^-6 M					Co 1/20 = 23,59 µg/l = 2,692*10^-7 M Co 1/80 = 12,477 µg/l = 1,424*10^-7 M				
			pH	C_{equil} [ppb] MS	б [ppb] C_{equil}	C_{sorb} [ppb]	Sorption [%]	pH	C_{equil} [ppb] MS	б [ppb] C_{equil}	C_{sorb} [ppb]	Sorption [%]	pH	C_{equil} [ppb] MS	б [ppb] C_{equil}	C_{sorb} [ppb]	Sorption [%]
1/20	pH6	I	4,49	**863,200**	14,800	28,820	3,231	5,56	**86,450**	0,849	16,090	15,691	6,03	**14,620**	0,194	8,972	38,030
		II	4,26	**859,800**	9,998	32,220	3,612	5,54	**86,630**	1,290	15,910	15,516					
		III											6,02	**16,410**	0,190	7,182	30,443
	pH7	I	4,87	**763,300**	15,180	128,720	14,430	6,82	**87,100**	1,364	15,440	15,058					
		II	4,92	**768,400**	11,950	123,620	13,858						6,74	**14,520**	0,136	9,072	38,454
		III						6,60	**84,210**	0,279	18,330	17,876	6,77	**14,330**	0,156	9,262	39,259
	pH8	I	6,68	**605,700**	7,130	286,320	32,098	7,55	**71,090**	0,322	31,450	30,671	7,81	**13,620**	0,130	9,972	42,269
		II	6,81	**580,000**	9,193	312,020	34,979										
		III			4,497			7,58	**76,340**	0,838	26,200	25,551	7,76	**14,040**	0,136	9,552	40,488
	pH9	I	7,8	**580,200**	7,109	311,820	34,957						8,71	**4,430**	0,154	19,162	81,222
		II	7,8	**546,600**	13,370	345,420	38,723	8,5	**60,910**	0,873	41,630	40,599	8,69	**9,883**	0,049	13,709	58,109
		III						8,5	**55,590**	0,852	46,950	45,787					
1/80	pH6	I	3,69	**869,900**	10,280	11,005	1,249						5,80	**12,060**	0,118	0,417	3,342
		II	3,93	**863,400**	9,135	17,505	1,987										
		III	3,90	**864,000**	7,884	16,905	1,919						5,93	**12,230**	0,135	0,247	1,980
	pH7	I						6,82	**85,540**	0,958	17,000	6,437	6,77	**10,760**	0,162	1,717	13,761
		II	3,55	**840,900**	14,660	40,005	4,541	6,72	**83,700**	0,460	18,840	8,450	6,61	**10,850**	0,119	1,627	13,040
		III	3,61	**843,200**	5,495	37,705	4,280						6,59	**10,840**	0,141	1,637	13,120
	pH8	I	6,50	**706,900**	8,687	174,005	19,753										
		II						7,71	**82,830**	0,992	19,710	9,401	7,78	**11,240**	0,124	1,237	9,914
		III	6,61	**701,600**	3,920	179,305	20,355	7,69	**83,890**	1,163	18,650	8,242	7,77	**11,370**	0,134	1,107	8,872
	pH9	I						8,6	**58,950**	1,291	43,590	35,521	8,66	**8,080**	0,071	4,397	35,241
		II	7,2	**597,400**	11,070	283,505	32,183										
		III	7,2	**618,700**	13,070	262,205	29,765	8,6	**71,000**	1,463	31,540	22,341	8,66	**9,615**	0,114	2,862	22,938
LOQ				0,450					0,000					0,010			
LOD				1,35					0,000					0,030			
Sample dilution				1/100					1/10					-			

Tab. A.10 Corrected final data set obtained from orthoclase-Sr^{2+} batch experiments (abbreviations correspond to Tab. A.8)

			Co 1/20 = 911,96 µg/L = 1,041*10^-5 M Co 1/80 = 897,195 µg/L = 1,024*10^-5 M					Co 1/20 = 107,872 µg/L = 1,231*10^-6 M Co 1/80 = 93,885 µg/L = 1,072*10^-6 M					Co 1/20 =27,464 µg/L = 3,134*10^-7 M Co 1/80 = 13,554 µg/L = 1,547*10^-7 M				
			pH	C_{equil} [ppb] MS	б [ppb] C_{equil}	C_{sorb} [ppb]	Sorption [%]	pH	C_{equil} [ppb] MS	б [ppb] C_{equil}	C_{sorb} [ppb]	Sorption [%]	pH	C_{equil} [ppb] MS	б [ppb] C_{equil}	C_{sorb} [ppb]	Sorption [%]
1/20	pH6	I															
		II	4,56	**897,300**	9,309	14,660	1,6076	5,52	**92,770**	0,449	15,102	14,0003					
		III	4,57	**877,300**	3,898	34,660	3,8006	5,72	**87,180**	0,500	20,692	19,1823					
	pH7	I	5,55	**754,200**	3,688	157,760	17,2990	6,42	**61,100**	0,425	46,772	43,3590	7,26	**25,440**	0,199	2,024	7,3685
		II											7,04	**26,480**	0,029	0,984	3,5817
		III	5,34	**757,800**	7,100	154,160	16,9043	6,47	**65,190**	0,653	42,682	39,5675	6,96	**24,740**	0,144	2,724	9,9174
	pH8	I	7,24	**547,200**	5,116	364,760	39,9974	7,90	**19,100**	0,072	88,772	82,2939					
		II	7,11	**531,400**	4,361	380,560	41,7299	7,82	**17,830**	0,120	90,042	83,4712					
		III	7,11	**609,600**	5,948	302,360	33,1550										
	pH9	I	8,05	**486,500**	4,951	425,460	46,6534										
		II	7,93	**494,600**	5,628	417,360	45,7652	8,72	**12,430**	0,041	95,442	88,4771					
		III	7,93	**461,900**	3,426	450,060	49,3509	8,56	**12,340**	0,084	95,532	88,5606					
1/80	pH6	I	3,97	**885,400**	10,550	11,795	1,3147						5,49	**15,080**	0,067	12,384	45,0911
		II	4,00	**884,900**	8,117	12,295	1,3704	5,47	**86,770**	0,961	7,115	7,5780	6,08	**14,760**	0,085	12,704	46,2563
		III						5,45	**84,290**	0,143	9,595	10,2195	5,65	**15,040**	0,079	12,424	45,2368
	pH7	I						6,37	**71,640**	0,310	22,245	23,6935	7,05	**12,320**	0,093	15,144	55,1407
		II						6,43	**69,380**	0,714	24,505	26,1007	7,12	**11,430**	0,038	16,034	58,3814
		III											7,06	**12,200**	0,101	15,264	55,5777
	pH8	I						7,75	**9,247**	0,054	84,638	90,1507					
		II	7,17	**632,000**	7,069	265,195	29,5582										
		III	6,92	**640,600**	5,166	256,595	28,5997	7,90	**9,340**	0,063	84,545	90,0516					
	pH9	I	7,81	**578,500**	6,054	318,695	35,5213	8,56	**7,550**	0,047	86,335	91,9582					
		II	7,81	**579,300**	3,662	317,895	35,4321	8,66	**7,678**	0,091	86,207	91,8219					
		III															
LOQ				2,47					2,47					2,47			
LOD				7,40					7,40					7,40			
Sample dilution				1/100					1/100					1/100			

Tab. A.11 Corrected final data set obtained from muscovite-Eu^{3+} batch experiments (abbreviations correspond to Tab. A.8)

			Co 1/20 = 1554,99 µg/L = 1.023*10^-5 M Co 1/80 = 1561,36 µg/L = 1,027*10^-5 M					Co 1/20= 155,499 µg/L = 1.023*10^-6 M Co 1/80= 156,136 µg/L = 1,027*10^-6 M					Co 1/20 = 15,55 µg/L = 1.023*10^-7 M Co 1/80= 15,61 µg/L = 1,027*10^-7 M					Co1/20 = 1,555 µg/L = 1.023*10^-8 M Co1/80 = 1,561 µg/L = 1,027*10^-8 M				
			pH	C_{equil} [ppb] MS	б [ppb] C_{equil}	C_{sorb} [ppb]	Sorption [%]	pH	C_{equil} [ppb] MS	б [ppb] C_{equil}	C_{sorb} [ppb]	Sorption [%]	pH	C_{equil} [ppb] MS	б [ppb] C_{equil}	C_{sorb} [ppb]	Sorption [%]	pH	C_{equil} [ppb] MS	б [ppb] C_{equil}	C_{sorb} [ppb]	Sorption [%]
1/20	pH6	I	3,94	**1036,000**	2,205	518,99	33,38	5,33	**3,140**	0,023	152,36	97,98						6,03	**0,026**	0,004	1,53	98,33
		II						5,34	**4,308**	0,046	151,19	97,23	6,07	**0,196**	0,005	15,35	98,74	5,98	**0,025**	0,001	1,53	98,39
		III	4,11	**1044,000**	12,880	510,99	32,86	5,22	**3,646**	0,035	151,85	97,66	6,08	**0,187**	0,006	15,36	98,80	6,10	**0,023**	0,002	1,53	98,52
	pH7	I	4,20	**765,000**	5,390	789,99	50,80						6,93	**0,000**	0,001	15,55	100,00	6,80	**0,006**	0,000	1,55	99,61
		II	4,17	**774,600**	10,190	780,39	50,19	6,79	**0,249**	0,008	155,25	99,84	6,81	**0,024**	0,004	15,53	99,85	6,84	**0,009**	0,000	1,55	99,42
		III						6,67	**0,492**	0,012	155,01	99,68	6,84	**0,027**	0,003	15,52	99,83	6,93	**0,008**	0,000	1,55	99,49
	pH8	I																7,72	**0,012**	0,000	1,54	99,23
		II	6,38	**18,130**	0,179	1536,86	98,83	7,59	**1,093**	0,009	154,41	99,30	7,76	**0,000**	0,001	15,55	100,00	7,83	**0,013**	0,000	1,54	99,16
		III	6,54	**12,740**	0,228	1542,25	99,18	7,59	**0,624**	0,018	154,87	99,60	7,81	**0,078**	0,001	15,47	99,50	7,85	**0,012**	0,000	1,54	99,23
	pH9	I	7,00	**0,179**	0,005	1554,81	99,99						8,89	**0,000**	0,001	15,55	100,00	8,81	**0,011**	0,000	1,54	99,29
		II						8,50	**1,584**	0,024	153,91	98,98	8,96	**0,084**	0,004	15,47	99,46	8,92	**0,007**	0,000	1,55	99,55
		III	7,00	**10,020**	0,109	1544,97	99,36	8,50	**1,795**	0,015	153,70	98,85	8,86	**0,165**	0,010	15,38	98,94	8,99	**0,015**	0,000	1,54	99,04
1/80	pH6	I	3,67	**1178,000**	18,210	383,36	24,24	4,82	**49,120**	0,356	107,02	68,41	6,13	**0,650**	0,015	14,96	95,82	6,20	**0,056**	0,001	1,51	96,40
		II	3,18	**1186,000**	6,092	375,36	23,73											6,05	**0,164**	0,001	1,40	89,45
		III	3,56	**1155,000**	13,780	406,36	25,72	4,99	**46,530**	0,663	109,61	70,08	5,95	**0,881**	0,010	14,73	94,33	5,97	**0,493**	0,002	1,07	68,30
	pH7	I	3,69	**1143,000**	12,010	418,36	26,49	6,45	**1,406**	0,028	154,73	99,10	7,02	**0,009**	0,002	15,60	99,94	6,96	**0,029**	0,000	1,53	98,14
		II	3,77	**1113,000**	8,999	448,36	28,42						7,00	**0,115**	0,004	15,50	99,26	6,84	**0,044**	0,001	1,52	97,17
		III						6,29	**4,044**	0,042	152,09	97,40						7,18	**0,024**	0,001	1,54	98,46
	pH8	I						7,35	**0,087**	0,005	156,05	99,94										
		II	5,59	**252,50**	0,424	1308,86	83,76	7,36	**4,549**	0,062	151,59	97,07	7,77	**0,338**	0,004	15,28	97,83	7,82	**0,023**	0,001	1,54	98,52
		III	5,34	**107,400**	0,805	1453,96	93,09						7,78	**0,410**	0,009	15,20	97,36	7,68	**0,014**	0,000	1,55	99,10
	pH9	I											8,86	**0,020**	0,001	15,59	99,87	8,90	**0,076**	0,000	1,49	95,11
		II	6,50	**113,100**	1,110	1448,26	92,73						9,04	**1,836**	0,052	13,78	88,19	8,80	**0,035**	0,000	1,53	97,75
		III	6,50	**119,900**	0,883	1441,46	92,29	8,00	**5,415**	0,066	150,72	96,52										
LOQ				1,350					0,000					0,000					0,000			
LOD				4,050					0,000					0,000					0,000			
Sample dilution				1 / 200					1 / 20					1 / 20					-			

Tab. A.12 Corrected final data set obtained from orthoclase-Eu^{3+} batch experiments (abbreviations correspond to Tab. A.8)

			Co 1/20, 1/80 = 1630 µg/L = 1,07*10^-5 M					Co 1/20 = 155,316 µg/L = 1,02*10^-6 M Co 1/80 = 155,165 µg/L = 1,02*10^-6 M					Co 1/20 = 15,532 µg/L = 1,02*10^-7 M Co 1/80 = 15,517 µg/L = 1,02*10^-7 M					Co 1/20 = 1,553 µg/L = 1,02*10^-8 M Co 1/80 = 1,552 µg/L = 1,02*10^-8 M				
			pH	C_{equil} [ppb] MS	б [ppb] C_{equil}	C_{sorb} [ppb]	Sorption [%]	pH	C_{equil} [ppb] MS	б [ppb] C_{equil}	C_{sorb} [ppb]	Sorption [%]	pH	C_{equil} [ppb] MS	б [ppb] C_{equil}	C_{sorb} [ppb]	Sorption [%]	pH	C_{equil} [ppb] MS	б [ppb] C_{equil}	C_{sorb} [ppb]	Sorption [%]
1/20	pH6	I						5,63	**7,799**	0,057	147,517	94,98	5,81	**0,081**	0,004	15,451	99,48	6,00	**0,010**	0,001	1,543	99,36
		II	4,34	**1454,000**	6,176	176,000	10,80						5,84	**0,086**	0,003	15,446	99,45	5,97	**0,010**	0,000	1,543	99,36
		III	4,38	**1446,000**	7,188	184,000	11,29	5,61	**7,990**	0,031	147,326	94,86	5,85	**0,062**	0,003	15,470	99,60	6,10	**0,009**	0,000	1,544	99,42
	pH7	I	4,78	**939,600**	7,705	690,400	42,36						7,17	**0,006**	0,002	15,526	99,96	6,96	**0,002**	0,000	1,551	99,87
		II	4,89	**877,800**	8,266	752,200	46,15	6,64	**0,018**	0,002	155,298	99,99	7,09	**0,004**	0,001	15,528	99,97	6,94	**0,002**	0,000	1,551	99,87
		III						6,73	**0,012**	0,003	155,304	99,99	7,20	**0,013**	0,003	15,519	99,92	7,11	**0,003**	0,000	1,550	99,81
	pH8	I	6,76	**0,886**	0,382	1629,114	99,95	7,58	**0,014**	0,002	155,302	99,99										
		II	6,72	**0,281**	0,058	1629,719	99,98											7,68	**0,005**	0,000	1,548	99,68
		III	6,69	**0,263**	0,038	1629,737	99,98	7,58	**0,028**	0,001	155,288	99,98										
	pH9	I	7,96	**0,780**	0,047	1629,220	99,95	8,62	**0,669**	0,007	154,647	99,57	8,49	**0,034**	0,005	15,498	99,78	8,79	**0,003**	0,000	1,550	99,81
		II	7,99	**0,840**	0,012	1629,160	99,95						8,53	**0,017**	0,001	15,515	99,89	8,87	**0,001**	0,000	1,552	99,94
		III	8,01	**0,618**	0,017	1629,382	99,96	8,62	**0,027**	0,002	155,289	99,98	8,56	**0,043**	0,003	15,489	99,72	8,81	**0,004**	0,000	1,549	99,74
1/80	pH6	I						4,98	**98,640**	0,492	56,525	36,43	5,74	**1,558**	0,018	13,959	89,96	5,99	**0,086**	0,001	1,466	94,46
		II	3,63	**1623,000**	6,259	7,000	0,43	5,15	**98,860**	0,833	56,305	36,29	5,74	**1,127**	0,017	14,390	92,74	6,08	**0,053**	0,001	1,499	96,58
		III	3,71	**1575,000**	5,925	55,000	3,37						5,80	**1,003**	0,019	14,514	93,54	6,11	**0,045**	0,001	1,507	97,10
	pH7	I	4,42	**1574,000**	5,806	56,000	3,44	5,43	**1,606**	0,016	153,559	98,96	7,34	**0,018**	0,002	15,499	99,88	6,99	**0,002**	0,000	1,550	99,87
		II											7,15	**0,021**	0,001	15,496	99,86	6,72	**0,005**	0,000	1,547	99,68
		III	4,06	**1628,000**	7,056	2,00	0,12	5,41	**0,740**	0,004	154,425	99,52	7,16	**0,012**	0,003	15,505	99,92	6,98	**0,001**	0,000	1,551	99,94
	pH8	I	6,68	**213,100**	2,432	1416,900	86,93	7,24	**0,019**	0,002	155,146	99,99	7,57	**0,005**	0,002	15,512	99,97	7,73	**0,006**	0,000	1,546	99,61
		II						7,20	**0,029**	0,003	155,136	99,98						7,72	**0,001**	0,000	1,551	99,94
		III	6,68	**218,300**	0,764	1411,70	86,61						7,62	**0,010**	0,000	15,507	99,94	7,73	**0,003**	0,000	1,549	99,81
	pH9	I	7,93	**1,953**	0,029	1628,047	99,88															
		II						8,68	**0,224**	0,004	154,941	99,86	8,50	**0,015**	0,003	15,502	99,90					
		III	7,90	**1,634**	0,048	1628,37	99,90	8,66	**0,259**	0,006	154,906	99,83	8,44	**0,002**	0,002	15,515	99,99	8,85	**0,001**	0,000	1,551	99,94
LOQ				0,6					0,03					0,000					0,000			
LOD				1,8					0,09					0,000					0,000			
Sample dilution				1/200					1/20					1/20					1/3			

A.7 Carbon mass balance and source term for DIC

One of the major components affecting the geochemical conditions and therewith the sorption values of contaminants is dissolved inorganic carbon (DIC). An important source for DIC is sedimentary organic carbon (SOC). By (microbial) degradation of SOC carbon dioxide might be formed. This process – preferably as microbially induced sulfate reduction – is observed in the aquifers and aquitards at the Gorleben site /KLI 07/ causing increased CO_2 partial pressures in the groundwater. Highest CO_2 partial pressures are observed in the upper aquifer with typical values in the range of $10^{-2.5}$ atm (section A.8). In order to estimate the magnitude and duration of such a CO_2 source, namely, whether the carbon source will be available for time periods in the range of one million years, the SOC content in the three considered sediments "upper aquifer" (UAF: Saalian and Weichselian meltwater sands), "aquitard" (AT: Lauenburg Clay Complex and Hamburg Clay) and "lower aquifer" (LAF: Miocene Lower Brown Coal Sands and Elsterian Sands) should be quatified. The data from Grimm /GRI XX/, already used to define the mineral compositions, are evaluated to determine average SOC contents of our sediments.

A.7.1 SOC content in sediments at the reference site Gorleben

A.7.1.1 Lower aquifer

The content of total SOC is available for 14 samples from the lower aquifer (LAF), namely for seven sediment samples of the Miocene sands, for five samples of the Elsterian sands and for two samples of the Elsterian channel sands (Tab. A.13). From these data a mean SOC content of about 2.5 wt% is derived for this aquifer.

Tab. A.13 SOC-content [wt%] in sediments of the lower aquifer

wt%	samples	mean (Miocene)	mean (Elster)	Mean (LAF)	st. dev. (LAF)
$C_{org.}$ [mg g^{-1}]	14	1.8	3.2	2.5	0.4

Part of the lower aquifer consists of the Lower Brown Coal Sands, which contain the upper part up to three brown coal beds. The lower two brown coal beds are commonly assigned to the 4th Lausitzer Flözhorizont, since an extensive distribution is lacking.

The third brown coal bed shows a continuous distribution approx. 10 m below the Hamburg Clay with a mean thickness between 1.5 m and 3.0 m. The amount of their total organic carbon (TOC) varies between 46.3 % and 50.7 % /KOE 07/. However, these brown coal beds are not considered in the estimations shown here.

A.7.1.2 Aquitard

Only three sediment samples of the aquitard (AT), namely from the Lauenburg Clay Complex were analyzed for their TOC content (Tab. A.14). The mean from these samples of 24.7 wt% is applied for the carbon formation rates of the aquitard.

Tab. A.14 TOC-content [wt%] in sediments of the aquitard

wt%	samples	Mean (AT)	st. dev. (AT)
$C_{org.}$ [mg g^{-1}]	3	24.7	6.5

Data for the carbon content of the Hamburg Clay are not available in the reports from Grimm /GRI XX/. It is reported that there are several coal beds within the Hamburg Clay, which locally rise the carbon content from 4.2 % to 36.9 % /KOE 07/.

A.7.1.3 Upper aquifer

Representing the upper aquifer (UAF), five sediment samples from the Saalian, four sediment samples from the Weichselian and four sediment samples from the Holocene were evaluated for TOC content (Tab. A.15). Almost all Quaternary sediments show a certain carbon content, because all of them contain relocated brown coal beds from the Tertiary. The mean value of 1.1 wt% is of course lower than in both other sediments.

Tab. A.15 TOC-content [wt%] in sediments of the upper aquifer

wt%	mean (Saalian)	mean (Weichselian)	mean (Holocene)	mean (UAF)	st. dev. (UAF)
$C_{org.}$ [mg g^{-1}]	1.0	0.8	1.4	1.1	0.1

A.7.2 Modeling of SOC degradation and CO_2 formation

In order to estimate formation rates for CO_2 in the respective sediments several assumptions are made. Firstly, it is assumed that SOC is homogeneously distributed within the respective sediment and all SOC is available for degradation and the degradation kinetics follows a first order reaction law. It is expected that the degradation rates are highest in the upper aquifer, under fresh water conditions and a high accessibility of the sedimentary organic carbon. Due to the currently high salinity of the groundwater in large parts of the lower aquifer a reduced degradation rate is expected there. In the argillaceous sediments of the aquitard with low pore volumes a reduced accessibility might also cause very low SOC degradation rates. For all sediments a rock density of 2500 kg m^{-3}, an average SOC density of 1500 kg m^{-3} and a porosity of 0.2 are assumed. For the mass balance the mean SOC contents described in section A.7.1 are used, which are summarized in Tab. A.16.

Tab. A.16 Organic carbon data for the three considered sediments

	samples	**SOC [wt%]**	**m_{soc} [kg C m^{-3}]**	**C^0_{SOC} [mol m^{-3}]**
Lower aquifer	14	1.1	62.5	5204
Aquitard	3	24.7	617.5	51411
Upper aquifer	13	2.5	27.5	2290

The SOC degradation might be described by a simplified reaction as

$$CH_2O + 0.5\ SO_4^{2-} + 2\ H^+ = CO_2 + 0.5\ H_2S + H_2O. \quad \text{(A.1)}$$

Assuming a first order reaction C_{CO2}, the amount of CO_2 per volume of groundwater, formed by SOC degradation can be calculated by

$$C_{CO2} = C^0_{SOC}(1-e^{-\lambda t})/\Theta \quad \text{(A.2)}$$

with C^0_{SOC} = initial amount of SOC per aquifer volume [mol m^{-3}]

λ = degradation rate

t = time

Θ = porosity

For all three aquifers, CO_2 formation rates are calculated. In order to derive CO_2 concentrations, the residence time of groundwater in the respective sediment needs to be estimated. This is done for the aquifers on the basis of the pathway length and the flow velocity. Corresponding partial pressures are calculated with PHREEQC (/PAR 99/) and are compared with typical values observed in the sedimentary layers. On that basis a CO_2 formation rate (DIC source) is proposed for each aquifer.

A.7.2.1 Lower aquifer

In Fig. A.7 it is shown how the CO_2 formation rates develop with time in the lower aquifer assuming three different SOC degradation rates. For SOC degradation rates of 10^{-7}, 10^{-8} and 10^{-9} a^{-1} the initial formation rates of CO_2 amounts to $2.6 \cdot 10^{-3}$, $2.6 \cdot 10^{-4}$, and $2.6 \cdot 10^{-5}$ mol a^{-1} m^{-3}, respectively.

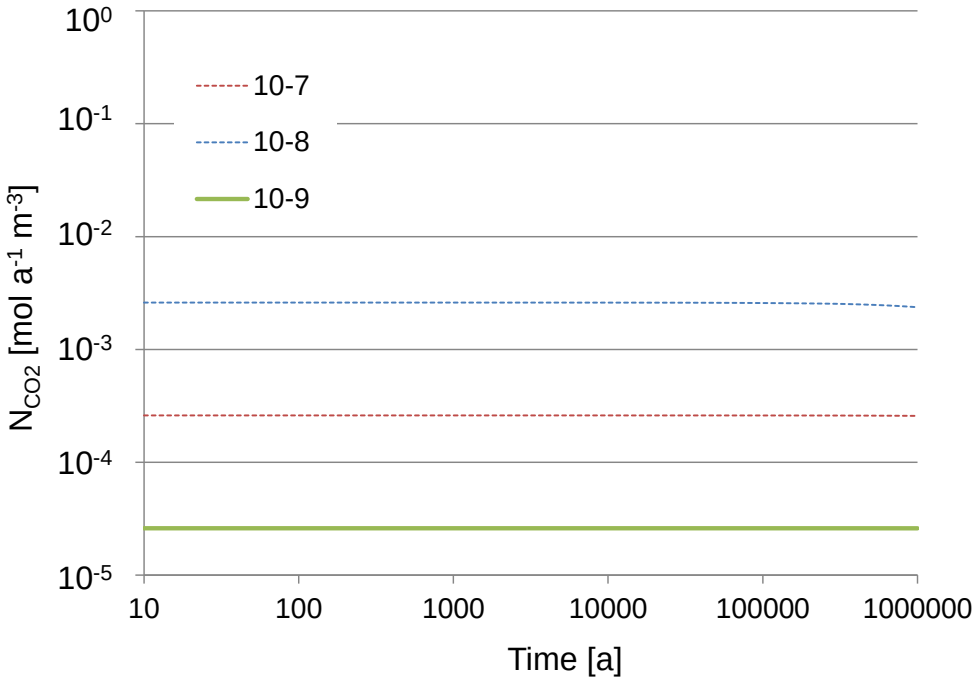

Fig. A.7 Calculated formation rates of CO_2 in the lower aquifer for three different SOC degradation rates 10^{-4}, 10^{-5} and 10^{-6} a^{-1}

The groundwater residence time, i. e. the transport pathway and flow velocity was estimated as follows: Based on a groundwater flow model by /FLU 09/, *Rübel et al.* performed 2D flow calculations for the Gorleben overburden /RUE 10/. The model geometry and the hydrogeological parameters and boundary conditions were derived from a basic North-South striking cross section of the Gorleben site /KLI 07/. Using the results

for the steady-state flow conditions, the major transport pathways from the contact to the salt dome in the lower aquifer to the biosphere were determined (Fig. A.8). In Tab. A.17 the parameters for the two transport pathways 2A and 2B are listed.

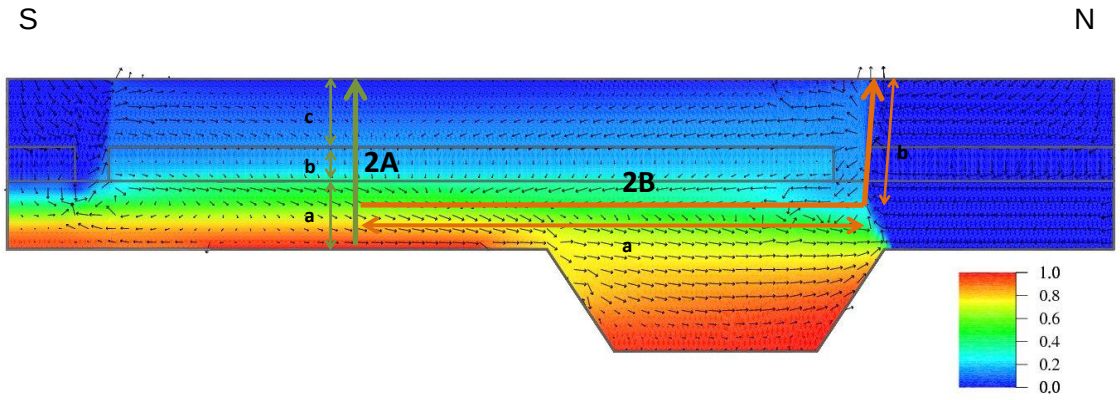

Fig. A.8 Definition and subdivision of the transport pathways from the contact to the salt dome in the lower aquifer to the biosphere /RUE 10/

Tab. A.17 Parameters for the two transport pathways

Transport pathway 2A		
Number of compartments		3
	Compartment 2Aa and 2Ac	Compartment 2Ab
Material	Sand	Clay
Pathway length [m]	100	50
Porosity	0.3	0.1
Cross section [m^2]	1 000	1 000
Mean Darcy velocity [$m \cdot a^{-1}$]	$1 \cdot 10^{-4}$	$1 \cdot 10^{-4}$
Transport pathway 2B		
Number of compartments		2
	Compartment 2Ba	Compartment 2Bb
Material	Sand	Sand
Pathway length [m]	7 740	100
Porosity	0.3	0.3
Cross section [m^2]	100	100
Mean Darcy velocity [$m \cdot a^{-1}$]	$2.1 \cdot 10^{-2}$	2.74

There are two major pathways in the lower aquifer: 2Aa and 2Ba. Average residence times of 111 000 a (horizontal pathway 2Ba) to 300 000 a (vertical pathway 2Aa) were calculated based on the values given in Tab. A.17.

In Tab. A.18 it is shown how the CO_2 concentrations in the aquifer water and therewith the corresponding CO_2 partial pressure p_{CO2} depend on the residence time of the water in the aquifer. It becomes clear that the CO_2 partial pressures for SOC degradation rates of 10^{-7} and 10^{-8} a^{-1} are significantly higher than the typical values (log p_{CO2} ~ -2.5) observed in the aquifers at the Gorleben site.

Tab. A.18 Concentration of CO_2 and corresponding CO_2 partial pressure for different SOC degradation rates and residence times for the conditions in the lower aquifer

	Residence time 100 years		**Residence time 10000 years**	
Degradation rate	C_{CO2} [mol m^{-3}]	log p_{CO2} [atm]	C_{CO2} [mol m^{-3}]]	log p_{CO2} [atm]
10^{-7} a^{-1}	0.26	-2.14	26	-0.12
10^{-8} a^{-1}	0.026	-3.18	2.6	-1.13
10^{-9} a^{-1}	0.0026	-4.29	0.26	-2.14

As shown the relatively low pore velocities in the lower aquifer suggest residence times of several 1000 years. Based on this a degradation rate of 10^{-9} a^{-1} is chosen here as reference and obviously represents an upper value. For a time frame of 1 million years this corresponds to a constant DIC source of $2.6 \cdot 10^{-5}$ mol m^{-3} a^{-1} (Fig. A.7), which is proposed for the transport calculations.

A.7.2.2 Aquitard

Due to a likely reduced accessibility in the aquitard compared to the upper aquifer but less saline conditions than in the lower aquifer a value of 10^{-7} a^{-1} is assumed as maximum degradation rate for this sediment. This leads to a constant CO_2 formation rate of 0.0257 mol m^{-3} a^{-1} for about 300 000 years decreasing to a value of 0.0234 after one million years (Fig. A.9). For the transport calculations it is proposed to use a constant DIC source with a rate of 0.025 mol m^{-3} a^{-1}.

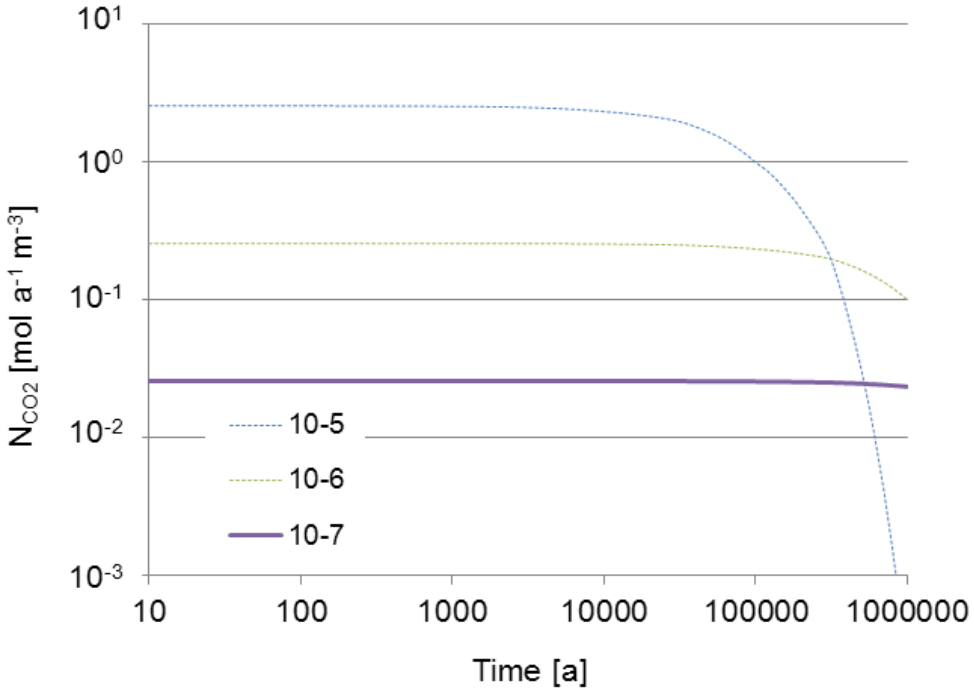

Fig. A.9 Calculated formation rates of CO_2 in the aquitard

A.7.2.3 Upper aquifer

In Fig. A.10 it is shown how the CO_2 formation rates develop with time assuming three different SOC degradation rates for the upper aquifer. The lower SOC content compared to the lower aquifer causes lower CO_2 formation rates in the upper aquifer. For SOC degradation rates of 10^{-5}, $5 \cdot 10^{-6}$ and 10^{-6} a^{-1} the initial formation rates of CO_2 amounts to 0.114, 0.0572, and 0.0114 mol a^{-1} m^{-3}, respectively.

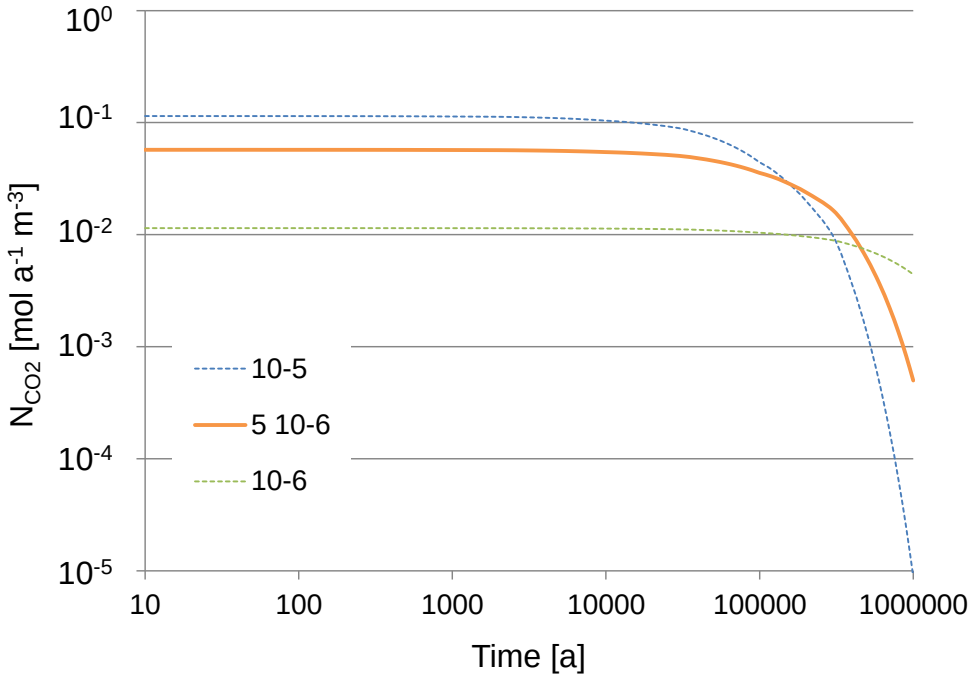

Fig. A.10 Calculated formation rates of CO_2 in the upper aquifer

As already shown in section A.7.2.1 two major transport pathways can be identified within the upper aquifer (2Ab and 2Bb, cf. Fig. A.8) /RUE 10/. The residence time within the upper aquifer differs strongly for these two pathways with 11 years for pathway 2Bb and 300 000 years for pathway 2Ab. For further calculations, the results for the transport pathway 2Bb were employed, because it is the more important transport pathway for radionuclides for the steady-state flow field /FLU 09/. Therefore residence times of few years are assumed for the upper aquifer. lue observed at Gorleben site.

Tab. A.19 shows that for residence times between 1 and 10 years degradation rates between 10^{-5} and 10^{-6} a^{-1} would lead to CO_2 pressures in the range of $10^{-2.5}$ atm, i. e. the typical value observed at Gorleben site.

Tab. A.19 Concentration of CO_2 and corresponding CO_2 partial pressure for different SOC degradation rates and residence times for the conditions in the upper aquifer

	Residence time 1 year		**Residence time 10 years**	
Degradation rate	C_{CO2} [mol m^{-3}]	log p_{CO2} [atm]	C_{CO2} [mol m^{-3}]	log p_{CO2} [atm]
10^{-5} a^{-1}	0.114	-2.5	1.14	-1.48
$5 \cdot 10^{-6}$ a^{-1}	0.0572	-2.81	0.572	-1.79
10^{-6} a^{-1}	0.0114	-3.56	0.114	-2.5

Here, a degradation rate of $5 \cdot 10^{-6}$ a^{-1} is assumed, which is suggest to be an upper limit. Considering a time frame of 1 million years this would lead to a decrease in the DIC source by two orders of magnitude, which need to be considered in the transport calculations, i. e. an exponentially decreasing DIC formation rate is proposed:

$$\dot{C}_{DIC} = C^0_{SOC} \lambda (1 - e^{-\lambda t}) / \Theta , \qquad \text{(A.3)}$$

with C^0_{SOC} = 2290 mol m^{-3}, $\lambda = 5 \cdot 10^{-6}$ a^{-1} and $\Theta = 0.2$.

A.7.3 Conclusions for the DIC source term

On the basis of the content of sedimentary organic carbon in the three sediments lower aquifer, aquitard and upper aquifer and of typical CO_2 partial pressures observed at the site CO_2 formation rates have been estimated for each sediment. First order degradation kinetics of SOC was assumed. The highest degradation rate of $5 \cdot 10^{-6}$ a^{-1} is applied for the upper aquifer. For the aquitard and the lower aquifer SOC degradation rates of 10^{-7} a^{-1} and 10^{-9} a^{-1} are assumed, respectively, taking into account a reduced accessibility in the low permeable clay layers and a significant lower microbial activity in the highly saline waters in the lower aquifer. As a consequence constant DIC sources are proposed for the latter two sediments and an exponentially decreasing DIC source for the upper aquifer. These estimations are based on average residence times derived from typical flow velocities calculated by /RUE 10/. They should be regarded as upper limits and might be modified, when concrete calculations with the new transport code are available. The most important result is that the carbon content in all three sediments is high enough to serve as a DIC source for a time frame of 1 million years.

A.8 Scoping calculations with PHREEQC (batch and 1D column)

The aim of the batch and transport calculations presented here was to reach a deeper understanding of the chemical reactions that influence the system behaviour of simple rock-water-systems as for example the aquifers in our model area under potential geochemical changes. Such reactions might be buffering of the pH-value, dissolution and precipitation as well as sorption processes.. Therefore a typical scenario, which will cause geochemical changes has been selected, i. e. salt water intrusion into an aquifer in Northern Germany after inundation by the North Sea during a warm stage.

Two kinds of calculations are performed, so-called batch reaction calculations and 1D transport calculations. Batch calculations are used to (i) identify a set of mineral phases in equilibrium with the groundwater to be used as “reference sediment” and (ii) to identify the most important reactions occurring by mixture of seawater with the water-sediment system of the aquifer. This is done stepwise, firstly only considering dissolution and precipitation reactions and secondly introducing ion exchange reactions. Surface complexation reactions have not been considered.

Transport calculations are performed to understand the temporal changes of the system, buffering capacities and to identify those minerals, which are consumed by reactions or which precipitate under typical flow conditions during the considered scenario. This is one basis for the conceptual model for implementation of geochemical reactions in the computer program r^3t /FEI 04/ (section 0). Finally, these calculations will serve as test case for verification of the modified version of r^3t.

A.8.1 Simulation tool and data base

The computer program PHREEQC /PAR 99/ was chosen as simulation tool because it is capable to simulate 1D geochemically coupled transport, i. e. it is possible to address 1D transport calculations with geochemically changing conditions as required for this task. For speciation and batch-reaction calculations, PHREEQC numerically solves sets of nonlinear mole-balance and mass-action equations. The 1D transport is modelled by solving partial differential equations.

For this study, the first tests have been performed with the thermodynamic data base **phreeqc.dat** provided by the USGS /PAR 99/. As this data base lacks actuality and

consistency, during the course of this project a new data base was developed, which is described in detail in section 3. All calculations presented in this report have been performed with the new data base. The mass-action equations for the mineral phases used in the following calculations are listed in Tab. 3.1.

A.8.2 Model site and scenario

The calculations with PHREEQC /PAR 99/ are performed for the following scenario: In the overburden of a salt dome – a potential host rock for a repository for radioactive waste – the sedimentary aquifer is in chemical equilibrium with the formation water. Following this first equilibrium stage seawater inundation caused by temperature increase with subsequent melting of ice sheets and seawater level rise during a warm stage leads to infiltration of North Seawater into the aquifer.

As already described in section 2.2 the tertiary and quaternary sediments deposited at the Gorleben area form a system of aquifers and aquitards with total thickness of up to 430 m. Further detailed information about the geological and hydrogeological properties of the Gorleben area are compiled in /KLI 07/. Four different types of groundwater can be distinguished: Ca-SO_4, Ca-HCO_3, Na-HCO_3, and Na-Cl water. The vertical sequence of the groundwater types is shown in Fig. A.11. The investigations are focussed on the upper aquifer, which would mainly be affected by a seawater intrusion. Therefore the $CaHCO_3$ groundwater was chosen for the calculations. The Ca-HCO_3 groundwater is the dominant groundwater type in this aquifer; only in the topmost 10 m Ca-SO_4 water is found preferably. Na-HCO_3 water occurs only locally, and NaCl-rich water prevails in the deeper aquifer near the salt rock body and the transition zone between salt water and fresh water.

The most relevant processes occurring in the upper aquifer and causing the Ca-HCO_3 water are dissolution of carbonates and microbial sulphate reduction (Fig. A.11). The total salt content in this type of water is about 250 mg L^{-1} /KLI 07/. This value and the proportions of the different ions shown in Fig. A.12 were used to calculate iteratively an initial chemical composition for the Ca-HCO_3 water, which is in the following denoted as formation water. In Tab. A.20 the resulting chemical composition is listed, which will be used as initial concentration for the PHREEQC calculations.

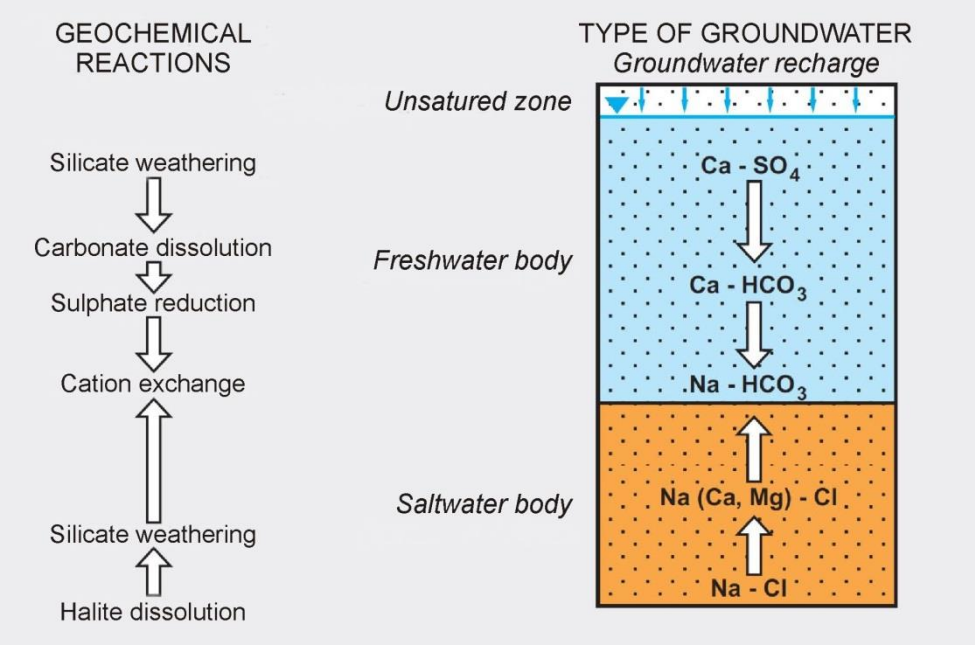

Fig. A.11 Vertical zoning of groundwater types /KLI 07/

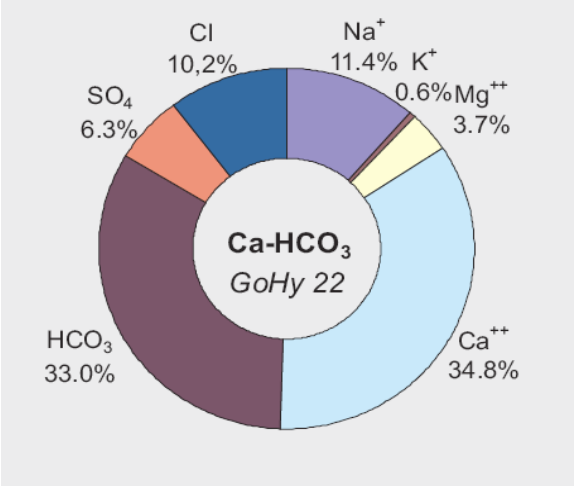

Fig. A.12 Chemical composition of a sample of Ca-HCO_3 groundwater in Gorleben (sample GoHy 22) /KLI 07/

Besides the formation water a second type of water had to be characterized for the calculations: the water of the North Sea, which is in the following denoted as seawater. Its composition was adopted from /LAN 02/ (section 2.4.3.2) and was modified by adding of missing silica and aluminium concentration values taken from /KAL 03/. The composition used in the calculations is also listed in Tab. A.20.

For the batch and transport calculations it was necessary to select a representative mineral phase composition. This was done on the basis of several sedimentary-

petrographical analyses of core samples from the Gorleben site by Grimm /GRI XX/. As in these studies mineral phases are only coarsely classified by major constituents, minor constituents and accessories results could only serve as rough indication.

Tab. A.20 Chemical composition of Ca-HCO_3 formation water and seawater used for PHREEQC calculations

Component	Formation water	Seawater
	concentration [mol L^{-1}]	concentration [mol L^{-1}]
pH	7.5	8.2
Na	$1.03 \cdot 10^{-3}$	$4.79 \cdot 10^{-1}$
K	$5.40 \cdot 10^{-5}$	$9.63 \cdot 10^{-3}$
Ca	$1.57 \cdot 10^{-3}$	$1.105 \cdot 10^{-2}$
Mg	$1.67 \cdot 10^{-4}$	$5.405 \cdot 10^{-2}$
Cl	$9.18 \cdot 10^{-4}$	$5.574 \cdot 10^{-1}$
C	$2.97 \cdot 10^{-3}$	$2.53 \cdot 10^{-3}$
S	$2.84 \cdot 10^{-4}$	$2.938 \cdot 10^{-2}$
Si	-	$1.0 \cdot 10^{-4}$
Al	-	$2.0 \cdot 10^{-8}$

First simulations therefore were conducted with different mineral phase compositions to determine by which of them the given composition of the formation water can be reproduced. In accordance with Grimm /GRI XX/, the proportion of the major constituent quartz (Qtz) was varied between 80 wt% and 90 wt%. Calcite (Cc) was assigned to be the second most common mineral phase with 5 wt%. Orthoclase (Or) with a proportion of 3 wt% together with quartz and calcite forms the basic composition of the sediment.

A further important variable is the CO_2 partial pressure in the aquifer. In the Gorleben aquifer system CO_2 pressures above the atmospheric level are observed, which is caused by microbial degradation of organic matter /KLI 07/. To obtain a representative CO_2 partial pressure, pH-values and their associated HCO_3^- contents at equilibrium were calculated for given CO_2 partial pressures. These values were plotted and compared with measured data pairs of Ca-HCO_3 groundwater at Gorleben. As shown in Fig. A.13, the simulated and measured data show a satisfactory agreement. The measured pH-values vary between 6.8 and 8.8. The median value is 7.5 and was used for further calculations. This pH-value corresponds to a CO_2 partial pressure of $10^{-2.5}$ atm, which is used as reference for our calculations. Regarding these values one

should bear in mind that not all reactions determining the pH-value were considered in the calculations but only the most important carbonate-bicarbonate equilibrium. As shown in section 0 carbon mass balance calculations for the upper aquifer suggest that a significant reduction of the degradation rate and therewith the CO_2 partial pressure is not expected before 100 000 years. For the calculations presented in this section which cover a time frame of less than 10 000 years this CO_2 partial pressure is assumed to be constant over time.

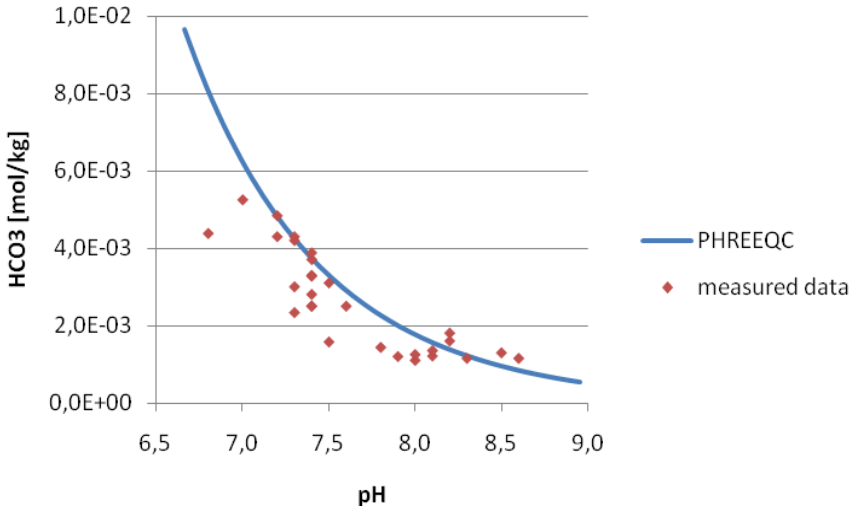

Fig. A.13 HCO_3^- concentrations versus pH achieved by variation of CO_2 partial pressure

Comparison of values calculated with PHREEQC with measured data from the Gorleben site.

Every sediment composition used in the calculations contained the above-mentioned mineral phases. In addition to this, one or several other phases were added to study their influence on the water composition obtained in equilibrium. An example for such a mineral phase composition is given in Tab. A.21. Further, for all calculations a CO_2 partial pressure of $10^{-2.5}$ atm was assumed in the formation water.

Tab. A.21 Example for a mineral phase composition used for calculations with PHREEQC

Mineral phase	Formula	Proportion [wt%]	Content [mol L^{-1}]
Quartz	SiO_2	90	158.78
Calcite	$CaCO_3$	5	5.30
Orthoclase	$KAlSi_3O_8$	3	1.14
Anorthite	*$CaAl_2Si_3O_8$*	*2*	*0.69*
Sum		100	165.91

A.8.3 Batch calculations

A.8.3.1 Equilibration of mineral phases with formation water

In these calculations, the formation water was equilibrated with different mineral phase compositions. At first, only one single mineral phase was added to the start composition of quartz, calcite, and orthoclase in a calculation. The aim of the test calculations was to discover, which processes, like mineral conversions, will be of relevance, if a certain mineral phase is present and in what manner the processes influence the pH-value and element concentrations.

In a second step simultaneously several mineral phases were added to the start composition. The aim was to determine a reference mineral phase composition to be used for the further calculations. This composition was supposed to fulfil the following conditions:

1. The mineral composition shall be as simple as possible (preferably with one or at most two representatives for each group of minerals (section 2.1), which belong to the major constituents).

2. The properties of the converted formation water at the end of the simulation – in equilibrium with the involved minerals – shall be within the range of the chemical properties of the Ca-HCO_3 formation water at Gorleben.

3. The intensity of mineral reactions and changes of system behaviour should be as small as possible as expected for minerals in equilibrium with this groundwater.

In a first step it was tested how individual single minerals added to the basis composition affect the equilibrium water composition and mineral conversions. The test calculations were done including alternately albite (Ab), anorthite (An), muscovite (Ms), chlorite (Chl), gypsum (Gp), kaolinite (Kln), montmorillonite (Mnt), illite (Ill), goethite (Gt), and gibbsite (Gbs). The amounts of the different minerals in the compositions are based on Tab. A.21. The start composition consists of the most relevant minerals in the aquifer quartz (Qtz), calcite (Cc) and orthoclase (Or). 2 % of the additional mineral phase is added to this mixture in each simulation.

The results of the test calculations with one mineral phase in addition to the start composition are listed in Tab. A.22. The table contains the pH-value, contents of ions in solution, differences between ion concentration of the initial and the equilibrium solution, and changes of the mineral phases for each mineral composition. A negative value for the change of a mineral phase represents dissolution, a positive precipitation of that phase. Analogous, for CO_2 a negative value means that CO_2 is dissolved and a positive value that the CO_2 partial pressure is increased.

Tab. A.22 Results of PHREEQC batch simulations for addition of one mineral phase to the basis composition

Changes in mineral phases and CO_2 are denoted Δ and kg water as kgw. For abbreviations and details see text.

Minerals / elements	**An**	**Ab**	**Ms**	**Chl**	**Gp**
pH	7.59	7.61	7.63	7.62	7.22
Total concentration of components in solution [mol kgw^{-1}]					
Al	$5.92 \cdot 10^{-4}$	$1.39 \cdot 10^{-5}$	$8.58 \cdot 10^{-8}$	$2.81 \cdot 10^{-6}$	$6.73 \cdot 10^{-7}$
C	$2.17 \cdot 10^{-3}$	$2.26 \cdot 10^{-3}$	$2.34 \cdot 10^{-3}$	$2.30 \cdot 10^{-3}$	$1.14 \cdot 10^{-3}$
Ca	$1.38 \cdot 10^{-3}$	$1.25 \cdot 10^{-3}$	$1.16 \cdot 10^{-3}$	$1.21 \cdot 10^{-3}$	$1.59 \cdot 10^{-2}$
Cl	$9.18 \cdot 10^{-4}$	$1.19 \cdot 10^{-3}$	$1.19 \cdot 10^{-3}$	$1.19 \cdot 10^{-3}$	$1.19 \cdot 10^{-3}$
K	$4.63 \cdot 10^{-8}$	$1.96 \cdot 10^{-6}$	$3.17 \cdot 10^{-4}$	$9.70 \cdot 10^{-6}$	$5.47 \cdot 10^{-5}$
Mg	$1.67 \cdot 10^{-4}$	$1.67 \cdot 10^{-4}$	$1.67 \cdot 10^{-4}$	$2.23 \cdot 10^{-4}$	$1.67 \cdot 10^{-4}$
Na	$1.03 \cdot 10^{-3}$	$1.10 \cdot 10^{-3}$	$1.03 \cdot 10^{-3}$	$1.03 \cdot 10^{-3}$	$1.03 \cdot 10^{-3}$
S	$2.84 \cdot 10^{-4}$	$2.84 \cdot 10^{-4}$	$2.84 \cdot 10^{-4}$	$2.84 \cdot 10^{-4}$	$1.55 \cdot 10^{-2}$
Si	$4.18 \cdot 10^{-4}$	$1.86 \cdot 10^{-4}$	$1.81 \cdot 10^{-4}$	$1.82 \cdot 10^{-4}$	$1.78 \cdot 10^{-4}$
Difference between concentrations in the initial and the equilibrium solution [mol kgw^{-1}]					
Al	$5.92 \cdot 10^{-4}$	$1.39 \cdot 10^{-5}$	$8.58 \cdot 10^{-8}$	$2.81 \cdot 10^{-6}$	$6.73 \cdot 10^{-7}$
C	$-8.04 \cdot 10^{-4}$	$-7.12 \cdot 10^{-4}$	$-6.30 \cdot 10^{-4}$	$-6.66 \cdot 10^{-4}$	$-1.83 \cdot 10^{-3}$
Ca	$-1.89 \cdot 10^{-4}$	$-3.20 \cdot 10^{-4}$	$-4.11 \cdot 10^{-4}$	$-3.61 \cdot 10^{-4}$	$1.43 \cdot 10^{-2}$
Cl	$1.79 \cdot 10^{-7}$	$2.69 \cdot 10^{-4}$	$2.69 \cdot 10^{-4}$	$2.69 \cdot 10^{-4}$	$2.68 \cdot 10^{-4}$
K	$-5.40 \cdot 10^{-5}$	$-5.20 \cdot 10^{-5}$	$2.63 \cdot 10^{-4}$	$-4.43 \cdot 10^{-5}$	$6.52 \cdot 10^{-7}$
Mg	$3.26 \cdot 10^{-8}$	$2.86 \cdot 10^{-8}$	$2.91 \cdot 10^{-8}$	$5.63 \cdot 10^{-5}$	$-6.44 \cdot 10^{-8}$
Na	$2.01 \cdot 10^{-7}$	$6.62 \cdot 10^{-5}$	$1.79 \cdot 10^{-7}$	$1.75 \cdot 10^{-7}$	$-3.97 \cdot 10^{-7}$
S	$5.54 \cdot 10^{-8}$	$4.87 \cdot 10^{-8}$	$4.94 \cdot 10^{-8}$	$4.83 \cdot 10^{-8}$	$1.52 \cdot 10^{-2}$
Si	$4.18 \cdot 10^{-4}$	$1.86 \cdot 10^{-4}$	$1.81 \cdot 10^{-4}$	$1.82 \cdot 10^{-4}$	$1.78 \cdot 10^{-4}$
Dissolution and precipitation of the mineral phases [mol kgw^{-1}]					
Δ CO_2	$2.92 \cdot 10^{-4}$	$3.92 \cdot 10^{-4}$	$2.20 \cdot 10^{-4}$	$3.05 \cdot 10^{-4}$	$9.51 \cdot 10^{-4}$
Δ Quartz	$6.63 \cdot 10^{-5}$	$-1.44 \cdot 10^{-4}$	$6.09 \cdot 10^{-4}$	$-2.65 \cdot 10^{-4}$	$-1.76 \cdot 10^{-4}$
Δ Calcite	$5.13 \cdot 10^{-4}$	$3.20 \cdot 10^{-4}$	$4.11 \cdot 10^{-4}$	$3.62 \cdot 10^{-4}$	$8.84 \cdot 10^{-4}$
Δ Orthoclase	$5.40 \cdot 10^{-5}$	$5.21 \cdot 10^{-5}$	$-3.95 \cdot 10^{-4}$	$4.43 \cdot 10^{-5}$	$-6.73 \cdot 10^{-7}$
Δ add. min.phase	$-3.23 \cdot 10^{-4}$	$-6.60 \cdot 10^{-5}$	$1.32 \cdot 10^{-4}$	$-1.90 \cdot 10^{-5}$	$-1.52 \cdot 10^{-2}$
pH	7.66	7.61	7.61	7.61	7.64

Tab. A.22 (cont.) Results of PHREEQC batch simulations for addition of one mineral phase to the start composition Qtz, Cc, and Or

Minerals/ elements	Kln	Mnt	Ill	Gt	Gbs
Total concentration of components in solution [mol kgw^{-1}]					
Al	$3.36 \cdot 10^{-8}$	$5.03 \cdot 10^{-7}$	$5.00 \cdot 10^{-7}$	$5.00 \cdot 10^{-7}$	$6.24 \cdot 10^{-8}$
C	$2.51 \cdot 10^{-3}$	$2.26 \cdot 10^{-3}$	$2.26 \cdot 10^{-3}$	$2.26 \cdot 10^{-3}$	$2.38 \cdot 10^{-3}$
Ca	$1.00 \cdot 10^{-3}$	$1.25 \cdot 10^{-3}$	$1.25 \cdot 10^{-3}$	$1.25 \cdot 10^{-3}$	$1.12 \cdot 10^{-3}$
Cl	$1.19 \cdot 10^{-3}$	$1.19 \cdot 10^{-3}$	$1.19 \cdot 10^{-3}$	$1.19 \cdot 10^{-3}$	$1.19 \cdot 10^{-3}$
K	$8.07 \cdot 10^{-4}$	$5.41 \cdot 10^{-5}$	$5.45 \cdot 10^{-5}$	$5.45 \cdot 10^{-5}$	$4.36 \cdot 10^{-4}$
Mg	$1.67 \cdot 10^{-4}$	$1.67 \cdot 10^{-4}$	$1.67 \cdot 10^{-4}$	$1.67 \cdot 10^{-4}$	$1.67 \cdot 10^{-4}$
Na	$1.03 \cdot 10^{-3}$	$1.03 \cdot 10^{-3}$	$1.03 \cdot 10^{-3}$	$1.03 \cdot 10^{-3}$	$1.03 \cdot 10^{-3}$
S	$2.84 \cdot 10^{-4}$	$2.84 \cdot 10^{-4}$	$2.84 \cdot 10^{-4}$	$2.84 \cdot 10^{-4}$	$2.84 \cdot 10^{-4}$
Si	$1.81 \cdot 10^{-4}$	$1.81 \cdot 10^{-4}$	$1.81 \cdot 10^{-4}$	$1.81 \cdot 10^{-4}$	$1.81 \cdot 10^{-4}$
Difference between concentrations in the initial and the equilibrium solution [mol kgw^{-1}]					
Al	$3.36 \cdot 10^{-8}$	$5.03 \cdot 10^{-7}$	$5.00 \cdot 10^{-7}$	$5.00 \cdot 10^{-7}$	$6.24 \cdot 10^{-8}$
C	$-4.59 \cdot 10^{-4}$	$-7.12 \cdot 10^{-4}$	$-7.12 \cdot 10^{-4}$	$-7.12 \cdot 10^{-4}$	$-5.91 \cdot 10^{-4}$
Ca	$-5.69 \cdot 10^{-4}$	$-3.20 \cdot 10^{-4}$	$-3.20 \cdot 10^{-4}$	$-3.20 \cdot 10^{-4}$	$-4.50 \cdot 10^{-4}$
Cl	$2.69 \cdot 10^{-4}$	$2.69 \cdot 10^{-4}$	$2.69 \cdot 10^{-4}$	$2.69 \cdot 10^{-4}$	$2.69 \cdot 10^{-4}$
K	$7.53 \cdot 10^{-4}$	$1.18 \cdot 10^{-7}$	$5.09 \cdot 10^{-7}$	$5.09 \cdot 10^{-7}$	$3.82 \cdot 10^{-4}$
Mg	$3.12 \cdot 10^{-8}$	$1.59 \cdot 10^{-7}$	$2.85 \cdot 10^{-8}$	$2.85 \cdot 10^{-8}$	$3.04 \cdot 10^{-8}$
Na	$1.92 \cdot 10^{-7}$	$3.06 \cdot 10^{-7}$	$1.76 \cdot 10^{-7}$	$1.76 \cdot 10^{-7}$	$1.88 \cdot 10^{-7}$
S	$5.30 \cdot 10^{-8}$	$4.85 \cdot 10^{-8}$	$4.85 \cdot 10^{-8}$	$4.85 \cdot 10^{-8}$	$5.18 \cdot 10^{-8}$
Si	$1.81 \cdot 10^{-4}$	$1.81 \cdot 10^{-4}$	$1.81 \cdot 10^{-4}$	$1.81 \cdot 10^{-4}$	$1.81 \cdot 10^{-4}$
Dissolution and precipitation of the mineral phases [mol kgw^{-1}]					
Δ CO_2	$-1.10 \cdot 10^{-4}$	$3.92 \cdot 10^{-4}$	$3.92 \cdot 10^{-4}$	$3.92 \cdot 10^{-4}$	$1.41 \cdot 10^{-4}$
Δ Quartz	$1.33 \cdot 10^{-3}$	$-1.79 \cdot 10^{-4}$	$-1.79 \cdot 10^{-4}$	$-1.79 \cdot 10^{-4}$	$9.65 \cdot 10^{-4}$
Δ Calcite	$5.69 \cdot 10^{-4}$	$3.20 \cdot 10^{-4}$	$3.20 \cdot 10^{-4}$	$3.20 \cdot 10^{-4}$	$4.50 \cdot 10^{-4}$
Δ Orthoclase	$-7.53 \cdot 10^{-4}$	$-1.09 \cdot 10^{-7}$	$-5.00 \cdot 10^{-7}$	$-5.00 \cdot 10^{-7}$	$-3.82 \cdot 10^{-4}$
Δ add. min.phase	$3.77 \cdot 10^{-4}$	$-3.95 \cdot 10^{-7}$	$4.00 \cdot 10^{-10}$	$-4.08 \cdot 10^{-14}$	$3.82 \cdot 10^{-4}$

The results show that in most cases changes in water composition and pH-value are relatively low. For all single mineral phases, except gypsum and kaolinite the changes in element concentration compared to initial $CaHCO_3$-water and also in mineral conversion are below 10^{-3} mol kgw^{-1}. For gypsum $1.52 \cdot 10^{-2}$ mol kgw^{-1} mineral is dissolved

causing an increase in sulphate and calcium in the same order of magnitude, indicating, as expected, that the system is not in equilibrium with gypsum. Gypsum is mainly found in the caprock of the salt dome at much greater depth. The consideration of kaolinite causes precipitation of $1.33 \cdot 10^{-3}$ mol kgw^{-1} quartz. Si is released from orthoclase and causes also kaolinite precipitation.

The pH-values change only marginally ranging from 7.59 to 7.66 except for gypsum (pH = 7.22). In all cases calcite precipitates and except for addition of kaolinite, a small amount of carbon dioxide is formed, i. e. released from the solution.

With respect to the other minerals no such clear tendencies are observed. In most cases an additional mineral causes dissolution of orthoclase. Only for chlorite and for the feldspars anorthite and albite, which are dissolved when added, orthoclase precipitation occurs. If a significant amount of orthoclase is dissolved, the increased amount of Si in solution leads to the precipitation of quartz.

However, from these calculations there is no clear indication to exclude any of the mineral phases except gypsum from our calculations.

In this step more than one mineral phase was added to the basic mineral composition. Three different mineral compositions were chosen for these calculations (Tab. A.23). Since feldspars are dominating minerals in the aquifers at the site, it is decided to include one additional feldspar mineral. Anorthite was chosen as a second mineral controlling Ca concentration. Further, one iron bearing mineral, goethite, and chlorite as an additional silicate mineral were selected. In the following this mineral mixture is denoted as composition 1.

Further it was decided to include in a second mixture additionally one clay mineral, although it is not clear whether the system is in equilibration with clay minerals. It was decided to include illite as representative mineral, since it leads to the lowest changes in pH in such a mixture, compared to the other observed clay minerals kaolinite and montmorillonite. It is known that in some of the sedimentary rocks at Gorleben small amounts of illite occur /GRI XX/. This mineral mixture is denoted as composition 2.

The third mineral mixture (composition 3) contains the same minerals as composition 2 but additionally gypsum. Gypsum is frequently present in the deeper sediments near the Gorleben salt dome /GRI XX/ but not in the upper aquifer. It is, however, an im-

portant source for calcium and sulphate and here the aim was to identify its effect on the water composition and mineral conversions.

Tab. A.23 Amount and proportions of the different mineral phases in the three mineral phase compositions for the further calculations

	Mineral phase composition 1		**Mineral phase composition 2**		**Mineral phase composition 3**	
Mineral phase	Proportion [wt%]	Content [mol]	Proportion [wt%]	Content [mol]	Proportion [wt%]	Content [mol]
Quartz	87	153.49	86	151.72	85	149.96
Calcite	5	5.30	5	5.30	5	5.30
Orthoclase	3	1.14	3	1.14	3	1.14
Anorthite	2	0.69	2	0.69	2	0.69
Goethite	2	2.39	2	2.39	2	2.39
Chlorite	1	0.19	1	0.19	1	0.19
Illite	-	-	1	0.28	1	0.28
Gypsum	-	-	-	-	1	0.69
sum	100	163.19	100	161.70	100	160.63

The compositions listed in Tab. A.23 were equilibrated with 1 kg of the formation water defined in chapter A.8.2. The results of these calculations can be found in Tab. A.24. Composition 2 produces the highest pH-value (8.19) and composition 1 the lowest one (7.58) and therewith the smallest change compared to the initial formation water. The system of composition 1 shows also by far the lowest conversions of mineral phases ($< 4.46 \cdot 10^{-4}$ mol kgw^{-1}). For composition 1 a small amount of CO_2 is released from solution, slight amounts of quartz, calcite, orthoclase and goethite precipitate and of anorthite and chlorite are dissolved. The aluminium concentration for these mineral formations originates from the dissolution of anorthite; potassium and calcium are withdrawn from the solution due to the formation of calcite and orthoclase. In summary magnesium, silicon, aluminium, and carbon are enriched in solution and potassium and calcium are depleted.

Tab. A.24 Results of the equilibration of the three mineral phase compositions 1, 2 and 3 with formation water

	Composition 1	Composition 2	Composition 3
pH	7.58	8.19	7.62
Components in solution [mol kgw^{-1}]			
Al	$5.77 \cdot 10^{-4}$	$5.64 \cdot 10^{-7}$	$2.11 \cdot 10^{-7}$
C	$2.11 \cdot 10^{-3}$	$8.97 \cdot 10^{-3}$	$5.42 \cdot 10^{-3}$
Ca	$1.47 \cdot 10^{-3}$	$1.09 \cdot 10^{-4}$	$8.07 \cdot 10^{-3}$
Cl	$1.19 \cdot 10^{-3}$	$1.20 \cdot 10^{-3}$	$1.17 \cdot 10^{-3}$
K	$4.77 \cdot 10^{-8}$	$5.10 \cdot 10^{-5}$	$3.28 \cdot 10^{-4}$
Mg	$1.78 \cdot 10^{-4}$	$4.61 \cdot 10^{-3}$	$5.55 \cdot 10^{-1}$
Na	$1.03 \cdot 10^{-3}$	$1.04 \cdot 10^{-3}$	$1.02 \cdot 10^{-3}$
S	$2.84 \cdot 10^{-4}$	$2.88 \cdot 10^{-4}$	$5.83 \cdot 10^{-1}$
Si	$4.11 \cdot 10^{-4}$	$1.84 \cdot 10^{-4}$	$1.52 \cdot 10^{-4}$
Mg	$1.78 \cdot 10^{-4}$	$4.61 \cdot 10^{-3}$	$5.55 \cdot 10^{-1}$
Na	$1.03 \cdot 10^{-3}$	$1.04 \cdot 10^{-3}$	$1.02 \cdot 10^{-3}$
S	$2.84 \cdot 10^{-4}$	$2.88 \cdot 10^{-4}$	$5.83 \cdot 10^{-1}$
Si	$4.11 \cdot 10^{-4}$	$1.84 \cdot 10^{-4}$	$1.52 \cdot 10^{-4}$
Differences between initial and equilibrium solution [mol kgw^{-1}]			
Al	$5.77 \cdot 10^{-4}$	$5.64 \cdot 10^{-7}$	$2.11 \cdot 10^{-7}$
C	$-8.57 \cdot 10^{-4}$	$6.00 \cdot 10^{-3}$	$2.45 \cdot 10^{-3}$
Ca	$-1.01 \cdot 10^{-4}$	$-1.46 \cdot 10^{-3}$	$6.50 \cdot 10^{-3}$
K	$-5.40 \cdot 10^{-5}$	$-2.98 \cdot 10^{-6}$	$2.74 \cdot 10^{-4}$
Mg	$1.08 \cdot 10^{-5}$	$4.45 \cdot 10^{-3}$	$5.55 \cdot 10^{-1}$
S	$5.50 \cdot 10^{-8}$	$3.63 \cdot 10^{-6}$	$5.83 \cdot 10^{-1}$
Si	$4.11 \cdot 10^{-4}$	$1.84 \cdot 10^{-4}$	$1.52 \cdot 10^{-4}$
Dissolution and precipitation of the mineral phases [mol kgw^{-1}]			
Δ CO2	$4.46 \cdot 10^{-4}$	$-6.97 \cdot 10^{-1}$	$-1.28 \cdot 10^{+0}$
Δ Quartz	$1.27 \cdot 10^{-4}$	$9.09 \cdot 10^{-1}$	$1.25 \cdot 10^{+0}$
Δ Calcite	$4.12 \cdot 10^{-4}$	$6.91 \cdot 10^{-1}$	$1.28 \cdot 10^{+0}$
Δ Orthoclase	$5.40 \cdot 10^{-5}$	$-6.72 \cdot 10^{-1}$	$-9.00 \cdot 10^{-1}$
Δ Anorthite	$-3.10 \cdot 10^{-4}$	$-6.90 \cdot 10^{-1}$	$-6.90 \cdot 10^{-1}$
Δ Goethite	$6.70 \cdot 10^{-6}$	$-1.95 \cdot 10^{-1}$	$1.02 \cdot 10^{-1}$

For composition 2 and 3 a quite similar behaviour with significant mineral conversions is observed. For composition 2 all mineral conversions (except goethite) are in a range

of $2 \cdot 10^{-1}$ to $9.1 \cdot 10^{-1}$ mol kgw^{-1}; for composition 3 they are even higher with changes up to 1.28 mol kgw^{-1}. In both systems CO_2 dissolves inducing precipitation of calcite. The amount of dissolved CO_2 and therewith precipitation of calcite is much higher in composition 3, where beside anorthite gypsum is available as additional Ca source. Likewise, for both mineral compositions orthoclase, anorthite, and chlorite are dissolved by concurrent formation of illite and quartz. The high amount of precipitating (iron bearing) illite also causes dissolution of high amounts of goethite. For composition 2 these reactions lead to an increase of all ions in solution except potassium and calcium, whereas for composition 3 the concentration of all ions is increased. For potassium this difference results from a slightly higher ratio of dissolved orthoclase to precipitated illite and the presence of the additional calcium source gypsum in composition 3.

The strong changes in groundwater composition and the extensive mineral conversions for mineral mixtures composition 2 and composition 3 indicate that these mixtures are not in equilibrium with the formation water. Only composition 1 can be assumed to be in equilibrium with the formation water. Our criteria formulated in section A.8.3.1 are only fulfilled by composition 1. For this reason composition 1 was selected as reference mineral mixture for the transport calculations.

A.8.3.2 Equilibration of mineral phases with seawater

In these batch calculations still all three compositions are regarded. They were equilibrated with seawater of the composition listed in Tab. A.20 in order to identify relevant reactions occurring for the considered scenario and as a basis for interpretation of the transport calculations. The results are listed in Tab. A.25. The pH-values are lower compared to the model systems with Ca-HCO_3 formation water, although the inflowing water has a pH-value of 8.2, and vary between 7.32 (composition 1) and 7.58 (composition 2). Hence, all three compositions strongly buffer the pH-value in the near neutral range. Now, as expected, the mineral conversions are higher for component 1 compared to the reaction with formation water. It seems that the pH of the system is buffered by precipitation of calcite. Calcium is provided by dissolution of anorthite. A small amount of CO_2 is released from solution. A high amount of quartz is dissolved leading – together with Al provided by anorthite – to a significant precipitation of orthoclase. Nearly no conversions of goethite and chlorite occur. Of course, sodium, magnesium and chloride are enriched compared to the initial formation water due to the higher concentrations of these ions in seawater.

Tab. A.25 Results of the equilibration of the three mineral phase compositions 1, 2 and 3 with seawater

	Composition 1	Composition 2	Composition 3
pH	7.32	7.58	7.39
Components in solution [mol kgw^{-1}]			
Al	$4.52 \cdot 10^{-5}$	$3.92 \cdot 10^{-8}$	$2.60 \cdot 10^{-8}$
C	$2.06 \cdot 10^{-3}$	$3.75 \cdot 10^{-3}$	$3.02 \cdot 10^{-3}$
Ca	$1.60 \cdot 10^{-2}$	$4.82 \cdot 10^{-3}$	$1.53 \cdot 10^{-2}$
Cl	$5.77 \cdot 10^{-1}$	$5.84 \cdot 10^{-1}$	$5.80 \cdot 10^{-1}$
K	$4.42 \cdot 10^{-7}$	$5.00 \cdot 10^{-4}$	$8.55 \cdot 10^{-4}$
Mg	$5.59 \cdot 10^{-2}$	$6.81 \cdot 10^{-2}$	$2.17 \cdot 10^{-1}$
Na	$4.96 \cdot 10^{-2}$	$5.02 \cdot 10^{-1}$	$4.98 \cdot 10^{-1}$
S	$3.04 \cdot 10^{-2}$	$3.08 \cdot 10^{-2}$	$1.98 \cdot 10^{-1}$
Si	$1.66 \cdot 10^{-4}$	$1.49 \cdot 10^{-4}$	$1.39 \cdot 10^{-4}$
Differences between initial and equilibrium solution [mol kgw^{-1}]			
Al	$4{,}52 \cdot 10^{-5}$	$1{,}92 \cdot 10^{-8}$	$6{,}02 \cdot 10^{-9}$
C	$-4{,}67 \cdot 10^{-4}$	$1{,}22 \cdot 10^{-3}$	$4{,}87 \cdot 10^{-4}$
Ca	$4{,}95 \cdot 10^{-3}$	$-6{,}23 \cdot 10^{-3}$	$4{,}28 \cdot 10^{-3}$
Cl	$1{,}93 \cdot 10^{-2}$	$2{,}67 \cdot 10^{-2}$	$2{,}23 \cdot 10^{-2}$
K	$-9{,}63 \cdot 10^{-3}$	$-9{,}13 \cdot 10^{-3}$	$-8{,}77 \cdot 10^{-3}$
Mg	$1{,}90 \cdot 10^{-3}$	$1{,}41 \cdot 10^{-2}$	$1{,}63 \cdot 10^{-1}$
Na	$1{,}68 \cdot 10^{-2}$	$2{,}29 \cdot 10^{-2}$	$1{,}91 \cdot 10^{-2}$
S	$1{,}03 \cdot 10^{-3}$	$1{,}41 \cdot 10^{-3}$	$1{,}68 \cdot 10^{-1}$
Si	$6{,}63 \cdot 10^{-5}$	$4{,}93 \cdot 10^{-5}$	$3{,}94 \cdot 10^{-5}$
Dissolution and precipitation of the mineral phases [mol kgw^{-1}]			
Δ CO_2	$1.10 \cdot 10^{-4}$	$-6.98 \cdot 10^{-1}$	$-8.53 \cdot 10^{-1}$
Δ Quartz	$-2.00 \cdot 10^{-2}$	$8.88 \cdot 10^{-1}$	$9.79 \cdot 10^{-1}$
Δ Calcite	$4.45 \cdot 10^{-4}$	$6.97 \cdot 10^{-1}$	$8.53 \cdot 10^{-1}$
Δ Orthoclase	$9.97 \cdot 10^{-3}$	$-6.61 \cdot 10^{-1}$	$-7.22 \cdot 10^{-1}$
Δ Anorthite	$-5.01 \cdot 10^{-3}$	$-6.90 \cdot 10^{-1}$	$-6.90 \cdot 10^{-1}$
Δ Goethite	$1.27 \cdot 10^{-10}$	$-1.90 \cdot 10^{-1}$	$-1.11 \cdot 10^{-1}$
Δ Chlorite	$-5.93 \cdot 10^{-10}$	$-3.84 \cdot 10^{-3}$	$-5.41 \cdot 10^{-2}$
Δ Illite		$7.89 \cdot 10^{-1}$	$8.60 \cdot 10^{-1}$
Δ Gypsum			$-1.66 \cdot 10^{-1}$

Composition 2 and 3 show similarities for the reaction with seawater, as already observed for the reaction with formation water. They also show a quite similar behaviour

as observed for the reactions with formation water. All mineral conversions except for chlorite are quite high, in a range of 10^{-1} to ~1 mol kgw^{-1}. The pH is buffered by dissolution of CO_2, precipitation of calcite and precipitation of illite. For both mineral compositions orthoclase, anorthite, and chlorite are dissolved by concurrent formation of illite and quartz. For composition 2 this leads to an increase of all ions in solution except potassium (only slight changes) and calcium, whereas for composition 3 all ions except potassium are increased. This difference in calcium concentration is again caused by the additional Ca source gypsum in composition 3. For composition 3 dissolution of gypsum is also responsible for the increased concentration of sulphur in solution.

A.8.3.3 Equilibration with seawater considering ion exchange

The calculations with an ion exchanger are only performed with composition 1. This mineral phase composition is equilibrated with seawater, considering ion exchange as an additional process.

It is assumed that montmorillonite is the major ion exchanger in our system. Data for the ion exchanger montmorillonite are available from NAGRA for MX-80 bentonite in a clay system. The exchange coefficients and the initial coverage of the different ions at the exchanger were taken from *Curti and Wersin* /CUR 02/, but were divided by a factor 100, because the considered aquifer sediment contains only less than 1 % of montmorillonite compared to about 80 % in MX-80 bentonite. The initial configuration of the ion exchanger is listed in Tab. A.26. However, the initial coverage is representative for bentonite in equilibrium with its porewater. Therefore equilibrium calculations with formation water are performed to pre-equilibrate the exchanger for our conditions. The coverage of the exchanger after 10 equilibration cycles calculated with PHREEQC is also listed in Tab. A.26. Pre-equilibration with formation water leads to a strong decrease of sodium sites and an increase in potassium covered sites, whereas all other ion contents on the exchanger are increased.

Tab. A.26 Initial configuration of the ion exchanger for the bentonite conditions assumed by NAGRA on the basis of /CUR 02/ and after equilibration with formation water

Exchanger	**NAGRA configuration [mol kgw^{-1}]**	**Pre-equilibration with formation water [mol kgw^{-1}]**
NaX	$3.00 \cdot 10^{-2}$	$6.642 \cdot 10^{-4}$
CaX_2	$1.49 \cdot 10^{-3}$	$1.556 \cdot 10^{-2}$
KX	$6.00 \cdot 10^{-4}$	$2.979 \cdot 10^{-4}$
MgX_2	$9.05 \cdot 10^{-4}$	$1.681 \cdot 10^{-3}$
HX	0.00	$1.786 \cdot 10^{-7}$
$AlOHX_2$	0.00	$2.297 \cdot 10^{-7}$
AlX_3	0.00	$2.315 \cdot 10^{-9}$
FeX_2	0.00	$3.315 \cdot 10^{-6}$

The reaction of seawater with composition 1 including an ion exchanger shows generally a very similar behaviour to the system without exchanger (Tab. A.27). In both systems quartz and anorthite are dissolved in a similar order of magnitude, orthoclase and calcite are precipitated and CO_2 is left from solution. However, the converted amount of minerals is slightly higher for the system with ion exchanger. Particularly more calcite is precipitated and more CO_2 left the solution in the system with exchanger. Differences exist for the mineral phases chlorite and goethite. In the system with exchanger iron-bearing chlorite precipitates and some goethite is dissolved. This is vice versa in the system without exchanger. But the conversions of both minerals are quite low, particular in the system without exchanger.

Tab. A.27 Results of the equilibration of the mineral phase composition 1 with seawater considering ion exchange

	Composition 1
pH	7.18
Components in solution [mol kgw^{-1}]	
Al	$3.23 \cdot 10^{-4}$
C	$1.55 \cdot 10^{-3}$
Ca	$3.01 \cdot 10^{-2}$
Cl	$5.77 \cdot 10^{-1}$
K	$1.80 \cdot 10^{-7}$
Mg	$5.48 \cdot 10^{-2}$
Na	$4.69 \cdot 10^{-1}$

Tab. A.27 (cont.) Results of the equilibration of the mineral phase composition 1 with seawater considering ion exchange

	Composition 1
S	$3.04 \cdot 10^{-2}$
Si	$2.73 \cdot 10^{-4}$
Differences between initial and equilibrium solution [mol kgw^{-1}]	
Al	$3.23 \cdot 10^{-4}$
C	$-1.42 \cdot 10^{-3}$
Ca	$2.85 \cdot 10^{-2}$
Cl	$5.76 \cdot 10^{-1}$
K	$-5.38 \cdot 10^{-5}$
Mg	$5.46 \cdot 10^{-1}$
Na	$4.68 \cdot 10^{-1}$
S	$3.01 \cdot 10^{-2}$
Si	$2.73 \cdot 10^{-4}$
Ions at the exchanger [mol kgw^{-1}]	
NaX	$2.69 \cdot 10^{-2}$
CaX_2	$1.47 \cdot 10^{-3}$
KX	$9.15 \cdot 10^{-5}$
MgX_2	$2.79 \cdot 10^{-3}$
HX	$5.43 \cdot 10^{-8}$
$AlOHX_2$	$2.15 \cdot 10^{-9}$
AlX_3	$6.72 \cdot 10^{-12}$
FeX_2	$2.29 \cdot 10^{-10}$
Differences between initial and equilibrium Ion exchanger [mol kgw^{-1}]	
NaX	$2.62 \cdot 10^{-2}$
CaX_2	$-1.41 \cdot 10^{-2}$
KX	$-2.06 \cdot 10^{-4}$
MgX_2	$1.11 \cdot 10^{-3}$
HX	$-1.24 \cdot 10^{-7}$
$AlOHX_2$	$-2.08 \cdot 10^{-7}$
AlX_3	$-2.25 \cdot 10^{-9}$
FeX_2	$-3.31 \cdot 10^{6}$
Dissolution and precipitation of the mineral phases [mol kgw^{-1}]	
Δ CO_2	$3.59 \cdot 10^{-4}$
Δ Quartz	$-2.02 \cdot 10^{-}$
Δ Calcite	$7.15 \cdot 10^{-4}$
Δ Orthoclase	$1.02 \cdot 10^{-2}$
Δ Anorthite	$-5.25 \cdot 10^{-3}$
Δ Goethite	$-4.10 \cdot 10^{-7}$
Δ Chlorite	$1.91 \cdot 10^{-6}$

Due to the high amount of sodium and magnesium in the seawater both ions become enriched at the ion exchanger. All other ions are to some extent released from the exchanger. Since the pre-equilibrated exchanger is preferably covered by calcium, this ion is released from the exchanger, although its concentration in seawater is relatively high.

As a consequence of the increased release of CO_2 from solution the concentration of carbon is lower in the system with ion exchanger compared to the one without. The higher amount of precipitated calcite is responsible for the lower pH 7.18 (compared to 7.32 of the system with ion exchanger). However, calcium is increased in solution, because the exchanger represents a source of calcium (see above). Sodium and magnesium are bound to the exchanger and, therefore, have lower concentrations than in the system without exchanger.

A.8.4 Transport calculations

One-dimensional transport calculations have been performed with the PHREEQC code using composition 1 as mineral mixture in a column. The transport conditions have been adapted to conditions expected for the scenario of seawater inundation of the area. Calculations from /FLU 09/ show that under such conditions flow velocities are low. Typical flow velocities of about $8 \cdot 10^{-3}$ m a^{-1} for the infiltration of seawater into the upper aquifer have been applied. The data used in the calculations are shown in Tab. A.28.

The initial concentration of the formation water used in the transport calculations is that obtained after equilibration with composition 1 (Tab. A.24). The initial content of mineral phases corresponds to that compiled in Tab. A.23.

Tab. A.28 Conditions used in the 1D transport calculations with PHREQC

Parameter [unit]	**Value**
Number of cells	40
Cell length [m]	0.125
Shifts (number of time steps)	400
Time step length [s]	$5 \cdot 10^{8}$
Flow velocity [m s^{-1}]	$2.5 \cdot 10^{-10}$
Diffusion coefficient [m^2 s^{-1}]	$1 \cdot 10^{9}$
Dispersion length [m]	0.5

The results of the transport calculations are shown as spatial distributions in Fig. A.14 to Fig. A.17 for the pH-value and important elements in solution and in Fig. A.18 to Fig. A.21 for the mineral phases. The calculations have been performed for 400 time steps (indicated by shifts in Tab. A.28), i. e. for about. 6370 years ($2 \cdot 10^{11}$ s). This value is in the range of the duration for past seawater transgressions during a warm stage. In all figures the time step is given. One time step corresponds to approximately 16 years. The distance is denoted in cells, i. e. the total length of the column corresponds to 5 m (40 cells).

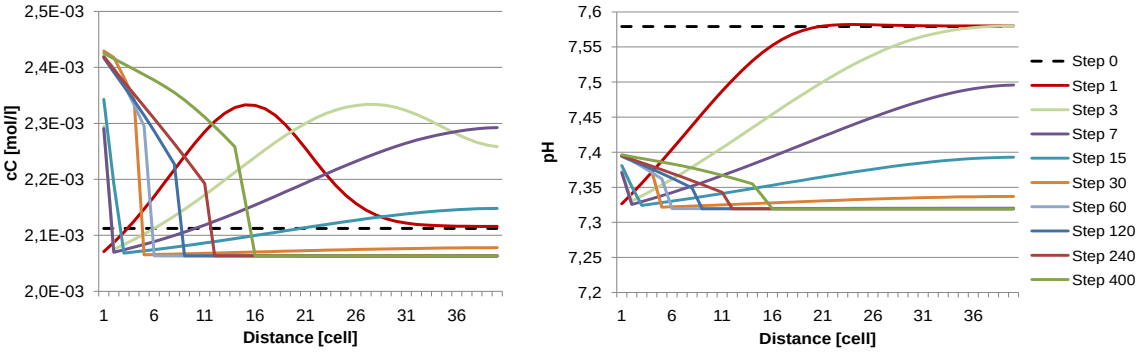

Fig. A.14 Spatial distribution of DIC concentration (left) and pH (right) in the column

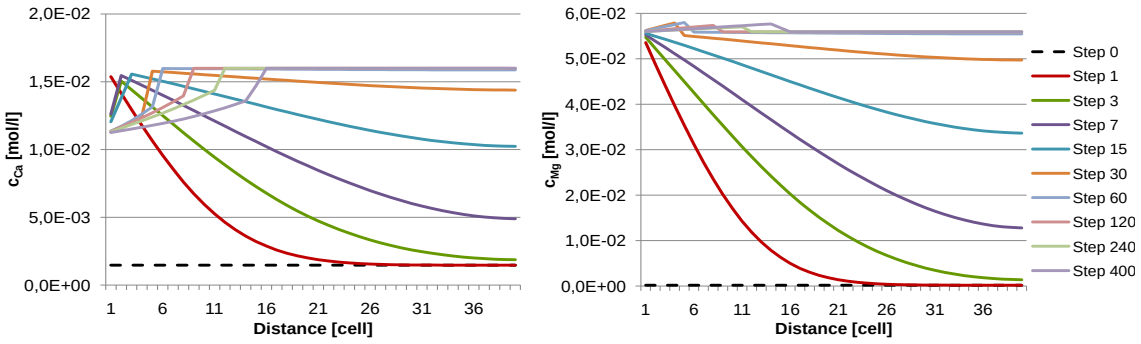

Fig. A.15 Spatial distribution of Ca (left) and Mg (right) concentration in the column

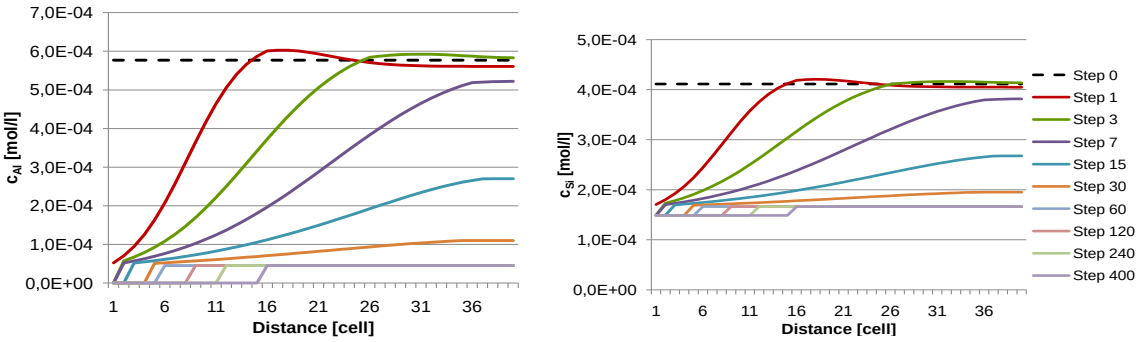

Fig. A.16 Spatial distribution of Al (left) and Si (right) concentration in the column

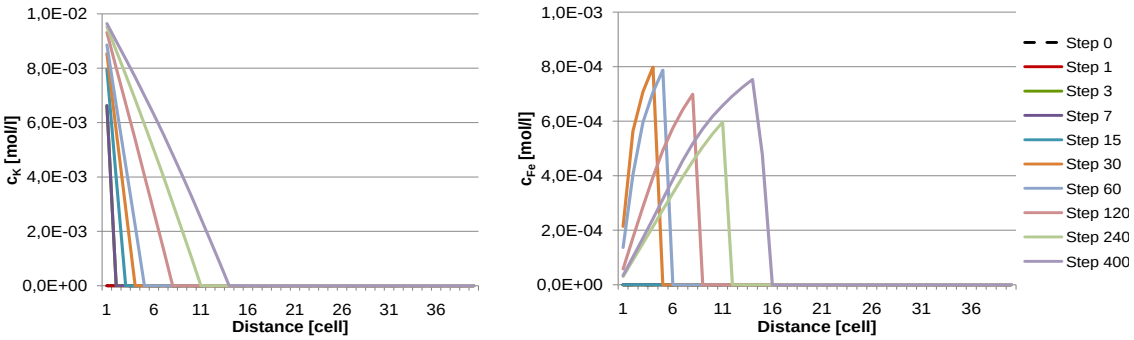

Fig. A.17 Spatial distribution of K (left) and Fe (right) concentration in the column

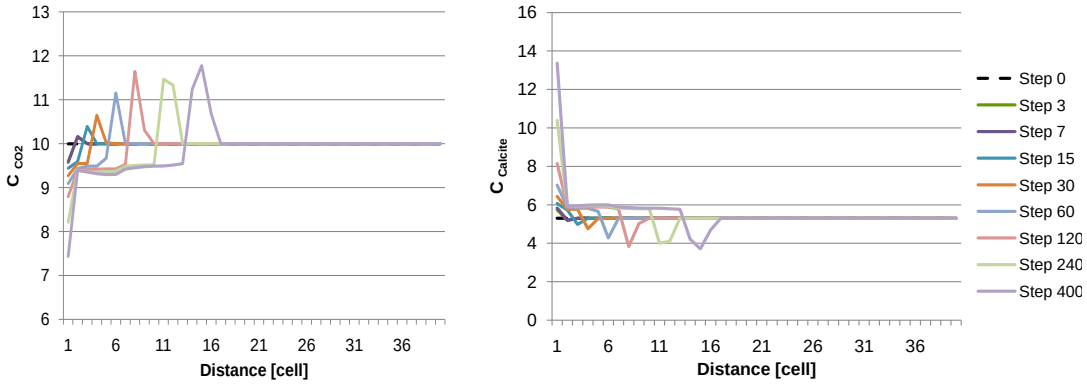

Fig. A.18 Spatial distribution of CO_2 (left) and calcite (right) in the column

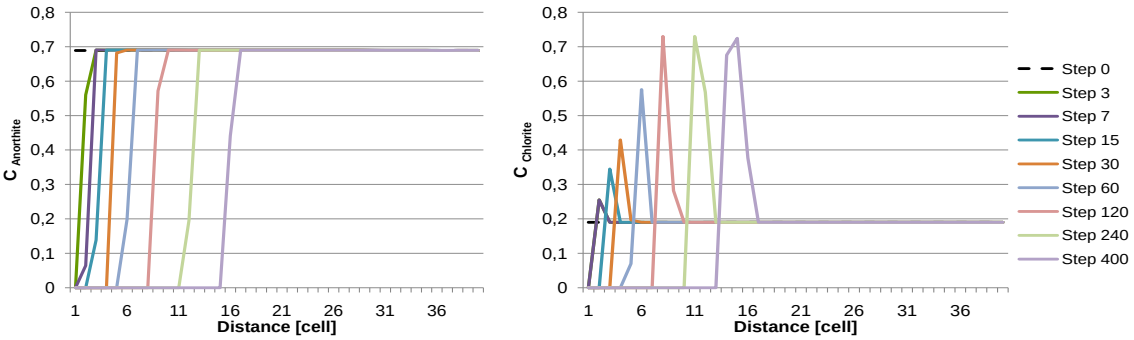

Fig. A.19 Spatial distribution of anorthite (left) and chlorite (right) in the column

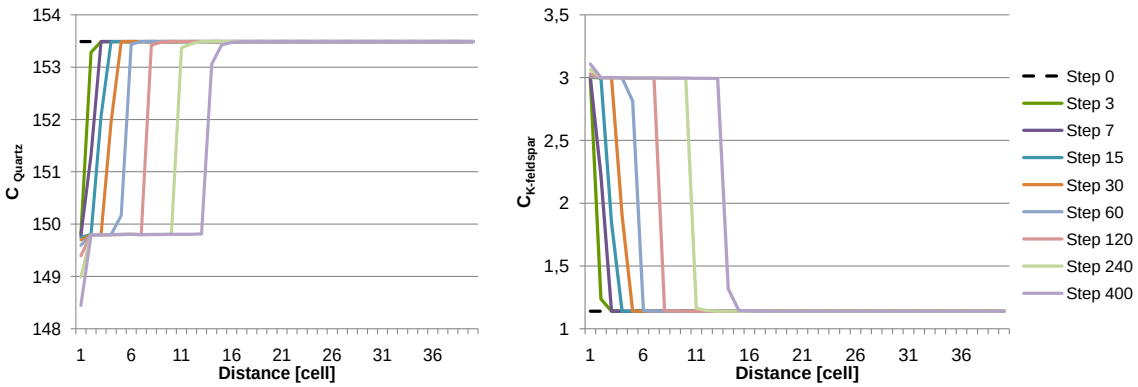

Fig. A.20 Spatial distribution of quartz (left) and orthoclase (right) in the column

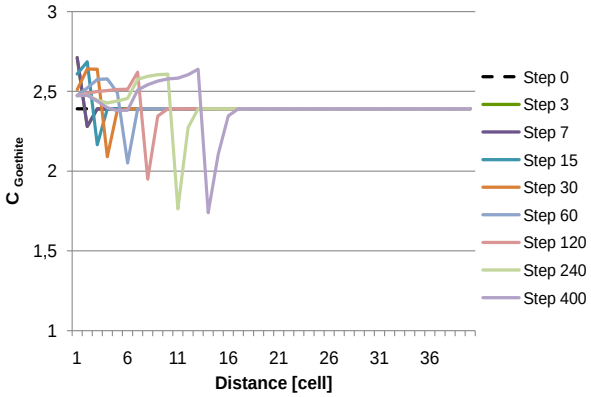

Fig. A.21 Spatial distribution of goethite in the column

The results for pH-value and concentrations in solution show that two fronts move through the column. The first one leads to changes in pH and all element concentrations over the whole 5 m column after 7 shifts already and results in an equilibrium state after 60 shifts (~960 a). The equilibration state is the same, which was calculated for the batch reaction of composition 1 with seawater, i. e. the pH-value and the concentration of all components in solution reach values as listed in Tab. A.25 for composition 1 (see also the discussion of the responsible reactions in this section). As can be seen, the initial pH-value of 7.58 of the formation water is rapidly reduced to 7.32 in the first cell after the first time step.

The second front is not homogeneous. It penetrates up to cell 16 (2 m) into the column after 400 shifts. The front occurs, when anorthite is fully dissolved and no more available, which is already the case in the first cell after 3 time steps. Ahead of the front there is an area, where calcite and goethite are dissolved, CO_2 is released from solution and chlorite and orthoclase precipitate. Under these conditions the pH is increased to about 7.36. Behind this peak the conditions are different, i. e. the amount of calcite and goethite is increased, CO_2 is dissolved and its amount becomes significantly reduced and chlorite is fully dissolved. For this part of the front the pH is increased to about 7.4. In this second front the concentrations of calcium, silica and aluminium decrease, whereas the concentrations of carbon, magnesium, potassium and iron increase. There are some indications, at least for calcite, CO_2, quartz and orthoclase that a third front is built up, but only affecting the first cell.

These results show that within the simulation time of 6370 years under the conditions expected for a seawater inundation changes of the chemical conditions occur deeply down into the upper aquifer, the affected depth is much larger than the considered 5 m

in our model. For the whole 5 m column changes in chemical conditions are already observed within 7 time steps (~110 years). The minerals of the reference composition strongly buffer the pH of the system in a near neutral pH-range. But the calculations show that some minerals are consumed by reaction with seawater leading to a further change of the conditions. A second front, which is formed, however penetrates only 2 m into the aquifer within 6370 years, which might not be of relevance for an aquifer of about 100 m thickness.

A.8.5 Conclusions for the calculation of seawater intrusion

PHREEQC calculations were performed to get a deeper understanding of relevant mineral phases and processes occurring in the upper sedimentary aquifer at Gorleben site in Northern Germany for the scenario seawater inundation. Firstly, the calculations helped to identify relevant mineral phases, which are likely in equilibrium with the Ca-HCO_3 water of the upper aquifer, as quartz, calcite, feldspar (orthoclase, anorthite), and chlorite.

The results indicate that in the case intrusion of seawater with a pH of 8.2 into the aquifer changes in pH and concentration of relevant major and trace elements like DIC, Ca, Mg, Fe and Al, which might influence the K_d-value of the radionuclides, occur. However, the high CO_2 partial pressure and the minerals calcite and anorthite buffer the pH in a way that values lower than that of the formation water were established. The transport calculations show that for this scenario different geochemical fronts move through the aquifer. For typical durations of this scenario, i. e. ~5000 years, some mineral phases like anorthite and chlorite might be dissolved, but this dissolution is restricted to only few meters. This supports the assumption in our conceptual model that anorthite is an important mineral phase likely affecting the Al concentration over long time scales.

In this project it is decided for reasons of clarity to restrict the description of the changing chemical conditions on mineral dissolution/precipitation processes. However, calculations including ion exchange reactions show that these impact to some extent pH-value and relevant ion concentrations in solution. Therefore, in a future project ion exchange processes should be included

Finally, this 1D transport calculation with spatially and temporally changing geochemical conditions represents a very good test case for verification of the new r^3t version.

A.9 Smart K_d-values and radionuclide concentration distributions

In the following, figures of smart K_d-values and radionuclide concentration distributions, which were not depicted in section 8, are given.

South **North**

a) 160,000 a, source term according to the U-248 source term, logarithmic scale [mol m^{-3}]

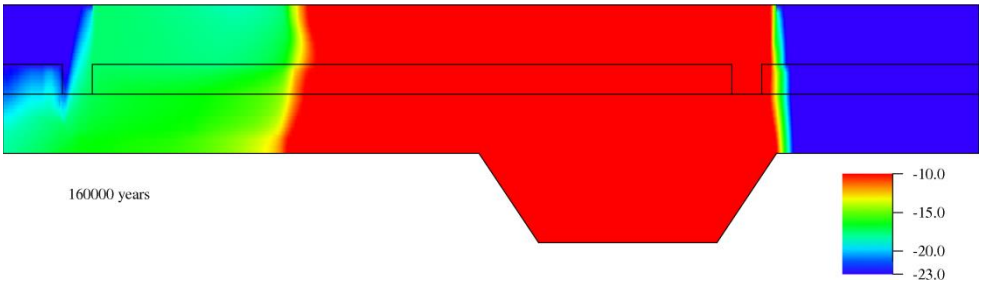

b) 176,500 a, source term according to the U-248 source term, logarithmic scale in [mol m^{-3}]

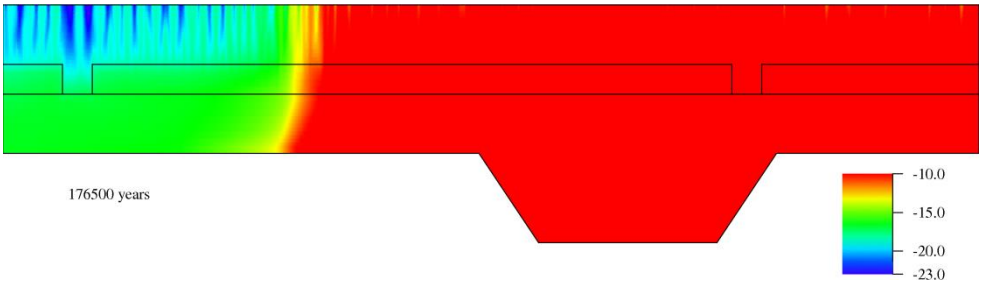

Fig. A.22 Distribution of the inert tracer after the constant boundary conditions (160,000 a) and after the seawater transgression (176,500 a) for the source terms in accordance to the source term of U-238

South **North**

a) Smart K_d-value, logarithmic scale [m3 kg^{-1}], 0 a

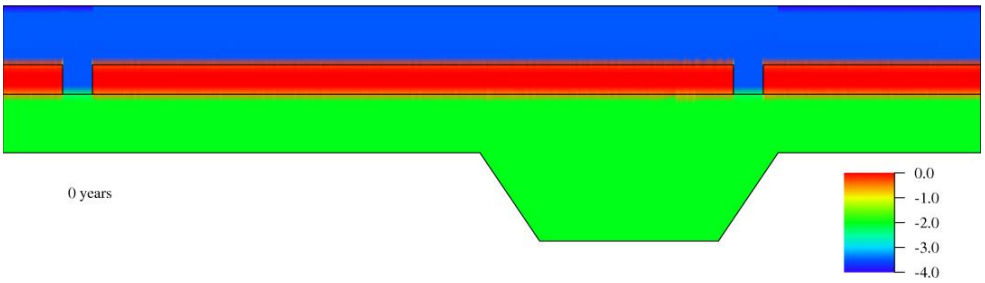

b) Smart K_d-value, logarithmic scale [m^3 kg^{-1}], 11,500 a

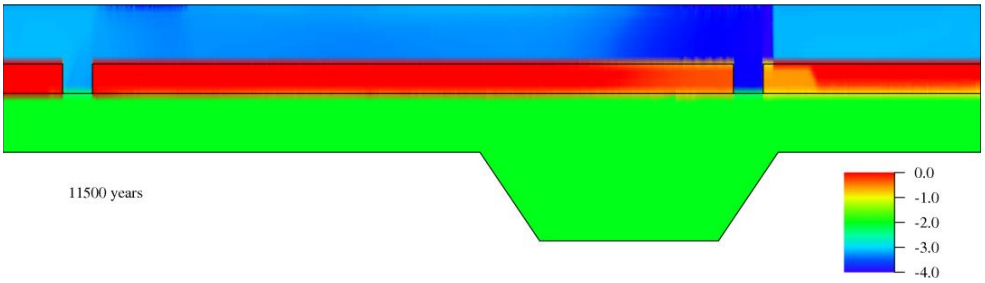

c) Smart K_d-value, logarithmic scale [m^3 kg^{-1}], 160,000 a

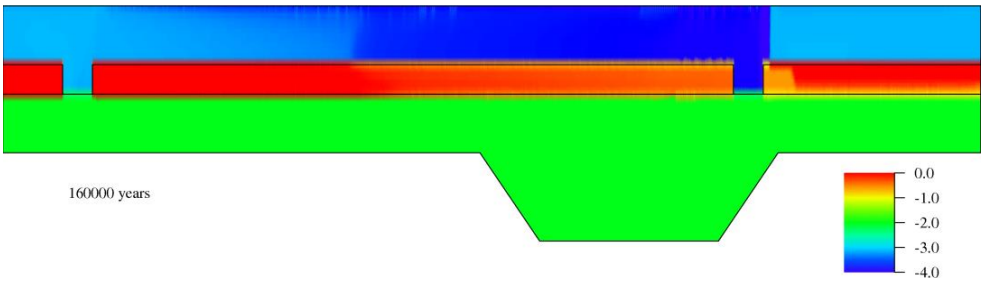

d) Smart K_d-value, logarithmic scale [m^3 kg^{-1}], 176,500 a

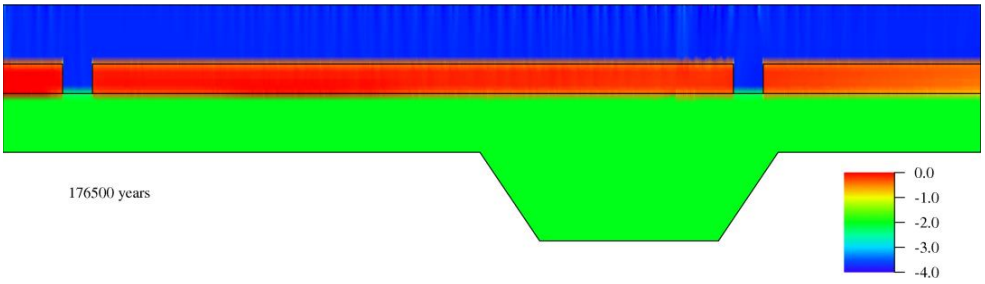

Fig. A.23 Smart K_d-values for Np-237 for different points in time

South **North**

a) Conventional K_d-value, 160,000 a, logarithmic scale [mol m^{-3}]

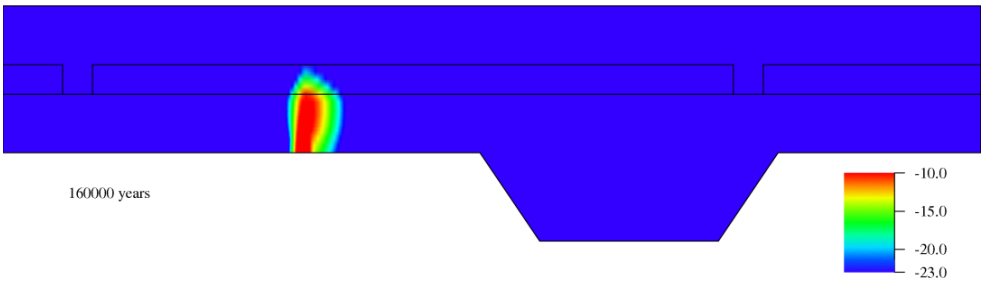

b) Smart K_d-value, 160,000 a, logarithmic scale [mol m^{-3}]

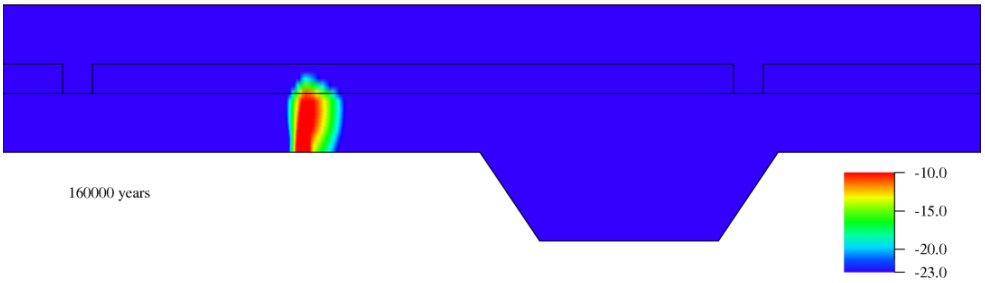

c) Conventional K_d-value, 176,500 a, logarithmic scale [mol m^{-3}]

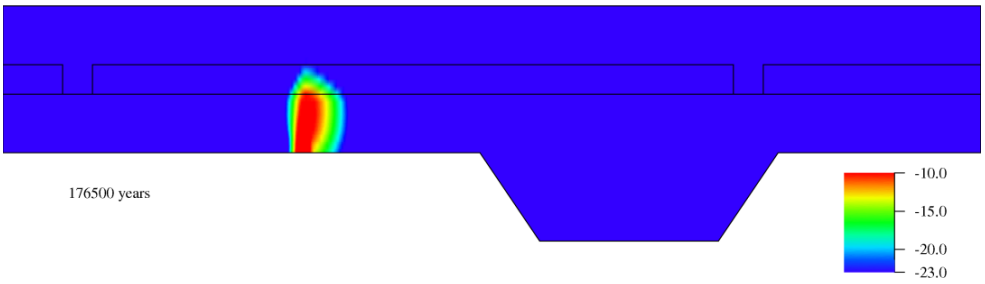

d) Smart K_d-value, 176,500 a, logarithmic scale [mol m^{-3}]

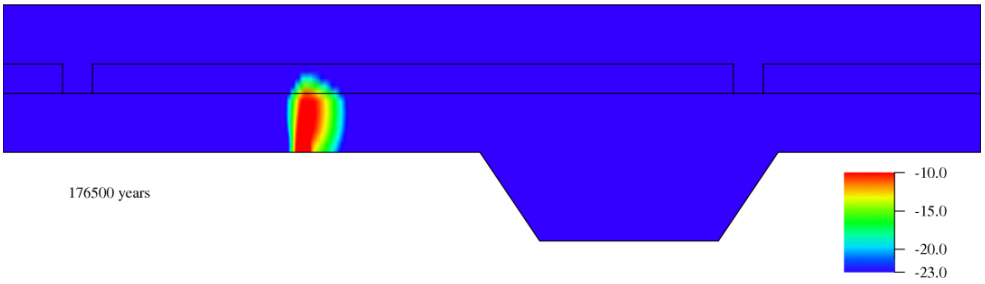

Fig. A.24 Distribution of Np-237 after the constant boundary conditions (160,000 a) and after the seawater transgression (176,500 a) employing the conventional K_d-value /SUT 98/ and the smart K_d-value

South **North**

a) Smart K_d-value, logarithmic scale [m^3 kg^{-1}], 0 a

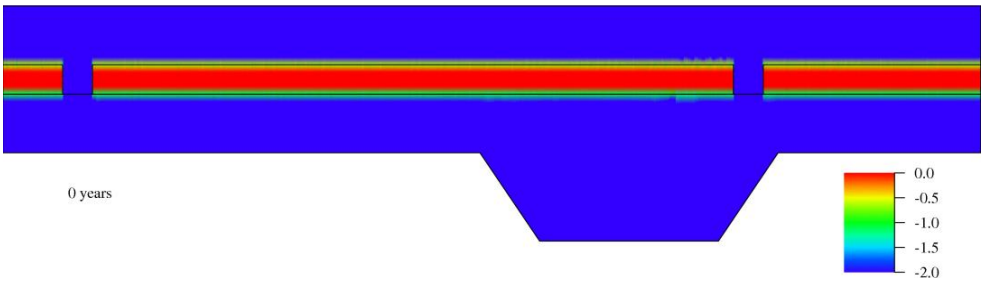

b) Smart K_d-value, logarithmic scale [m^3 kg^{-1}], 11,500 a

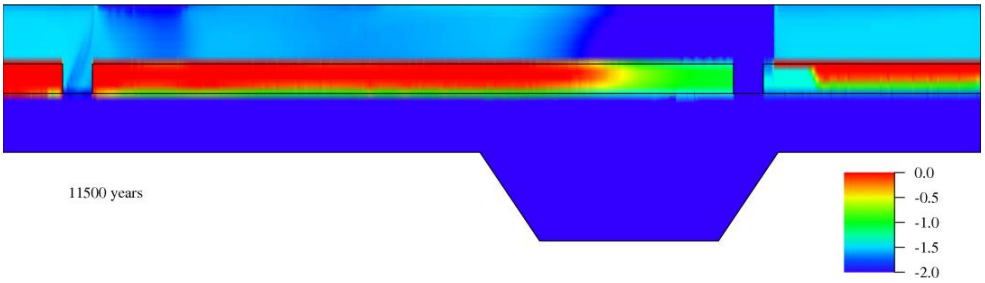

c) Smart K_d-value, logarithmic scale [m^3 kg^{-1}], 160,000 a

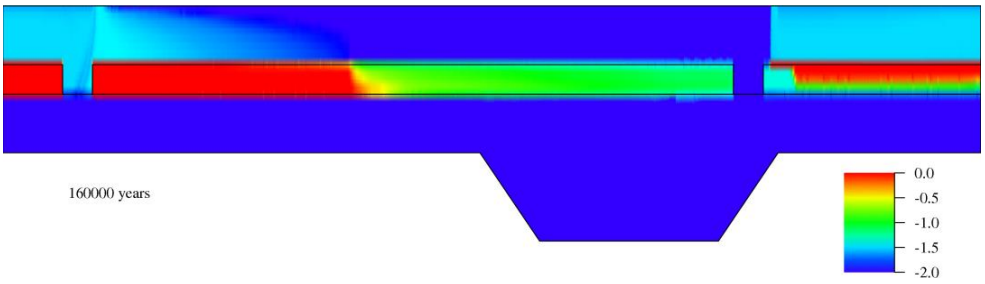

d) Smart K_d-value, logarithmic scale [m^3 kg^{-1}], 176,500 a

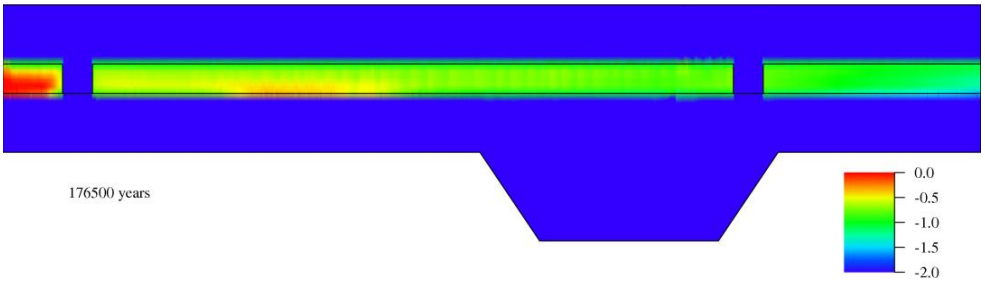

Fig. A.25 Smart K_d-values for Ni-59 for different points in time

South **North**

a) Conventional K_d-value, 160,000 a, logarithmic scale [mol m^{-3}]

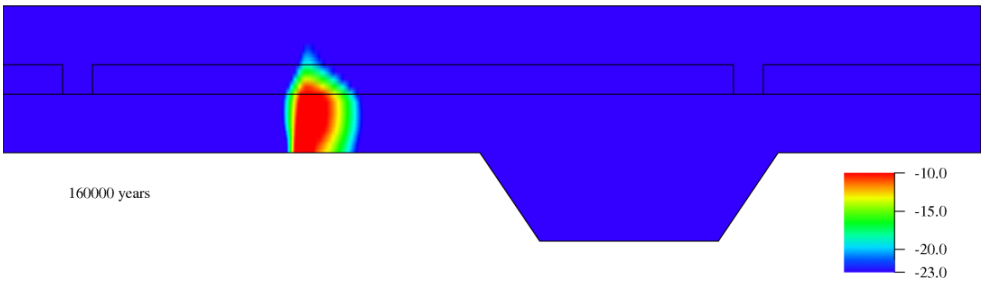

b) Smart K_d-value, 160,000 a, logarithmic scale [mol m^{-3}]

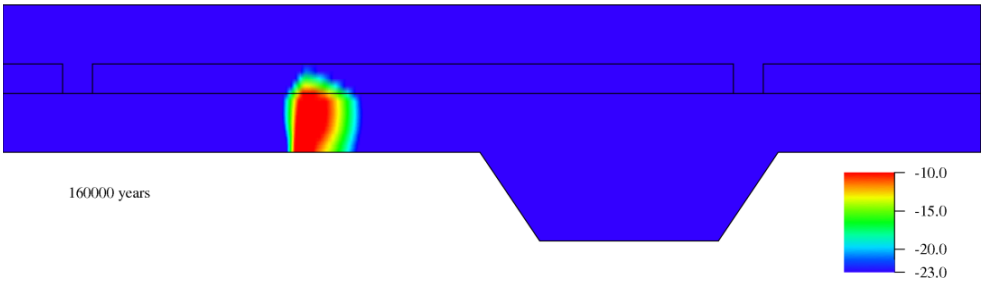

c) Conventional K_d-value, 176,500 a, logarithmic scale [mol m^{-3}]

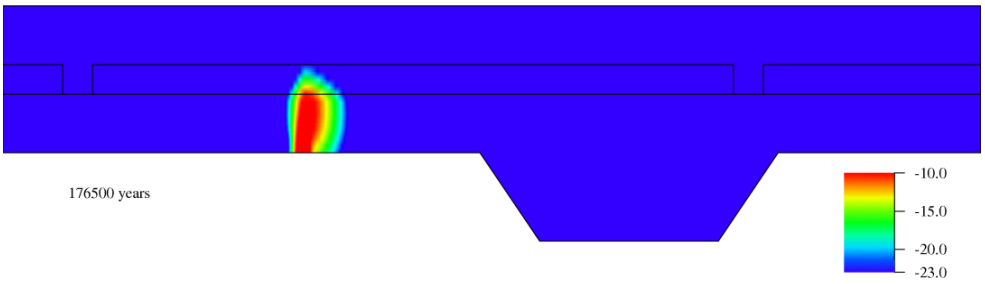

d) Smart K_d-value, 176,500 a, logarithmic scale [mol m^{-3}]

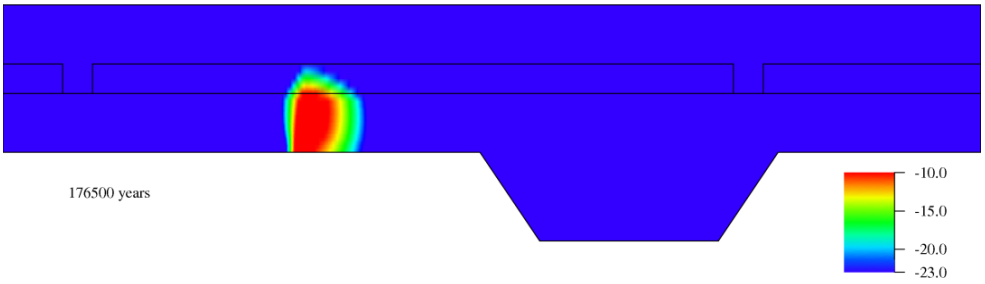

Fig. A.26 Distribution of Ni-59 after the constant boundary conditions (160,000 a) and after the seawater transgression (176,500 a) employing the conventional K_d-value /SUT 98/ and the smart K_d-value

South **North**

a) Smart K_d-value, logarithmic scale [m^3 kg^{-1}], 0 a

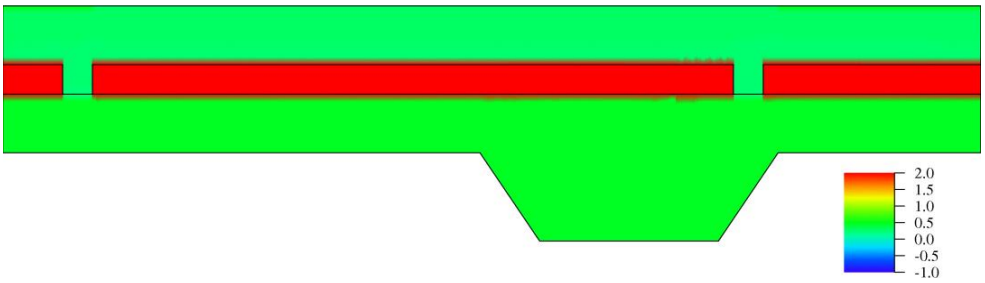

b) Smart K_d-value, logarithmic scale in [m^3 kg^{-1}], 11,500 a

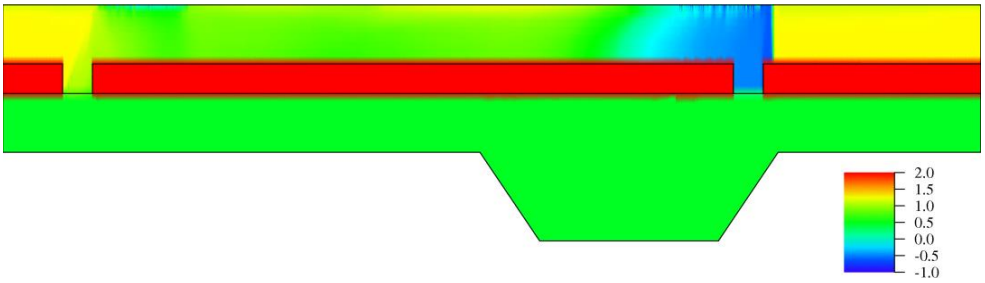

c) Smart K_d-value, logarithmic scale in [m^3 kg^{-1}], 160,000 a

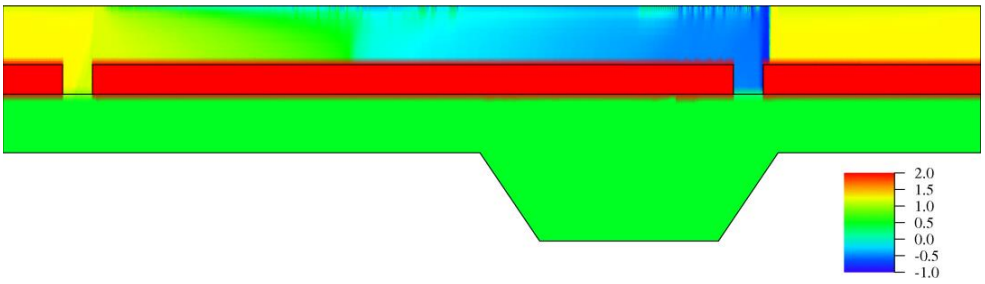

d) Smart K_d-value, logarithmic scale in [m^3 kg^{-1}], 176,500 a

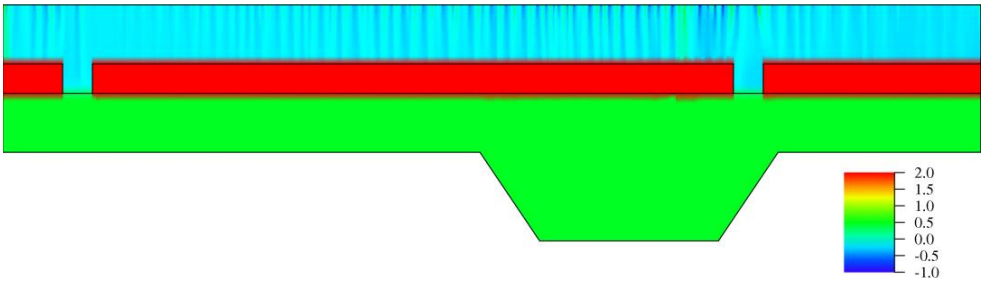

Fig. A.27 Smart K_d-values for Am-243 for different points in time

South **North**

a) Conventional K_d-value, 160,000 a, logarithmic scale [mol m^{-3}]

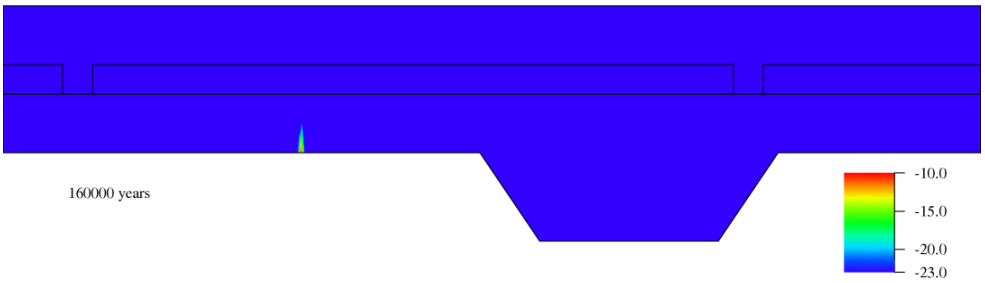

b) Smart K_d-value, 160,000 a, logarithmic scale [mol m^{-3}]

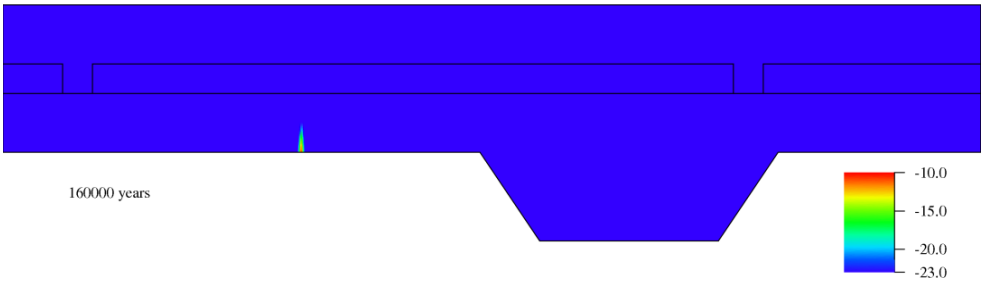

c) Conventional K_d-value, 176,500 a, logarithmic scale [mol m^{-3}]

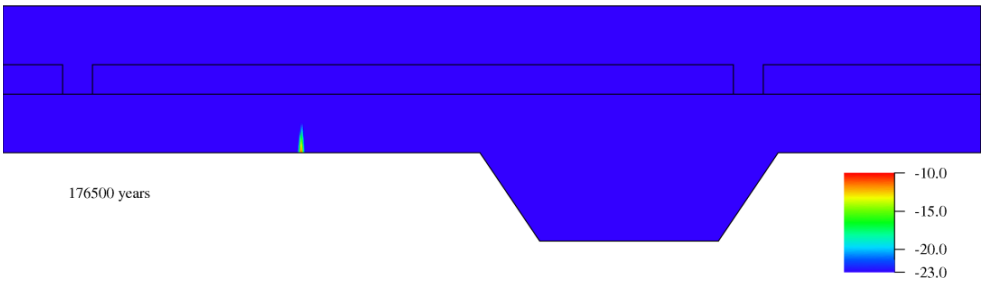

d) Smart K_d-value, 176,500 a, logarithmic scale [mol m^{-3}]

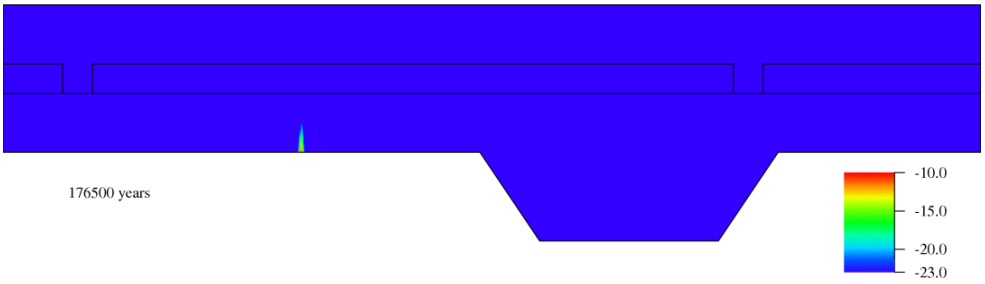

Fig. A.28 Distribution of Am-243 after the constant boundary conditions (160,000 a) and after the seawater transgression (176,500 a) employing the conventional K_d-value /SUT 98/ and the smart K_d-value

South **North**

a) Smart K_d-value, logarithmic scale [m^3 kg^{-1}], 0 a

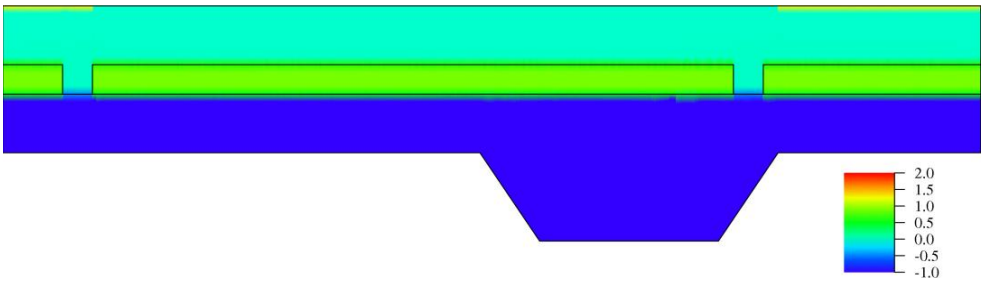

b) Smart K_d-value, logarithmic scale [m^3 kg^{-1}], 11,500 a

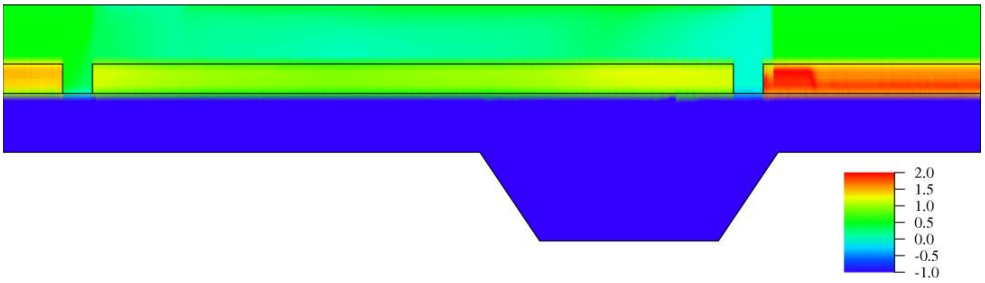

c) Smart K_d-value, logarithmic scale [m^3 kg^{-1}], 160,000 a

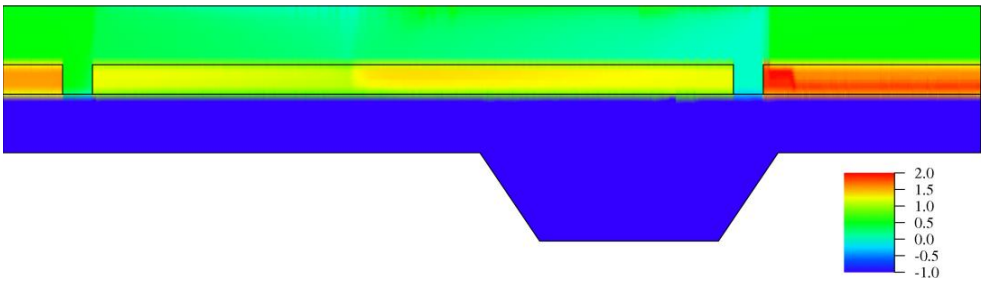

d) Smart K_d-value, logarithmic scale [m^3 kg^{-1}], 176,500 a

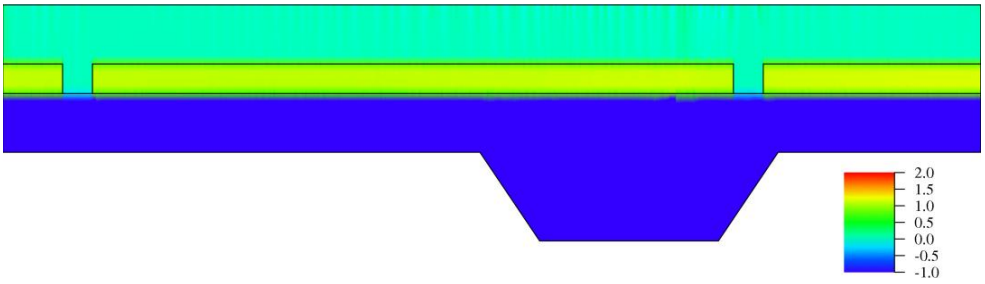

Fig. A.29 Smart K_d-values for Pu-239 for different points in time

South **North**

a) Conventional K_d-value, 160,000 a, logarithmic scale [mol m^{-3}]

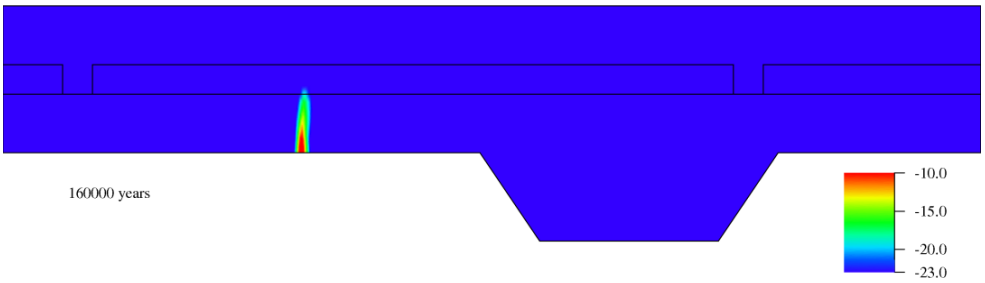

b) Smart K_d-value, 160,000 a, logarithmic scale [mol m^{-3}]

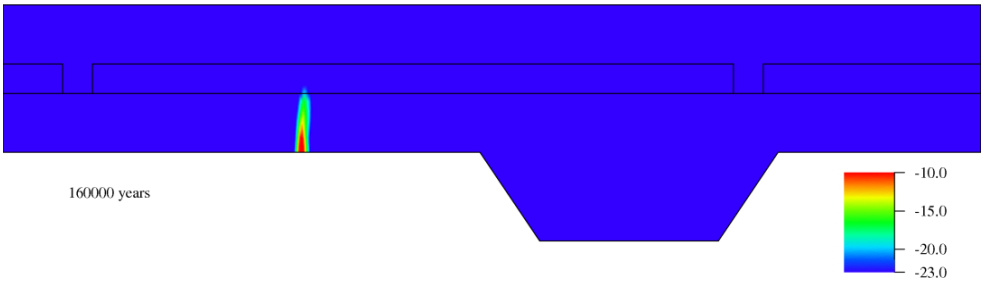

c) Conventional K_d-value, 176,500 a, logarithmic scale [mol m^{-3}]

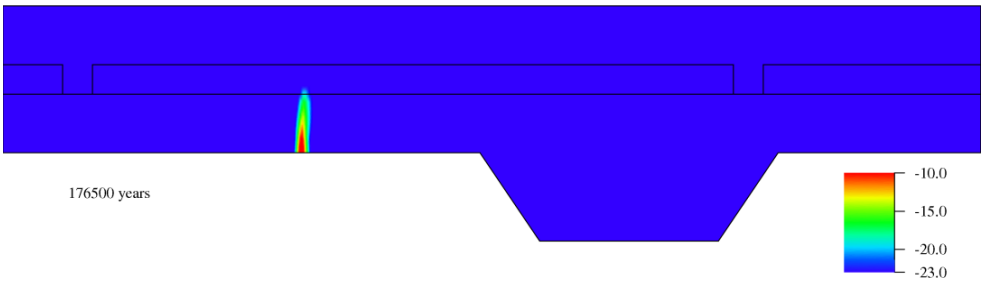

d) Smart K_d-value, 176,500 a, logarithmic scale [mol m^{-3}]

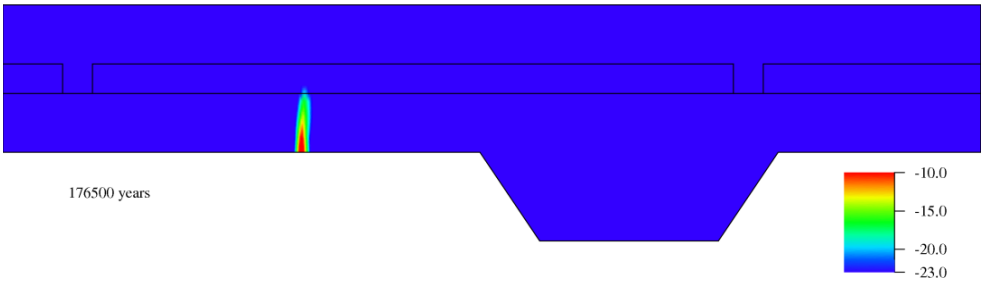

Fig. A.30 Distribution of Pu-239 after the constant boundary conditions (160,000 a) and after the seawater transgression (176,500 a) employing the conventional K_d-value /SUT 98/ and the smart K_d-value

South **North**

a) Conventional K_d-value, 160,000 a, logarithmic scale [mol m^{-3}]

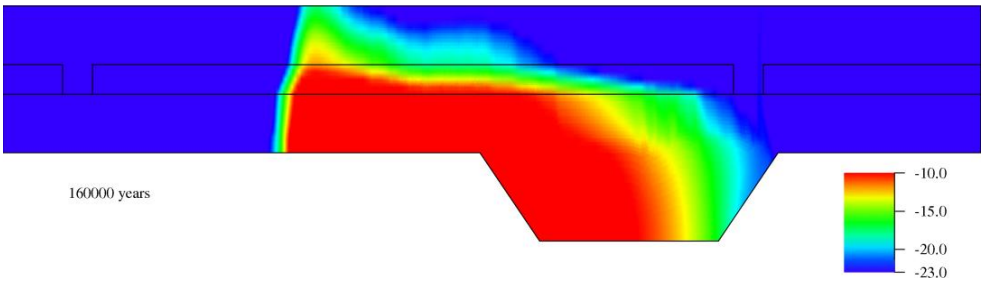

b) Smart K_d-value, 160,000 a, logarithmic scale [mol m^{-3}]

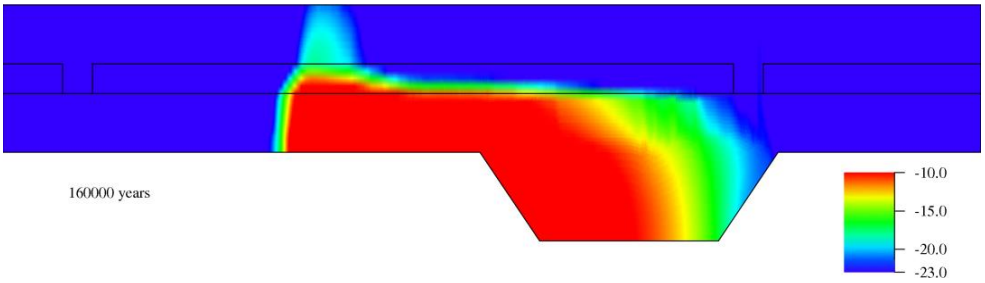

Fig. A.31 Distribution of U-238 after the constant boundary conditions (160,000 a) employing the conventional K_d-value /SUT 98/ and the smart K_d-value. Respective smart K_d-values in Fig. 8.20

South **North**

a) Conventional K_d-value, 160,000 a, logarithmic scale [mol m^{-3}]

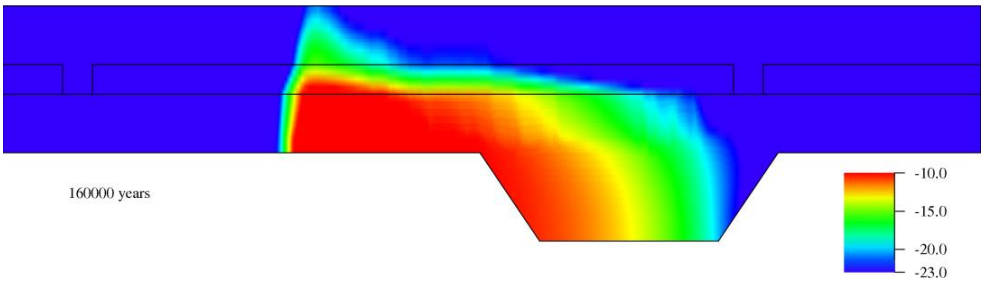

b) Smart K_d-value, 160,000 a, logarithmic scale [mol m^{-3}]

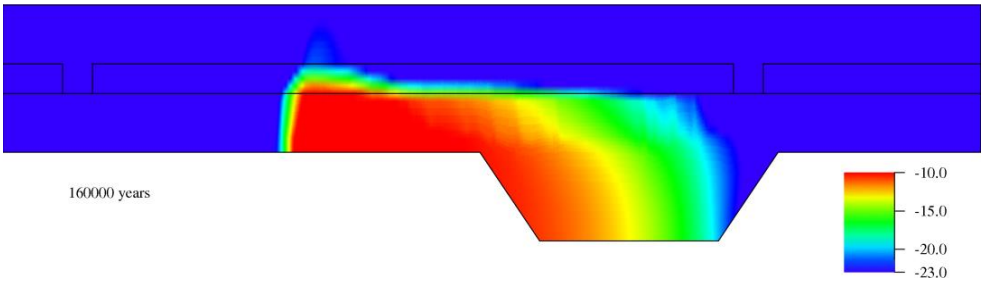

Fig. A.32 Distribution of U-234 after the constant boundary conditions (160,000 a) employing the conventional K_d-value /SUT 98/ and the smart K_d-value. Respective smart K_d-values in Fig. 8.20

South **North**

a) Smart K_d-value, logarithmic scale [m^3 kg^{-1}], 0 a

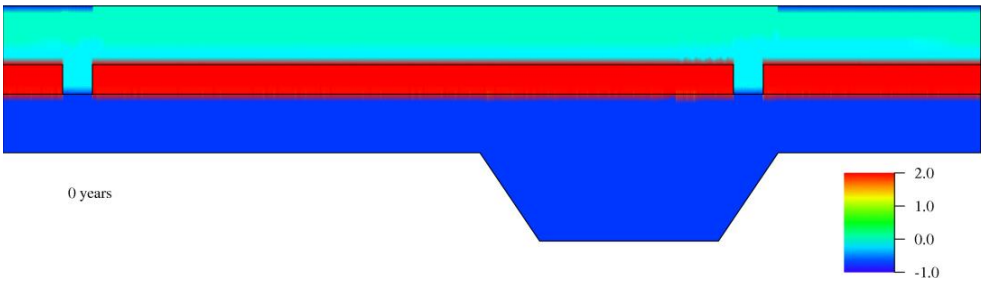

b) Smart K_d-value, logarithmic scale [m^3 kg^{-1}], 11,500 a

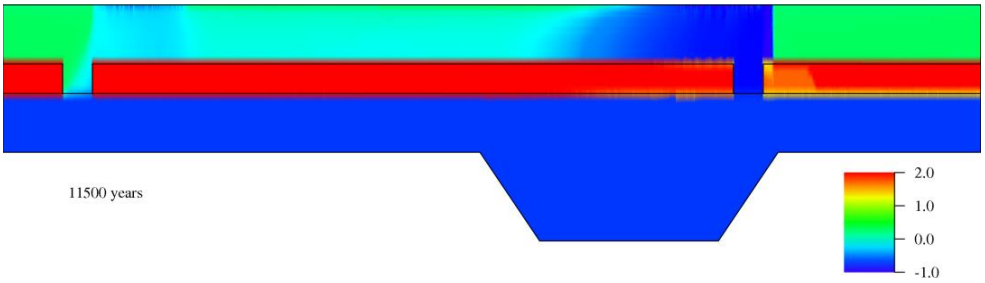

c) Smart K_d-value, logarithmic scale [m^3 kg^{-1}], 160,000 a

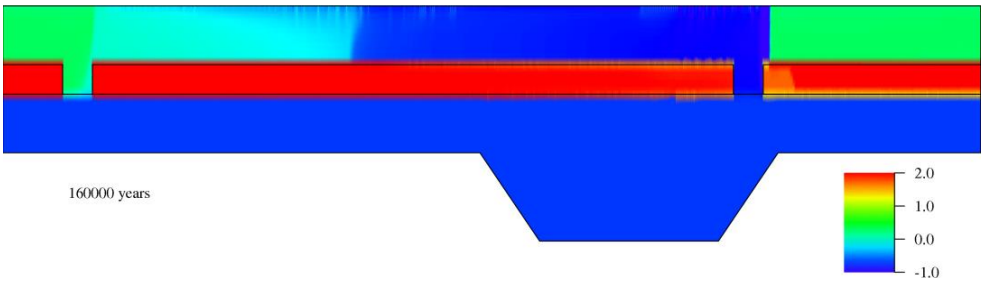

d) Smart K_d-value, logarithmic scale [m^3 kg^{-1}], 176,500 a

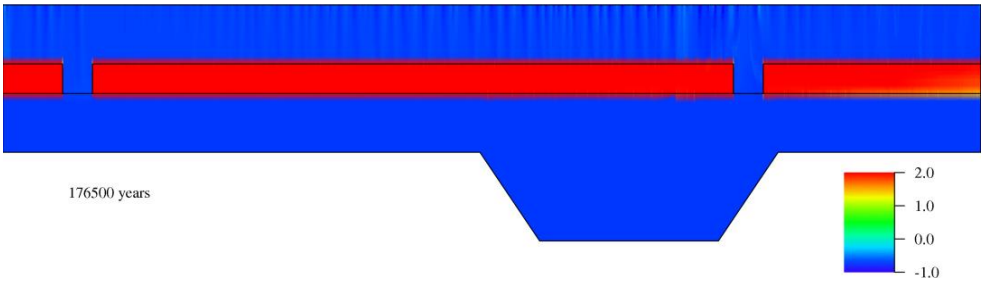

Fig. A.33 Smart K_d-values for Ra-230 for different points in time

South **North**

a) Conventional K_d-value, 160,000 a, logarithmic scale [mol m^{-3}]

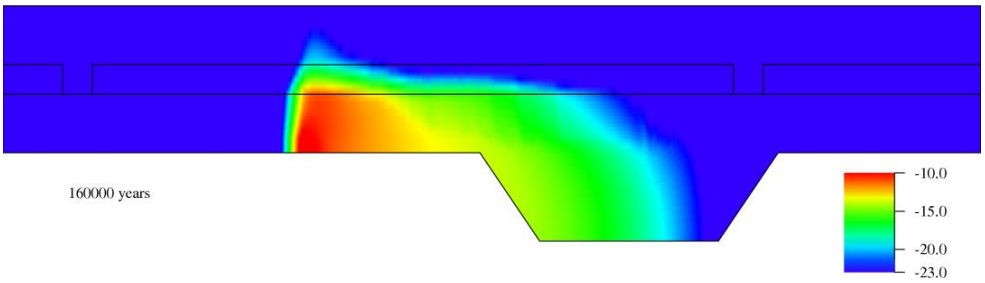

b) Smart K_d-value, 160,000 a, logarithmic scale [mol m^{-3}]

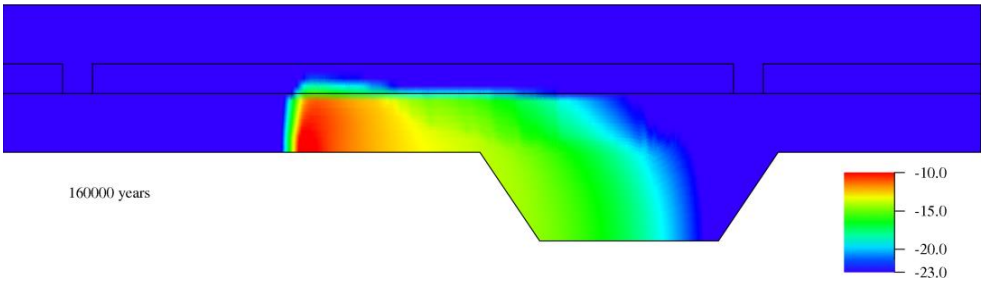

Fig. A.34 Distribution of Ra-230 after the constant boundary conditions (160,000 a) employing the conventional K_d-value /SUT 98/ and the smart K_d-value. Respective smart K_d-values in Fig. 8.20

Gesellschaft für Anlagen- und Reaktorsicherheit (GRS) mbH

Schwertnergasse 1
50667 Köln
Telefon +49 221 2068-0
Telefax +49 221 2068-888

Forschungszentrum
85748 Garching b. München
Telefon +49 89 32004-0
Telefax +49 89 32004-300

Kurfürstendamm 200
10719 Berlin
Telefon +49 30 88589-0
Telefax +49 30 88589-111

Theodor-Heuss-Straße 4
38122 Braunschweig
Telefon +49 531 8012-0
Telefax +49 531 8012-200

www.grs.de

Helmholtz-Zentrum Dresden-Rossendorf e.V. (HZDR) Institut für Ressourcenökologie
Postfach 51 04 19
01314 Dresden

Goethe-Universität Frankfurt a. M. Goethe-Zentrum für wissenschaftliches Rechnen (G-CSC)
Kettenhofweg 139
60325 Frankfurt am Main

ISBN 978-3-939355-76-2